Controlling the coupled particle field dynamics of laser illuminated atoms close to an optical nanofibre

Dissertation zur Erlangung des akademischen Grades Doctor of Philosophy

eingereicht an der

Fakultät für Mathematik, Informatik und Physik der Leopold-Franzens-Universität Innsbruck

von

Daniela Holzmann, M.Sc.

Betreuung der Dissertation:
Univ.-Prof. Dr. Helmut Ritsch,
Institut für Theoretische Physik,
Universität Innsbruck

Mitbetreuung:
Dr. Matthias Sonnleitner

Innsbruck, Juni 2021

Eidesstattliche Erklärung

Ich erkläre hiermit an Eides statt durch meine eigenhändige Unterschrift, dass ich die vorliegende Arbeit selbständig verfasst und keine anderen als die angegebenen Quellen und Hilfsmittel verwendet habe. Alle Stellen, die wörtlich oder inhaltlich den angegebenen Quellen entnommen wurden, sind als solche kenntlich gemacht.
Die vorliegende Arbeit wurde bisher in gleicher oder ähnlicher Form noch nicht als Magister-/Master-/Diplomarbeit/Dissertation eingereicht.

Datum Unterschrift

Zuammenfassung

Das Fangen und Manipulieren der Bewegung von Teilchen mittels Laserlichtfeldern ist seit Jahren ein aktives und stark wachsendes Forschungsfeld. In dieser Arbeit werden die Wechselwirkungen von Teilchen mittels dem evaneszenten Lichtfeld einer optischen Nanofaser untersucht. Lichtfasern können Licht über lange Strecken fast ohne Absorption oder Beugungsverluste transportieren. Mit speziellen Verfahren können solche Fasern so dünn gezogen werden, dass ihr Durchmesser nur einen Bruchteil der Lichtwellenlänge beträgt und nur eine einzelne fundamentale Mode propagieren kann, wobei ein Teil des Lichts außerhalb des Fasermaterials geführt wird. Teilchen nahe der Oberfläche der Faser können mit diesem Licht wechselwirken und induzieren eine teilweise Reflexion der entlang der Faser propagierenden Lichtwellen. Werden die Teilchen mit einem Pumpfeld von der Seite beleuchtet, können sie einen Teil dieses Feldes in die Faser streuen. Somit ändert ein Teilchen das Faserfeld in einem sehr großen Raumbereich, was zu kollektiven langreichweitigen Wechselwirkungen zwischen mehreren Teilchen nahe derselben Faser führt. Unter geeigneten Bedingungen streuen die Teilchen das Licht genau so, dass sie dadurch ihre eigene Falle bauen und sich entlang dieser Faser anordnen. Typischerweise ordnen sie sich dabei so an, dass sich wie zwischen zwei Spiegeln hohe Intensitäten zwischen Teilchengruppen aufbauen, ähnlich einem optischen Resonator. Solche Konfigurationen sind stabil im Grenzfall von schwacher Rückstreuung des Faserfeldes durch ein einzelnes Teilchen. Für größere Teilchenanzahlen können mehrfache Streuungen und Absorption zu dynamischen Instabilitäten führen. Verschiebt man ein Teilchen leicht aus seiner stabilen Position, ändert das die Kraft auf alle anderen Teilchen und sie beginnen kollektiv innerhalb ihrer Falle zu oszillieren.
Wählt man ein breitbandiges Feld für die transversale Beleuchtung, dann fällt die Wechselwirkung zwischen den Teilchen, abhängig von der Bandweite des Lichtfeldes, exponentiell mit dem Abstand ab. Die Teilchen entlang der Faser ordnen sich meist jedoch immer noch in stabilen Konfigurationen an. Verwendet man mehrere breitbandige Felder mit unterschiedlicher Frequenz und Intensität, dann kann die resultierende Kraft

zwischen Teilchenpaaren als eine Cosinus-Fourierreihe angeschrieben werden. Dies erlaubt die Wechselwirkungen zwischen den Teilchen sehr genau zu kontrollieren. Je nach Intensität und Frequenz der unterschiedlichen eingestrahlten Feldfrequenzen können die Wechselwirkungen zwischen den Teilchen fast beliebig angepasst und auch zwischen bestimmten Teilchenpaaren ausgeschaltet werden. Mithilfe dieser Kontrolle erscheint es möglich, komplexe Quantensysteme analog simulieren zu können und auch digitale Quantengatter zu implementieren. Als spezielles Beispiel wird hier gezeigt, wie man Coulombwechselwirkungen zwischen Ionen simulieren und universelle Gatter designen kann.
Eine weitere spannende Möglichkeit ergibt sich, wenn man eine Mikrofaser mit etwas größerem Durchmesser verwendet, sodass auch transversale Moden höherer Ordnung in der Faser propagieren können. Dies erlaubt eine stärkere Kopplung der Teilchen an die Faser. Da die Teilchen in diesem Fall auch Licht zwischen den unterschiedlichen Moden streuen können, lässt sich dadurch auch eine seltsam wirkendende Traktorkraft auf die Teilchen entgegen der Einfallsrichtung des Faserlichts erzeugen.

Abstract

Trapping and manipulating particles in optical fields has seen tremendous progress in the past decades with several Nobel prizes awarded in the field. In this thesis I present a more recent implementation, where particles are trapped in the evanescent field of light travelling along an optical nanofibre. Such fibres can guide light almost unattenuated and without diffraction over long distances. By heating and pulling one can produce very thin fibres with a diameter smaller than the wavelength of the propagating light field, so that only the fundamental mode can propagate and a large evanescent field outside the fibre arises. The particles along the fibre can reflect or transmit light from this fibre field. Additionally the particles are illuminated by a transverse pump field and they can scatter light from this field into the fibre. In this way, the particles reorder the fibre field, which leads to collective long-range interactions between the particles along the fibre. The particles scatter the fibre field in a way so that they build their own trap and self-order along the fibre acting like mirrors and trapping high intensities between them. These stationary configurations are stable in the weak scattering limit, where backscattering of the fibre field can be neglected, while for large particle numbers multiple scattering and absorption can lead to dynamical instabilities. When slightly shifting one particle from its stable position, it changes the forces on all particles and they start to collectively oscillate inside their traps.
Using a broadband field as transverse pump field the interactions between the particles exponentially decay with the bandwidth of the field and the distances between the particles, but the particles still find stable configurations. When shining broadband fields with different frequencies onto the particles the force between the particles is a Fourier cosine function, and thus the interactions between the particles can be tailored. Depending on the intensities and frequencies of the different fields, the interactions between the particles can be tuned and even turned off for special particle pairs. This property is a very powerful tool for simulating complex quantum systems, but also to implement quantum gates. In this thesis the simulation of Coulomb interactions

between ions and the designing of universal gates are demonstrated.
When using a microfibre with larger diameter also higher order modes can propagate along the fibre. In this case the coupling strength between the particles and the fibre is enhanced. The particles can scatter light between the different modes, which can even lead to a stationary tractor force against the injection direction.

Danksagung

Besonders bedanken möchte ich mich bei Univ.-Prof. Dr. Helmut Ritsch für die Möglichkeit in seiner Forschungsgruppe zu arbeiten. Stets hat er sich Zeit genommen für meine Anliegen und meine Fragen beantwortet. Er hat es geschafft mein Interesse an spannenden Themen zu wecken und ich hatte viel Spaß bei der Arbeit in einem so interessanten Forschungsgebiet. Auch für die Möglichkeit Familie und Arbeit zu kombinieren, möchte ich mich hier bedanken.
Ebenfalls ein besonderer Dank gilt auch Matthias Sonnleitner, der sich mit viel Geduld meinen Fragen widmete und mir aus jeder Sackgasse herausgeholfen hat. Seine strukturierte Arbeitsweise half mir Ordnung in mein Chaos zu bringen. Sein Spaß an der Physik ist ansteckend und hat mich immer wieder neu motiviert.
Ich hatte das Glück in einem großartigen Arbeitsumfeld zu arbeiten und dafür möchte ich mich bei der gesamten Arbeitsgruppe bedanken. Für spannende Diskussionen, aber auch einfach gemütliches Gequatsche möchte ich mich bei euch bedanken.
Auch für die nette und produktive Zusammenarbeit mit Christiane Ebongue, Aili Maimaiti, Viet Giang Truong und Univ.-Prof. Dr. Sile Nic Chormaic möchte ich mich bedanken.
Auch bei meinen Freunden, meiner Familie und meiner Schwiegerfamilie möchte ich mich für die bedingungslose Unterstützung während des gesamten Studiums bedanken.
Zuletzt gilt mein Dank an den vier wichtigsten Menschen in meinem Leben, die zwar nicht besonders förderlich für das Gelingen der Arbeit waren, aber ohne denen mein Leben nicht halb so schön wäre. Danke, an meinen Mann Fabian, meinen Kindern Nelia und Lian und dem kleinen Baby, das hoffentlich im September gesund zur Welt kommen wird.

Contents

1. Introduction

In 1619 Johannes Kepler (1571-1630) came up with the idea that light contains momentum as he observed that comet tails always point away from the sun [1]. He postulated that this force acting on interstellar particles arises due to the radiation pressure of light. Centuries later, in 1970, Ashkin could show that this radiation pressure force can be used to accelerate particles in the propagation direction of the laser beam or to trap particles when using two counterpropagating beams [2]. For a strongly focused light beam, far detuned from any atomic resonances, a second force plays an important role, the so-called dipole force. This force can be used to trap particles in the center of the beam at positions of maximal intensity. In 2018 Ashkin was awarded with the Nobel prize for this invention of using the dipole force to trap particles in optical tweezers [3]. His experiment proved the possibility of trapping particles by a single beam for the first time and opened up a lot of new opportunities for trapping and manipulating particles by a light field.

An improved approach for using optical forces to trap and cool atoms are optical cavities [4; 5], where even self-ordering of the particles could be observed [6]. In such cavities the light is reflected by mirrors placed at both sides of the atoms before leaking out of the cavity and thus passes the atoms more often, which increases the coupling between the light and the atoms. Depending on the cavity geometry only certain spatial field distributions called cavity modes are resonantly enhanced at well defined frequencies [7; 8].

An alternative route to achieve a local high field concentration is transverse confinement of the field. Due to diffraction, in free space this method is limited to a very tiny focal spot. This problem can be overcome by using an optical waveguide system instead of a cavity. In such a waveguide the light travels almost lossless and is transversely strongly confined over a very large distance, which leads to much stronger interactions between the atoms and the light field than in free space. In contrast to a cavity system, here, the photons can propagate for very long distances along the waveguide and are not restricted

to specific resonance frequencies. As photons carry energy and momentum they mediate interactions between particles at different locations. In a quantum description they carry quantum information in the form of flying qubits. Hence such a setup is a very promising tool to build a quantum network sometimes termed as a quantum internet [9]. When using very thin waveguides, so called nanofibres [10], with a diameter smaller than the wavelength of the light field, not all light is confined within the fibre material and a strong evanescent field arises outside the fibre. In this case the interaction between the nanofibre light modes and the particles can be so strong, that the particles are trapped in this evanescent field of the fibre, when a carefully chosen combination of light frequencies is sent through the fiber [11]. Any particle trapped in a corresponding particle chain "sees" the light reflected and transmitted through the waveguide by all the other particles. This leads to collective quantum effects, as e.g. Bragg reflection, sub- [12] and superradiance [13], correlated photon emission [14] or mechanical self-ordering of mobile particles along the waveguide [15; 16].
Recent progress in fibre and laser technology has also shown that such waveguides are a very promising tool for quantum computation and simulation [17–23]. Some examples are the creation of Schrödinger cat states [24], the design of quantum gates [25; 26], entangled states [27; 28] or the realization of the Bose–Hubbard Hamiltonian [29; 30].
In the approach presented in this thesis the particles are assumed to be optically trapped in a 1D potential along the nanofibre. In addition they are transversely illuminated and thus will scatter light from this transverse pump field into the fibre [15; 16]. By a proper choice of the spectral composition and intensity of this pump field, interactions between particles at different positions can be designed. This gives one the possibility to simulate symmetric interactions with a very general spatial dependence or in specific cases to implement quantum gates.
In this thesis in chapter 2 I will first introduce the basic theoretical concepts and specific ideas allowing to trap particles along a nanofibre. Such nanofibres are constructed so that they exhibit a strong evanescent field. Particles along the fibre interact with this evanescent field via the induced optical dipole force as well as radiation pressure. Fundamental properties of nanofibres and the field propagation within are also described in this first chapter. Trapping and manipulating atoms or molecules along a nanofibre has been of strong interest for the past few years and a lot of experimental investigations have been developed. I will mention some of these experimental implementations and discuss their advantages and disadvantages.

The model presented in this work is based on a new generalized approach for such implementations as shown in chapter 3. Here the particles do not only interact with the fibre field but they are also illuminated by a transverse pump field and can scatter light from this pump field into the fibre. This field scattered into the fibre by the particles then propagates through the fibre and changes the currently present field. Fortunately, as the physics is essentially one dimensional, the scattering processes of the field by the particles can be effectively described by a beamsplitter matrix approach. Photons passing by a particle are either reflected backwards, transmitted forward or scattered out of the fibre. A simple corresponding model then connects the amplitudes of the fields on both sides of a particles. Based on their relation the Maxwell-stress-tensor can be used to calculate the missing momentum in the field and thus the force acting on the particle.

In the weak coupling limit most photons are transmitted and we can safely assume that most of the force arises due to the scattering of the transverse pump field into the fibre and neglect force contributions from backscattering of the light field within the fibre. This is a good approximation at least for small particle numbers but is not valid for large system sizes where collective scattering gets significant. But in the weak coupling limit the force on a particle is the sum of all pair forces between this particle and all the other particles which allows to define an effective optical potential.

The particles along the nanofibre collectively redistribute the light in a way that they build their own optical trap which induces self-ordering along the fibre. In part I we study the stability and oscillations of such a crystalline structure. While in the weak scattering limit the particles form stable configurations along the fibre, scattering and absorption of the light field can destabilize the structure for large system sizes.

Using a broadband field as pump changes the interactions between the particles in a very variable form and one can tune the very long-range interactions even to only nearest neighbour interactions depending on the bandwidth of the incoming field. The behaviour of particles in such a field is investigated in part II. The particles still self-order in stable configurations. There, we even consider the extreme case of a thermal radiation field with a Planck spectrum, where multiple scattering effects lead to a complex interplay of attraction and repulsion at distances around the thermal radius.

The combination of several broadband fields with different frequencies gives the possibility to tune the interactions between the particles. In that case one can write the pair forces as a Fourier cosine function, which leads to complex force shapes. So, the

interaction between the particles can be designed by choosing the properties of the incoming field and even turned off for special particle pairs.
This nice feature is a very promising tool for quantum computation and simulation. In part III we derive a quantum model by quantizing the motional degrees of freedom of the particles. The particles then can be described by quantum oscillators interacting via the fibre field. By a proper choice of the properties of the incoming field this model can be used to simulate Coulomb interactions between ions. When describing the oscillator states as qubits this approach can be used to design quantum gates or to entangle states.
Another route to generality and better control of the particles involves microfibres with a somewhat larger diameter so that also higher order transverse modes can propagate. As shown in part IV in such fibres the coupling between the particles and the fibre field is typically larger than in a single mode fibre. As one intriguing consequence of scattering between the different fibre modes, a stationary tractor force against the injection direction can be implemented.

2. Coupled atom-field dynamics near an optical nanofibre

In this section we shortly review the physics of light propagation in an optical fibre and discuss how polarizable particles can interact via the the fibre field. Subsequently, some generic experimental realizations are introduced and the advantages and disadvantages of these implementations will be discussed.

2.1. Light propagation inside a fibre

Optical fibres are used to transport information over thousands of kilometres. The light inside the fibre is strongly confined in the transverse direction and can be transmitted over long distances almost lossless and unperturbed as it is well isolated from the environment [31]. Typical fibres consist of a core and a cladding as depicted in fig. 2.1. As the refractive index of the core is higher than the refractive index of the cladding, the light is totally reflected at the border between the core and the cladding, when launched into the fibre at a special angle [32]. Usually the cladding of such fibres is made of silica and the core of silica doped with Germanium to increase the refractive index [33]. The

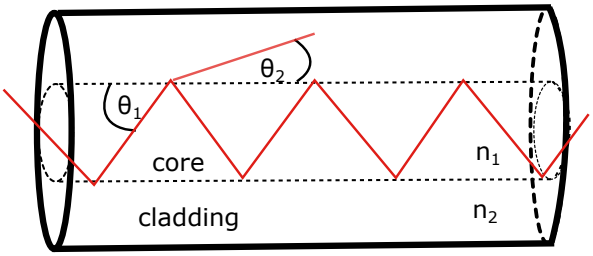

Figure 2.1.: A fiber consists of a core and a cladding with the refractive indices $n_1 > n_2$. Guided modes (red line) are totally reflected at the border between the core and the cladding, when θ_1 larger than the critical angle.

rays totally reflected at the boundary of the fibre core has to cover different path lengths. Due to interference between these rays, some of them will interfere destructively and so are not able to propagate through the waveguide.
Due to the wave character of light some properties of optical fibres can not be explained by this ray theory, but one needs to model it based on the electromagnetic wave theory:

$$\vec{E}(\vec{r},t) = \vec{E}(r,\phi)e^{ikx-i\omega t}, \tag{2.1a}$$
$$\vec{H}(\vec{r},t) = \vec{H}(r,\phi)e^{ikx-i\omega t}, \tag{2.1b}$$

for the electric and magnetic fields $\vec{E}(\vec{r},t)$ and $\vec{H}(\vec{r},t)$ at position $\vec{r}$ and time t propagating along the fibre axes x, with frequency ω, wavenumber k, radial distance from the fibre axes r and ϕ the angle between the fibre axes and the position. For a given frequency and wavevector the field has to fulfil the Helmholtz equation [34]

$$\left(\Delta + n^2k^2 - \beta^2\right)\begin{pmatrix}\vec{E}(\vec{r},t)\\ \vec{H}(\vec{r},t)\end{pmatrix} = 0, \tag{2.2}$$

with β the modal propagation constant and n the refractive index. The solutions to this equation are the so called fibre modes, which are Bessel and modified Bessel functions. For the exact mathematical description of the modes, one can look at [35].
The fibre modes can be divided into guided and radiation modes. Only the guided modes can propagate along the fibre, while radiation modes are refracted waves and carry energy out of the core. Fibre modes describe the propagation of the light field through the fibre. In the fibre system we are not limited to special frequencies, but the fibre can support a broad frequency spectrum. Depending on the V number [36]

$$V = \frac{2\pi a}{\lambda}\sqrt{n_1^2 - n_2^2}, \tag{2.3}$$

with the fibre radius a, refractive indices of the core and the cladding n_1 and n_2 and wavelength of the light field λ, different numbers of modes can propagate inside the fibre. For $V < 2.405$ only a single mode can be supported by the fibre. To fulfil this condition, the fibre has to be very thin and the difference between the refractive indices small.
The light field propagating through the fibre does not drop immediately to zero at the

border of the core but there is still some part of the light exponentially decaying inside the cladding, the so called evanescent field. The evanescent field drops exponentially outside the waveguide and can transport energy along the boundary. Imagine a light wave impinging on the boundary between the waveguide core and the cladding at an angle θ_1 larger than the critical angle for total reflection. A part of this wave is then totally reflected back to the core and a part E_t transmitted and refracted into the cladding at an angle θ_2 as depicted in fig. 2.1. So the wave in the cladding can be described by

$$E_2 = E_t e^{ik_2(x\cos(\theta_2)+y\sin(\theta_2))}, \tag{2.4}$$

with x the fibre axes, y perpendicular to the fibre axes and k_2 the wavevector for the field in the cladding. Using Snell's law $n_1\cos(\theta_1) = n_2\cos(\theta_2)$, with n_1 and n_2 the refractive indices of the core and the cladding, we rewrite

$$E_2 = E_t e^{ik_2\left(x\frac{n_1}{n_2}\cos(\theta_1)+y\sqrt{1-\frac{n_1^2}{n_2^2}\cos^2(\theta_1)}\right)}. \tag{2.5}$$

As the square root term in the exponent is imaginary for the angles larger than the critical angle, we can define $\sqrt{1-\frac{n_1^2}{n_2^2}\cos^2(\theta_1)} = \pm i\kappa$ and, thus

$$E_2 = E_t e^{-\kappa k_2 y} e^{ik_2 x\frac{n_1}{n_2}\cos(\theta_1)}. \tag{2.6}$$

So the wave in the cladding decays exponentially perpendicular to the fibre axes and propagates along the waveguide [36].

When using very thin fibers with a diameter smaller than the wavelength of the light travelling inside the fibre, so called nanofibres, this evanescent field can be very strong [35]. Such fibres can be produced by heating and carefully pulling a usual glass fibre [10; 33]. Then the fibre core is reduced to virtually zero diameter and plays no role any more. The light then is guided in the cladding region with a significant portion of the energy contained in the evanescent field outside the fibre.

Usually such fibres are so thin that only the fundamental HE_{11}-mode can propagate along the fibre. Using fibres with a larger diameter, where also higher order modes are guided through the fibre, more light could be coupled inside the fibre, and the coupling between the fibre light and the particles could be increased [37–39].

2.2. Optical forces

When shining light on a particle, the interaction between the particle and the light field exchanges energy and momentum between the light and the particle. The mechanical interaction can be explained by two optical forces: the dipole force and the radiation pressure [40; 41].

To understand these two forces we will use the classical Lorentz model. Here we will mostly follow the work of Steck [42]. Let us imagine a light field shining on an atom. The atom consists of an electron with mass m_e and charge $-e$ elastically bound to a nucleus with charge $+e$ and frequency ω_0, driven by an external electric field $\vec{E}(t) = \vec{E}_0 e^{i\omega t} + \vec{E}_0^* e^{-i\omega t}$, with frequency ω. Here one can assume that the size of the atom is much smaller than the wavelength of the electric field, so that the nucleus and the electron "see" the same field. Considering also damping γ due to charge acceleration or atom collisions the equation of motion for the electron can be written as

$$m_e \ddot{x} + m\gamma\dot{x} + m\omega_0^2 x = -e\left(\vec{E}_0 e^{i\omega t} + \vec{E}_0^* e^{-i\omega t}\right), \tag{2.7}$$

with $\vec{F}_e = -e\vec{E}$ the force on the electron due to the electric field.

Using the ansatz $x(t) = x_0 e^{i\omega t} + x_0^* e^{-i\omega t}$, one finds

$$x_0 = \frac{e\vec{E}_0/m_e}{\omega^2 - \omega_0^2 + i\gamma\omega}. \tag{2.8}$$

So the light field shining on the atom induces an electric dipole and the particles start to oscillate at the same frequency as the incoming light field.

The dipole moment of the atom is defined as $\vec{d} = -e\vec{x} = \alpha(\omega)\vec{E}$, with α the polarizability describing the reaction of the atom to the electric field

$$\alpha(\omega) = \frac{-e^2/m_e}{\omega^2 - \omega_0^2 + i\gamma\omega}, \tag{2.9}$$

with

$$\Re(\alpha) = \frac{e^2/m_e\,(\omega_0^2 - \omega^2)}{\gamma^2\omega^2 + (\omega_0^2 - \omega^2)^2}, \tag{2.10a}$$

$$\Im(\alpha) = \frac{e^2/m_e\gamma\omega}{\gamma^2\omega^2 + (\omega^2 - \omega_0^2)^2}. \tag{2.10b}$$

While $\Re(\alpha)$ depends on the detuning of the field and is positive for red detuned light and negative for blue detuned light, $\Im(\alpha)$ is always positive. As we will see later the real part of the polarizability is proportional to the dipole force and the imaginary part is proportional to the radiation pressure force.

2.2.1. Dipole force

The incoming light field induces an oscillating dipole in the atom. This dipole then radiates light, which interferes with the incoming light field and, thus, leads to forces on the particle. The potential on the induced dipole reads

$$V_{\text{dip}} = -\frac{\vec{d}\vec{E}}{2} = -\frac{\left(\vec{d}_0 e^{i\omega t} + \vec{d}_0^* e^{-i\omega t}\right)\left(\vec{E}_0 e^{i\omega t} + \vec{E}_0^* e^{-i\omega t}\right)}{2}. \tag{2.11}$$

The terms $\propto e^{\pm 2i\omega t}$ oscillate twice as fast as the electric field and cancel out when averaging over time, and thus

$$V_{\text{dip}} = -\Re(\alpha)\,|\vec{E}_0|^2 \propto -\Re(\alpha)\,I, \tag{2.12}$$

with intensity I. So the dipole potential is proportional to $\Re(\alpha)$ and, thus, is negative for red detuned light and positive for blue detuned light. Consequently, to minimize the potential the particle is pushed towards higher intensities for red detuned light and towards lower intensities for blue detuned light.

2.2.2. Radiation pressure

The radiation pressure arises due to absorption and incoherent re-emission of the incoming light field. When the incoming photons are all coming from the same direction but are uniformly emitted in a random direction, this leads to a net momentum transfer onto the particle and the particle is pushed away from the light source.

The electric and magnetic field of an oscillating dipole at position $\vec{r}$ reads [43]

$$\vec{E}_0(\vec{r},t) = \frac{1}{4\pi\epsilon_0}\left(3\left(\vec{\epsilon}\cdot\vec{r}\right)\vec{r}-\vec{\epsilon}\right)\left(\frac{\vec{d}_0(t_r)}{r^3}+\frac{\dot{\vec{d}}_0(t_r)}{cr^2}\right)+\frac{1}{4\pi\epsilon_0}\left(\left(\vec{\epsilon}\cdot\vec{r}\right)\vec{r}-\vec{\epsilon}\right)\frac{\ddot{\vec{d}}_0(t_r)}{c^2r}, \quad (2.13a)$$

$$\vec{H}_0(\vec{r},t) = \frac{c}{4\pi}\left(\vec{\epsilon}\times\vec{r}\right)\left(\frac{\dot{\vec{d}}_0(t_r)}{cr^2}+\frac{\ddot{\vec{d}}_0(t_r)}{c^2r}\right), \quad (2.13b)$$

with the retarded time $t_r = t - r/c$, the polarization unit vector $\vec{\epsilon}$ and $r = |\vec{r}|$.
As only the terms $\propto 1/r$ transports energy to infinity we only keep these terms

$$\vec{E}_0(\vec{r},t) \approx \frac{1}{4\pi\epsilon_0}\left(\left(\vec{\epsilon}\cdot\vec{r}\right)\vec{r}-\vec{\epsilon}\right)\frac{\ddot{\vec{d}}_0(t_r)}{c^2r}, \quad (2.14a)$$

$$\vec{H}_0(\vec{r},t) \approx \frac{1}{4\pi}\left(\vec{\epsilon}\times\vec{r}\right)\frac{\ddot{\vec{d}}_0(t_r)}{cr}. \quad (2.14b)$$

The transport of energy can be described by the Poynting vector

$$\langle\vec{S}\rangle = \vec{E}_0\times\vec{H}_0^* + \vec{E}_0^*\times\vec{H}_0 = \frac{1}{8\pi^2\epsilon_0c^2}\frac{|\ddot{\vec{d}}_0(t_r)|^2}{r^2}\left(1-|\vec{r}\cdot\vec{\epsilon}|^2\right)\vec{r}, \quad (2.15)$$

with $\left(\left(\vec{\epsilon}\cdot\vec{r}\right)\vec{r}-\vec{\epsilon}\right)\times\left(\vec{\epsilon}^*\cdot\vec{r}\right) = \left(1-|\vec{r}\cdot\vec{\epsilon}|^2\right)\vec{r} = \vec{r}\sin^2(\theta)$ for a linear polarized light field, and θ the angle from the z-axis.
The power P can be calculated by integrating the Poynting vector over the area

$$P = \oint \vec{S}\cdot d\vec{A}. \quad (2.16)$$

With

$$\frac{dP}{d\Omega} = \frac{|\ddot{\vec{d}}_0|^2}{8\pi^2\epsilon_0c^2}\sin^2(\theta). \quad (2.17)$$

the total radiated power can then be found by integrating over the solid angle

$$P = \frac{|\ddot{\vec{d}}_0|^2}{8\pi^2\epsilon_0c^2}. \quad (2.18)$$

Using

$$\vec{d} = \alpha\left(\vec{E}_0e^{i\omega t}+\vec{E}_0^*e^{-i\omega t}\right), \quad (2.19)$$

and thus

$$\ddot{\vec{d}} = -\omega^2 \vec{d}, \tag{2.20}$$

we can easily rewrite the radiated power in terms of the polarizability and intensity I

$$P = \frac{\omega^4 |\alpha(\omega)|^2}{6\pi\epsilon_0^2 c^4} I = \frac{\omega^3 e^2}{6\pi\epsilon_0 c^4 \gamma m} \Im(\alpha)\, I. \tag{2.21}$$

As the force is proportional to the radiated power, we can see that in this case the force depends on the imaginary part of the polarizability.
Note, that for far detuned light fields $\Re(\alpha)$ scales with $1/(\omega_0^2 - \omega^2)$, while $\Im(\alpha)$ scales with $1/(\omega_0^2 - \omega^2)^2$. Consequently, in this case, the dipole force dominates the radiation pressure.

2.3. Experimental implementations

These optical forces can be used to trap and manipulate particles along the fibre axes and lead to self-organization of the particles. As shown above the direction of the dipole force depends on the frequency detuning. For red detuned light the particles are pushed towards higher intensities and for blue detuned light towards lower intensities. This feature can be used to create an optical trap formed by two evanescent waves [44]. The idea of creating such a trap is to produce a short-range repulsive and a long-range attractive force. This can be done by using a blue detuned light field with small penetration depth and a red detuned light field with large penetration depth into the vacuum. Note, that both fields have to be far detuned so that the radiation pressure is small compared to the dipole force to produce a trap with a large coherence time and a large trap lifetime [45].
In 2010 Rauschenbeutel and coworkers used this idea to trap Caesium atoms in the evanescent field of a nanofibre [11; 45]. If one launches a blue and a red detuned light field into the fibre, the blue detuned light field repels the particles from the fibre, while the red detuned light attracts the particles towards the fibre surface. The combination of the two fields leads to a potential minimum near the fibre surface. Additionally they launched a second red detuned counterpropagating field into the fibre, so that the two counterpropagating red detuned light fields generated periodically-spaced potential wells. In such a system thousands of atoms can be trapped and strong collective effects

could be observed [14]. Even an external excitation laser could be included, which has to be adjusted in a way to counteract recoil and heating mechanisms. The particles then scatter this field and a part of it couples to the nanofibre-guided mode [46].
An important parameter for such systems is the coupling efficiency β between the particles and the waveguide which is defined as the radiative decay rate of a single emitter γ_{guid} into the fibre compared to the total decay rate γ_{tot}

$$\beta = \frac{\gamma_{\text{guid}}}{\gamma_{\text{tot}}}. \tag{2.22}$$

For atoms along a nanofibre only an efficiency of $\beta \approx 10\,\% - 20\,\%$ could be obtained [47], but recently the system could be improved by using hole-tailored nanofibers and a coupling efficiency of 62.8 % could be reached [48].
The coupling between the particles and the fibre could be enhanced when using photonic crystal waveguides, which offers new possibilities to control the atom-light interaction. In such photonic crystal waveguides the light is reflected multiple times off the dielectric modulation, so that the interaction time with the particles is extended. The emission rate into the fibre in such systems can reach $89\,\% - > 99\,\%$, when using quantum dots [49–51]. One special photonic crystal waveguide is the so called "alligator" photonic crystal waveguide, where an efficiency of 100 % was obtained [52].
As such waveguide systems are not always perfect, some problems can arise, which can also affect the particle-light-interactions. One of the most famous problems is the Anderson localization where light is confined instead of guided through the waveguide due to scattering disorder. Another problem is atomic adsorption on the waveguide surface, which can generate electric field fluctuations [53], change the refractive index or heat up the system [54].
A very nice feature of such nanofibre systems is the chirality of the atom-photon coupling [55–57] arising due to longitudinal components of the electric field in a nanofibre which, dependent on the propagation direction, can induce a different circular polarized field component close to the fiber edge. Depending on the polarization and propagation direction of the light field, the transition dipole moment of each emitter and the position of the particles on the fibre surface, the direction of the scattering can be adjusted [58; 59]. Such properties can be used for integrated optical circulators [60] or for a spin-controlled photon switch [61].

3. Theoretical Models

Let us consider N linear polarizable particles, for example atoms, molecules, nanospheres, along a single mode fibre interacting with the evanescent field of this fibre as depicted in figure 3.1. The modes of this fibre can be described by two counterpropagating light fields. Additionally the particles are illuminated by a transverse pump field and they can scatter light from this field into the fibre. Then this field propagates to the next particle and this particle then can reflect or transmit part of this field and so on. So the particles redistribute the fibre field, which leads to collective interactions between the particles. The way every particle scatters the light depends on the position of the particles along the fibre. So even if only one particle is replaced, it changes the forces on every other particle [16]. Note that here we assume that the particles are distributed far enough so that dipole-dipole interactions between the particles can be neglected.
While in a cavity the frequency of the light field has to fulfil special resonant conditions in order to produce a mode, a nanofibre can guide a broad frequency spectrum. So, here, the incoming light field consists of several fields with different frequencies $\omega = kc$

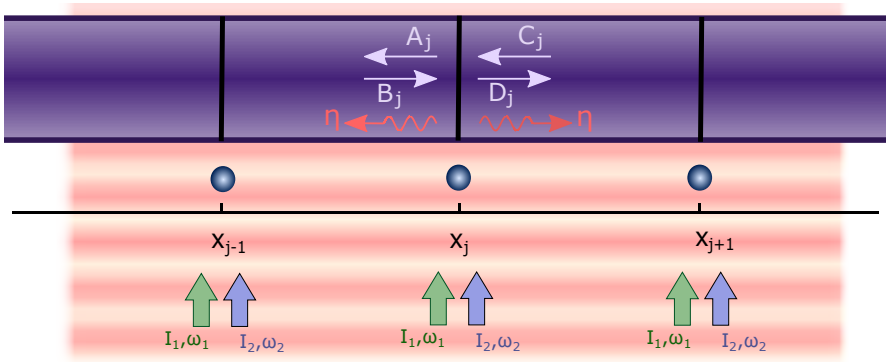

Figure 3.1.: Particles trapped in the evanescent field along a nanofibre and transversely illuminated by a pump field.

and intensities I_k

$$\vec{E}\,(x,t) = \sum_k \sqrt{\frac{2I_k}{c\epsilon_0}} e^{ikx - i\omega t}. \tag{3.1}$$

We assume that the frequencies are only space but not time coherent and thus do not interfere. In this case the induced dipole by the field, oscillates with a superposition of the single frequencies.

3.1. Beam splitter method

The propagation of the light field through the fibre can be described by the beam splitter method [62–64]. Imagine every particle scatters light into the fibre and can reflect or transmit the field scattered by the other particles. These scattering processes can be described by a beam splitter approach. Note that here we introduce this concept for a single frequency as the generalization to multi frequency fields is trivial. One can approximate the fibre field by a Gaussian beam, with diameter much larger than the wavelength. So the field is a simple planewave $E(x,t) = E(x)\exp(-i\omega t)$, with $E(x) = E_1 \exp(ikx)$. The propagation of the light field through the fibre, can be described by the inhomogeneous Helmholtz equation

$$\Delta\vec{E}(x) + \frac{\omega^2}{c^2}\vec{E}(x) = \mu_0\omega^2\vec{P}, \tag{3.2}$$

with μ_0 the magnetic permeability and $\vec{P}$ the polarization [43]. The density of N particles at positions x_i is $\rho = \sum_{n=i}^{N} \delta(x - x_i)$. With this one can find the polarization $P(x) = \alpha E(x) \sum_{i=1}^{N} \delta(x - x_i)$, with the linear polarizability α and, thus, eq. (3.2) changes to

$$\left(\partial_x^2 + k^2\right) E(x) = -\frac{k^2\alpha}{\epsilon_0} \sum_{i=1}^{N} \delta(x - x_i). \tag{3.3}$$

Defining a coupling constant proportional to the polarizability of the particles

$$\zeta = k\frac{\alpha}{2\epsilon_0}, \tag{3.4}$$

the Helmholtz equation changes to

$$\left(\partial_x^2 + k^2\right) E(x) = -2kE(x)\zeta \sum_{n=i}^{N} \delta(x - x_i). \tag{3.5}$$

The electric field between two particles can be described by the superposition of two counterpropagating light fields

$$E(x_{i-1} < x < x_i) = A_i e^{-ik(x-x_i)} + B_i e^{ik(x-x_i)} = C_{i-1} e^{-ik(x-x_i)} + D_{i-1} e^{ik(x-x_i)}, \tag{3.6}$$

with the amplitudes of the left propagating field A_i and C_{i-1} and of the right propagating field B_i and D_{i-1} as defined in fig. 3.2. If we assume that the particles are much smaller than the wavelength of the light field, the electric field has to be continuous at both sides of a particle

$$E(x_i - 0) = E(x_i + 0), \tag{3.7a}$$

$$A_i + B_i = C_i + D_i. \tag{3.7b}$$

A second boundary condition can be found when integrating the Helmholtz equation (3.5) from $x_i - \epsilon$ to $x_i + \epsilon$ for $\epsilon \to 0$

$$\begin{aligned}
\int_{x_i-\epsilon}^{x_i+\epsilon} \left(\partial_x^2 + k^2\right) E(x)dx &= \int_{x_i-\epsilon}^{x_i+\epsilon} -2kE(x)\zeta \sum_{i=1}^{N} \delta(x - x_i)dx, \\
\underbrace{\int_{x_i-\epsilon}^{x_i+\epsilon} \partial_x^2 E(x)dx}_{\partial_x E(x_i+\epsilon) - \partial_x E(x_i-\epsilon)} + \int_{x_i-\epsilon}^{x_i+\epsilon} k^2 E(x)dx &= -2k\zeta \underbrace{\int_{x_i-\epsilon}^{x_i+\epsilon} E(x) \sum_{n=i}^{N} \delta(x - x_i)dx}_{E(x_i)}, \\
\partial_x E(x_i + \epsilon) - \partial_x E(x_i - \epsilon) + \int_{x_i-\epsilon}^{x_i+\epsilon} k^2 E(x)dx &= -2k\zeta E(x_i), \\
\lim_{\epsilon\to 0} \left(\partial_x E(x_i + \epsilon) - \partial_x E(x_i - \epsilon)\right) + \underbrace{\lim_{\epsilon\to 0} \int_{x_i-\epsilon}^{x_i+\epsilon} k^2 E(x)dx}_{\to 0} &= -2k\zeta E(x_i), \\
\Rightarrow \partial_x E(x_i + 0) - \partial_x E(x_i - 0) &= -2k\zeta E(x_i),
\end{aligned} \tag{3.8}$$

when using the condition from eq. (3.7a) in the last line. Inserting eq. (3.6) into the boundary condition (3.8) and using eq. (3.7b), we find the following condition for the

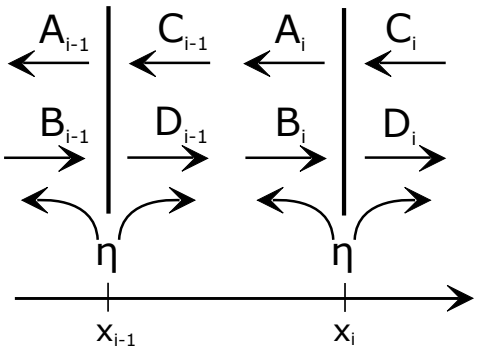

Figure 3.2.: Name convention for the amplitudes of the electric field at the position of the beam splitters x_i.

amplitudes of the propagating fields

$$\begin{aligned} -ikC_i + ikD_i + ikA_i - ikB_i &= -2k\zeta\left(A_i + B_i\right), \\ iA_i - iC_i &= \zeta\left(A_i + B_i\right), \\ \Rightarrow A_i &= \frac{i\zeta}{1-i\zeta}B_i + \frac{1}{1-i\zeta}C_i, \end{aligned} \tag{3.9}$$

and

$$\begin{aligned} -ikC_i + ikD_i + ikA_i - ikB_i &= -2k\zeta\left(C_i + D_i\right), \\ iD_i - iB_i &= \zeta\left(C_i + D_i\right), \\ \Rightarrow D_i &= \frac{1}{1-i\zeta}B_i + \frac{i\zeta}{1-i\zeta}C_i. \end{aligned} \tag{3.10}$$

If we define a reflection and transmission coefficient

$$r = i\zeta/(1-i\zeta), \tag{3.11a}$$

$$t = 1/(1-i\zeta), \tag{3.11b}$$

with $-ir/t = \zeta$, we can write

$$A_i = rB_i + tC_i, \tag{3.12a}$$

$$D_i = tB_i + rC_i. \tag{3.12b}$$

So the outgoing fields A_i and D_i consist of a reflected and a transmitted part of the incoming fields B_i and C_i.
The transverse pump field with amplitude η in the system introduced above can easily be included by simply adding it on the equations (3.12)

$$A_i = rB_i + tC_i + \frac{\eta}{\sqrt{2}}, \tag{3.13a}$$

$$D_i = tB_i + rC_i + \frac{\eta}{\sqrt{2}}. \tag{3.13b}$$

Note that here the transverse pump field is symmetrically scattered into both directions with $I_{\eta_{\text{left}}} = \alpha^2\ I_0 = 1/2\ I_0$ and $I_{\eta_{\text{right}}} = \beta^2\ I_0 = 1/2\ I_0$, with $\alpha^2 + \beta^2 = 1$ and the intensity of the transverse pump field $I_0 = |\eta|^2 c\epsilon_0/2$, but by changing α and β also chiral scattering could be easily included [16].
We reorder these equations and describe the fields to the left side of a particle by the fields to the right side of a particle

$$A_i = \frac{1}{t}\left(\left(t^2 - r^2\right) C_i + rD_i + (t - r)\,\frac{\eta}{\sqrt{2}}\right) = (1 + i\zeta)\,C_i + i\zeta D_i + (1 - i\zeta)\,\frac{\eta}{\sqrt{2}}, \tag{3.14a}$$

$$B_i = \frac{1}{t}\left(-rC_i + D_i - \frac{\eta}{\sqrt{2}}\right) = -i\zeta C_i + (1 - i\zeta)\,D_i + (i\zeta - 1)\,\frac{\eta}{\sqrt{2}}, \tag{3.14b}$$

and define a beam splitter matrix $\mathbf{M}_{BS}$ describing the scattering processes by a particle

$$\begin{pmatrix} A_i \\ B_i \\ \eta \end{pmatrix} = \mathbf{M}_{BS} \begin{pmatrix} C_i \\ D_i \\ \eta \end{pmatrix} \tag{3.15}$$

with

$$\mathbf{M}_{BS} = \frac{1}{t}\begin{pmatrix} t^2 - r^2 & r & \frac{t-r}{\sqrt{2}} \\ -r & 1 & -\frac{1}{\sqrt{2}} \\ 0 & 0 & t \end{pmatrix} = \begin{pmatrix} 1 + i\zeta & i\zeta & \frac{1-i\zeta}{\sqrt{2}} \\ -i\zeta & 1 - i\zeta & \frac{i\zeta-1}{\sqrt{2}} \\ 0 & 0 & 1 \end{pmatrix}. \tag{3.16}$$

When having more than one particle, also the propagation of the light field between two particles have to be considered. This can be taken into account by the propagation

matrix $\mathbf{P}$

$$\mathbf{P}(d_i) = \begin{pmatrix} e^{ikd_i} & 0 & 0 \\ 0 & e^{-ikd_i} & 0 \\ 0 & 0 & 1 \end{pmatrix}, \tag{3.17}$$

with $d_i = x_{i+1} - x_i$. The scattering processes by a system with N particles illuminated by a transverse pump field and interacting via the fibre field can be easily described by these propagation and beam splitter matrices. One only has to multiply the single beam splitter and propagation matrices

$$\begin{pmatrix} A_1 \\ B_1 \\ \eta \end{pmatrix} = \mathbf{M}_{BS} \cdot \mathbf{P}(d_1) \cdot \mathbf{M}_{BS} \cdot \mathbf{P}(d_2) \cdots \mathbf{M}_{BS} \cdot \mathbf{P}(d_{N-1}) \cdot \mathbf{M}_{BS} \begin{pmatrix} C_N \\ D_N \\ \eta \end{pmatrix}. \tag{3.18}$$

So the fields to the left of the system could be calculated out of the fields to the right of the system. Note that in this work we mostly set $B_1 = C_N = 0$ as we only assume a transverse pump field as an incoming field.

3.2. Maxwell's stress tensor

In the previous section we explained how the fields to the left and to the right of the particles could be calculated. In this section we describe how one can calculate the forces acting on a particle when knowing the amplitudes of the fields on both sides of the particles. This can be done by calculating Maxwell's stress tensor.
We follow the derivation in [65] and start with Maxwell's equation for neutral particles and no electric current

$$\nabla \cdot \vec{D} = 0, \tag{3.19a}$$

$$\nabla \cdot \vec{B} = 0, \tag{3.19b}$$

$$\nabla \times \vec{E} = -\frac{\partial \vec{B}}{\partial t}, \tag{3.19c}$$

$$\nabla \times \vec{H} = \frac{\partial \vec{D}}{\partial t}, \tag{3.19d}$$

with the electric displacement $\vec{D} = \epsilon_0 \vec{E} + \vec{P}$ and the magnetic field $\vec{B} = \mu_0 \vec{H}$. From Poynting's theorem follows that the total force onto an object in an electromagnetic

field is the sum of the mechanical and the field force

$$\vec{F} = \vec{F}_{\text{mech}} + \vec{F}_{\text{field}} = \frac{1}{c^2} \int_V \frac{d}{dt} \left(\vec{E} \times \vec{H} \right) \cdot dV. \tag{3.20}$$

Operating on eq. (3.19c) by $\times \epsilon_0 \vec{E}$ and on eq. (3.19d) by $\times \mu_0 \vec{H}$ and adding the two equations we get

$$\epsilon_0 \underbrace{\left(\nabla \times \vec{E} \right) \times \vec{E}}_{= \nabla \cdot \left(\vec{E} \otimes \vec{E} - \frac{|\vec{E}|^2}{2} \mathbb{I} \right)} + \mu_0 \underbrace{\left(\nabla \times \vec{H} \right) \times \vec{H}}_{= \nabla \cdot \left(\vec{H} \otimes \vec{H} - \frac{|H|^2}{2} \mathbb{I} \right)} = \frac{1}{c^2} \underbrace{\left(-\frac{\partial \vec{H}}{\partial t} \times \vec{E} + \frac{\partial \vec{E}}{\partial t} \times \mu_0 \vec{H} \right)}_{= \frac{d}{dt} \left(\vec{E} \times \vec{H} \right)},$$

$$\nabla \cdot \left(\epsilon_0 \vec{E} \otimes \vec{E} + \mu_0 \vec{H} \otimes \vec{H} - \frac{1}{2} \left(\epsilon_0 |\vec{E}|^2 + \mu_0 |\vec{H}|^2 \right) \mathbb{I} \right) = \frac{d}{dt} \frac{1}{c^2} \left(\vec{E} \times \vec{H} \right), \tag{3.21}$$

with $\mu_0 \epsilon_0 = 1/c^2$. We derived at the definition of Maxwell's stress tensor

$$\mathbf{T} = \epsilon_0 \vec{E} \otimes \vec{E} + \mu_0 \vec{H} \otimes \vec{H} - \frac{1}{2} \left(\epsilon_0 |\vec{E}|^2 + \mu_0 |\vec{H}|^2 \right) \mathbb{I}, \tag{3.22}$$

which describes the interaction between electromagnetic forces and mechanical momentum. Integrating eq. (3.21) over an arbitrary volume gives

$$\int_V \nabla \cdot \mathbf{T} \cdot dV = \int_V \frac{d}{dt} \frac{1}{c^2} \left(\vec{E} \times \vec{H} \right) \cdot dV. \tag{3.23}$$

To solve this equation we can use Gauss's integration law

$$\int_V \nabla \cdot \mathbf{T} \cdot dV = \int_{\partial V} \mathbf{T} \cdot \vec{n} \cdot dA, \tag{3.24}$$

with ∂V the surface of V, $\vec{n}$ the unit vector perpendicular to the surface and dA an infinitesimally small surface element. So the force acting on an arbitrary body within the surface ∂V follows then immediately

$$\vec{F} = \int_{\partial V} \mathbf{T} \cdot \vec{n} \cdot dA. \tag{3.25}$$

3.3. Optical forces on particles along a nanofibre

Now, let us investigate how we can calculate the optical forces acting on the particles along the nanofibre. For the present model we are only interested into the forces acting along the fibre axis x

$$\vec{F} = \int_{\partial V} \mathbf{T} \cdot \vec{n}_x \cdot dA, \tag{3.26}$$

with

$$\mathbf{T} = \frac{\epsilon_0}{2}\left(E_x^2 - E_y^2 - E_z^2 + c^2\left(B_x^2 - B_y^2 - B_z^2\right)\right). \tag{3.27}$$

As the electric and magnetic fields are always orthogonal to the propagation direction $B_x = E_x = 0$ and as electromagnetic fields are transversal $c|\vec{B}| = |\vec{E}|$ Maxwell's stress tensor changes to

$$T_{xx} = -\epsilon_0 \vec{E}^2. \tag{3.28}$$

To calculate the forces acting on the i-th particle, we enclose this particle in a fictitious box and integrate over the boundaries of this box. As we assume that this particle is small compared to the wavelength of the light field we only have to take into account the planes orthogonal to the x-axes and found for the force on the i-th particle [64]

$$F_i = \frac{\epsilon_0}{2}\left(|A_i|^2 + |B_i|^2 - |C_i|^2 - |D_i|^2\right). \tag{3.29}$$

This force describes the missing photons, which transmits momentum onto the particles. The part $\propto -(|C_i|^2 - |A_i|^2)$ describes the missing photons coming from the right side, which leads to a force towards the left direction and the part $\propto |B_i|^2 - |D_i|^2$ describes the missing photons coming from the left side, which leads to a force towards the right direction. Inserting the amplitudes from eq. (3.14) into the force equation one can find for the force on a particle [16]

$$F_i = \frac{\sigma_{\mathrm{sc}}}{c}\left(\frac{2\left(I_l - I_r\right)\left(|\zeta|^2 + \Im\left(\zeta\right)\right)}{|1 - i\zeta|^2} - \frac{4\sqrt{I_l I_r}\Re\left(\zeta\right)\sin\left(2kx_i\right)}{|1 - i\zeta|^2} + \sqrt{2I_0}\left(\sqrt{I_r} - \sqrt{I_l}\right)\cos\left(kx_i\right)\right), \tag{3.30}$$

with $I_l = \frac{|B_i|^2 c\epsilon_0}{2}$, $I_r = \frac{|C_i|^2 c\epsilon_0}{2}$, $I_0 = \frac{|\eta|^2 c\epsilon_0}{2}$ and σ_{sc} the scattering cross section between the particles and the beam. The first term is proportional to the imaginary part of ζ and arises due to the radiation pressure and points towards the weaker source. The

second term arises due to the dipole force and the last term due to the interference between the transverse and the longitudinal fields.

3.4. Scattering into the fibre

In this section the scattered intensity of the transverse pump field into the fibre by the particles is calculated. We describe the particles along the fibre as two level atoms far detuned from any resonances. To make sure that the particles scatter the light symmetrically into both direction one has to choose an appropriate laser polarization and transition dipole moment of each emitter. Note, for simplification, here the fibre axis is the z-axis, so that the system can be described by cylindrical coordinates. We assume a single mode fibre with the HE_{11}-mode linearly polarized in the x-direction

$$\vec{e}^{\,(\delta)}(\omega, r, \phi) = \sqrt{2}(\hat{r}e_r(\omega, r, \phi) + \delta\hat{z}e_z(\omega, r, \phi)), \tag{3.31}$$

with $e_r(\omega, r, \phi)$ and $e_z(\omega, r, \phi)$ the cylindrical components of the guided modes [35; 47] and $\delta = -1$ for a left and $\delta = +1$ for a right propagating field. Fermi's golden rule can be used to describe the emission into the fibre by the particles [35; 47]

$$\gamma_{\text{guid}} = \frac{\omega\beta'}{2\epsilon_0\hbar}\sum_{\delta}|\vec{de}^{\,(\delta)}(\omega, r, \phi)|^2, \tag{3.32}$$

with $\beta' = d\beta/d\omega$ and β the modal propagation constant. If the dipole components d_z and d_x of the atoms have the same phase, and thus are linearly polarized in the xz-plane, the emission into the fibre does not depend on the propagation direction. We assume that the electric dipole is linearly polarized into the z direction

$$\gamma_{\text{guid}} = \frac{2\omega\beta'}{\epsilon_0\hbar}|d_z|^2|e_z|^2, \tag{3.33}$$

so that the particles symmetrically scatter the light into both directions.
The scattering rate into the fibre can then be calculated out of the emission rate and the excited state fraction ρ_{ee} [42]

$$R_{\text{sc}} = \gamma_{\text{guid}}\rho_{\text{ee}}(t \to \infty). \tag{3.34}$$

For a two level atom and a weak driving field one finds

$$\rho_{\mathrm{ee}} = \frac{1}{2}\frac{I/I_{\mathrm{sat}}}{1+4\Delta^2/\Gamma^2+I/I_{\mathrm{sat}}} \approx \frac{1}{2}\frac{I/I_{\mathrm{sat}}}{1+4\Delta^2/\Gamma^2} \ll 1, \tag{3.35}$$

with I the intensity shining on the particles, I_{sat} the saturation density of the atoms, Δ the detuning and Γ the spontaneous emission rate into free space.
The intensity scattered into the fibre is the power P per area A. The power is simply the scattering rate times the photon energy

$$I_k = \frac{P}{A} = \frac{\hbar\omega R_{\mathrm{sc}}}{A} \approx \frac{\omega^2\beta'}{A\epsilon_0}\frac{I/I_{\mathrm{sat}}}{1+4\Delta^2/\Gamma^2}|d_z|^2|e_z|^2. \tag{3.36}$$

For Cesium particles along a nanofibre with radius $r = 200$ nm, the fiber cross section area $A = r^2\pi$, the Cesium D2-line $\omega \approx 2.2 \cdot 10^{15}$ Hz with $\Gamma = 33 \cdot 10^6$ 1/s and the mass of Cesium $m \approx 220 \cdot 10^{-27}$ kg, and a detuning $\Delta = 100\ \Gamma$ we find for the intensity scattered into the fiber $I_k \approx 6.2 \cdot 10^{-4}\ I_0/I_{sat}$ W/m^2.

3.5. Weak scattering limit

In our calculations we often assume the weak scattering limit. In the weak scattering limit the backscattering by each particle in the fibre is neglected, so that only the scattering of the transverse pump field into the fibre leads to a force onto the particles. In this case the forces on the particles arises due to interference between these fields scattered into the fibre by the particles. Thus for the weak scattering limit we set $\zeta = r = 0$. So let us investigate how accurate the actual interactions can be approximated in this limit.
The scattering efficiency for backscattering of a guided mode by a particle can be written as [47]

$$\tilde{\eta}_{\mathrm{bw}} = |r|^2 = \frac{\hbar\omega R_{\mathrm{bw}}}{P_z} = \frac{\hbar\omega\gamma_{\mathrm{bw}}\rho_{\mathrm{ee}}}{I_z \cdot A} = \frac{\hbar\omega\gamma_{\mathrm{guid}}}{4AI_{\mathrm{sat}}}\frac{1}{1+4\Delta^2/\Gamma^2}, \tag{3.37}$$

with the emission into the backscattered field $\gamma_{\mathrm{bw}} = \gamma_{\mathrm{guid}}/2$ and incoming intensity I_z leading to a power P_z. Consequently, the part transmitted by a particle is the remaining part which is not reflected and not scattered into radiation modes $\tilde{\eta}_{\mathrm{rad}}$

$$|t|^2 = 1 - \tilde{\eta}_{\mathrm{bw}} - \tilde{\eta}_{\mathrm{rad}}. \tag{3.38}$$

We assume that the emission into the radiation modes γ_{rad} is approximately the free space emission Γ, which is a good approximation according to [47] and find

$$\tilde{\eta}_{\mathrm{rad}} = \frac{\hbar\omega\Gamma_{\mathrm{rad}}\rho_{\mathrm{ee}}}{I_z \cdot A} \approx \frac{\hbar\omega\gamma\rho_{\mathrm{ee}}}{I_z \cdot A} = \frac{\hbar\omega\Gamma}{2AI_{\mathrm{sat}}} \frac{1}{1+4\Delta^2/\Gamma^2} \tag{3.39}$$

and, thus

$$|t|^2 = 1 - \frac{\hbar\omega(\gamma_{\mathrm{guid}}/2+\Gamma)}{2AI_{\mathrm{sat}}(1+4\Delta^2/\Gamma^2)}. \tag{3.40}$$

Recalling the definition of the reflection and transmission coefficients from eq. (3.11) one can find $|r|^2 + |t|^2 = 1 - 2|t|^2\Im(\zeta)$ and it follows

$$\tilde{\eta}_{\mathrm{rad}} = 2|t|^2\Im(\zeta)\,. \tag{3.41}$$

So the imaginary part of ζ reads

$$\Im(\zeta) = \frac{\tilde{\eta}_{\mathrm{rad}}}{2|t|^2} = \frac{1}{2}\frac{\hbar\omega\Gamma}{2AI_{\mathrm{sat}}\left(1+4\Delta^2/\Gamma^2\right) - \hbar\omega\left(\gamma_{\mathrm{guid}}/2+\Gamma\right)}. \tag{3.42}$$

With

$$r = |r|e^{i\phi_r}, \tag{3.43a}$$

$$t = |t|e^{i\phi_t}, \tag{3.43b}$$

it follows

$$\zeta = -\frac{ir}{t} = -\frac{i|r|}{|t|}e^{i(\phi_r-\phi_t)}. \tag{3.44}$$

The phases can be found when knowing the imaginary part of ζ. For Cesium atoms with radius $r = 200$ nm, the fiber cross section area $A = r^2\pi$, the Cesium D2-line $\omega \approx 2.2 \cdot 10^{15}$ Hz with $\Gamma = 33 \cdot 10^6$ 1/s and the mass of Cesium $m \approx 220 \cdot 10^{-27}$ kg, $I_{\mathrm{sat}} = 1.65$ mW/cm^2 and a detuning $\Delta = 100\ \Gamma$ we find

$$\zeta = 3 \cdot 10^{-3} + 7.2i \cdot 10^{-5}. \tag{3.45}$$

Fig. 3.3 compares the forces acting on the particles using this small value of ζ and setting $\zeta = 0$. For small particle numbers the forces are almost equal, but for large particle numbers they are totally different. Even a small backscattering leads to large

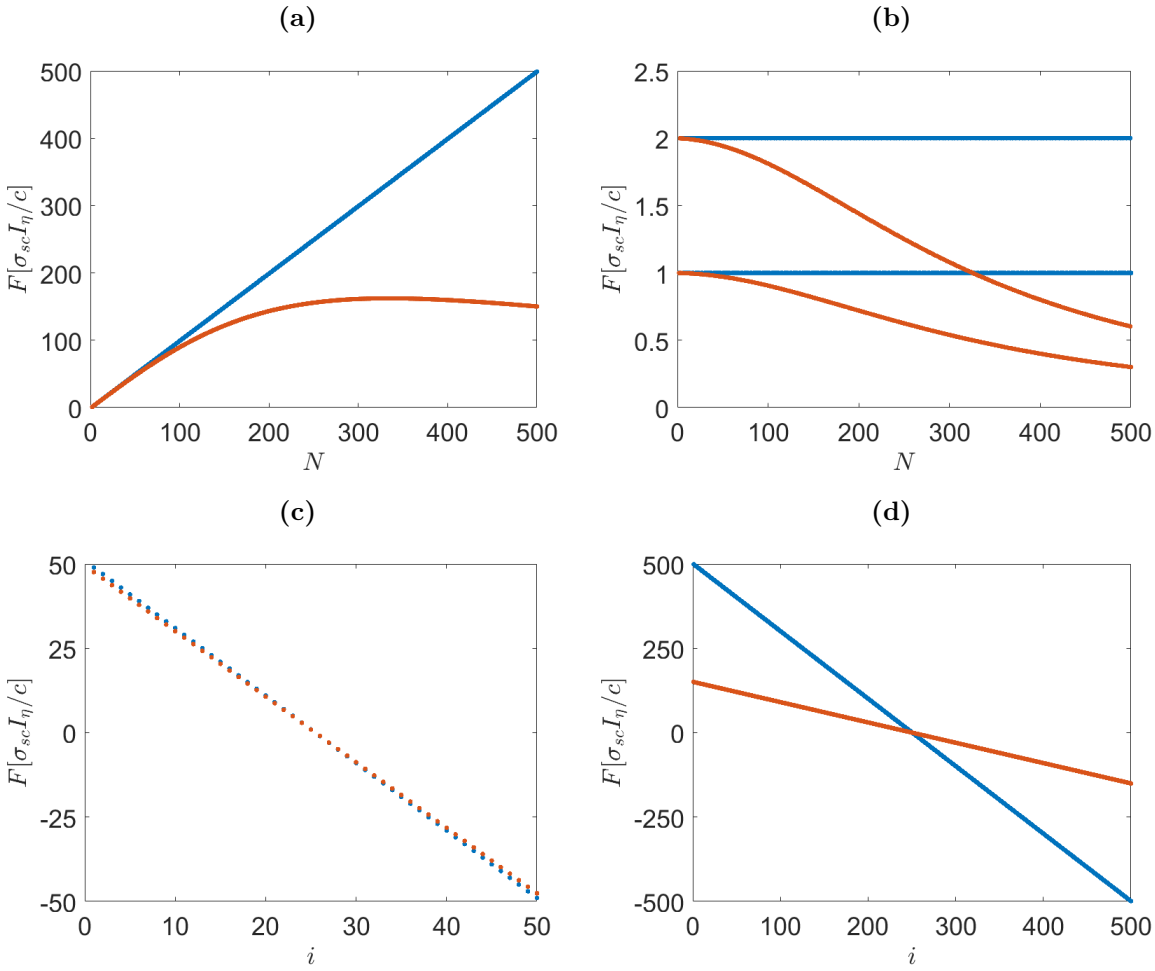

Figure 3.3.: Comparison between the forces on the particles for $\zeta = 0$ (blue) and for $\zeta = 3 \cdot 10^{-3} + 7.2i \cdot 10^{-5}$ (orange), when separated at a distance $d_i = \lambda$. Figure (a) and (b) compare the forces acting on the particles depending on the number of particles in the chain. Fig. (a) shows the force on the first particle and Fig. (b) on a particle near the center of the chain ($i = N/2$ for even particle numbers and $i = (N-1)/2$ for odd particle numbers). Fig. (c) and (d) compare the forces on all particles for a chain with 50 and 500 particles.

effects for large particle numbers as every particle reflects a small part of the field. Interestingly the effect is larger for particles at the beginning or the end of the chain than for particles in the centre. In the latter case the backscattering effects from both sides of the particle cancel each other, while the particles at the outer side "see" the reflection of all particles along the chain. In summary the weak scattering limit is a good approximation for small system sizes up to $\approx 50 - 70$ particles, but for larger particle numbers we have to consider backscattering effects.
The weak scattering limit has the advantage that for this case the forces acting on the particles can be written as the sum of two particle forces

$$F_i = \sum_{i=1}^{N} f_{\text{pair}}(x_i, x_j) = \sum_{i=1}^{N} \sum_{k} \frac{\sigma_{\text{sc}} I_k \cos\left(k\left(x_j - x_i\right)\right)}{c}. \tag{3.46}$$

In that case we can even define a potential $U(x_1, \ldots, x_N)$ such that

$$F_i = -\partial_{x_i} U(x_1, \ldots, x_N). \tag{3.47}$$

Note that when choosing $\zeta \neq 0$ the forces are not conservative and no potential could be defined for more than two particles.

Part I.

Self-ordering and stability of laser illuminated point particles near the fibre

4. Introduction

Particles trapped along a nanofibre collectively scatter and reorder the fibre field in a way, so that they build their own trap [16]. Here, the fibre field is generated by interference between the scattered and the pump field. The particles order in a way so that they trap high field intensities between them, which reminds of a self assembled cavity QED system. In this chapter we study the stability of these self-ordered configurations. In such configurations all forces on the particles vanish and the particles experience a restoring force when shifted from their equilibrium position. The particles then start to oscillate around their trapping position with frequencies depending on the intensity and frequency of the pump field, the coupling constant ζ, the mass of the particles and the number of particles in the chain. For large system sizes scattering and absorption of the light field can be very strong and destabilize the structure.

5. Publication

Collective scattering and oscillation modes of optically bound point particles trapped in a single mode waveguide field

Daniela Holzmann[1] and Helmut Ritsch

Collective coherent scattering of laser light induces strong light forces between polarizable point particles. These dipole forces are strongly enhanced in magnitude and distance within the field of an optical waveguide so that at low temperature the particles self-order in strongly bound regular patterns. The stationary configurations typically exhibit super-radiant scattering with strong particle and light confinement. Here we study collective excitations of such self-consistent crystalline particle-light structures as function of particle number and pump strength. Multiple scattering and absorption modify the collective particle-field eigenfrequencies and create eigenmodes of surprisingly complex nature. For larger arrays this often leads to dynamical instabilities and disintegration of the structures even if additional damping is present.

Optics Express 23, 31793-31806 (2015) doi:10.1364/OE.23.031793

[1]D.H. performed all of the calculations in this publication, while H.R. contributed in an advisory role.

5.1. Introduction

Laser light scattering off free particles is accompanied by momentum transfer and thus forces. If the incident light fields are far detuned from any optical resonance, energy absorption and spontaneous re-emission play only a minor role and a coherent redistribution of photon momenta determines the force. As such coherent scattering from different particles largely preserves the laser phase, these fields interfere and thus the resulting force on each particle depends on its distance to nearby particles and acquires a collective nature, which depends on all other particle positions [66; 67]. While in a 3D geometry the interaction strongly decays with distance and is averaged out by phase randomization from particle positions and motion, in regular particle arrays or in a spatially confined geometry, this interaction can become very strong [68; 69]. Particularly strong effects appear if the light fields are optically confined in resonators [70], guided by optical structures as mirrors [71] or confined in waveguides [15; 16; 72; 73]. Besides cold dilute gases, closely related effects have been studied using various kinds of nano-particles in solution [74–76].

Following first predictions by Chang and coworkers for near resonant weak pumping of atomic dipoles [15; 73], we have recently shown that cold particles illuminated far of resonance, who can freely move along or within an optical nano-fiber field, tend to form regular but complex optical structures through optical long range coupling. They collectively scatter light into the fiber mode and self-trap in the optical potential generated by interference of the scattered light and the pump field [16]. Surprisingly we see that not only the light confines the particle motion but the particles also confine the light forming Bragg like atom mirrors at their outer edges. Numerical simulations predict that in certain cases even more complex structures as cavity arrays are self-formed by the particles [72]. This potentially generates a self-ordered cavity QED system with strong particle photon coupling via so called atomic mirrors [77]. While such dipole energy minimizing configurations were also studied for conventional 1D optical lattices, they could be shown to be generally unstable [78].

In this work we theoretically study the dynamics and stability of such self-organized cavity QED systems. Already in our previous work we could identify configurations where all forces on the particles vanish and one gets a restoring force towards these equilibrium positions for small shifts for each particle. Nevertheless, displacing one particle immediately changes the fields at all other particle positions and creates

perturbation forces on them. Here we cannot expect any energy conservation for the particle motion as we are dealing with an open system where the pump laser forms a non depleting energy and momentum reservoir [79; 80]. Hence perturbing one particle induces nonconservative collective motion of all particles. Eventually these oscillations exhibit exponential growth and lead to a disintegration of the whole structure. A central aim of this work is to calculate and study the frequencies and stability of the corresponding linearized eigenmodes of the coupled atom field systems and their application to induce tailored long range interactions in this system. Of course the system is inherently nonlinear so that the full dynamics can only be captured numerically.
Our work is organized as follows. First we quickly overview the results of our recent paper [16]. Out of these, in order to investigate the stability of the particles, we linearize the forces acting on the particles around their equilibrium positions. Calculating the eigenvalues of the so obtained coupling matrix we find a condition which enables and limits the formation of stable configurations. With this we first study configurations in the negligible coupling limit and then pass over to more realistic complex coupling parameters.

5.2. Scattering matrix approach to light induced motion in 1D

Let us first briefly recall our previously developed multiple scattering approach to calculate the stationary fields and forces on a linear array of particles with transverse illumination as schematically depicted in Fig. 5.1 [16] . For a given spatial arrangement of point scatterers in the field of a 1D waveguide the light field can be calculated by a scattering matrix approach [64; 80–82]. The contribution of each particle is represented by a single 3×3 matrix parametrized by an effective coupling constant ζ proportional to its linear polarizability $\tilde{\alpha}$ and the field mode amplitude at its position. This determines the interaction between the particle and the fiber mode as well as the scattering amplitude in and out of the fiber η. The transmission and reflection coefficients are related to the coupling constant via $t = 1/(1 - i\zeta)$ and $r = i\zeta/(1 - i\zeta)$. For symmetric scattering the coupling between the amplitudes left and right of a particle can then be expressed using the following beam splitter matrix $\mathbf{M}_{BS}$ [16]

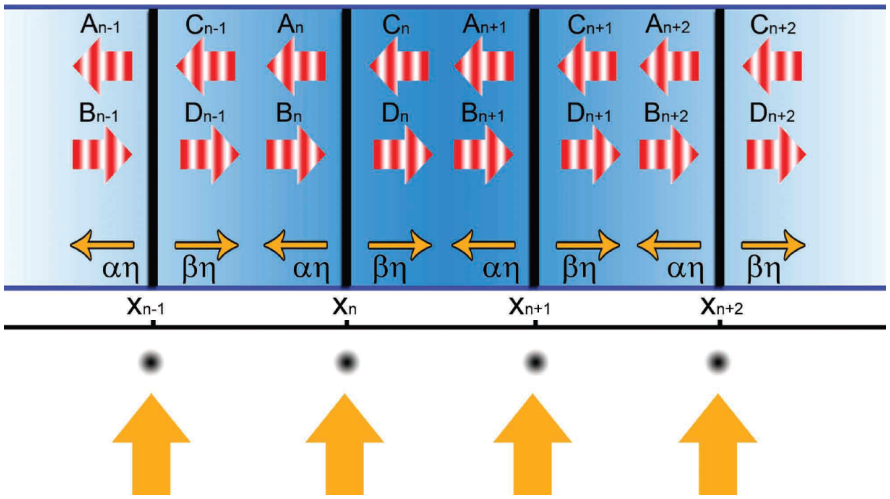

Figure 5.1.: A 1D array of point particles scattering light in and out of an optical nano-structure can be modelled as a collection of beam splitters interacting with a plane wave.

$$\begin{pmatrix} A_j \\ B_j \\ \eta \end{pmatrix} = \frac{1}{t} \begin{pmatrix} t^2 - r^2 & r & \frac{1}{\sqrt{2}}(t-r) \\ -r & 1 & -\frac{1}{\sqrt{2}} \\ 0 & 0 & t \end{pmatrix} \begin{pmatrix} C_j \\ D_j \\ \eta \end{pmatrix} = \begin{pmatrix} 1+i\zeta & i\zeta & \frac{1}{\sqrt{2}}(1-i\zeta) \\ -i\zeta & 1-i\zeta & \frac{1}{\sqrt{2}}(i\zeta-1) \\ 0 & 0 & 1 \end{pmatrix} \begin{pmatrix} C_j \\ D_j \\ \eta \end{pmatrix}, \tag{5.1}$$

where B_j, C_j, η are the incoming fields allowing to determine the outgoing fields A_j, D_j, *cf.* Fig. 5.1. These in turn are used as inputs to neighbouring scatterers as $C_{j-1} = A_j \exp(ik(x_j - x_{j-1}))$ and $D_{j-1} = B_j \exp(-ik(x_j - x_{j-1}))$. Multiplying all the matrices including the propagation phase shifts then allows to determine the field distribution corresponding to the momentary particle positions. Note that we neglect the propagation time of the light within the structure compared to particle motion.
Using simple arguments based on the Maxwell stress tensor the momentary field then determines the optical force on the j-th particle along the x-axis [64; 83]:

$$F_j = \frac{\epsilon_0}{2} \left(|A_j|^2 + |B_j|^2 - |C_j|^2 - |D_j|^2 \right). \tag{5.2}$$

We will use this optical force then as ingredient to obtain Newton's equations for the particle motion, where we add damping describing additional light or background gas induced friction. In previous work we and others have seen that under quite general

conditions stationary equilibrium positions can be found, where all particles are force free and feel a restoring force against small shifts. However, in contrast to a standard 1D optical lattice, the absence of a force does not enforce an unaltered propagation of the light [64] but just guarantees a balance between internal and external light scattering [16]. Following Ref. [64] and including a linear friction term proportional to μ the equations of motion for the point particles of mass m then read:

$$m\ddot{x}_j = -\mu\dot{x}_j + F_j(x_1, \ldots, x_N). \tag{5.3}$$

Stationary structures require $F_j(x_1, \ldots, x_N) = 0$ for all j. Here these are not simple equidistant lattices, but rather complex particle arrangements with regular central parts including the formation of Bragg like reflectors at both ends of the equilibrium particle distribution denoted as $x_j^{(0)}$ [16].

5.3. Collective excitations around equilibrium positions

When a particle is weakly displaced from its equilibrium $x_j(t) = x_j^{(0)} + \xi_j(t)$, it feels a restoring force and at the same time induces a global light field modification generating forces on all other particles. Once set free the perturbed particles start a correlated oscillatory motion around their equilibrium positions $x_j^{(0)}$. In the following we study the spatial properties and eigenfrequencies of such small amplitude particle oscillations analogous to phonons of a lattice. Note that the existence of a stationary stable equilibrium configuration does not guarantee stability with respect to even very small such collective oscillations, which in general can grow in amplitude and disintegrate the particle array.

A Taylor expansion of the forces gives the following set of coupled differential equations

$$m\ddot{\xi}_j = -\mu\dot{\xi}_j + \sum_{l=1}^{N} D_{jl}\xi_l, \tag{5.4}$$

with nonlocal coupling matrix

$$D_{jl} = \frac{\partial}{\partial x_l} F_j(x_1 = x_1^{(0)}, \ldots, x_N = x_N^{(0)}) = \lim_{\xi\to 0} \frac{1}{\xi} F_j(x_v = x_v^{(0)} + \delta_{lv}\xi,\ v = 1, \ldots, N). \tag{5.5}$$

Note that these coupling constants would be an ideal basis for a coupled oscillator model in the ultracold gas limit. For the classical point particle model here we simply use the ansatz $\vec{\xi} = \vec{A}e^{i\omega t}$ in equations (5.4) and solve for the eigensystem of $\mathbf{D}$, where the oscillation frequencies can be calculated from the eigenvalues λ_ν via

$$\omega_\nu = \frac{i\mu \pm \sqrt{-\mu^2 - 4m\lambda_\nu}}{2m}, \tag{5.6}$$

yielding the linearized solutions:

$$\xi_j = \left(A_j e^{\frac{i\sqrt{-\mu^2-4m\lambda_\nu}}{2m}t} + B_j e^{\frac{-i\sqrt{-\mu^2-4m\lambda_\nu}}{2m}t} \right) e^{-\frac{\mu t}{2m}}. \tag{5.7}$$

The eigenfrequencies include a real part describing damping or antidamping depending on its sign. If positive, it leads to an amplification of the oscillation amplitude and the particles can not form a stable stationary configuration. Hence, to ensure stable configurations the eigenvalues have to fulfil the condition [64]:

$$m(\Im(\lambda_\nu))^2 \leq -\mu^2 \Re(\lambda_\nu). \tag{5.8}$$

Note that added damping can restore the stability only as long as all real parts of the eigenvalues are negative. Without external friction, $\mu = 0$, Eq. (5.7) simplifies to

$$\xi_j = A_j e^{i\sqrt{\frac{-\lambda_\nu}{m}}} + B_j e^{-i\sqrt{\frac{-\lambda_\nu}{m}}} \tag{5.9}$$

and as long as we have no imaginary parts of the eigenvalues λ_ν and the real parts are negative the particles are simply oscillating around their equilibrium position.

5.3.1. Negligible mode coupling limit $\zeta = 0$

In the special case when particle mode coupling is very weak but we have a strong transverse pump field applied, one can set $\zeta = 0$ while still keeping a nonzero scattering into the fiber, thus $\eta \neq 0$. Here the scattering of the field by the particles within the fiber is neglected and any two particles interact equivalently. As predicted before [15] and also found by us in Ref. [16], in this limit the particles in a stationary state are

equidistantly distributed and the transfer matrix can easily be calculated explicitly:

$$\mathbf{M}_{TM} = (\mathbf{M}_{BS} \cdot \mathbf{P}(d))^{N-1} \cdot \mathbf{M}_{BS} = \mathbf{M}^{N-1} \cdot \mathbf{M}_{BS}. \tag{5.10}$$

Here the collectively scattered field intensities are symmetric to right and left and read

$$I_{ol} = I_{or} = \frac{I_\eta}{2} \left(\frac{\sin(\frac{Nkd}{2})}{\sin(\frac{kd}{2})} \right)^2 \tag{5.11}$$

and for the force on the j-th of N particles we get:

$$F_j = -\frac{P_\eta \cos(Nkd/2) \sin((2j-N-1)kd/2)}{\sin(kd/2)}, \tag{5.12}$$

with $P_\eta = I_\eta/c$ the radiation pressure resulting from the transverse pump field.
This force vanishes for different lattice constants $d = (2n-1)\lambda/(2N)$ with $n \in \mathbb{N}$ giving potential stationary solutions. We will now calculate the linearized coupling matrices $\mathbf{D}$ for a small displacement of the l-th particle within such a solution. For the amplitude perturbation at the j-th cloud from displacing the l-th cloud by $\xi = \epsilon k$ we have to distinguish between the two cases if it is at the right or left side of the displaced l-th cloud:

$$\begin{pmatrix} A_j \\ B_j \\ \eta \end{pmatrix} = \mathbf{M}^{N-j+1} \mathbf{P}(-d) \left(\begin{pmatrix} 0 \\ D_N \\ \eta \end{pmatrix} + \epsilon \begin{pmatrix} 0 \\ b \\ 0 \end{pmatrix} \right), \tag{5.13}$$

with the perturbation $\vec{b}$. For $j < l$ the amplitudes can be calculated as follows

$$\begin{pmatrix} A_j \\ B_j \\ \eta \end{pmatrix} = \mathbf{M}^{l-j} \mathbf{P}(\frac{\epsilon}{k}) \mathbf{M}_{BS} \mathbf{P}(-\frac{\epsilon}{k}) \mathbf{P}(d) \mathbf{M}^{N-l} \mathbf{P}(-d) \left(\begin{pmatrix} 0 \\ D_N \\ \eta \end{pmatrix} + \epsilon \begin{pmatrix} 0 \\ b \\ 0 \end{pmatrix} \right). \tag{5.14}$$

Let us first look at the stability of the solution with the maximal possible lattice distance $n = N$, i.e. $d = (2N-1)\lambda/(2N)$, where the force on the j-th particle induced by the perturbation of the l-th particle reads:

$$F_j\left(d = \frac{2N-1}{2N}\lambda\right) = \begin{cases} P_\eta \epsilon \sin\left(\frac{|j-l|\pi}{N}\right), & \text{for } j \neq l \\ -P_\eta \epsilon \frac{\cos(\frac{\pi}{2N})}{\sin(\frac{\pi}{2N})}, & \text{for } j = l, \end{cases} \tag{5.15}$$

and so $D_{jl} = \frac{k}{\epsilon} F_j$ is:

$$D_{jl} = P_\eta k \left(\sin\left(\frac{|j-l|\pi}{N} \right) - \delta_{jl} \cot\left(\frac{\pi}{2N} \right) \right). \tag{5.16}$$

D is a symmetric matrix with all eigenvalues λ_ν real and as it is a circulant matrix, they and the eigenvectors $\vec{z}_\nu$ can easily be calculated to give:

$$\lambda_\nu = -2P_\eta k \frac{\cot\left(\frac{\pi}{2N}\right) \sin^2\left(\frac{\pi(\nu-1)}{N}\right)}{\cos\left(\frac{\pi}{N}\right) - \cos\left(\frac{2\pi(\nu-1)}{N}\right)},\ \vec{z}_\nu = \left(e^{\frac{2\pi i(\nu-1)(j-1)}{N}} \right)_{j=1}^{N}. \tag{5.17}$$

As we have seen in Eq. (5.9), stably oscillating configurations require real and negative eigenvalues. Hence this configuration is stable and we find N phonon modes with frequencies

$$\omega_\nu = \sqrt{\frac{P_\eta k}{m} \left(\cot\left(\frac{\pi}{2N}\right) + \frac{\sin\left(\frac{\pi}{N}\right)}{\cos\left(\frac{\pi}{N}\right) - \cos\left(\frac{2\pi(\nu-1)}{N}\right)} \right)} = \omega_{2,0} \sqrt{\frac{\cot\left(\frac{\pi}{2N}\right) \sin^2\left(\frac{\pi(\nu-1)}{N}\right)}{\cos\left(\frac{\pi}{N}\right) - \cos\left(\frac{2\pi(\nu-1)}{N}\right)}}, \tag{5.18}$$

where we have defined $\omega_{2,0} = \sqrt{\frac{2P_\eta k}{m}}$ as binding oscillation frequency for two particles at $\zeta = 0$. As expected from translation invariance of the system, the lowest $\nu = 1$-mode corresponding to the center of mass motion has a zero eigenfrequency. Interestingly our result exactly coincides with the prediction based on nonlocal fiber enhanced resonant dipole-dipole interaction obtained before in Ref. [15]. In the limit of large particle numbers we find:

$$\omega_\nu \approx 2(\nu-1)\omega_{2,0} \sqrt{\frac{N}{\pi(3+4\nu(\nu-2))}}. \tag{5.19}$$

Consequently the particle binding frequency grows with $\sqrt{N}$ for large particle numbers stiffening the structure with particle number. Fig. 5.2 shows the phonon frequency as a function of mode number for different particle numbers. It demonstrates that the second and the N-th mode posses higher frequencies than all the other modes which are almost degenerate. It is now interesting to see how the atoms interact with respect to their distance. For this we insert Eq. (5.5) into Eq. (5.4) and calculate the perturbation

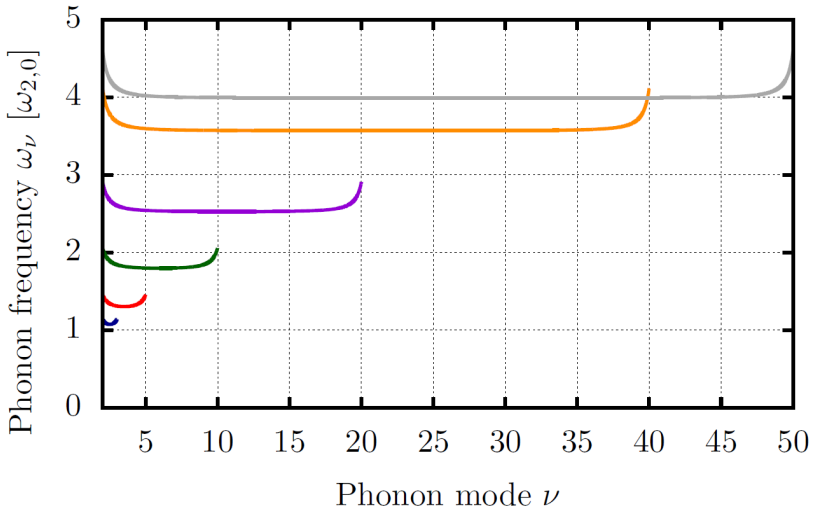

Figure 5.2.: Phonon frequency as a function of the phonon mode ν for $\zeta = 0$ beginning with $\nu = 2$. The blue line corresponds to $N = 3$, the red line to $N = 5$, the green line to $N = 10$, the violet line to $N = 20$, the orange line to $N = 40$ and the grey line to $N = 50$.

induced forces explicitly:

$$F_j = P_\eta k \left(\sum_{l \neq j} \sin\left(\frac{|j-l|\pi}{N} \right) (\xi_l - \xi_j) \right), \tag{5.20}$$

exhibiting a coupling between the oscillators proportional to $\sin\left(\frac{|j-l|\pi}{N}\right)$ depending on the distance $|j-l|$ and particle number N. Maximum coupling occurs between center and boundary particles at $N = 2|j-l|$ and it vanishes for $|j-l| \ll N$.
Let us now insert other zero force solutions at smaller distances $d_n = \frac{2n-1}{2N}\lambda$ into Eq. (5.5). Here we can explicitly calculate the eigenvalues in the limit of large particle numbers

$$\lambda_\nu = P_\eta k \frac{2(2n-1)^2}{4(\nu-1)^2 - (2n-1)^2}. \tag{5.21}$$

As according to Eq. (5.8) fully stable configurations are only possible if all eigenvalues are negative, we see that the first case, $n = N$, was the only stable configuration with a distance below λ. An example how the particles evolve over time is plotted in Fig. 5.3, where we compare stable configurations setting $n = N$ (Fig. (a)) with unstable ones setting $n = N - 1$ (Fig. (b)). Note that starting from a stable configuration we obtain correlated oscillations of particles and fields around the stable position with a slow

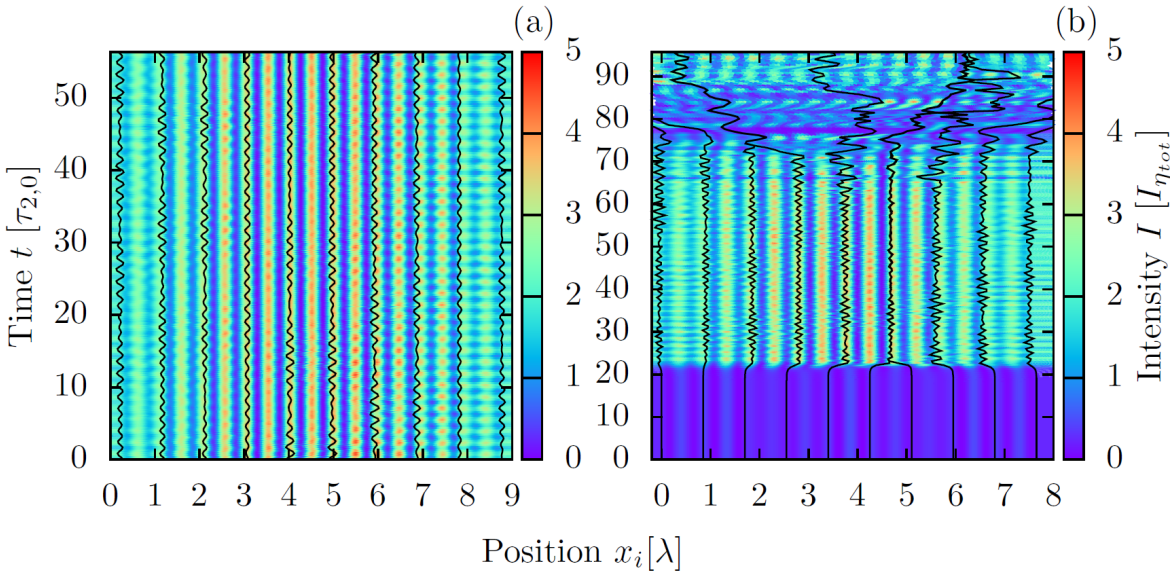

Figure 5.3.: Ten particles evolving over time with only transverse pump and $\zeta = 0$. In Fig. (a) we have chosen $d = \frac{2N-1}{2N}\lambda$ $(n = N)$ as initial condition slightly perturbed by $\xi_{initial} = 0.1\lambda$, while in Fig. (b) the particles are initially positioned at an unstable zero force distance $d = \frac{N-1}{N}\lambda$ $(n = N-1)$. $\tau_{2,0}$ is defined as $\tau_{2,0} = \frac{2\pi}{\omega_{2,0}}$.

nonlocal excitation transfer between the sites. At negligible coupling, $\zeta = 0$, one finds neither damping nor amplification of the oscillation modes but we still see a higher light intensity confined at the center of the structure. Starting from an unstable zero-force configuration the particles keep their position only for a short time until two particles collapse and the other particles reorder. Nevertheless, also this new configuration is not stable and the whole order disintegrates.

5.3.2. Collective dynamics for finite particle field interaction parameter ζ

Particles within the fiber mode will not only couple pump light in and out of the fiber, but also scatter it to the opposite propagation direction, into free space or absorb it. This is effectively described by a non-zero complex value of ζ [64]. As a first consequence this immediately leads to spatially inhomogeneous fields in the mode and thus non-equidistant stationary configurations, which, in general, do not allow for analytic treatment. Although the equation for the force (5.2) still looks very simple, its explicit form gets already complicated for more than three particles and even the

zero-force points can not be found analytically. Hence to still get some analytical insights we first study systems of only two and three particles.

Two particles

For two particles with no fields injected along the fiber, the light scattered by one particle only interferes with the light scattered by the second particle. Translation and spatial inversion invariance of the system here implies a vanishing sum of the forces on the two particles as long as we neglect asymmetric chiral coupling [84]. The force as function of the real part ζ_r and imaginary part ζ_i then depends only on particle distance d [16]:

$$F_1 = -F_2 = \frac{P_\eta |1 - i\zeta|^2 \cos(kd)}{4\left(|\zeta|^2 + \zeta_i\right)\cos^2(\frac{kd}{2}) + 2\zeta_r \sin(kd) + 1}, \tag{5.22}$$

and the zero force distances $d_0 = \frac{\lambda}{2}\left(\frac{1}{2} + n\right), n \in \mathbb{N}$ are independent on ζ. Interestingly even for strongly absorbing particles as e.g. gold nano-particles $\zeta_i >> \zeta_r$, we thus obtain the same force free binding distances [69]. Intuitively this can be understood from the $\pi/2$ relative phase shift of the two scattered fields at this distance preventing interference. To study the stability and strength of binding we calculate the coupling matrix $\mathbf{D}$:

$$D_{jl} = (-1)^{l-j} \frac{P_\eta k |1 - i\zeta|^2 \left(\sin(kd)\left(2|\zeta|^2 + 2\zeta_i + 1\right) + 2\zeta_r\right)}{\left(2\left(\cos(kd) + 1\right)\left(|\zeta|^2 + \zeta_i\right) + 2\sin(kd)\zeta_r + 1\right)^2}, \tag{5.23}$$

and its eigenvalues. Inserting the zero force distances $d = \left(\frac{1}{4} + n\right)\lambda$ the nonzero eigenvalue reads

$$\lambda_2 = \frac{2kP_\eta |1 - i\zeta|^2}{1 + 2(|\zeta|^2 + \zeta_i - \zeta_r)}, \tag{5.24}$$

and for $d = \left(\frac{3}{4} + n\right)\lambda$ we get the same eigenvalue with opposite sign. As the non-zero eigenvalue for the latter case is real and negative, these are stable configurations. The phonon frequency characterizing the optical binding strength then reads:

$$\omega = \omega_{2,0}\sqrt{\frac{|1 - i\zeta|^2}{1 + 2(|\zeta|^2 + \zeta_i - \zeta_r)}}, \tag{5.25}$$

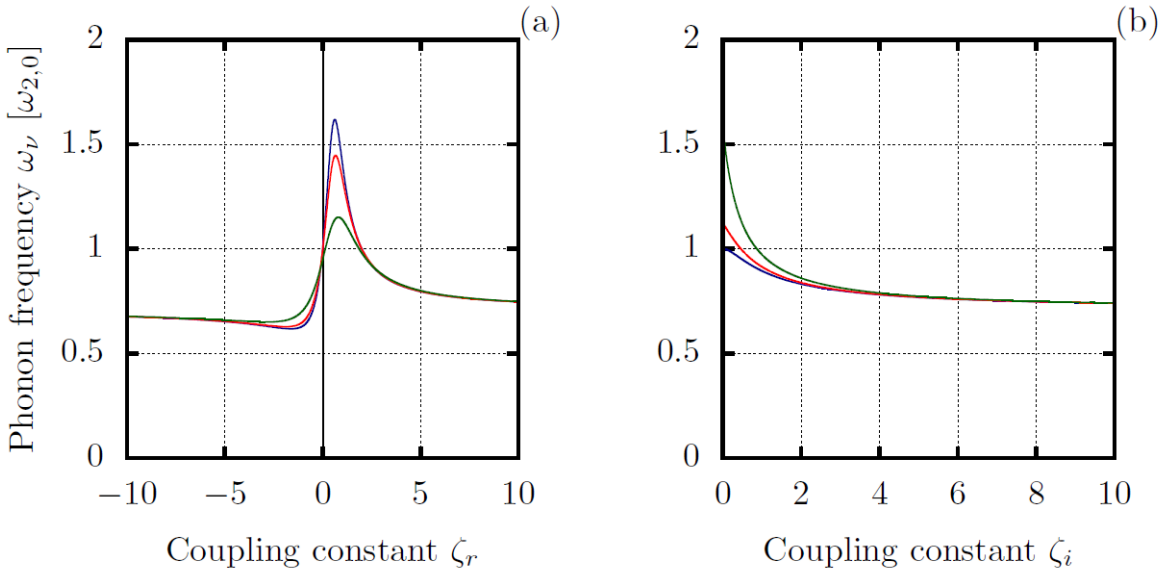

Figure 5.4.: Fig. (a) shows the phonon frequency ω_ν as a function of the real part of the coupling constant ζ_r. The blue line corresponds to $\zeta_i = 0$, the red line to $\zeta_i = \frac{1}{9}$ and the green line to $\zeta_i = \frac{1}{2}$.
Fig. (b) shows the phonon frequency ω_ν as a function of the imaginary part of the coupling constant ζ_i. The blue line corresponds to $\zeta_r = 0$, the red line to $\zeta_r = \frac{1}{9}$ and the green line to $\zeta_r = \frac{1}{2}$.
We can see that the function goes to $\frac{\omega_{2,0}}{\sqrt{2}}$ for large values of ζ. For the real part of ζ we can find a maximum for $\zeta_r > 0$.

which for large values of ζ stays finite and converges to $\frac{\omega_{2,0}}{\sqrt{2}}$ below the noninteracting value. Nevertheless for real ζ ω_2 reaches a maximum of $\omega_{2,0}\sqrt{3+\sqrt{5}}$ at $\zeta \simeq 0.618$ (Fig. 5.5(a)), while we find a minimum coupling frequency for blue detuning at $\zeta \simeq -1.618$ of $\omega_2 = \omega_{2,0}\sqrt{3-\sqrt{5}}$ (Fig. 5.5(b)). The dynamics in these two extreme cases is shown in figure 5.5. Note that in both cases we can observe that the particles and fields oscillate and are periodically pushed apart whenever the intensity of the light trapped between them is maximal. Note that even in the blue detuned case for low field seeking particles we find stable trapping but much slower oscillations, i.e. weaker confinement.

Three particle dynamics

Let us now add a third particle. Due to symmetry we will restrict ourselves to equidistant configurations and calculate the total transfer matrix. Again the amplitudes of the electric field to the left and right of the particles yield the forces acting on the particles,

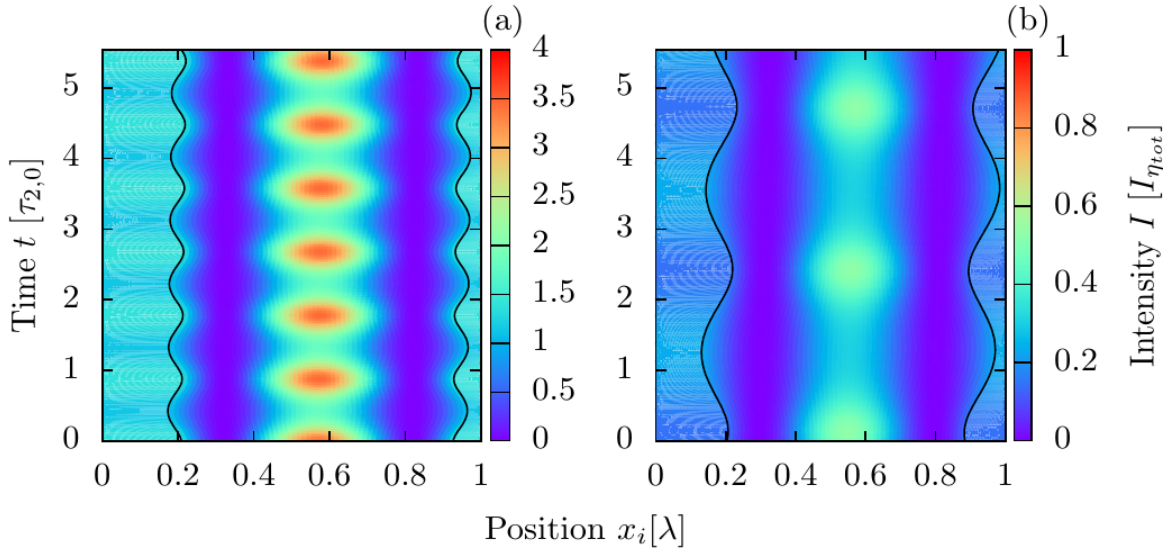

Figure 5.5.: Two particles evolving over time with only transverse pump oscillating after a small perturbation with maximal frequency at $\zeta = 0.618$ (a), and minimal frequency at $\zeta = -1.618$ (b).

where as a consequence of symmetry the force on the middle particle is zero and the remaining two sum up to zero, i.e.:

$$F_1 \simeq P_\eta \left(\cos(kd) + \cos(2kd) - \zeta(2\sin(2kd) + \sin(3kd) + \sin(4kd))\right) + O[\zeta]^2, \quad (5.26a)$$

$$F_2 = 0, \quad (5.26b)$$

$$F_3 = -F_1. \quad (5.26c)$$

Here the general expressions are complex so that we only present some special cases to exhibit the stability of the particles. For real $\zeta = \frac{1}{9}$ only one stable equidistant configuration exists with $d_1 = d_2 \simeq (0.8276 + n)\lambda$. Adding an imaginary part, $\zeta = \frac{1+i}{9}$, the stationary distances are enlarged to $d_1 = d_2 \simeq (0.8305+n)\lambda$. As shown in Fig. 5.6 the trajectories of the particles here show surprising features. Although the stationary state is symmetric with respect to the middle particle, a small perturbation from this equilibrium induces an intricate superposition of two oscillations, namely fast relative oscillations superimposed on a much slower and large amplitude a center of mass oscillation. As the system possesses translational invariance implying momentum conservation, it could be expected in principle to not allow any center of mass oscillations. This is at first sight also confirmed by the oscillation eigenvalues $\{0, -3.83P_\eta k, -3.51P_\eta k\}$ calculated

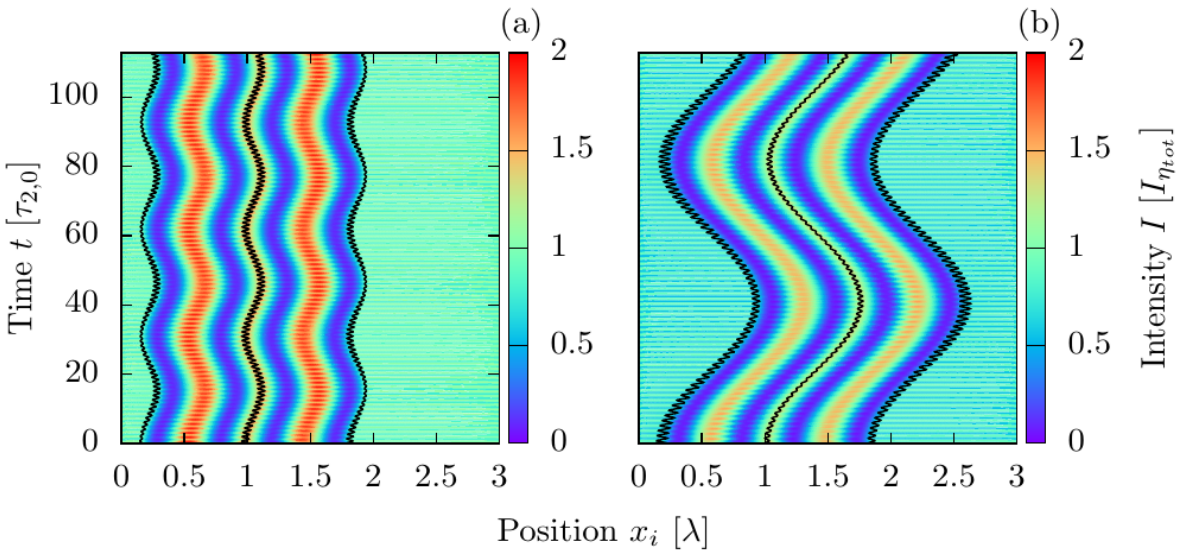

Figure 5.6.: Three particles evolving over time with only transverse pump, $\zeta = \frac{1}{9}$ (a), $\zeta = \frac{1+i}{9}$ (b) and a small perturbation $\xi_{initial} = 0.1\lambda$.

for real $\zeta = 1/9$ with eigenvectors

$$z_1 = \frac{1}{\sqrt{3}} \begin{pmatrix} 1 \\ 1 \\ 1 \end{pmatrix}, \; z_2 = \begin{pmatrix} 0.287 \\ -0.914 \\ 0.287 \end{pmatrix}, \; z_3 = \frac{1}{\sqrt{2}} \begin{pmatrix} -1 \\ 0 \\ 1 \end{pmatrix}. \tag{5.27}$$

The eigenvalue λ_1 corresponding to the center of mass oscillation z_1 is indeed zero. However, we can see that the eigenvector z_2, corresponding to the case where two outer particles oscillate together against the middle particle includes a center of mass oscillation, as the middle particle moves much more then the sum of the outer two. This is also clearly visible in figure 5.6. At this point we have to recall that we have a strongly coupled atom field system where the pump laser constitutes an external energy and momentum reservoir, which can provide or accept momentum from the particles and conservation is only true for the combined atom field system. The asymmetric oscillation z_2 thus periodically channels momentum in and out of the light field inducing these unexpected center of mass oscillations. The dynamics gets even more complicated if we allow for light absorption and investigate the eigensystem for an imaginary coupling

constant, $\zeta = \frac{1+i}{9}$. We find the eigenvalues $\{0, -2.98P_\eta k, -2.89P_\eta k\}$ with eigenvectors

$$z_1 = \frac{1}{\sqrt{3}} \begin{pmatrix} 1 \\ 1 \\ 1 \end{pmatrix}, \; z_2 = \begin{pmatrix} 0.349 \\ -0.869 \\ 0.349 \end{pmatrix}, \; z_3 = \frac{1}{\sqrt{2}} \begin{pmatrix} -1 \\ 0 \\ 1 \end{pmatrix}. \tag{5.28}$$

Again we observe a large amplitude center of mass oscillation due to the non inversion symmetric initial perturbations which lead to even amplified center of mass motion. Hence we see that while we have stationary equilibrium configuration, the system tends to disintegrate due to dynamical instability when no external friction force is provided.

5.4. Numerical studies of the dynamics of larger ensembles

While the momentary light field for a given configuration of many particles can still be found by simple matrix multiplication, the explicit expression for the forces soon becomes prohibitively complicated and their common zeros cannot be analytically obtained any more. Numerically, however, this still can be done efficiently even for hundreds of particles and the solutions of the corresponding dynamical equations of motion are still possible. In order to capture typical features of the resulting many particle dynamics but still obtain readable plots, here we study the case of ten particles for various coupling strengths and damping. Fig. 5.7 compares the time evolution for real polarizability ζ (Fig. 5.7(a)) with the case of partial absorption, where ζ also possesses a small imaginary part (Fig. 5.7(b)). In the first case a small perturbation simply induces small correlated oscillations in the vicinity of local field maxima with some slow energy exchange between the particles. In the second case with absorption, the particles start to oscillate first, but these oscillations grow until one reaches the nonlinear regime leading to a complete destruction of the order. As shown in a recent paper [16] one can still find a stable configuration for this case in the over damped limit. The mathematical origin for this instability is that due to the imaginary part of ζ the eigenvalues also acquire imaginary parts. This instability still can be suppressed up to a limiting value by introducing an additional friction coefficient as in Eq. (5.8).
We had demonstrated that in the weak-coupling-limit, $\zeta = 0$, one has stable oscillatory

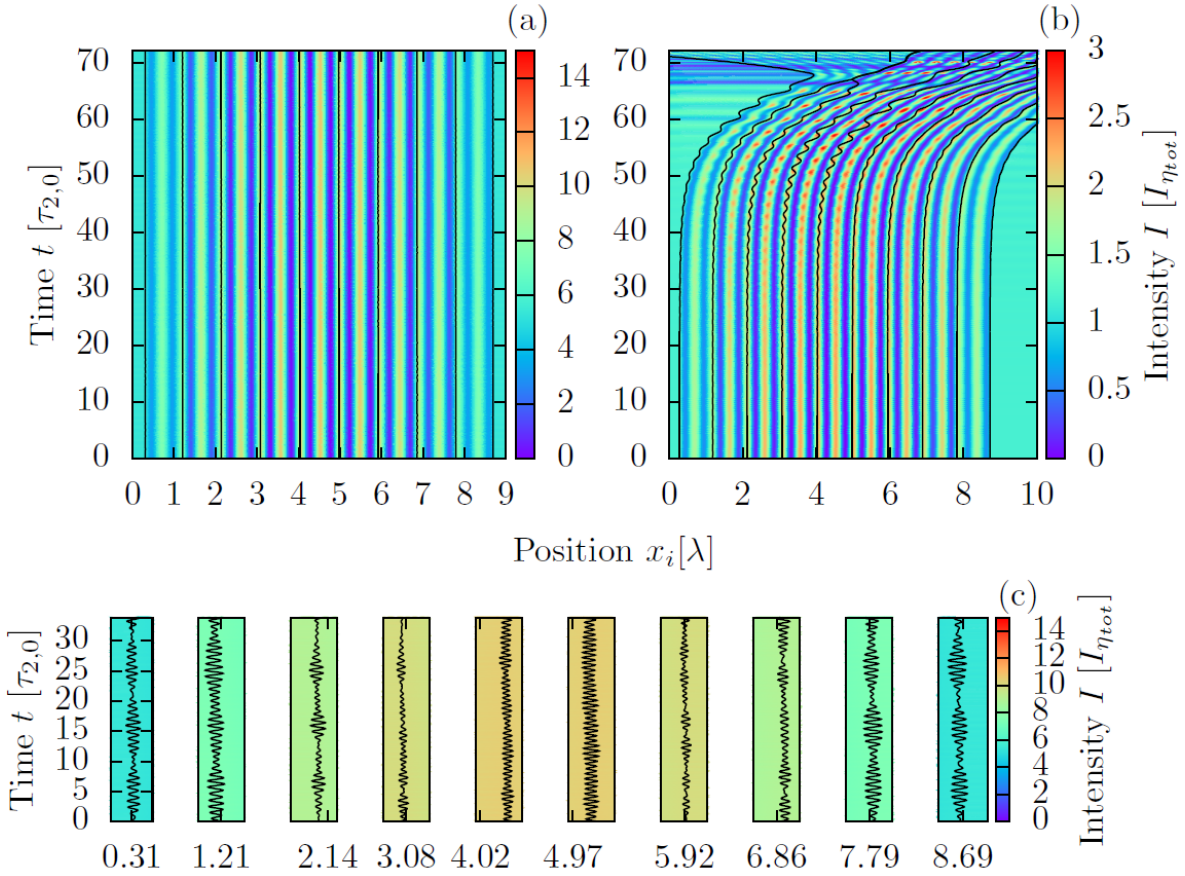

Figure 5.7.: Ten particles evolving over time with only transverse pump, $\zeta = \frac{1}{9}$ (a), $\zeta = \frac{1+i}{9}$ (b) and a small perturbation of $\zeta_{initial} = 0.001\lambda$. Fig. (c) shows the oscillation of the particles. Here we magnify the trajectories of Fig. (a) and plotted a range of 0.01λ. In the second case the particles, first, start to oscillate around their equilibrium positions, but the perturbation leads to antidamping, which, in the end, destroys the configuration. The eigenvalues of the first case are all negative and real, while the eigenvalues of the second case acquire positive and negative imaginary parts.

solutions without the need of damping. Introducing $\zeta \neq 0$ this behaviour is often lost and even for rather small perturbations the particle oscillations grow beyond the linearized regime. This leads to the collapse of the particle structure and they are expelled to the sides. It is now interesting to study the grade of instability in such a system, which turn out to be very parameter and size sensitive. To quantitatively show this we compute the eigenvalues of $\mathbf{D}$ and examine the real parts of them characterizing the magnitude of the corresponding instabilities. The maximum real part of all the nonzero eigenvalues of $\mathbf{D}$ is plotted in Fig. 5.8 as a function of real and imaginary part of ζ for different system sizes N. If this value is negative, in principle one can always add enough extra damping to stabilize the configuration, while a positive value implies dynamical instability in any case. The figures show that for odd particle number we get a boundary line to the left of which at least one eigenvalue is positive and Eq. (5.8) thus predicts an instability, which can not be removed by damping. For negative real ζ and even particle numbers (Fig. (b) and (d)) we find stable configurations with negative eigenvalues but they are very very close to zero. In this case the system is very sensitive to small perturbations and needs strong extra damping for stabilization. Here in numerical simulations we often find unstable dynamics despite using a nominally stable parameter set, as validity of the linearized equations is very limited.
An analogous phenomenon occurs for large particle numbers (Fig. (d)) and large values of ζ_r. In this case it is difficult to distinguish between stable configurations with eigenvalues close to zero and unstable configurations. We can observe that for large ζ positive eigenvalues appear, especially for imaginary ζ, which prevent the formation of stable configurations. In general only for small and mostly real ζ (blue region in Fig. 5.8) robust stable configurations can be expected.

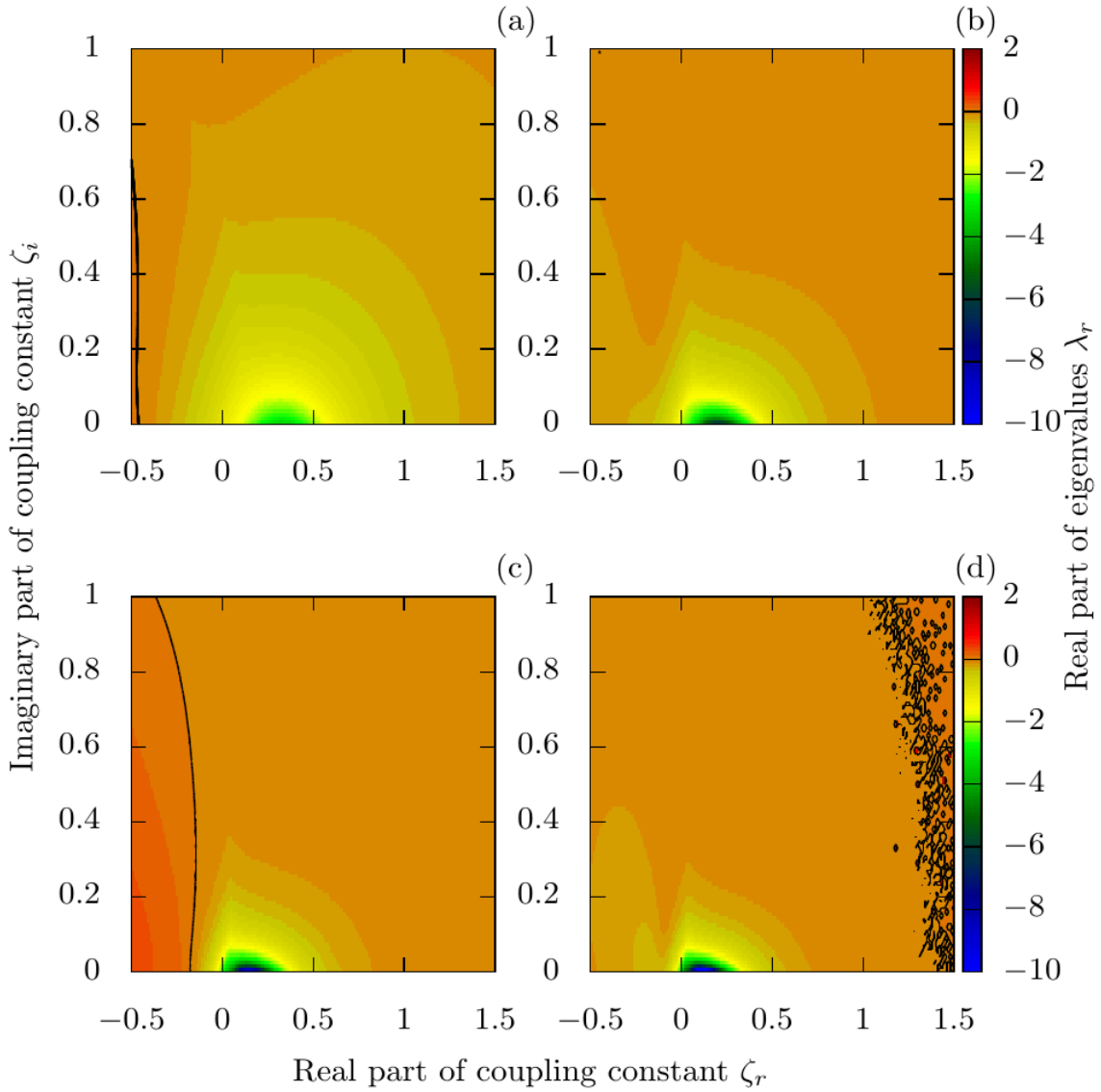

Figure 5.8.: Maximum real part of the nonzero eigenvalues as function of real and imaginary part of ζ. Fig. (a) corresponds to $N = 5$ particles, (b) to $N = 10$, (c) to $N = 15$ and (d) to $N = 20$. Black lines show the zero value contour lines.

5.5. Conclusions

Coherently illuminated particles in a 1D trap order in strongly bound regular arrays induced by the interference of the scattered and pump light. If the scattered light is guided by nano-optical waveguide structures one finds very strong binding and long range order with phonon frequencies growing approximately with the square root of the particle number. In general the scatterers arrange in configurations, where the scattered light is resonantly confined within the structure to maximize the optical trapping potential for the particles. This can be seen as a controllable prototype 1D implementation of an atom light crystal. In this regime absorption and scattering of the fields by the particles within the waveguide create a strongly nonlinear dynamical response of the system, which limits the size of stable arrays even in the presence of additional friction forces. This hints at the possibility to create self-ordered nano-cavity QED systems where the particles simultaneously form the resonator via atom mirrors [85] as well as the optical active system. As a next task towards a quantized field treatment one of course would need to estimate the magnitude of the self-ordered single photon coupling strength, which requires a sort of dynamic mode description. Generalizations to several frequencies, polarizations or higher order transverse modes should generate even more intriguing complex physics. In principle similar mechanisms should also be at work in planar 2D setups [76] leading to even stronger transverse light confinement and limiting the extension of optical matter.

Acknowledgements: We thank D. Chang for helpful discussions. This work has been supported by the Austrian Science Fund (FWF) through SFB Foqus project F4013.

6. Detailed calculations

In this section the single steps to find the oscillation frequency of the shifted particles in the weak scattering limit from eq. (5.18) are explained and the restoring forces (5.20) calculated.
In the weak-scattering-limit the beam-splitter-matrix (3.16) reads

$$\mathbf{M}_{BS} = \begin{pmatrix} 1 & 0 & \frac{1}{\sqrt{2}} \\ 0 & 1 & -\frac{1}{\sqrt{2}} \\ 0 & 0 & 1 \end{pmatrix}. \tag{6.1}$$

We define the following matrix $\mathbf{M}$

$$\mathbf{M} = \mathbf{M}_{BS} \cdot \mathbf{P}(d), \tag{6.2}$$

with

$$\mathbf{M}^N = \begin{pmatrix} e^{ikdN} & 0 & \frac{e^{ikdN}-1}{\sqrt{2}\left(-1+e^{ikd}\right)} \\ 0 & e^{-ikdN} & \frac{e^{ikd}\left(e^{-ikdN}-1\right)}{\sqrt{2}\left(-1+e^{idk}\right)} \\ 0 & 0 & 1 \end{pmatrix}. \tag{6.3}$$

For an equidistant lattice the amplitudes can be calculated by

$$\begin{pmatrix} A_1 \\ 0 \\ \eta \end{pmatrix} = (\mathbf{M}_{BS} \cdot \mathbf{P}(d))^N \mathbf{P}(-d) \begin{pmatrix} 0 \\ D_N \\ \eta \end{pmatrix} = \mathbf{M}^N \mathbf{P}(-d) \begin{pmatrix} 0 \\ D_N \\ \eta \end{pmatrix}, \tag{6.4}$$

with $B_1 = C_N = 0$. For the outgoing amplitudes at both side of the system then follows

$$A_1 = D_N = \frac{(e^{ikdN} - 1)\eta}{\sqrt{2}(e^{ikd} - 1)}. \tag{6.5}$$

Furthermore, the eigenvectors $\vec{u}$, $\vec{v}$, $\vec{w}$ and eigenvalues λ_1, λ_2, λ_3 of $\mathbf{M}$ are

$$\lambda_1 = e^{ikd} \qquad \vec{u} = \begin{pmatrix} 1 \\ 0 \\ 0 \end{pmatrix}, \tag{6.6a}$$

$$\lambda_2 = e^{-ikd} \qquad \vec{v} = \begin{pmatrix} 0 \\ 1 \\ 0 \end{pmatrix}, \tag{6.6b}$$

$$\lambda_3 = 1 \qquad \vec{w} = \begin{pmatrix} \frac{1}{\sqrt{2}(1-e^{ikd})} \\ \frac{e^{ikd}}{\sqrt{2}(1-e^{ikd})} \\ 1 \end{pmatrix}. \tag{6.6c}$$

Using

$$\mathbf{P}(-d) \begin{pmatrix} 0 \\ D_N \\ \eta \end{pmatrix} = \eta \begin{pmatrix} 0 \\ \frac{e^{ikd}(e^{ikdN}-1)}{\sqrt{2}(e^{ikd}-1)} \\ 1 \end{pmatrix} = \eta\vec{w} - \frac{\eta}{\sqrt{2}(1-e^{ikd})}\vec{u} - \frac{\eta e^{ikd(1+N)}}{\sqrt{2}(1-e^{ikd})}\vec{v} \tag{6.7}$$

we find for the amplitudes to both sides of a particle j

$$\begin{aligned} \begin{pmatrix} A_j \\ B_j \\ \eta \end{pmatrix} &= \mathbf{M}^{N-j+1}\mathbf{P}(-d) \begin{pmatrix} 0 \\ D_N \\ \eta \end{pmatrix} \\ &= \mathbf{M}^{N-j+1} \left(\eta\vec{w} - \frac{\eta}{\sqrt{2}(1-e^{ikd})}\vec{u} - \frac{\eta e^{ikd(1+N)}}{\sqrt{2}(1-e^{ikd})}\vec{v} \right) \\ &= \eta\vec{w} - \frac{\eta e^{ikd(N-j+1)}}{\sqrt{2}(1-e^{ikd})}\vec{u} - \frac{\eta e^{ikdj}}{\sqrt{2}(1-e^{ikd})}\vec{v}, \end{aligned} \tag{6.8}$$

and consequently, the outgoing intensity to the left of the system yields

$$\begin{pmatrix} A_1 \\ 0 \\ \eta \end{pmatrix} = \eta\vec{w} - \frac{\eta e^{ikd}}{\sqrt{2}(1-e^{ikd})}\vec{v} - \frac{\eta e^{ikdN}}{\sqrt{2}(1-e^{ikd})}\vec{u}. \tag{6.9}$$

When displacing the l-th cloud by ξ eq. (6.9) changes to

$$\eta\vec{w} - \frac{\eta e^{ikd}}{\sqrt{2}(1-e^{ikd})}\vec{v} - \frac{\eta e^{ikdN}}{\sqrt{2}(1-e^{ikd})}\vec{u} + \frac{\xi}{k}\begin{pmatrix} a \\ 0 \\ 0 \end{pmatrix}$$
$$= \mathbf{M}^{l-1}\mathbf{P}(\xi)\mathbf{M}_{BS}\mathbf{P}(-\xi)\mathbf{P}(d)\mathbf{M}^{N-l}\left(\eta\vec{w} - \frac{\eta}{\sqrt{2}(1-e^{ikd})}\vec{u} - \frac{\eta e^{ikd(1+N)}}{\sqrt{2}(1-e^{ikd})}\vec{v} + \frac{\xi}{k}e^{ikd}\begin{pmatrix} 0 \\ b \\ 0 \end{pmatrix}\right), \tag{6.10}$$

with the perturbations:

$$\vec{a} = \begin{pmatrix} a \\ 0 \\ 0 \end{pmatrix} = a\vec{u} \tag{6.11}$$

and similar for $\vec{b}$

$$\vec{b} = \begin{pmatrix} 0 \\ b \\ 0 \end{pmatrix} = b\vec{v}. \tag{6.12}$$

We define $\epsilon = \frac{\xi}{k}$ and $\mathbf{A} = \begin{pmatrix} 0 & 0 & 1 \\ 0 & 0 & 1 \\ 0 & 0 & 0 \end{pmatrix}$. Using $\mathbf{P}(\frac{\epsilon}{k})\mathbf{M}_{BS}\mathbf{P}(-\frac{\epsilon}{k}) = \mathbf{M}_{BS} + i\frac{\epsilon}{\sqrt{2}}\mathbf{A} + \mathcal{O}(\epsilon^2)$, we get

$$\epsilon a\vec{u} + \eta\vec{w} - \frac{\eta e^{ikd}}{\sqrt{2}(1-e^{ikd})}\vec{v} - \frac{\eta e^{ikdN}}{\sqrt{2}(1-e^{ikd})}\vec{u} =$$
$$\mathbf{M}^{l-1}(\mathbf{M}_{BS} + \frac{i\epsilon}{\sqrt{2}}\mathbf{A})\mathbf{P}(d)\mathbf{M}^{N-l}\left(\eta\vec{w} - \frac{\eta}{\sqrt{2}(1-e^{ikd})}\vec{u} - \frac{\eta e^{ikd(1+N)}}{\sqrt{2}(1-e^{ikd})}\vec{v} + \epsilon e^{ikd}b\vec{u}\right). \tag{6.13}$$

Out of this relation, we find

$$a = \frac{i\eta e^{ikd(l-1)}}{\sqrt{2}}, \tag{6.14a}$$
$$b = -\frac{i\eta e^{ikd(N-l)}}{\sqrt{2}}. \tag{6.14b}$$

Now we can calculate the amplitudes to the left of the j-th cloud in the perturbed lattice. We have to distinguish between three cases. In the first case the j-th cloud is at the right side of the displaced l-th cloud, thus $j > l$

$$\begin{aligned}\begin{pmatrix} A_j \\ B_j \\ \eta \end{pmatrix} &= \mathbf{M}^{N-j+1}\mathbf{P}(-d)\left(\begin{pmatrix} 0 \\ D_N \\ \eta \end{pmatrix} + \epsilon \begin{pmatrix} 0 \\ b \\ 0 \end{pmatrix}\right) \\ &= \eta\vec{w} - \frac{\eta e^{ikdj}}{\sqrt{2}(1-e^{ikd})}\vec{v} - \frac{\eta e^{ikd(N-j+1)}}{\sqrt{2}(1-e^{ikd})}\vec{u} - \frac{i\epsilon}{\sqrt{2}}\eta e^{ikd(j-l)}\vec{v}, \end{aligned} \tag{6.15}$$

and similar for the case where the j-th cloud is at the left side of the displaced cloud l $j < l$

$$\begin{aligned}\begin{pmatrix} A_j \\ B_j \\ \eta \end{pmatrix} &= \mathbf{M}^{l-j}\mathbf{P}(\frac{\epsilon}{k})\mathbf{M}_{BS}\mathbf{P}(-\frac{\epsilon}{k})\mathbf{P}(d)\mathbf{M}^{N-l}\mathbf{P}(-d)\left(\begin{pmatrix} 0 \\ D_N \\ \eta \end{pmatrix} + \epsilon \begin{pmatrix} 0 \\ b \\ 0 \end{pmatrix}\right) \\ &= \eta\vec{w} - \frac{\eta e^{ikdj}}{\sqrt{2}(1-e^{ikd})}\vec{v} + \left(\frac{\eta e^{ikd(N-j+1)}}{\sqrt{2}(e^{ikd}-1)} + \frac{i\epsilon}{\sqrt{2}}\eta e^{ikd(l-j)}\right)\vec{u}. \end{aligned} \tag{6.16}$$

To calculate the difference of the intensities, we use $C_j = A_j - \frac{\eta}{\sqrt{2}}$ and $D_j = B_j + \frac{\eta}{\sqrt{2}}$ and get

$$|A_j|^2 + |B_j|^2 - \left(|C_j|^2 + |D_j|^2\right) = |A_j|^2 + |B_j|^2 - \left(|A_j - \frac{\eta}{\sqrt{2}}|^2 + |B_j + \frac{\eta}{\sqrt{2}}|^2\right). \tag{6.17}$$

For $j > l$, then, this results in

$$\begin{aligned}|A_j|^2 + |B_j|^2 - (|C_j|^2 + |D_j|^2) &= \frac{|\eta|^2}{2\sin\left(\frac{kd}{2}\right)}\left(\epsilon\cos\left(\frac{kd(2(j-l)+1)}{2}\right)\right. \\ \left.-\epsilon\cos\left(\frac{kd(2(l-j)+1)}{2}\right) + \sin\left(\frac{kd(1-2j)}{2}\right) + \sin\left(\frac{kd(1+2(n-j))}{2}\right)\right) \end{aligned} \tag{6.18}$$

and, thus, we find for the force on the j-th particle due to the perturbation on the l-th particle

$$F_{j>l}\left(d = \frac{2N-1}{2N}\lambda\right) = \frac{I_\eta \epsilon}{c}\sin\left(\frac{(j-l)\pi}{N}\right). \tag{6.19}$$

For $j < l$, it yields

$$|A_j|^2 + |B_j|^2 - (|C_j|^2 + |D_j|^2) = \frac{|\eta|^2}{2\sin\left(\frac{kd}{2}\right)} \left(-\epsilon \cos\left(\frac{kd(2(j-l)+1)}{2}\right) \right.$$
$$\left. +\epsilon \cos\left(\frac{kd(2(l-j)+1)}{2}\right) + \sin\left(\frac{kd(1-2j)}{2}\right) + \sin\left(\frac{kd(1+2(n-j))}{2}\right)\right) \quad (6.20)$$

and, consequently, in this case we find for the force

$$F_{j<l}\left(d = \frac{2N-1}{2N}\lambda\right) = -F_{j>l}\left(d = \frac{2N-1}{2N}\lambda\right) = -\frac{I_\eta \epsilon}{c} \sin\left(\frac{(j-l)\pi}{N}\right). \quad (6.21)$$

Additionally, we have to treat separately the case where $j = l$. For this case the amplitudes to the right of the beam-splitter j, C_j and D_j, have to be calculated as for the case where $j > l$

$$\begin{pmatrix} C_j \\ D_j \\ \eta \end{pmatrix} = \mathbf{M}^{-1} \begin{pmatrix} A_j \\ B_j \\ \eta \end{pmatrix}_{j>l} = \begin{pmatrix} A_j - \frac{\eta}{\sqrt{2}} \\ B_j + \frac{\eta}{\sqrt{2}} \\ \eta \end{pmatrix}$$
$$= \eta\vec{w} + \left(\frac{-\eta e^{ikdl}}{\sqrt{2}\,(1-e^{ikd})} + \frac{\eta(1-i\epsilon)}{\sqrt{2}}\right)\vec{v} - \left(\frac{\eta e^{ikd(N-l+1)}}{\sqrt{2}\,(1-e^{ikd})} + \frac{\eta}{\sqrt{2}}\right)\vec{u}, \quad (6.22)$$

and it follows

$$|C_j|^2 + |D_j|^2 = \frac{|\eta|^2}{4\sin^2(\frac{kd}{2})} \left(2 - \cos(kdl) - \cos(kd(l-N))\right.$$
$$\left. -\epsilon \sin(kd) - \epsilon \sin(kd(l-1)) + \epsilon \sin(kdl)\right) + \mathcal{O}(\epsilon^2). \quad (6.23)$$

The amplitudes to the left of the beam-splitter $j = l$ have to be calculated as for the case $j < l$

$$\begin{pmatrix} A_j \\ B_j \\ \eta \end{pmatrix} = \eta\vec{w} - \frac{\eta e^{ikdl}}{\sqrt{2}(1-e^{ikd})}\vec{v} + \left(\frac{\eta e^{ikd(N-l+1)}}{\sqrt{2}(e^{ikd}-1)} + \frac{i\epsilon}{\sqrt{2}}\eta\right)\vec{u}, \quad (6.24)$$

which leads to

$$|A_j|^2 + |B_j|^2 = \frac{|\eta|^2}{4\sin^2(\frac{kd}{2})}\left(2 - \cos\left(kd(N-l+1)\right) - \cos\left(kd(l-1)\right)\right.$$
$$\left. +\epsilon\sin\left(kd\right) - \epsilon\sin\left(kd(l-N)\right) - \epsilon\sin\left(kd(N-l+1)\right)\right) + \mathcal{O}(\epsilon^2). \quad (6.25)$$

With

$$|A_j|^2 + |B_j|^2 - (|C_j|^2 + |D_j|^2) = \frac{|\eta|^2}{4\sin^2(\frac{kd}{2})}\left(-\cos\left(kd(l-1)\right) + \cos\left(kdl\right)\right)$$
$$+\cos\left(kd(l-N)\right) - \cos\left(kd(N-l+1)\right) + 2\epsilon\sin\left(kd\right) + \epsilon\sin\left(kd(l-1)\right)$$
$$\left. +\epsilon\sin\left(kd(N-l)\right) - \epsilon\sin\left(kdl\right) - \epsilon\sin\left(kd(N-l+1)\right)\right), \quad (6.26)$$

we obtain for the force on the perturbed lattice

$$F_{j=l}\left(d = \frac{2N-1}{2N}\lambda\right) = -\frac{I_\eta\epsilon\cos\left(\frac{\pi}{2N}\right)}{c\sin\left(\frac{\pi}{2N}\right)}. \quad (6.27)$$

Using Eq. (6.19), Eq. (6.21) and Eq. (6.27), we can easily read off $D_{jl} = \frac{k}{\epsilon}F_j$:

$$D_{jl} = \frac{I_\eta k}{c}\left(\sin\left(\frac{|j-l|\pi}{N}\right) - \delta_{jl}\cot\left(\frac{\pi}{2N}\right)\right) \quad (6.28)$$

The matrix $\mathbf{D}$ is symmetric, thus all eigenvalues are real. Because it is also a circulant matrix, the eigenvalues can be easily calculated [86]. Therefore, the matrix can be rewritten in the following way

$$\mathbf{D} = \begin{pmatrix} a_0 & a_{N-1} & \dots & a_2 & a_1 \\ a_1 & a_0 & \dots & a_3 & a_2 \\ \vdots & \vdots & \vdots & \vdots & \vdots \\ a_{N-1} & a_{N-2} & \dots & a_1 & a_0 \end{pmatrix} = a_0\mathbb{1} + \sum_{i=1}^{N-1}\mathbf{Z}^i, \quad (6.29)$$

with

$$\mathbf{Z} = \begin{pmatrix} 0 & 0 & \dots & 0 & 1 \\ 1 & 0 & \dots & 0 & 0 \\ 0 & 1 & \dots & 0 & 0 \\ \vdots & \vdots & \vdots & \vdots & \vdots \\ 0 & 0 & \dots & 1 & 0 \end{pmatrix}. \tag{6.30}$$

The matrix $\mathbf{Z}$ has N different eigenvalues z_k, which have the following form

$$z_k = e^{\frac{2\pi i(k-1)}{N}}, \tag{6.31}$$

with the eigenvectors

$$\vec{z}_k = \begin{pmatrix} 1 \\ z_k \\ z_k^2 \\ z_k^3 \\ \vdots \\ z_k^N \end{pmatrix}. \tag{6.32}$$

All circulant matrices have the same basis of eigenvectors $\vec{z}$ with the eigenvalues

$$\lambda_\nu = \sum_{i=0}^{N-1} a_i z_\nu^i. \tag{6.33}$$

Inserting Eq. (6.31) into Eq. (6.33), we obtain the eigenvalues λ_ν for the matrix $\mathbf{D}$

$$\begin{aligned} \lambda_\nu &= -\frac{I_\eta k}{c}\left(\cot\left(\frac{\pi}{2N}\right) + \frac{\sin\left(\frac{\pi}{N}\right)}{\cos\left(\frac{\pi}{N}\right) - \cos\left(\frac{2\pi(\nu-1)}{N}\right)}\right) \\ &= -\frac{2I_\eta k}{c}\frac{\cot\left(\frac{\pi}{2N}\right)\sin^2\left(\frac{\pi(\nu-1)}{N}\right)}{\cos\left(\frac{\pi}{N}\right) - \cos\left(\frac{2\pi(\nu-1)}{N}\right)}. \end{aligned} \tag{6.34}$$

It ensues that the eigenvalues are all negative, which, according to Eq. (5.9), enables the particles to form stable configurations at this distance, even if the lattice is slightly perturbed.

In the absence of damping, $\mu = 0$, we find N phonon modes with frequency (5.18)

$$\begin{aligned}\omega_\nu &= \sqrt{\frac{I_\eta k}{mc}\left(\cot\left(\frac{\pi}{2N}\right) + \frac{\sin\left(\frac{\pi}{N}\right)}{\cos\left(\frac{\pi}{N}\right) - \cos\left(\frac{2\pi(\nu-1)}{N}\right)}\right)} \\ &= \sqrt{\frac{2I_\eta k}{mc}\frac{\cot\left(\frac{\pi}{2N}\right)\sin^2\left(\frac{\pi(\nu-1)}{N}\right)}{\cos\left(\frac{\pi}{N}\right) - \cos\left(\frac{2\pi(\nu-1)}{N}\right)}} = \omega_{2,0}\sqrt{\frac{\cot\left(\frac{\pi}{2N}\right)\sin^2\left(\frac{\pi(\nu-1)}{N}\right)}{\cos\left(\frac{\pi}{N}\right) - \cos\left(\frac{2\pi(\nu-1)}{N}\right)}},\end{aligned} \tag{6.35}$$

Inserting Eq. (5.5) into Eq. (5.4) we obtain the forces (5.20) acting on the particle j when perturbing particle l:

$$F_j = \frac{I_\eta k}{c}\left(-\cot\left(\frac{\pi}{2N}\right)\xi_j + \sum_{l\neq j}\sin\left(\frac{|j-l|\pi}{N}\right)\xi_l\right) \tag{6.36}$$

$$= \frac{I_\eta k}{c}\left(\left(-\cot\left(\frac{\pi}{2N}\right) + \sum_{l\neq j}\sin\left(\frac{|j-l|\pi}{N}\right)\right)\xi_j + \sum_{l\neq j}\sin\left(\frac{|j-l|\pi}{N}\right)(\xi_l - \xi_j)\right) \tag{6.37}$$

$$\begin{aligned}= \frac{I_\eta k}{c}\Bigg(\Bigg(&-\cot\left(\frac{\pi}{2N}\right) + \sum_{l=1}^{j-1}\sin\left(\frac{l\pi}{N}\right) + \sum_{l=1}^{N-1}\sin\left(\frac{l\pi}{N}\right)\Bigg)\xi_j \\ &+ \sum_{l\neq j}\sin\left(\frac{|j-l|\pi}{N}\right)(\xi_l - \xi_j)\Bigg)\end{aligned} \tag{6.38}$$

$$\begin{aligned}= \frac{I_\eta k}{c}\Bigg(\Bigg(&-\cot\left(\frac{\pi}{2N}\right) + \frac{\sin\left(\frac{(j-1)\pi}{2N}\right)\sin\left(\frac{(j)\pi}{2N}\right) + \sin\left(\frac{(N-1)\pi}{2N}\right)}{\sin\left(\frac{\pi}{2N}\right)}\Bigg)\xi_j \\ &+ \sum_{l\neq j}\sin\left(\frac{|j-l|\pi}{N}\right)(\xi_l - \xi_j)\Bigg)\end{aligned} \tag{6.39}$$

$$= \frac{I_\eta k}{c}\left(\left(-\cot\left(\frac{\pi}{2N}\right) + \cot\left(\frac{\pi}{2N}\right)\right)\xi_j + \sum_{l\neq j}\sin\left(\frac{|j-l|\pi}{N}\right)(\xi_l - \xi_j)\right) \tag{6.40}$$

$$= \frac{I_\eta k}{c}\left(\sum_{l\neq j}\sin\left(\frac{|j-l|\pi}{N}\right)(\xi_l - \xi_j)\right). \tag{6.41}$$

Part II.

Finite range interparticle forces and self-ordering in broadband illumination

7. Introduction

A nice feature of nanofibres is, that they can guide a broad frequency spectrum. Launching a broadband light field into the fibre changes the interaction properties of the particles. Depending on the bandwidth of this field the interparticle forces decay exponentially and one can tune the interactions from infinite range to nearest neighbor interactions. In such a field the particles still self-order in stable configurations. In this case the force between the particles is a special case of a Fourier cosine series and, thus, the combination of various fields gives one the possibility to tune the forces between the particles depending on the properties of these fields. So, by choosing specific combinations of the intensities, frequencies and the bandwidths of the fields, one can design different force shapes. This gives one even the possibility to turn off the forces between special particle pairs.

8. Publication

Tailored long range forces on polarizable particles by collective scattering of broadband radiation

Daniela Holzmann[1] and Helmut Ritsch

Collective coherent light scattering by polarizable particles creates surprisingly strong, long range inter-particle forces originating from interference of the light scattered by different particles. While for monochromatic laser beams this interaction decays with the inverse distance, we show here that in general the effective interaction range and geometry can be controlled by the illumination bandwidth and geometry. As generic example we study the modifications inter-particle forces within a 1D chain of atoms trapped in the field of a confined optical nanofiber mode. For two particles we find short range attraction as well as optical binding at multiple distances. The range of stable distances shrinks with increasing light bandwidth and for a very large bandwidth field as e.g. blackbody radiation we find a strongly attractive potential up to a critical distance beyond which the force gets repulsive. Including multiple scattering can even lead to the appearance of a stable configuration at a large distance. Such broadband scattering forces should be observable contributions in ultra-cold atom interferometers or atomic clocks setups. They could be studied in detail in 1D geometries with ultra-cold atoms trapped along or within an optical nanofiber. Broadband radiation force interactions might also contribute in astrophysical scenarios as illuminated cold dust clouds.

New Journal of Physics 18 103041(2016) doi:10.1088/1367-2630/18/10/103041
Erratum in New Journal of Physics 18 119602(2016) doi:10.1088/1367-2630/18/11/119602

[1]D.H. performed all of the calculations in this publication, while H.R. contributed in an advisory role.

8.1. Introduction

Light scattering from point like particles is connected to momentum and energy exchange between the particles and the field. The interference of the fields scattered from different particles in an extended ensemble leads to important modifications of the total force on the ensemble [87; 88] and introduces long range inter-particle light-forces [89]. These forces, which originate from coherent scattering stay sizable even if the light fields are far detuned from any optical resonance [90]. The full coupled nonlinear interaction in a cloud thus leads to a very rich and complex dynamics [91] including trapping, optical binding [74; 92] and selfordering [75; 93]. Interestingly, many of the key physical effects can already be found and studied in effective 1D geometries [72]. One particularly interesting example are atoms coupled to 1D optical micro structures [11; 94] as *e. g.* an optical nanofiber, where even a single atom can significantly modify light propagation [77; 95; 96].
In a milestone experiment, Rauschenbeutel and coworkers recently managed to trap cold atoms alongside a tapered optical nanofiber [11], a result which has been repeated and improved in several new setups [58; 77; 97–99]. As a key consequence of the strong atom-fiber coupling, optical dipole interaction and light forces between two atoms are now mediated over basically the whole fiber length. Corresponding calculations of the collective particle dynamics exhibit enhanced inter-particle forces supporting the formation of periodical self-ordered regular arrays [15; 16; 72], where light and motion is strongly coupled and correlated [100].
Even for large ensembles, illumination with monochromatic laser light generates a translation invariant 1D geometry. To lowest order this implements equal strength infinite range coupling of each particle to all the others [77]. At sufficiently low kinetic temperature this induces crystallization of the particles and light fields with characteristic phonon excitations [72; 77; 100; 101]. It has already been shown, that adding a second laser frequency enhances particle-particle interaction at controllable distances [80]. Note that using circularly polarized light, asymmetric chiral scattering and interaction can be implemented in such systems as well to generate very exotic chiral spin models [102]. Here for simplicity we will assume transverse linear polarization though to keep inversion symmetry.

In this work we generalize this coupled atom-field dynamics to incoherent light with a large bandwidth and no stable phase relation between the different frequency

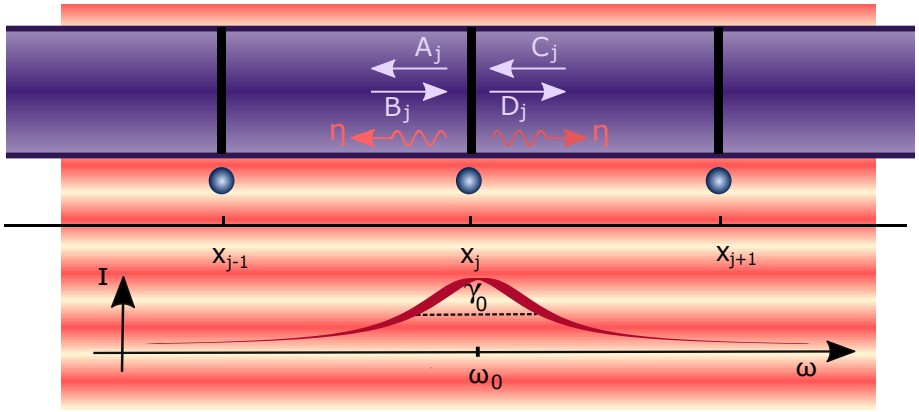

Figure 8.1.: A 1D array of point particles scattering light in and out of an optical nano-structure can be modelled as a collection of beam splitters interacting with a plane wave.

components. Hence the incoming radiation field is space and time translation invariant, but now possesses a finite correlation length. Surprisingly there appear substantial and partly even enhanced inter particle forces, for which we can control the effective interaction length via the spectral shape of the incoming radiation. Note that such broadband finite range forces were recently also predicted and observed in a seminal nano particle experiment with incoherent 3D illumination in a solution [103]. As the corresponding full 3D model is rather complex to solve and understand, we will restrict ourselves to a quasi 1D setup as mentioned above and depicted in 8.1 allowing an at least partially analytic treatment. Nevertheless we expect the model to exhibit the essential underlying multiple scattering physics. Note that instead of shaping the incoming light spectrum, one can alternatively envisage to tailor the waveguide dispersion relation by nano-structuring to manipulate propagation lengths [104; 105].

This work is organized as follows. We first generalize the basic definitions and dynamical equations of the proven multiple scattering model for light forces in 1D systems [63; 64; 81; 106] towards fields with finite bandwidth, orthogonally impinging on small particles in a 1D trap along an optical waveguide structure *cf.* 8.1. For two particles we analytically calculate the resulting inter-particle forces as function of bandwidth and separation. These results are then numerically extended to higher particle numbers studying the self-consistent coupled particle field dynamics for small ensembles and varying bandwidth. As a final case we will study temperature dependent forces in thermal radiation fields.

8.2. Multiple scattering approach for a point particle chain in broadband light

Let us assume an incoming broadband radiation field with all the wavelength components larger than the particle size and detuned from any optical resonance. The particles move in a 1D trap close enough to an optical fiber so that they can coherently scatter light into and out of the propagating fiber modes. For simplicity we assume a nanofiber, which supports only a single transverse mode propagating in each direction and a single peaked frequency distribution for the incident light field with center frequency ω_0 and width γ_0. Its maximum intensity is I_0 so that:

$$I(\omega) = \frac{I_0}{\pi} \frac{\gamma_0}{\gamma_0^2 + (\omega - \omega_0)^2}, \tag{8.1}$$

which can be considered as a generic model of a broadband laser field or fluorescence of a large atomic ensemble. The scattered field spectrum by a single point like scatterer will than largely be proportional to the incoming distribution. For very broad light fields as generated from an LED source or ultimately using blackbody radiation with a very broad Planck spectrum, one would of course get corrections from the frequency dependent scattering amplitude η. We will only address this limit a bit at the end of this work.

8.2.1. Optical binding forces between two particles

To get some first insight we start with the simplest nontrivial example of two particles at a distance $d = x_2 - x_1$ scattering light into the fiber. Inside the fiber the fields scattered from the two particles will interfere and a part of the field scattered by the first particle will be backscattered from the second one and vice versa. As shown in previous work, this situation can be modeled by a beam splitter approach via a 3×3 coupling matrix [16]. Each beam splitter is parametrized by a complex polarizability ζ with dispersive part ζ_r, absorptive part ζ_i and an effective scattering amplitude η_0, which for simplicity we assume to be frequency independent. In this case the multiple scattering can be summed to all orders and still allows for analytic calculations of the total self-consistent fields and forces by integrating over the whole spectrum. Note that as only the product of the spectral polarizability and the illumination spectrum appears

in the calculations any frequency dependence can be absorbed into a more complex effective pump distribution.
For two particles and small $\zeta = \zeta_r + i\zeta_i$ [16] as well as small relative bandwidth $\gamma_0 \ll \omega_0$, integration over the whole frequency range (8.1) yields:

$$\begin{aligned} F_1 &= \frac{I_{\eta_0}}{\pi c} \int_{-\infty}^{\infty} \frac{\gamma_0}{\gamma_0^2 + (\omega - \omega_0)^2} \cos\left(\frac{\omega d}{c}\right) \left(1 - 2\zeta_i \cos\left(\frac{\omega d}{c}\right) - 2\zeta_r \sin\left(\frac{\omega d}{c}\right)\right) d\omega \\ &= \frac{I_{\eta_0}}{c} \left(e^{-\frac{\gamma_0 d}{c}} \cos\left(\frac{\omega_0 d}{c}\right) - \zeta_i \left(1 + e^{-2\frac{\gamma_0 d}{c}} \cos\left(\frac{2\omega_0 d}{c}\right)\right) - \zeta_r e^{-2\frac{\gamma_0 d}{c}} \sin\left(\frac{2\omega_0 d}{c}\right)\right). \end{aligned} \tag{8.2}$$

In contrast to the infinite range for a monochromatic field [16] we find an additional exponential decay of the inter-particle force determined solely by the illumination bandwidth. This behavior is exhibited in figure 8.2, where the forces on the first particle for different bandwidths are compared. We still find stable configurations (optical binding) at several different distances, which can be calculated from the zero-points of the force in (8.2). Note that as a reference value we also have included the case of an unrealistically broad distribution of width $\gamma_0 = \omega_0$ to get some qualitative insight for the infinite bandwidth limit.
For a stable point we need zero average force and that the derivative of the force on the first beam-splitter with respect to distance is positive and negative for the second one. Surprisingly for non-absorbing particles with vanishing imaginary part (negligible absorption) of ζ, $\zeta_i = 0$, these stable distances d_0 do not depend on the bandwidth and are equal as for a monochromatic case [16]:

$$d_0 = \left(\frac{3}{4} + n\right) \lambda_0, \ n \in \mathbb{N}. \tag{8.3}$$

When we also take absorption into account by introducing an imaginary part of ζ, this adds extra outward radiation pressure to the force and shifts the stable distances to larger values. Eventually for too large ζ_i no stable configuration can be found as shown in figure 8.3 and 8.4. Note that scattering of light to non propagating field modes simply appears as effective loss in the imaginary part ζ_i. Once knowing the forces we can also simulate the coupled particle field dynamics for non-equilibrium conditions. Adding some effective friction to particle motion we simply integrate the equations of

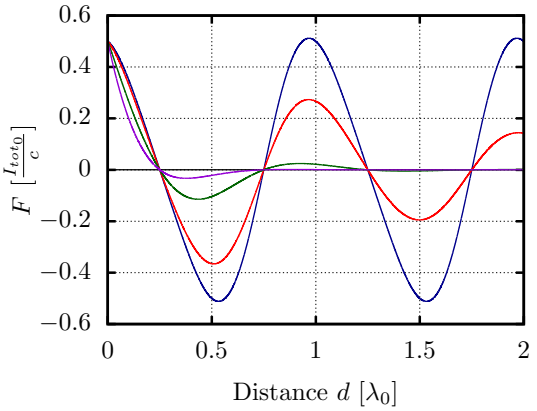

Figure 8.2.: Light force on the left of two particles as function of their distance d for $\zeta = 1/9$ and different bandwidths. Blue corresponds to $\gamma_0 = 0$, red to $\gamma_0 = 0.1\ \omega_0$, green to $\gamma_0 = 0.5\ \omega_0$ and violet to $\gamma_0 = \omega_0$.

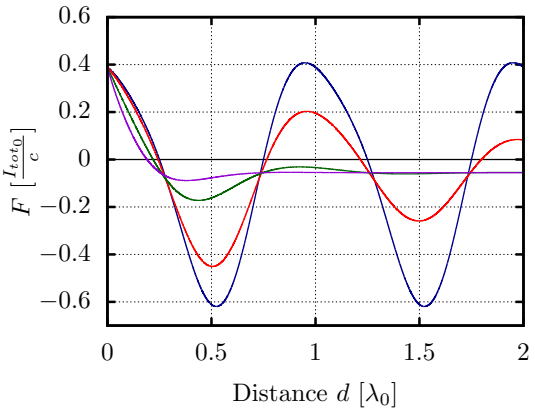

Figure 8.3.: Same as above for $\zeta = (1 + i)/9$. Blue corresponds to $\gamma_0 = 0$, red to $\gamma_0 = 0.1\ \omega_0$, green to $\gamma_0 = 0.5\ \omega_0$ and violet to $\gamma_0 = \omega_0$.

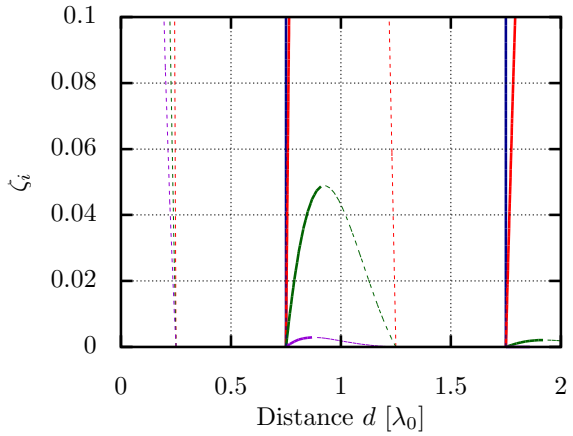

Figure 8.4.: Optical binding distances d for two particles as a function of absorption coefficient ζ_i for fixed dispersive component $\zeta_r = 1/9$. Blue corresponds to zero bandwidth $\gamma_0 = 0$, red to $\gamma_0 = 0.1\ \omega_0$, green to $\gamma_0 = 0.5\ \omega_0$ and violet to $\gamma_0 = \omega_0$. Solid lines show stable while dashed lines show unstable configurations.

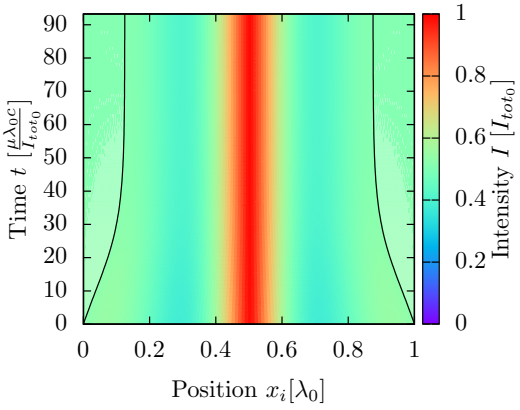

Figure 8.5.: Trajectories of two particles as a function of time for $\zeta = 1/9$ and $\gamma_0 = 0.1\ \omega_0$.

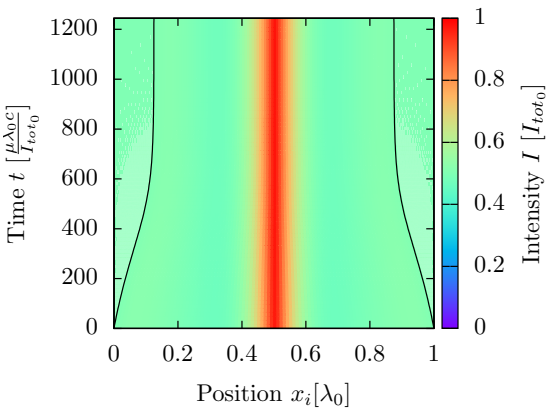

Figure 8.6.: Same as above for $\zeta = 1/9$ and $\gamma_0 = \omega_0$.

motion and let the coupled particle field system evolve towards stable configurations. This is shown in figures 8.5 and 8.6, where such trajectories for different illumination bandwidths γ_0 are compared. Indeed the simulations confirm the independence of the stable distance on the line width of the radiation. Note that in all cases the particles act like resonators creating a field intensity maximum in between them, while they themselves do not sit at either a field maximum or minimum as one might expect from simple light shift considerations. As a clear signature of multiple scattering we also get a strong spectral filtering response reminiscent of a Fabry Perot cavity from our particle pair. While some frequencies are strongly confined, others are dominantly transmitted depending on the particle distance. As a consequence the spectral distribution of the intensity emitted into the fiber outside the particle pair is strongly modified from the input. It also substantially changes with varying polarizability ζ and the line width γ_0. This is depicted in some typical examples in figure 8.7 and 8.8. Unexpectedly the intensities are not spectrally symmetric, which is a consequence of the strong frequency-dependent scattering of the beam-splitters. In this case some frequencies are filtered by particles, while others can pass them. Which frequencies can pass does not only depend on ζ and γ_0 but also at which of the stable distances the particles order. Thus, one can directly get information on the distance of the particles by measuring the frequency distribution of the outgoing intensity.

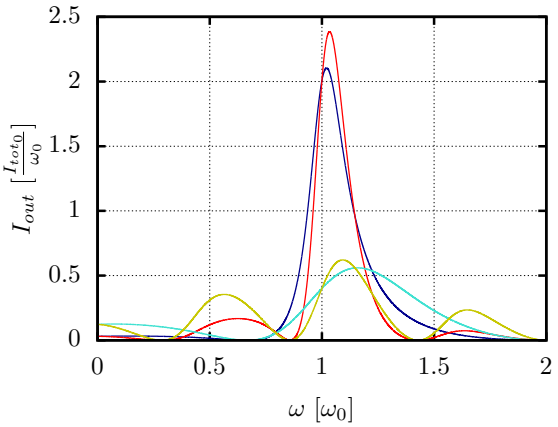

Figure 8.7.: Spectral intensity distribution of the light emitted into the fiber outside the particles for $\zeta = \frac{1}{9}$ for various pump bandwidths. Blue corresponds to $\gamma_0 = 0.1\ \omega_0$ and $d = \frac{3}{4}\ \lambda_0$, red to $\gamma_0 = 0.1\ \omega_0$ and $d = \frac{7}{4}\ \lambda_0$, cyan to $\gamma_0 = 0.5\ \omega_0$ and $d = \frac{3}{4}\ \lambda_0$, and yellow to $\gamma_0 = 0.5\ \omega_0$ and $d = \frac{7}{4}\ \lambda_0$.

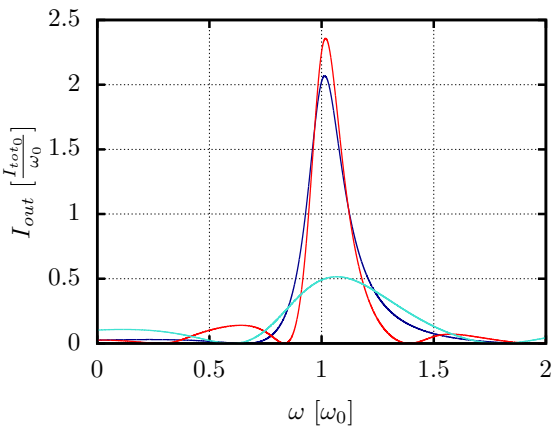

Figure 8.8.: Same as above for $\zeta = \frac{1+i}{9}$. Blue corresponds to $\gamma_0 = 0.1\ \omega_0$ and $d = 0.77\ \lambda_0$, red to $\gamma_0 = 0.1\ \omega_0$ and $d = 1.8\ \lambda_0$, and cyan to $\gamma_0 = 0.3\ \omega_0$ and $d = 0.83\ \lambda_0$.

8.2.2. Forces and selfordering for several beam splitters

In principle determining the field distributions, the forces and stationary states for a larger number of beam splitters is straightforward by multiplying the corresponding scattering and propagation matrices. In practice, useful analytic results can only be obtained by ignoring backscattering and setting $\zeta = 0$ as multiple scattering leads to very complex expressions. In contrast to the monochromatic case the particles in steady state here are not equidistantly distributed, which leads to a much more complex transfer matrix. Nevertheless, for $\zeta = 0$ the transfer matrix still can be calculated analytically for N particles and integrated over the frequency distribution to yield the following expression for the total force:

$$\begin{aligned} F_{j,N} &= \frac{I_{\eta_0}}{c\pi} \int_{-\infty}^{\infty} d\omega \frac{\gamma_0}{\gamma_0^2 + (\omega - \omega_0)^2} \left(\sum_{l=j}^{N-1} \cos\left(\frac{\omega \sum_{i=j}^{l} d_i}{c} \right) - \sum_{l=1}^{j-1} \cos\left(\frac{\omega \sum_{i=l}^{j-1} d_i}{c} \right) \right) \\ &= \frac{I_{\eta_0}}{c} \left(\sum_{l=j}^{N-1} e^{-\sum_{i=j}^{l} \frac{\gamma_0 d_i}{c}} \cos\left(\frac{\omega \sum_{i=j}^{l} d_i}{c} \right) - \sum_{l=1}^{j-1} e^{-\sum_{i=l}^{j-1} \frac{\gamma_0 d_i}{c}} \cos\left(\frac{\omega \sum_{i=l}^{j-1} d_i}{c} \right) \right). \end{aligned} \tag{8.4}$$

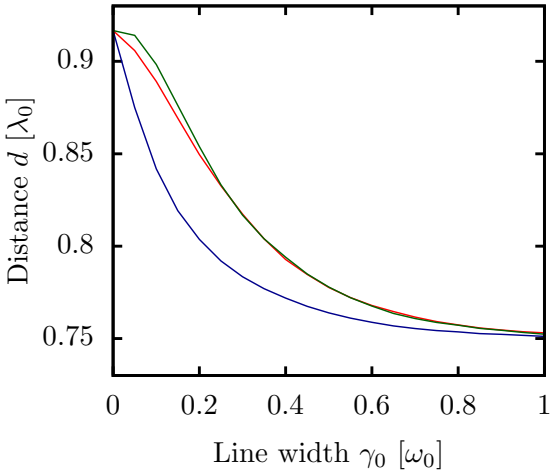

Figure 8.9.: Shortest stable distances for a symmetric configuration of six particles as a function of bandwidth γ_0. Blue corresponds to the distance between the first two particles, red to the distance between the second and the third and green to the distance between the third and the fourth particle.

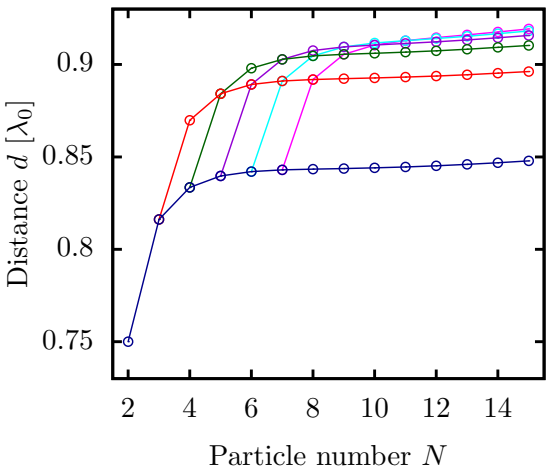

Figure 8.10.: Shortest stable distances as a function of the number of particles N for $\gamma = 0.1\ \omega_0$. The blue line corresponds to the distance between the first two particles d_1, red to d_2, green to d_3, violet to d_4, light blue to d_5 and magenta to d_6.

As the zeros of this function yielding the stable configurations are determined by a transcendent equation they can not be calculated analytically. Nevertheless a numerical solution requires very little effort. So in figure 8.9 we plot the closed configuration of stationary distances for six particles as a function of the bandwidth γ_0. Interestingly the particles are only equidistantly ordered in the two extreme limits of zero bandwidth $\gamma_0 = 0$ and a very large bandwidth, where interactions are short distance. For finite γ_0 the distances between the inner particles are larger than the distances between the outer ones.

For large bandwidth γ_0 the particles only significantly interact with their direct neighbors yielding equidistant order at a distance $d \approx \frac{3}{4}\ \lambda_0$. This is the same distance as for two particles as a consequence of the short range of the force. Note that by controlling the input bandwidth we thus can switch from infinite range to nearest neighbor interaction. This behavior is also shown in figure 8.10, where the dependence of the stable distance as function of the number of particles is compared for different bandwidth γ_0. The

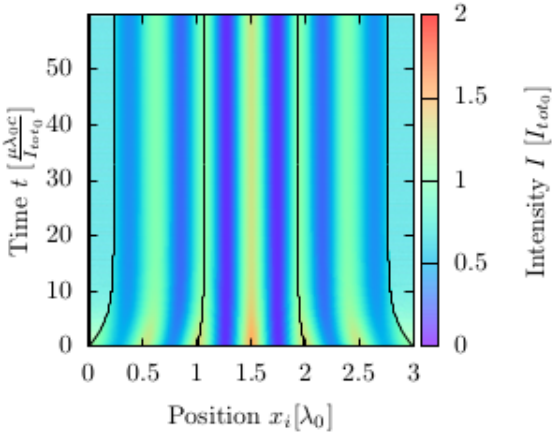

Figure 8.11.: Time evolution of atom-field distribution for four particles for $\zeta = 0$ and initial distance $\gamma_0 = 0.1\ \omega_0$.

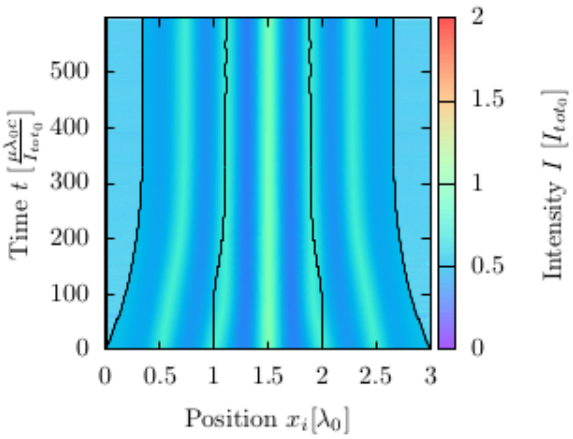

Figure 8.12.: Same as above for $\zeta = 0$ and initial distance $\gamma_0 = 0.5\ \omega_0$.

distance between the particles for larger γ_0 is closer to the two-particle-distance $\frac{3}{4}\ \lambda_0$. Additionally they again confirm that the outer particles are closer than the inner ones and that the distances for the outer ones become more and more equal for large particle numbers. Again the couple atom-field dynamics shows intriguing physics. Figure 8.11 and 8.12 show two examples for the time evolution of four particles in a broadband field. Again the distance between the outer particles is larger than between the inner particles. Interestingly the particles tend to create high field intensities between them, with the outer two providing trap sites for the inner pair and a total field maximum generated at the center. This effect, more prominent for smaller bandwidth, reminds of a self assembled cavity QED system.

8.3. Interparticle forces induced by blackbody radiation

As a final and extreme limit of broadband radiation let us consider the particles to be illuminated by a thermal radiation field (BBR) with a Planck spectrum. At temperature T with Boltzmann constant k_B, Planck constant $\hbar$ and light velocity c the spectral distribution reads:

$$I_0(\omega) = \frac{\hbar}{2\pi^2 c^2} \frac{\omega^3}{e^{\frac{\hbar\omega}{k_B T}} - 1}. \tag{8.5}$$

Of course the assumption of constant linear polarizability is only approximately valid throughout the whole Planck spectrum. Nevertheless it has been shown recently, that

for atoms with a first excited state in the UV region as e.g. atomic hydrogen, this approximation is surprisingly good up to temperatures of $T \approx 6000\ K$ [103; 107]. Introducing a more realistic frequency dependent polarizability and resonances will introduce some quantitative changes, but one can expect qualitative agreement as long as the majority of the incident power is sufficiently detuned from resonances. This is generally the case for low temperature radiation with a peak below the visible.
It has been shown before that the emitted BBR field from a hot source itself induces a surprising attractive force pulling atoms towards the hot object [107]. Here we start with two temperature less particles illuminated from the side by a BBR field. Again we integrate the fiber mediated scattering force between them over the BBR frequency range in (8.5), which still can be done analytically to obtain

$$F_1 = -F_2 = \frac{\hbar\omega_T^4}{2\pi^2 c^3}\left(\frac{\cosh\left(\frac{2d}{r_T}\right)+2}{\sinh^4\left(\frac{d}{r_T}\right)} - 3\left(\frac{r_T}{d}\right)^4\right), \tag{8.6}$$

where we defined a thermal length $r_T = \frac{\hbar c}{\pi k_B T}$ and a thermal frequency $\omega_T = \frac{\pi k_B T}{\hbar}$. For particles in an environment with room temperature the thermal length gives $r_{300K} \approx \frac{7.3\cdot 10^{-4}}{T}\ m\cdot K \approx 2.4\cdot 10^{-6}\ m$, which is much larger then a typical optical wavelength. Of course the long wavelength components will not be significantly guided by the fiber, but due to their low energy and momentum content, these parts are not relevant for the resulting force anyway.
From (8.6) we can expect a distance and temperature dependent sign change of this force including a zero force distance. In fact as depicted in figure 8.13, the particles will attract each other if they are close but very surprisingly this changes to repulsion at distances larger than the thermal radius r_T. We thus find no stable equilibrium distance. The strongest force appears at short distances and will induce a capture range below which two particles will collapse together. This will large determine the effective scattering size of two particles. As said, the zero force equilibrium point ($d_0 = 1.37\ r_T$) is not stable and a small perturbation causes collapse or separation. This behavior is plotted in figure 8.14 and 8.15, where in the first case the particles are attracted by the high intensity peak forming between them, while they are repelled in the second case. While the quantitative accuracy of this prediction can be doubted such a qualitative behavior should be generally true, as 3D calculations yield similar attractive behavior [103]. This could imply important changes in the dynamics of ultra

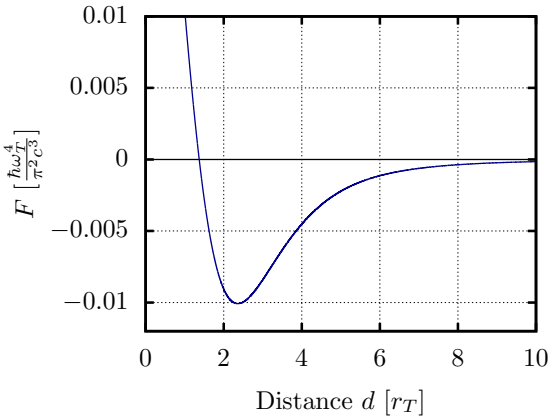

Figure 8.13.: Force on the first of two particles in a blackbody radiation field as a function of the distance for $\zeta = 0$.

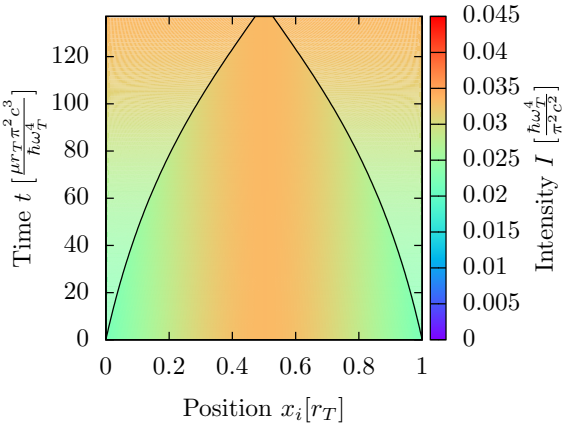

Figure 8.14.: Trajectories of two particles at $\zeta = 0$ with initial distance $d = \lambda_0$.

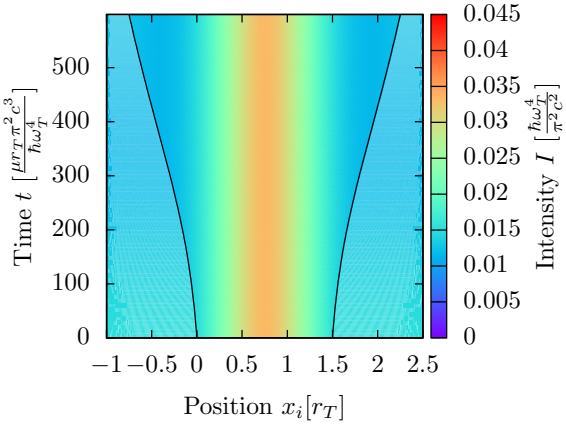

Figure 8.15.: Same as above for $\zeta = 0$ with initial distance $d = 1.5\ \lambda_0$.

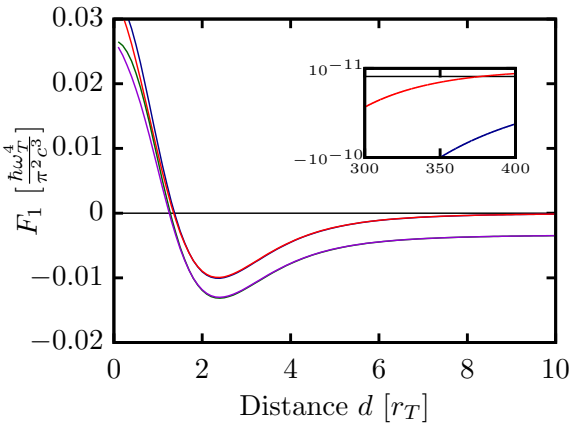

Figure 8.16.: Force on the first of two particles as a function of the distance. Blue corresponds to $\zeta = 0$, red to $\zeta = 0.1$, green to $\zeta = 0.1i$ and violet to $\zeta = 0.1(1+i)$.

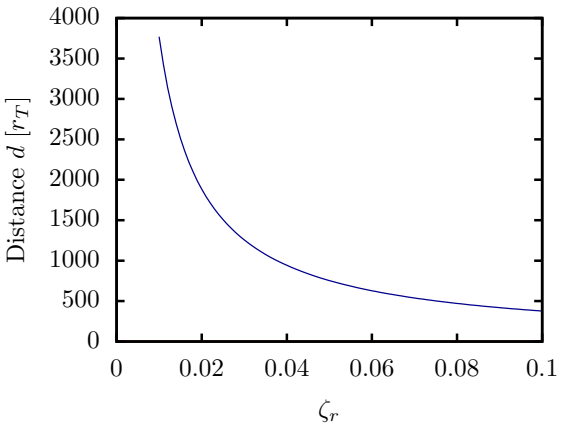

Figure 8.17.: Stable zero-points of the force on two particles as a function of the distance d and ζ_r.

cold particle ensembles in thermal radiation fields with even astrophysical consequences. Interestingly, the physics changes when we include backscattering and absorption of the radiation by the particles via introducing a finite ζ-parameter. Figure 8.16 and 8.17 show that for real $\zeta > 0$ we get long range attraction and can even find a second zero point of the force at a large distance. As this effect is very tiny it might be more of academic than practical interest, but this separation is even stable against perturbations. Including absorption via imaginary parts of ζ has the opposite effect on the particles as expected. The force is modified in a way that in the limit $\zeta_r \ll 1$ no stable configurations can be found due to long range radiation pressure contributions. Similar to the previous case the particle also filter the light and sculpt an oscillating transmission pattern into the outgoing light. Figure 8.18 shows the outgoing intensities for a blackbody radiation field, which keep the gross shape of BBR but again the particles tend to filter some frequencies.

8.3.1. Larger ensembles in BBR fields

BBR induced forces on larger ensembles can be calculated in the same way as before. As expected this leads to the rather complex analytic expression in terms of simple sums for the forces that govern the dynamics of the cloud, but allows simple numerical

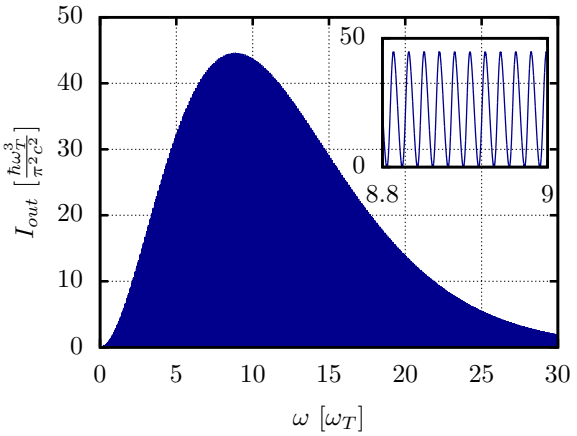

Figure 8.18.: Outgoing intensity as a function of ω for $\zeta = \frac{1}{9}$ at the stable position $d_0 = 377\ r_T$.

evaluation:

$$
\begin{aligned}
F_\Omega &= \frac{\hbar}{2\pi^2c^3}\int_0^\infty d\omega \frac{\omega^3}{e^{\frac{\hbar\omega}{k_BT}}-1}\left(\sum_{l=j}^{N-1}\cos\left(k\sum_{i=j}^{l}d_i\right)-\sum_{l=1}^{j-1}\cos\left(k\sum_{i=l}^{j-1}d_i\right)\right)\\
&= \frac{\hbar\omega_T^4}{2\pi^2c^3}\left(\sum_{l=j}^{N-1}\left(\frac{\cosh\left(\frac{2\sum_{i=j}^{l}d_i}{r_T}\right)+2}{\sinh^4\left(\frac{\sum_{i=j}^{l}d_i}{r_T}\right)}-\frac{3r_T^4}{\left(\sum_{i=j}^{l}d_i\right)^4}\right)\right.\\
&\left.-\sum_{l=1}^{j-1}\left(\frac{\cosh\left(\frac{2\sum_{i=l}^{j-1}d_i}{r_T}\right)+2}{\sinh^4\left(\frac{\sum_{i=l}^{j-1}d_i}{r_T}\right)}-\frac{3r_T^4}{\left(\sum_{i=l}^{j-1}d_i\right)^4}\right)\right).
\end{aligned}
\tag{8.7}
$$

As it is rather hopeless to analytically find the zeros of this function, in order to get some first insight in figure 8.19 we simply plot the force on the outermost particle as function of the distance for an equidistant particle array and weak backscattering amplitude. Note that the magnitude of the near field attraction strongly increases with the particle number, while its range decreases at the same time. Hence this would trigger a fast collapse of a particle cloud once a certain small distance (high density) has been reached. At larger distances the force on the first particle does not depend on the total particle number and is repulsive. This effect is also visible in figure 8.20. Figure 8.21, which shows the force on the first five of ten particles clearly shows that the force on the inner particles is smaller than on the outer ones. Only for some smaller

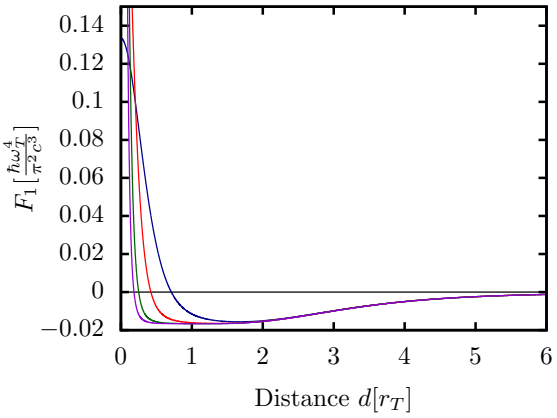

Figure 8.19.: Force on the first of 5 (blue), 10 (red), 20 (green), 30 (violet) particles as a function of the distance for $\zeta = 0$.

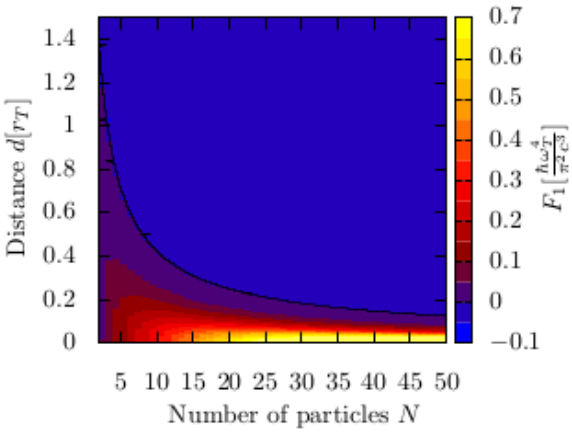

Figure 8.20.: Contour-plot of the force as a function of the particle number N and the distance d for $\zeta = 0$. The black line corresponds to the zero-force line.

distances this is not true, which is also shown in figure 8.22, while we choose a larger distance in figure 8.23. The simulations confirm that the particles do not form stable configurations but tend either to collapse together or repulse each other towards infinity. This effect can also be observed for four particles in figure 8.24 and 8.25. For this case large intensities between the particles push them apart. Here definitely more extensive and detailed simulations would be needed to fully understand the dynamics, which, however, is beyond the scope of this work.

8.4. Conclusions

We have shown that fiber mediated broadband light scattering from linear arrays of polarizable particles induces a much more rich and complex inter particle forces than simple repulsive radiation pressure. In fact one can tailor the interaction from infinite range to nearest neighbor coupling by a suitable choice of the bandwidth. This originates from the frequency and distance dependent interference of the various frequency components in the field, which appears for dispersive as well as for absorptive scattering. For a wide range of bandwidths, one finds multi-stable regular ordering of the particles and long range forces as for optical binding in monochromatic fields. The range of inter particle interactions can be well tuned via the bandwidth of the

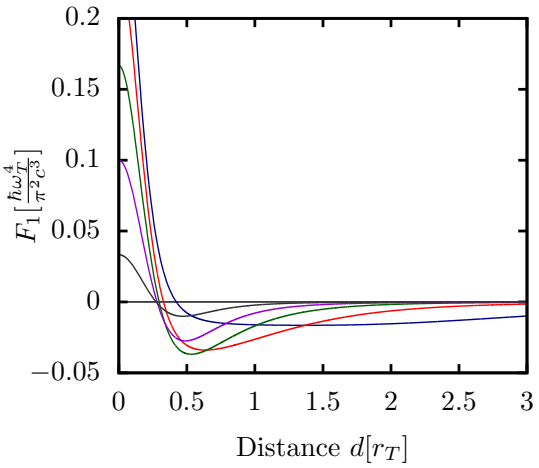

Figure 8.21.: Force on the first (blue), second (red), third (green), fourth (violet), fifth (grey) of ten particles as a function of the distance for $\zeta = 0$.

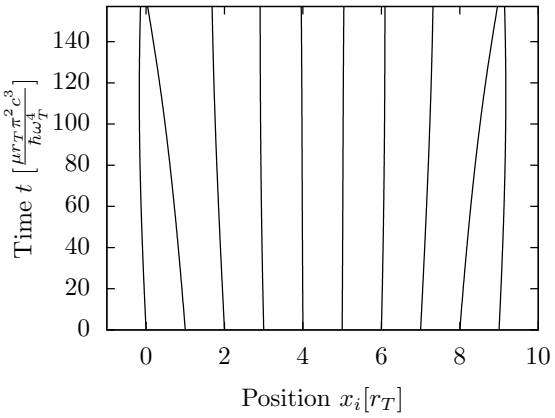

Figure 8.22.: Time evolution for ten particles for $\zeta = 0$ and initial distance $d = \lambda_0$.

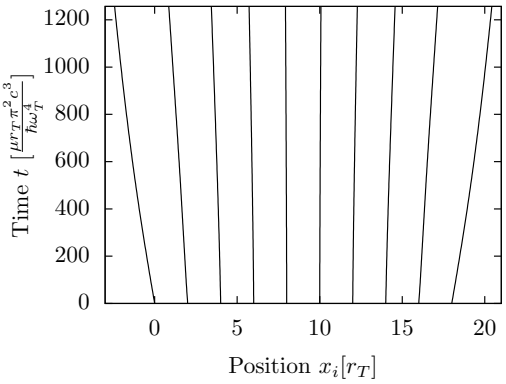

Figure 8.23.: Same as above for $\zeta = 0$ and initial distance $d = 2\ \lambda_0$.

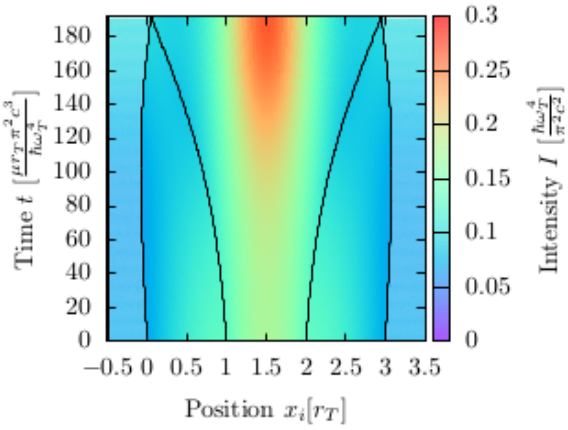

Figure 8.24.: Time evolution for four particles for $\zeta = 0$ and initial distance $d = \lambda_0$.

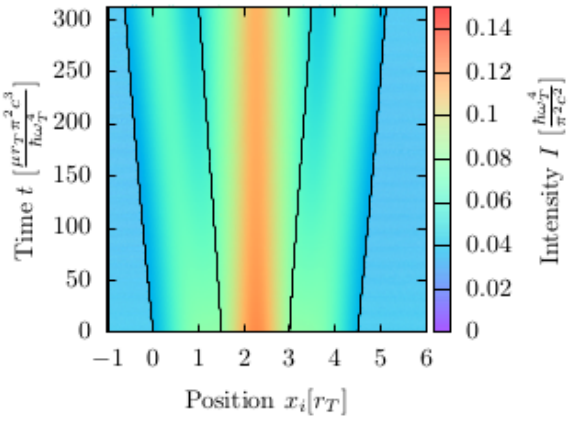

Figure 8.25.: Same as above for $\zeta = 0$ and initial distance $d = 1.5\ \lambda_0$.

incoming field. While we have only studied single peaked frequency distributions to limit interaction ranges, multiple peaks can be expected to allow for a much more general design of controlling interaction strength with distance. The physical effect of these generally quite weak interactions can be significantly enhanced and studied in a controlled way by coupling via optical nanostructures as nanofibers. Some preliminary calculations, nevertheless, show that qualitatively analogous behavior survives in 2D and 3D situations.

Surprisingly even for very broadband BBR fields one finds multi particle collective effects and a complex interplay of attraction and repulsion at distances around the thermal radius, which will lead to a complex nonlinear dynamics and response of larger ensembles. While this certainly is hard to observe in standard setups [103] it still could have significant influence on longer time scales. Alternatively it could be measurable in very force sensitive setups such as atom interferometers where it should induce extra density dependent shifts and dephasing.

Acknowledgements: We thank Juan José Sáenz, Holger Muller and Tobias Griesser for stimulating discussions. We acknowledge support via the Austrian Science Fund grant SFB F4013 .

9. Supplement on details of the analytical calculations

In this section I explain how the integrals in the paper above can be calculated.
The cosine integral used in eq. (8.2) and (8.4) can be calculated using

$$\begin{aligned}\int_{-\infty}^{\infty} \frac{\cos(a\omega)}{\gamma_0^2+(\omega-\omega_0)^2}d\omega &= \int_{-\infty}^{\infty} \frac{\cos(a(x-\omega_0))}{\gamma_0^2+x^2}dx \\ &= \frac{1}{\gamma_0}\int_{-\infty}^{\infty} \frac{\cos(a\gamma_0(y-\omega_0/\gamma_0))}{1+y^2}dy \\ &= \frac{1}{\gamma_0}\int_{-\infty}^{\infty} \frac{\cos(a\gamma_0 y)\cos(a\gamma_0\omega_0/\gamma_0)+\sin(a\gamma_0 y)\sin(a\gamma_0\omega_0/\gamma_0}{1+y^2}dy, \quad (9.1)\end{aligned}$$

with

$$\int_{-\infty}^{\infty} \frac{\cos(ay)}{1+y^2}dy = \Re\left(\int_{-\infty}^{\infty} \frac{e^{icy}}{1+y^2}dy\right) = \int_{-\infty}^{\infty} \frac{\cos(ay)}{1+y^2}dy = \begin{cases}\Re\left(2\pi i \sum_{y:\Im(y)>0} \frac{e^{icy}}{1+y^2}dy\right) & for\ c>0 \\ \Re\left(2\pi i \sum_{y:\Im(y)<0} \frac{e^{icy}}{1+y^2}dy\right) & for\ c<0\end{cases} = \pi e^{-|a|} \quad (9.2)$$

For $c > 0$ the integral is proportional to $e^{i|c|y}$ and we have to integrate over the upper halfplane (pole i), while for $c < 0$ the integral is proportional to $e^{-i|c|y}$ and we have to integrate over the lower halfplane (pole $-i$).
The sine integral can be solved in a similar way

$$\int_{-\infty}^{\infty} \frac{\sin(ay)}{1+y^2}dy = \Im\left(\int_{-\infty}^{\infty} \frac{e^{icy}}{1+y^2}dy\right) = \Im\left(\pi e^{-|a|}\right) = 0. \quad (9.3)$$

With these one can find

$$\int_{-\infty}^{\infty} \frac{\cos(a\omega)}{\gamma_0^2 + (\omega - \omega_0)^2} d\omega = \frac{1}{\gamma_0} \pi e^{-|a|\gamma_0} \cos(a\omega_0). \tag{9.4}$$

In the same way we can also solve the sine-integral of eq. (8.2)

$$\int_{-\infty}^{\infty} \frac{\sin(a\omega)}{\gamma_0^2 + (\omega - \omega_0)^2} d\omega = \frac{1}{\gamma_0} \int_{-\infty}^{\infty} \frac{\sin(a\gamma_0 x)\cos(a\omega_0) - \sin(a\omega_0)\cos(a\gamma_0 x)}{1 + x^2} dx = - \frac{\pi}{\gamma_0} e^{-|a|\gamma_0} \sin(a\omega_0) \tag{9.5}$$

For the $\cos^2$ integral from eq. (8.2) we use

$$\int_{-\infty}^{\infty} \frac{\cos^2(a\omega)}{\gamma_0^2 + (\omega - \omega_0)^2} d\omega = \frac{1}{2} \int_{\infty}^{\infty} \frac{1 + \cos(2a\omega)}{\gamma_0^2 + (\omega - \omega_0)^2} d\omega = \frac{1}{2\gamma_0} \pi e^{-|a|\gamma_0} \cos(a\omega_0) + \frac{1}{2} \int_{\infty}^{\infty} \frac{1}{\gamma_0^2 + (\omega - \omega_0)^2} d\omega, \tag{9.6}$$

with

$$\int_{\infty}^{\infty} \frac{1}{\gamma_0^2 + (\omega - \omega_0)^2} d\omega = \int_{\infty}^{\infty} \frac{1}{\gamma_0^2 + x^2} dx = \frac{1}{\gamma_0} \int_{\infty}^{\infty} \frac{1}{1 + y^2} dy = \frac{1}{\gamma_0} \arctan(y) \Big|_{-\infty}^{\infty} = \frac{\pi}{\gamma_0} \tag{9.7}$$

and find

$$\int_{-\infty}^{\infty} \frac{\cos^2(a\omega)}{\gamma_0^2 + (\omega - \omega_0)^2} d\omega = \frac{\pi}{2\gamma_0} \left(1 + e^{-2|a|\gamma_0} \cos(2a\omega_0)\right). \tag{9.8}$$

For the cosine-integral in eq. (8.6) and (8.7) let us recall the geometric series

$$\sum_{n=1}^{\infty} e^{-nx} = \sum_{n=1}^{\infty} \left(\frac{1}{e^x}\right)^n = \frac{1}{1 - e^{-x}} - 1 = \frac{1}{e^x - 1}, \tag{9.9}$$

and get

$$\int_0^\infty \frac{\omega^3}{e^{a\omega}-1}\cos(b\omega)d\omega = \frac{1}{a^4}\int_0^\infty \frac{x^3}{e^x-1}\cos\left(\frac{b}{a}x\right)dx = \frac{1}{2a^4}\sum_{n=1}^\infty \int_0^\infty x^3 e^{-nx}\left(e^{i\frac{b}{a}x}+e^{-i\frac{b}{a}x}\right)dx = \frac{1}{2a^4}\sum_{n=1}^\infty \int_0^\infty x^3\left(e^{-nx+i\frac{b}{a}x}+e^{-nx-i\frac{b}{a}x}\right)dx. \tag{9.10}$$

Using

$$\int_0^\infty x^3 e^{-ax}dx = -\frac{x^3e^{-ax}}{a}\Big|_0^\infty + \frac{1}{a}\int_0^\infty 3x^2e^{-ax}dx = -\frac{x^3e^{-ax}}{a}\Big|_0^\infty + \frac{1}{a}\int_0^\infty 3x^2e^{-ax}dx = \frac{3x^2e^{-ax}}{a^2}\Big|_0^\infty + \frac{1}{a^2}\int_0^\infty 6xe^{-ax}dx = -\frac{6x^2e^{-ax}}{a^3}\Big|_0^\infty + \frac{1}{a^3}\int_0^\infty 6xe^{-ax}dx = \frac{6}{a^4}, \tag{9.11}$$

and the Polygamma-function ψ_m:

$$\begin{aligned}
\psi_m(z) &= (-1)^{m+1}m!\sum_{n=0}^\infty \frac{1}{(z+n)^{m+1}} \\
\psi_3(z) &= 6\sum_{n=0}^\infty \frac{1}{(z+n)^4} \qquad \psi_m(z+1) = \psi_m(z) + (-1)^m m! z^{-m-1} \\
\psi_3(z+1) &= \psi_3(z) - 6z^{-4} \\
(-1)^m\psi_m(1-z) - \psi_m(z) &= \pi\frac{d^m}{dz^m}\cot(\pi z) \\
-\psi_3(1-iz) - \psi_3(iz) &= -2i\pi^4\frac{2+\cosh(2\pi z)}{\sinh^4(\pi z)},
\end{aligned} \tag{9.12}$$

we find

$$\int_0^\infty \frac{\omega^3}{e^{a\omega}-1}\cos(b\omega)d\omega = \frac{3}{a^4}\sum_{n=1}^\infty\left(\frac{1}{\left(n-\frac{ib}{a}\right)^4}+\frac{1}{\left(n+\frac{ib}{a}\right)^4}\right) = \frac{1}{2a^4}\left(\psi_3\left(1-\frac{ib}{a}\right)+\psi_3\left(\frac{ib}{a}\right)-\frac{6a^4}{b^4}\right) = \frac{\pi^4\left(2+\cosh\left(\frac{2\pi b}{a}\right)\right)}{a^4\sinh^4\left(\frac{\pi b}{a}\right)} - \frac{3}{b^4}. \tag{9.13}$$

For the $\cos^2$ integral in eq. (8.6) we calculate

$$\int_0^\infty \frac{\omega^3}{e^{a\omega}-1}\cos^2(b\omega)d\omega = \int_0^\infty \frac{\omega^3}{e^{a\omega}-1}\left(\cos(2b\omega)+1\right)d\omega = \frac{\pi^4\left(2+\cosh\left(\frac{4\pi b}{a}\right)\right)}{a^4\sinh^4\left(\frac{2\pi b}{a}\right)} - \frac{3}{16b^4} + \int_0^\infty \frac{\omega^3}{e^{a\omega}-1}d\omega. \quad (9.14)$$

With

$$\int_0^\infty \frac{\omega^3}{e^{a\omega}-1}d\omega = \frac{1}{a^4}\sum_{n=1}^\infty \int_0^\infty x^3 e^{-nx}dy = \frac{6}{a^4}\sum_{n=1}^\infty \frac{1}{n^4} = \frac{\pi^4}{15a^4}, \quad (9.15)$$

where we used Parzeval's theorem $\sum_{n=1}^\infty \frac{1}{n^4} = \frac{\pi^4}{90}$, we get

$$\int_0^\infty \frac{\omega^3}{e^{a\omega}-1}\cos^2(b\omega)d\omega = \frac{\pi^4}{a^4}\left(\frac{1}{15} + \frac{\cosh\left(\frac{4\pi b}{a}\right)+2}{\sinh\left(\frac{2\pi b}{a}\right)}\right) - \frac{3}{16b^4}. \quad (9.16)$$

For the sine integral in eq. (8.6) we find

$$\int_0^\infty \frac{\omega^3}{e^{a\omega}-1}\sin(b\omega)d\omega = \frac{1}{a^4}\sum_{n=1}^\infty \int_0^\infty x^3 e^{-nx}\sin\left(\frac{b}{a}x\right)dx = \frac{1}{2ia^4}\sum_{n=1}^\infty \int_0^\infty x^3\left(e^{-nx+i\frac{b}{a}x} - e^{-nx-i\frac{b}{a}x}\right)dx = \frac{1}{2ia^4}\sum_{n=1}^\infty \left(\frac{6}{\left(n-\frac{ib}{a}\right)^4} - \frac{6}{\left(n+\frac{ib}{a}\right)^4}\right) = \frac{i}{2a^4}\left(\psi_3\left(1-\frac{ib}{a}\right) - \psi_3\left(1+\frac{ib}{a}\right)\right). \quad (9.17)$$

10. Publication

Synthesizing variable particle interaction potentials via spectrally shaped spatially coherent illumination

Daniela Holzmann[1], Matthias Sonnleitner and Helmut Ritsch

Collective scattering of spatially coherent radiation by separated point emitters induces inter-particle forces. For particles close to nano-photonic structures as, for example, nano-fibers, hollow core fibers or photonic waveguides, this pair-interaction induced by monochromatic light is periodic and virtually of infinite range. Here we show that the shape and range of the optical interaction potential can be precisely controlled by spectral design of the incoming illumination. If each particle is only weakly coupled to the confined guided modes the forces acting within a particle ensemble can be decomposed to pairwise interactions. These forces can be tailored to almost arbitrary spatial dependence as they are related to Fourier transforms with coefficients controlled by the intensities and frequencies of the illuminating lasers. We demonstrate the versatility of the scheme by highlighting some examples of unconventional pair potentials. Implementing these interactions in a chain of trapped quantum particles could be the basis of a versatile quantum simulator with almost arbitrary all-to-all interaction control.

New Journal of Physics 20 103009(2018) doi:10.1088/1367-2630/aae3bf

[1]D.H. performed all of the calculations in this publication, while M.S. and H.R. contributed in an advisory role.

10.1. Introduction

Advances in laser cooling and manipulation of atoms and nano-particles nowadays allow one to prepare very low temperature ensembles where inter-particle light forces play an important role in the motional interaction. In 3D geometries the forces on two particles induced by collective light scattering or dipole-dipole interaction are typically of rather short range decaying as $(1/\text{distance})^3$ [108]. However, by help of optical structures one can significantly increase the magnitude and range of light-mediated forces [109]. As the most prominent example single-mode high-Q optical cavities implement resonantly enhanced infinite-range couplings [110], which generate virtual all-to-all interactions and gives the basis for spontaneous crystallization into a regular lattice structure at high illumination power [70].
Similarly, in an alternative approach to enhance optical interactions one can use optical structures which tightly confine the radial extension of the electromagnetic field, allowing propagation only in one dimension. In the simplest example optical fibers can guide light virtually unattenuated over a very long range and consequently mediate optical forces over very long distances [16; 111]. For monochromatic illumination this can lead to an even more intriguing ordering phenomenon where light confines the particle motion and the particles confine the light along the fiber [72].
Let us briefly recall the basic idea behind this here. Atoms trapped near a fiber or a 1D-photonic structure interact with the light field coupled into the fiber from its ends. This radiation field then travels along the chain of particles and encounters one atom after the other. Each atom then reflects and transmits some fraction of the light such that effective inter-particle forces emerge. However, as an alternative second method one can shine light transversely directly onto the atoms. Each atom then scatters some of this transverse pump field into the fiber where the light can travel and interact with the light field injected by other particles. Depending on whether the two fields interfere constructively or destructively the force on a pair of particles will be attractive or repulsive. This of course depends on the particle distance in units of the wavelength of the light.
In previous works [16; 100; 111; 112] we already demonstrated that such a configuration gives new tools to design particle-particle interactions. Especially the use of a broadband spectrum for the transverse pump beam gives finite-range forces which are very different from the interactions obtained in a longitudinally pumped fiber. Interestingly, the

extreme case of very broadband black body radiation leads to very short range attraction and longer range repulsion.
In this work we go one step further and explore the effects of a transverse pump using multiple broadband beams of different central frequencies and bandwidths. As we will show in section 10.2 such a setup allows one to design almost arbitrary multi-particle interaction forces. Although these forces depend on the positions of each particle, to lowest order in the particle field coupling they can be written as a sum of two-particle interactions which in turn can be written as a Fourier series with coefficients given by the intensities of the transverse pump beams.
The option to design particle-particle interactions opens a host of possibilities and some of these shall be explored here in a generic way. In section 10.3 we discuss how this gives rise to new types of self-organisation. In section 10.4 we explore opportunities for particles trapped in external potentials where tunable, position dependent interactions might be useful for quantum computation and simulation.

10.2. Model

Let us consider a set of linearly polarizable point-like emitters trapped in the evanescent field of light modes propagating in an effective 1D geometry. Typical examples are tapered nano-fibers, nano-waveguides or photonic crystal structures. As indicated in Fig. 10.1 the particle motion is guided along the light propagation direction along which an additional lattice potential could be added, cf. section 10.4. When illuminated from the side the particles coherently scatter a fraction of the pump light into the guided modes characterized by an effective scattering amplitude η. Similarly some of the guided light is reflected into the reverse direction or scattered into free space. The injected photons propagate within the optical structure where they thus couple over very long distances to all other particles trapped near the fiber along their path. The particle-particle interaction mostly originates from the interference between the incoupled light amplitudes by the different particles. Closely related configurations have been experimentally realized with atoms [11; 58; 98; 113] or nano-particles [114].
In the case of a single or a few particles a detailed numerical modeling of the setup is possible with good agreement to the experiment. However, as shown recently, the key physics can be already modeled and understood from a much simplified semi-analytical

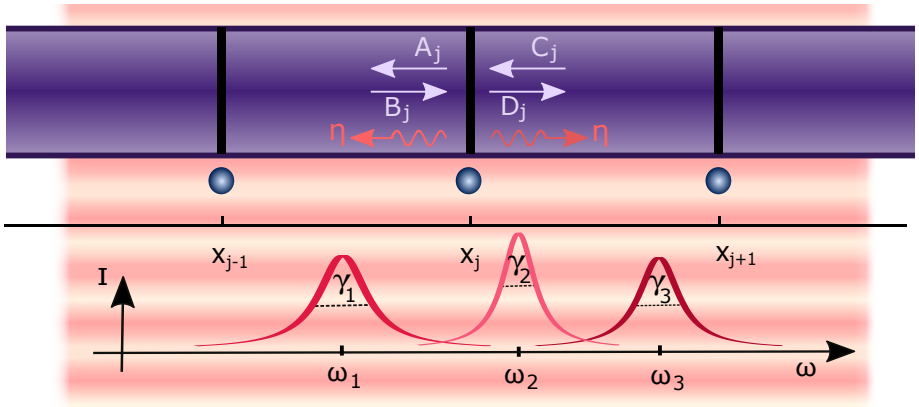

Figure 10.1.: A one-dimensional array of point particles scattering light into and out of an optical nano-structure can be modeled as a collection of beam splitters interacting with a plane wave. In this work we consider broadband transverse illumination characterized by the intensities, central frequencies and spectral widths of the incoming beams.

scattering model [115]. We will generalize this model here towards multifrequency illumination and extract the key physics originating from frequency control.

As our toy model is, of course, strongly oversimplified, we will explicitly mention some of these simplifications here for clarity. We assume a scalar linear polarizability of the particles, while typical atoms have more than one or two contributing internal levels and thus exhibit a polarization, frequency and intensity dependent light shift. This is avoided using a $J = 0$ to $J = 1$ transition at very low magnetic field and light power. Similarly, the optical field around a nano-structure naturally exhibits radial and longitudinal polarization gradients, which sometimes generates even chiral couplings [116]. This is ignored here but actually can be an extra asset to control the system, which we do not make use of here. We also simply assume a frequency independent polarizability and a flat fiber dispersion curve over a large frequency range, which is hardly the case. However, as only the product of polarizability times spectral density enters into the force, this poses no serious restriction to the generality of our model. As a further simplification we ignore radial forces acting against the transverse trap of the particles [115], which will give upper limits on the possible illumination powers, but generally do not seriously affect the longitudinal dynamics.

10.2.1. Beam-splitter model for transversely illuminated particles

As we have outlined in a previous work [16] a set of particles next to a waveguide can be effectively modeled using a scattering matrix approach. Here for light propagating in the fiber, the particles simply act as beam splitters with a complex polarizability ζ with dispersive part $\Re(\zeta)$ and absorptive part $\Im(\zeta)$. The transmission and reflection coefficients $t = 1/(1 - i\zeta)$ and $r = i\zeta/(1 - i\zeta)$ describe how the particles modulate the field inside the fiber. At the same time each illuminated particle also acts as a local source of light scattered into the propagating mode with (real) pump amplitude η. The interaction between a particle and the fiber modes as well as the scattering into and out of the fiber can thus be effectively described by a 3×3 beam splitter matrix $\mathbf{M}_{BS}$:

$$\begin{aligned}\begin{pmatrix} A_j \\ B_j \\ \eta \end{pmatrix} &= \frac{1}{t}\begin{pmatrix} t^2 - r^2 & r & \frac{1}{\sqrt{2}}(t-r) \\ -r & 1 & -\frac{1}{\sqrt{2}} \\ 0 & 0 & t \end{pmatrix}\begin{pmatrix} C_j \\ D_j \\ \eta \end{pmatrix} \\ &= \begin{pmatrix} 1 + i\zeta & i\zeta & \frac{1}{\sqrt{2}}(1 - i\zeta) \\ -i\zeta & 1 - i\zeta & \frac{1}{\sqrt{2}}(i\zeta - 1) \\ 0 & 0 & 1 \end{pmatrix}\begin{pmatrix} C_j \\ D_j \\ \eta \end{pmatrix}. \end{aligned} \tag{10.1}$$

Here B_j, C_j are the amplitudes of the fields traveling within the fiber towards the j-th particle, while A_j, D_j are the amplitudes of the outgoing fields. The parameter η gives the effective amplitude of the light scattered into the fiber and coming from the transverse pump field. For simplicity here we assume that all atoms see the same pump field amplitude and phase such that η is the same for all particles.

While the beam splitter relations above describe how the particles redistribute the light in and outside the fiber, a propagation matrix $\mathbf{M}_P(d)$ is needed to describe the propagation of light along the fiber between two particles with distance d,

$$\mathbf{M}_P(d) = \begin{pmatrix} e^{ikd} & 0 & 0 \\ 0 & e^{-ikd} & 0 \\ 0 & 0 & 1 \end{pmatrix}, \tag{10.2}$$

with the wave vector $k = n(\omega)\omega/c$, frequency ω, speed of light c and refractive index $n(\omega)$, which we assume to be equal for all frequencies $n(\omega) \approx n$.

Multiplying the individual beam splitter and propagation matrices for a given particle

distribution allows one to determine the field distribution along the fiber depending on the particle positions. The optical force on the j-th particle can then be calculated by inserting the calculated field amplitudes in the Maxwell stress tensor, which here simply gives [43; 63; 64]

$$F_j = \frac{\epsilon_0}{2}\left(|A_j|^2 + |B_j|^2 - |C_j|^2 - |D_j|^2\right). \tag{10.3}$$

The standard way to induce light forces on the particles is of course to send the light through the fiber. A standing light wave in the fiber creates thus a perfect one-dimensional lattice potential along the propagating directions. Note that the transverse field gradients can be also used to create trapping in the radial direction [58; 117]. In the case of many particles trapped simultaneously, multiple scattering modifies this potential and already creates long range interactions and nonlinear dynamics [64]. In general these interactions are tiny compared to the single particle potential as the backscattering per particle typically is small. However, when only a transverse pump is applied, all the light in the fiber is created from atomic scattering of the pump light. Here the atoms then interact not only via rescattering of this light, but even more prominently via interference of the light scattered by different atoms into the fiber [16]. In special cases this leads to ordering and self-organization of the atoms [72] very similar as in transversely pumped cavities [70]. But in contrast to a cavity there are no preselected modes defining the sensitivity of the system to the frequency of the incoming light.

10.2.2. Forces due to transverse illumination

The central aim of this work is to explore the possibilities to implement and design specific inter-particle forces induced by scattering of spatially coherent transverse pump fields with a variable spectrum. The forces stem from collective scattering into the fiber mode on the one hand and multiple rescattering of this light within the mode on the other hand. To simplify our model here we assume that the coupling of the particles to the fiber field is very weak, *i. e.* $|\zeta| \ll 1$, so that higher order scattering will be negligible. As shown in a previous work [112] one can even assume the limit $\zeta \to 0$ with only small error. Although the two coupling strengths η and ζ both equally depend on the polarizability of the particles [37] and the evanescent guided mode amplitude at

their position, both parameters can be adjusted independently as only η is proportional to the pump amplitude. Hence η dominates for strong transverse pump compensating the weak coupling.
In the limit $\zeta \to 0$ the forces on the particles can then be understood as a sum of long range two-particle interactions between all particle pairs at their positions x_l and x_j with $x_1 < x_2 < \cdots < x_N$ and the force can be considered as a sum of contributions from different frequency components. As derived in some more detail in a previous work [112] for the spectral force density on the j-th of N particles, i.e. the force contribution at frequency ω with intensity $I(\omega)$, we then get

$$\begin{aligned} f_{j,N}(\omega, x_1, x_2, \ldots, x_N) &= \frac{I(\omega)}{c}\left(\sum_{l=j+1}^{N} \cos\left(\frac{n\omega(x_l - x_j)}{c}\right) - \sum_{l=1}^{j-1} \cos\left(\frac{n\omega(x_l - x_j)}{c}\right)\right) \\ &= \sum_{l=j+1}^{N} f_{1,2}(\omega, x_j, x_l) + \sum_{l=1}^{j-1} f_{2,2}(\omega, x_j, x_l). \end{aligned} \tag{10.4}$$

Here $I(\omega)$ is the intensity distribution of the transverse pump field and the total force on this particle is then given by $F_{j,N}(x_1, \ldots, x_N) := \int f_{j,N}(\omega, x_1, \ldots, x_N) d\omega$.
The second line of Eq. (10.4) can be understood as follows: $f_{1,2}(\omega, x_j, x_l)$ gives the force density on the first of two particles located at x_j and x_l with $j < l$. Likewise $f_{2,2}(\omega, x_j, x_l)$ gives the force on the second particle of the pair, with $f_{2,2}(\omega, x_j, x_l) = -f_{1,2}(\omega, x_j, x_l)$. Hence the first sum describes the pairwise interaction with all particles to the right of x_j while the second sum gives the interaction with all particles to the left.
For the sake of analytical integrability we will assume the incident light field $I(\omega)$ as a sum of single transverse mode Lorentzian spectral lines with different central frequencies $\omega_m = 2\pi c/\lambda_m$, wave lengths λ_m, peak intensities $I_m = |\eta_m|^2 c\epsilon_0/2$ and widths γ_m:

$$I(\omega) = \sum_m \frac{I_m}{\pi} \frac{c\gamma_m}{c^2\gamma_m^2 + n^2(\omega - \omega_m)^2}. \tag{10.5}$$

We also ignore here the frequency dependent polarizability of the scattering amplitude η as this can be incorporated in a suitable frequency dependent effective pump strength.

Integrating the force density Eq. (10.4) using this intensity distribution gives

$$F_{1,2}(x_j, x_l) = \sum_m \frac{I_m}{\pi} \int_{-\infty}^{\infty} \frac{\gamma_m}{c^2\gamma_m^2 + n^2(\omega - \omega_m)^2} \cos\left(\frac{n\omega(x_l - x_j)}{c}\right) d\omega$$
$$= \sum_m \frac{I_m}{nc} e^{-\gamma_m |x_l - x_j|} \cos\left(k_m(x_l - x_j)\right), \tag{10.6}$$

where from inversion symmetry we see $F_{1,2}(x_j, x_l) = -F_{2,2}(x_j, x_l)$. Using the fact that the force for a larger set of N particles can be described using only pairwise interactions, we can define $F_{1,2}(x_j, x_l) = -F_{2,2}(x_j, x_l) \equiv F_{\text{pair}}(x_l - x_j) \equiv F_{\text{pair}}(d_{jl})$, with distance $d_{jl} = |x_l - x_j|$. Note that in this case $F_{\text{pair}}(d_{jl})$ describes the force on the particle on the left.

Let us mention again here that we completely neglect possible interference effects between distant spectral components of the beams as we assume that they are only spatially but not time coherent and quickly average out in time. By help of the beam splitter method developed for single frequencies we thus can directly calculate the forces for each frequency component separately and then add them up to obtain the full force on the particles. Note that this implicitly also assumes low particle velocities so that the Doppler shifts on reflection do not couple different parts of the spectrum.

In a previous work on this model assuming a single illumination line with a finite bandwidth [112] we could identify stable stationary configurations of the particles where all forces vanish. As a central property for such stable particle configurations the outermost particles arranged to form Bragg mirrors and act like an optical resonator to trap high field intensities and the other particles between them. This behaviour vanishes for a large enough absorptive part $\Im(\zeta)$, where no stable solutions can be found due to outward radiation pressure in the chain. In addition the key effect of a finite laser bandwidth resulted in forces with exponential decay over distance proportional to the inverse bandwidth of the pump. The interaction range between the particles thus can be controlled via the spectral width of the incoming field. By changing γ from small to large values, the interaction can be tailored from infinite range to nearest-neighbour coupling. This leads to the expectation that a more general spectral control of the input field should give much wider opportunities to tailor interaction potentials.

Two-particle forces and potentials

The radiation field inside the fiber is the result of collective scattering by all N particles. As a result, the force on each of these particles depends on the positions of all N particles. But as discussed above, the total force on the j-th of N particles can be rewritten as a sum of two-particle interactions depending only on the distance between these two particles.
The two-particle force given in Eq. (10.6) can be expressed in terms of a potential, $F_{\text{pair}}(d_{jl}) = -\partial_{x_j} U_{\text{pair}}(d_{jl})$ with

$$U_{\text{pair}}(d_{jl}) = \sum_m \frac{I_m e^{-\gamma_m d_{jl}}}{nc(k_m^2 + \gamma_m^2)} \left(k_m \sin(k_m d_{jl}) - \gamma_m \cos(k_m d_{jl})\right) . \tag{10.7}$$

Due to translational invariance of the setup, this potential depends only on the distance $d_{jl} = |x_l - x_j|$. The positions of global (local) minima of $U_{\text{pair}}(d_{jl})$ gives the distances for stable (metastable) two-particle configurations. Clearly the potential is simply periodic for a single monochromatic transverse pump beam, but as shown in Fig. 10.2, adding a second beam already gives intricate shapes for the pair-potential. Fig. 10.2 shows the potential for two particles illuminated by two broadband fields of varying intensity I_2 and width γ_2. We see that these two parameters as well as the frequency ω_2 can be used to adjust the stable two-particle distances. The potential generated by a single beam has equidistant minima in the near field whose depth changes with γ in the far field. For two fields we find non-equidistantly distributed equilibrium distances at short range. The relative intensity of the two fields can be used to adjust the relative depth of the potential wells. Note that in the chosen example no three minima of the potential have distances which are multiples of each other. So adding a third particle directly leads to frustration effects [118; 119] as the particles have to leave the stable pairwise configuration in order to find a configuration where all three particles are trapped. Finally, allowing for a finite range γ of the second field as in Fig. 10.2b) recovers the long range periodic potential with distortions resembling a defect at small distances. To further study the versatility of interaction potentials created by adding many frequency components we compare the expression for the two-particle force (10.6) to the definition of a general Fourier series

$$f(t) = \frac{a_0}{2} + \sum_{m=1}^{\infty} \left(a_m \cos(mt) + b_m \sin(mt)\right) , \tag{10.8}$$

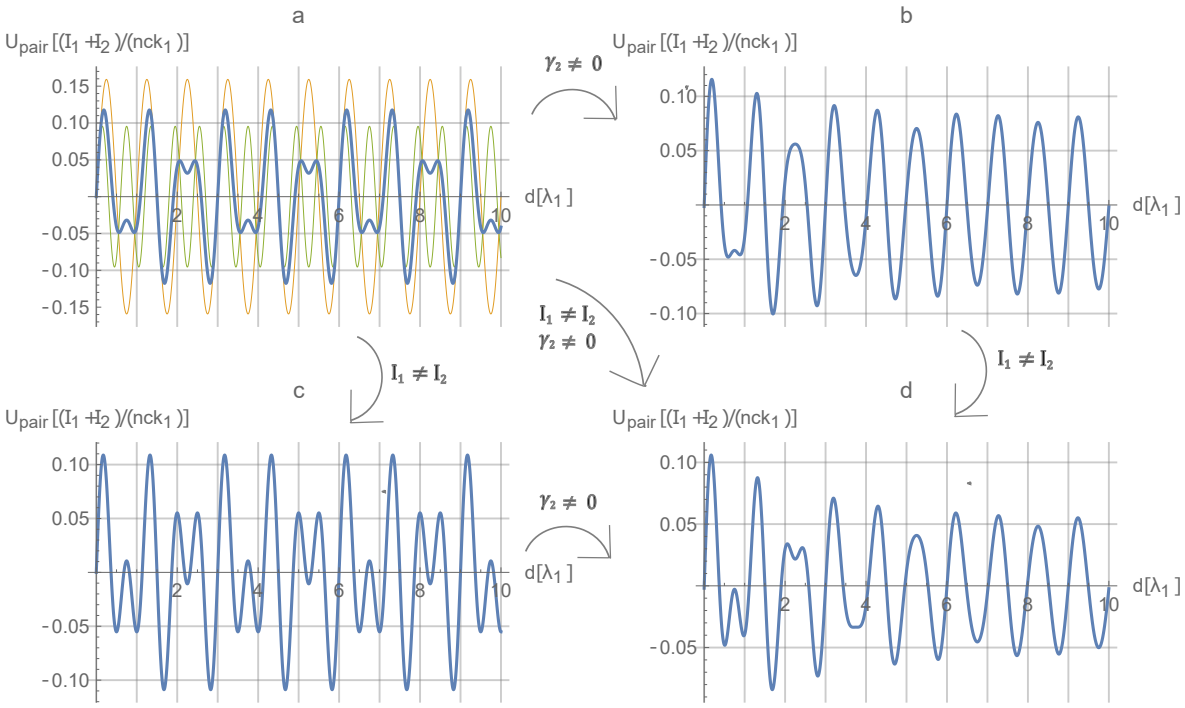

Figure 10.2.: Pair potential from Eq. (10.7) for two particles illuminated by two fields with frequencies k_1 and $k_2 = \frac{5}{3}\ k_1$ as a function of the distance d. a) Adding two beams of equal intensity and without decay ($I_2 = I_1$, $\gamma_1 = \gamma_2 = 0$) creates a periodic potential landscape. Thin lines in the back show the individual fields with wave numbers k_1 (yellow) and $k_2 = \frac{5}{3}\ k_1$ (green) separately. Changing the intensity ratios and/or introducing finite bandwidths γ_2 can create more complicate potentials: b) $I_2 = I_1$, $\gamma_1 = 0$, $\gamma_2 = 0.05\ k_1$, c) $I_2 = 2\ I_1$, $\gamma_1 = \gamma_2 = 0$, d) $I_2 = 2\ I_1$, $\gamma_1 = 0$, $\gamma_2 = 0.05\ k_1$.

and see that the force (10.6) is a special case of a Fourier cosine series with $a_0 = b_m = 0$, $a_m = \frac{I_m}{nc}$ and $\gamma_m = 0$. Since $a_0 = b_m = 0$ we can only generate symmetric functions. Including a finite bandwidth $\gamma_m \neq 0$ this is no longer a classical Fourier series, but opens the possibility to change every single component of the series and design different force shapes as shown in Fig. 10.3. When choosing specific combinations of I_m, ω_m and γ_m we can model very peculiar force shapes such as, for example, a triangular wave. When changing γ_m to non-zero values this triangle wave changes strongly in the far field (Fig. 10.3a). Also a square wave can be modeled and when introducing γ_m it changes to a simple sine wave (Fig. 10.3b) in the far field. Fig. 10.3c) shows an example with strong localizing forces appearing preferably around chosen distances. γ_m can then be used to tune the forces between the peaks. An even more unusual case is a Lorentz distribution (Fig. 10.3d) where very strong inter-particle forces appear specifically in a

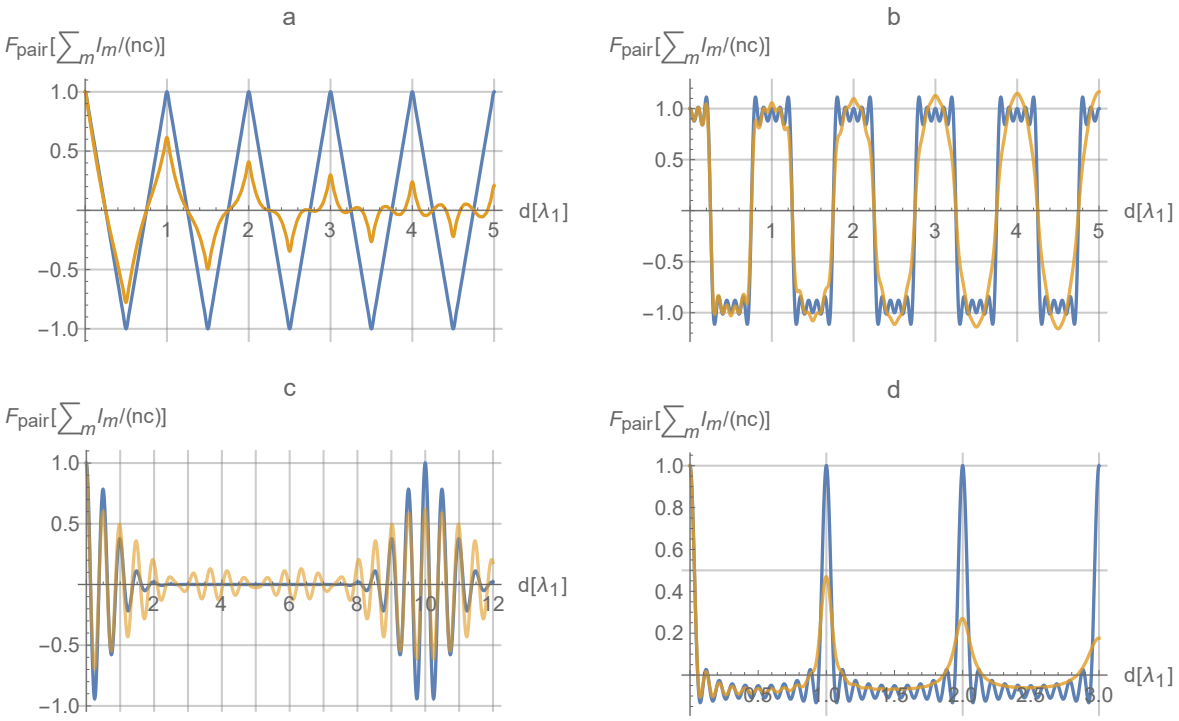

Figure 10.3.: Pair forces $F_{\text{pair}}(d)$ of Eq. (10.6) for two particles illuminated by a sum of $m_{\max}$ fields with wave numbers $k_1, \ldots, k_{m_{\max}}$ as a function of the distance d with $\gamma_m = 0$ (blue) and $\gamma_m \neq 0$ (yellow). As the forces can be written as a Fourier series one can implement shapes including a) triangles, $I_m = \frac{1}{(2m-1)^2}\ I_1$, $k_m = (2m-1)\ k_1$, $m_{\max} = 10$, blue: $\gamma_m = 0$, yellow: $\gamma_1 = 0.1\ k_1$, $\gamma_{m>1} = 0$; b) rectangular waves, $I_m = \frac{\sin(m\pi/2)}{m}\ I_1$, $k_m = m\ k_1$, $m_{\max} = 10$, blue: $\gamma_m = 0$, yellow: $\gamma_m = 0.1(1 - 1/m)\ k_1$; c) clusters of strong oscillating forces with a Gaussian intensity distribution $I_m = e^{-(m-10)^2/10}\ e^{8.1}\ I_1$, $k_m = (1 + 0.1m)\ k_1$, $m_{\max} = 20$, blue: $\gamma_m = 0$, yellow: $\gamma_{m=\{1-8,13-20\}} = 0.1\ m\ k_1$, $\gamma_{m=\{9-12\}} = 0$; d) or very thin Lorentz peaks $I_m = (1 - (m-1)/10)\ I_1$, $k_m = m\ k_1$, $m_{\max} = 10$ and blue: $\gamma_m = 0$, yellow: $\gamma_m = 0.03\ m\ k_1$.

very narrow interval of distances. This includes a very sharp gradient of the force at the equilibrium positions providing for very strong particle confinement with deep potential wells. Investigating the parameters more closely we can see that the examples given in Figs. 10.3a), b) and d) rely on a setup spanning a very broad frequency range of several octaves: Starting with a far infrared beam (CO_2-laser) at ($\lambda_1 = 10\,000\ nm$), the doubled frequency is at ($\lambda_2 = 5\,000\ nm$) and even higher harmonics would reach the visible regime. Continuing this up to ten octaves more would thus certainly be hardly possible. The example of Fig. 10.3c) shows a more accessible setup with a confined range of frequencies.

Extension to many particles

Summing up all pair-particle potentials Eq. (10.7) we can calculate the position dependent light shift (optical potential) experienced by a single particle keeping all the other particles at a fixed position as

$$U_{j,N}(x_1,\ldots,x_N) = \sum_{l=1}^{j-1} U_{\text{pair}}(d_{jl}) + \sum_{l=j+1}^{N} U_{\text{pair}}(d_{jl})\,. \tag{10.9}$$

Using $\partial_{x_j} U_{\text{pair}}(d_{jl}) = -\partial_{x_l} U_{\text{pair}}(d_{jl})$ we obtain the force acting on a particle of Eq. (10.3) from $F_{j,N} = -\partial_{x_j} U_{j,N}(x_1,\ldots,x_N)$. The total potential energy of the system can then be calculated by summing up all these potentials:

$$U_{\text{tot}}(x_1,\ldots,x_N) = \frac{1}{2}\sum_{j=1}^{N} U_{j,N}(x_1,\ldots,x_N)\,. \tag{10.10}$$

10.3. Tailored forces for free particles and frustration effects of self-organization

As we have seen and illustrated in figure 10.3 there are many possibilities to tailor the forces acting between particle pairs. Using the fact that the equation for the force is a symmetric Fourier series we can produce every symmetric periodic function. Allowing for a bandwidth γ_m for the various illumination lines allows to change the range of the individual frequency components tailoring the long range part of the force shape. In particular we can create forces with a very sharp gradient at the stable positions around zero force values, which implies narrow potential wells and very well localized configurations. We can also produce forces which only affect particles at certain chosen distances, while particles at other distances can move almost freely. In figure 10.4 we show a set of three atoms arranging themselves under the influence of rectangular-wave two-particle forces as depicted in figure 10.3b). Here, two particles order at a distance given by the very sharp zero points of the force, which is at $d_{12} = 0.75\ \lambda_1$ for the given parameters. If a third particle is added, each pair will seek to arrange itself at a distance given by the (stable) zero of the respective pair-force. But from fig. 10.3b) we see that these stable distances are distributed such that this is impossible. The group of particles thus will have to “compromise" and settle at distances $d_{12} = d_{23} \approx 0.78\ \lambda_1$. This

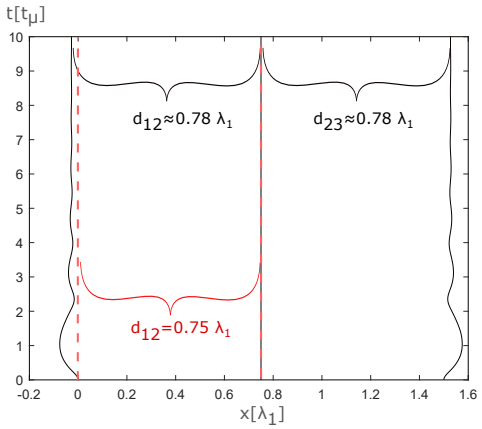

Figure 10.4.: Trajectories for three particles (black lines) illuminated by transverse pump-beams generating an approximately rectangular pair-force profile as shown in Fig. 10.3b) with $I_m = \sin(m\pi/2)/m\ I_1$, $k_m = m\ k_1$, $m_{\max} = 10$ and $\gamma_m = 0$. Red dashed lines show the case of two particles which remain at the minimum equilibrium distance. For this force pattern, three or more particles cannot arrange themselves such that the separation between each pair corresponds to a minimum of the respective pair-potential. The setup thus shows frustration as the particles have to reorder and find a shifted common equilibrium if a third particle is added. In this simulation we assume an environment with a friction coefficient μ, the time time scale t_μ depends on λ_1, I_m, n, μ and the particle-mass M.

situation thus shows (classical) frustration [118], similar to magnets on a triangular grid which cannot arrange themselves such that each pair of magnets is in an anti-parallel configuration [119].

10.4. Designing interaction potentials between trapped particles

In the previous section we discussed how free particles organize themselves and interact via tailored multi-particle forces generated by the scattered transverse light field. In many optical trapping applications, however, the particles are already trapped by a prescribed external lattice potential generated by standing wave light fields propagating through the nano-structure [58; 120]. As illustrated in figure 10.5 the forces generated by the transverse pump field then provide a versatile tool to generate almost arbitrary interactions between particles trapped in the periodic minima of the external potential. Similar to the case of a multimode cavity this could be the basis of complex

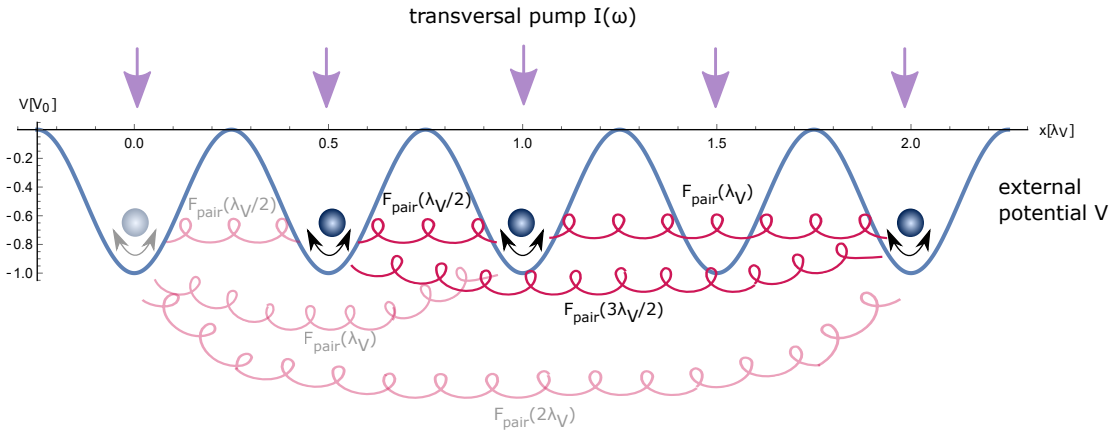

Figure 10.5.: Schematic illustration of particles trapped in an external periodic potential and illuminated by a transverse pump field. This transverse field leads to pair-interactions between the particles which slightly disturb the particles' trapping positions. Darker drawn lines correspond to the three particle setup used in Figs. 10.6a) and b). The configuration used in Fig. 10.6c) uses a fourth particle, indicated here with pale lines.

simulations [121]. We consider a strong periodic external potential

$$V(x) = -V_0 \cos^2(k_V x), \tag{10.11}$$

with $V_0 = \frac{2I_V}{nk_V c}$ depending on the intensity I_V of the two incoming fields, k_V the wave vector of the two fields, and examine the interaction between the particles due to the transverse pump field. For example, using an initial condition $d_{12} = 0.5\ \lambda_V$ and $d_{23} = \lambda_V$ places three particles in the first, second and fourth potential well, as depicted in Fig. 10.5. Adding transverse beams generates inter-particle forces which are given by the sum of pair-forces as shown in Eq. (10.4). Fig. 10.6 shows these pair-forces and the resulting trajectories of the particles. In Fig. 10.6a) we find that the total force on the third particle is the negative of the sum of the pair-force between the first and the third particle at a distance of $d_{13} = 1.5\ \lambda_V$ and between the second and the third particle at $d_{23} = \lambda_V$, which sum up to zero. So in this case only the first and the second particle interact. For Fig. 10.6b) we can observe the same for the first and the third particle. If we consider the four-particle case with the particles trapped in the first, second, third and fifth potential well as shown in Fig. 10.5, the example Fig. 10.6c) shows that by using two fields we can change the coupling between the particles and decouple the two particles in the middle. In general the scattering forces on $N > 2$

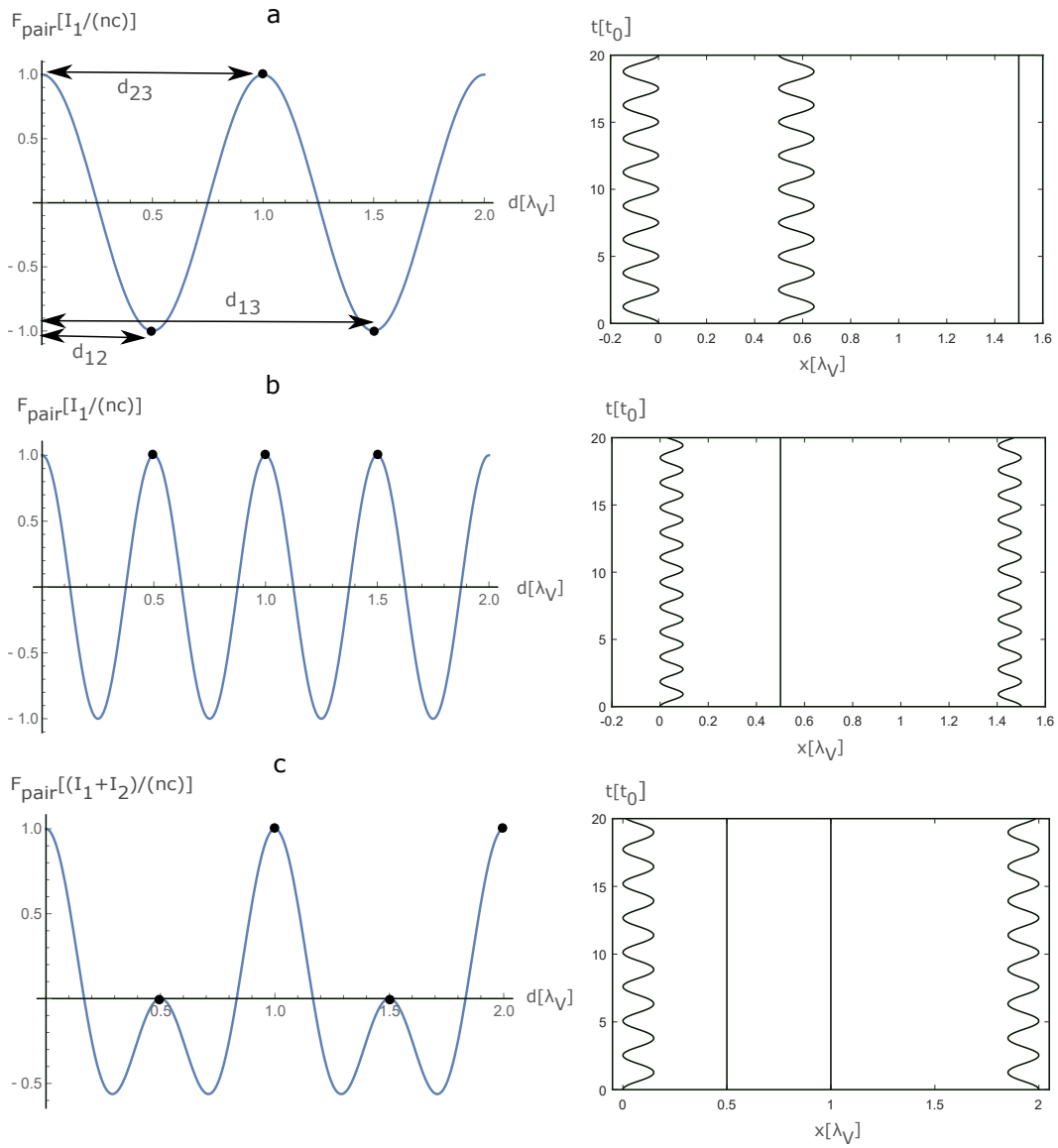

Figure 10.6.: The figures in the left column show distance-dependent forces between atom pairs for three different configurations of transverse fields and prescribed potentials, see also Fig. 10.5. The black dots indicate the respective pairwise separations of three (four) particles given by the periodic potential and chosen as starting points. In the figures on the right we show the corresponding trajectories of the particles reacting to these forces. We see that the pair-forces induced by the transverse beam induce coupled oscillation between a chosen pair of particles, while the forces conspire to leave the remaining particle(s) unaffected. The parameters here are $\gamma_1 = \gamma_2 = 0$, $I_1 = I_2$ for a) three particles, $k_1 = k_V$, b) three particles, $k_1 = 2\ k_V$, and c) four particles, $k_1 = k_V$, $k_2 = 2\ k_V$. The time-scale of the dynamics here is $t_0 = \sqrt{Mnc(1/\sum_m I_m + 1/I_V)}$. The two particle interactions shown in a) connect particle one and two, b) particle one and three, and c) particle one and four. It demonstrates how the single pair-forces can be combined to tailor the coupling between particles trapped in an additional periodic potential.

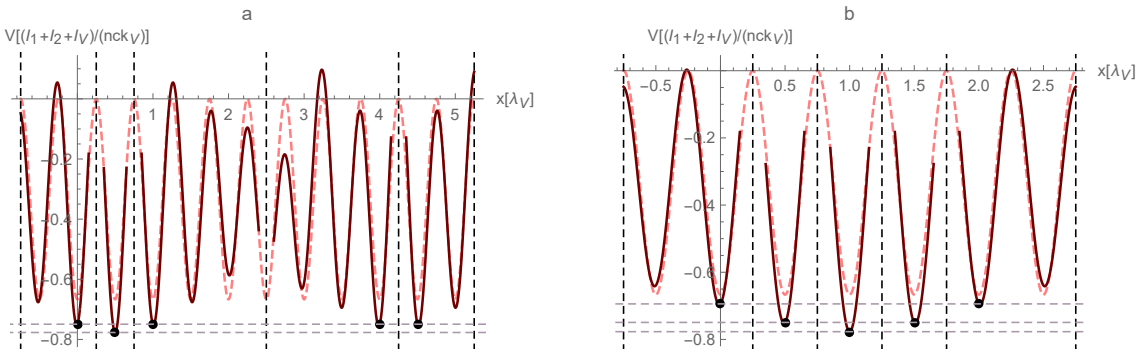

Figure 10.7.: Potential for five particles trapped in an external potential and interacting via two transverse fields with intensities $I_1 = I_2 = I_V$, wave numbers $k_1 = k_V$, $k_2 = 5/3\, k_V$ and spectral widths $\gamma_1 = \gamma_2 = 0$. Red dashed lines show the external potential $V(x)$, black points the particle positions. For each particle the respective potential $U_{j,N}$ is drawn in solid red curves between the dashed vertical lines. That is, for example, between the first two vertical lines we show the potential $U_{1,N}$ if the position of the first particle is varied while the other particles are fixed at the positions marked by the black dots. The configuration of particles placed in the first, second, third, ninth and tenth well shown here is the one minimizing the total potential energy. A configuration where all particles are in neighbouring wells as shown on the right has a higher total energy.

particles cannot be described by a common potential [64] and the dynamics of the particles does not necessarily conserve energy as the pump provides for a non-depleting energy and momentum source. However, to lowest order in particle-field coupling as considered above, every particle pair has its own relative potential energy $U_{\text{pair}}(d_{jl})$ and in Eq. (10.9) we gave the potential energy for each particle, if the positions of other particles are fixed. But changing the position of one particle affects the optical potential of all other particles.

But of course, for every set of parameters (the number of particles, strength of the external potential and settings for transverse beams) there will be a configuration of particle positions minimizing the total potential energy given in Eq. (10.10). For N particles, this is an $N-1$-dimensional optimization problem which is conceptually visualized in Figs. 10.7 and 10.8. There we show the sum of the external potential $V(x)$ and single particle potentials $U_{j,N}$ for $N = 5$ particles. For the chosen parameters Fig. 10.7a) shows that the lowest energy occurs where the particles are trapped in the first, second, third, ninth and tenth potential minima (indicated by the black dots). Comparing this to Fig. 10.7b) we find that the total potential is not minimized if the

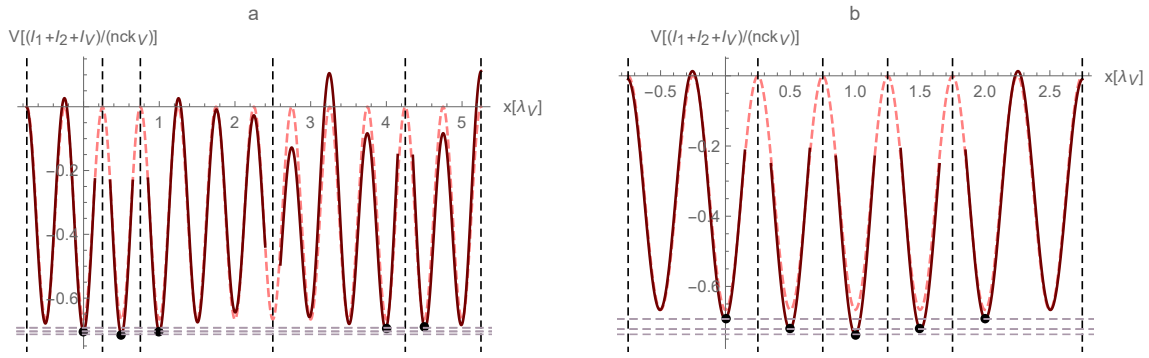

Figure 10.8.: The same as in figure 10.7, but with a broad spectral width of the second transverse beam, $\gamma_2 = 0.1\ k_V$. For these parameters we see that the particles minimize their collective total potential energy if they are in neighbouring wells as shown on the right hand side. Introducing γ_2 to the system thus modulates the long-range interactions between the particles, such that now the configuration on the left is less favourable.

particles are placed in neighbouring wells. The transverse beams in Fig. 10.7 are chosen with a vanishing linewidth $\gamma_{1,2} = 0$. But introducing a broad spectrum for the second laser, $\gamma_2 = 0.1\ k_V$, changes the interactions in the far field such that placing the particles in neighbouring wells gives the lowest-energy configuration, as shown in Fig. 10.8.
Such a system thus offers the possibility to manipulate and rearrange particles trapped in an external potential. Changing the intensities, frequencies and widths of the fields we can suppress or push the individual two-particle-interactions. These controlled couplings then give the opportunity to realize a desired energy landscape useful, for example, in analog quantum simulation or quantum annealing [17; 121; 122].
In a setup where the inter-particle forces are weaker than the strong external potential V given in Eq. (10.11), one can expand the position of the particles around the minima of the external trap, $x_j = x_j^0 + \Delta_j$ where $k_V x_j^0 = z_j \pi$ for an integer z_j with $z_j > z_l$ if $j > l$. One can then write the total external potential as a sum of harmonic oscillators

$$\sum_{j=1}^{N} V(x_j) \simeq -\sum_{j=1}^{N} V_0 \left(1 - k_V^2 \Delta_j^2\right). \tag{10.12}$$

Setting $\gamma_m = 0$ we get for the pair interaction

$$U_{\text{pair}}(d_{jl}) \simeq \sum_m \frac{I_m}{nck_m} \Bigg(\sin(|z_j - z_l|\pi k_m/k_V) \left(1 - \frac{k_m^2}{2}\left(\Delta_j - \Delta_l\right)^2\right) + \cos(|z_j - z_l|\pi k_m/k_V) k_m \left(\Delta_j - \Delta_l\right) \Bigg). \quad (10.13)$$

Tuning the frequency ratios k_m/k_V thus allows one to design quadratic or linear interactions between each pair of particles while choosing a finite bandwidth γ_m gives control over long-range coupling. One can imagine that this might be useful to implement specifically designed multi-particle Hamiltonians with coupled motional states of atoms trapped in specific distant lattice sites.

10.5. Conclusions

Cold atoms, molecules or point-like nano-particles trapped along light-guiding nanostructures constitute a powerful setup to study the physics of collective light scattering in general and long range light mediated inter-particle forces in particular. Several experiments have now entered the domain, where the contribution of even a single particle to the field scattered into and out of the confined modes is significant and directly observable [52; 123]. So far experiments and virtually all theoretical approaches have concentrated on the action of monochromatic laser light coupled into single field modes. In this work, at the hand of a simplified effective model, we theoretically exhibit the wealth of new possibilities arising from applying a transverse pump field with a freely designable spectrum. Typically such a multispectral field can be composed by a set of independent spatially coherent laser beams of different central frequency and spectral width. Alternatively spectrally reshaped white light sources could be envisaged. We showed that in the limit of weak internal backscattering the two-particle forces arising in such a setup can be synthesized from different spectral components each contributing a component to a Fourier cosine series of the force with an amplitude proportional to the field intensity scattered into the fiber. Hence, in principle, one can almost arbitrarily shape the two-particle forces along one dimension and implement any real symmetric function of distance. As the force is based on coherent scattering it constitutes a conservative force without significant heating. Hence a generalization

to trapped quantum particles for the implementation of a quantum simulator with virtually all to all coupling can be envisaged.

At this point our simplified effective model exhibited very promising results which have to be confirmed in more realistic models. In particular, implementing the strong confinement and low temperatures of the transverse motion are very challenging although some experiments achieved close to ground-state cooling [98]. Thus fluctuations of the coupling strength should be included. We also have ignored issues of polarization gradients and chirality, which add technical challenges, but also further enhance the versatility of the implementations [120; 124].

In summary, although an actual physical implementation is challenging, the forces due to multimode transverse illumination provide a powerful and very versatile tool to explore many-particle self-organization, unconventional interactions and possibly also implement quantum simulations allowing to address individual particles in 1D optical lattices.

Acknowledgements: This work was funded by the Austrian Science Fund FWF grants No. F4013 SFB FOQUS and J3703.

Part III.

Quantum description of coupled particle motion

11. Introduction

In this chapter we develop a quantum approach of the model by quantizing the motional degrees of freedom of the particles. The particles then can be described by quantum oscillators. In the previous chapter we have shown how the interactions between the particles can be tuned by designing the shape of the incoming field. This can be used to simulate any symmetric two-body interaction. As an example we show here how Coulomb interactions can be simulated in our model. When describing the oscillator states as qubits we can even implement quantum gates and entangle states.

11.1. Theoretical background

11.1.1. Quantum simulation

The simulation of quantum models is very challenging even for supercomputers as it needs a huge memory to describe a quantum state. Without any approximation the memory scales exponentially with the system size [17].
In 1982 Feynman [19] came up with the idea to simulate a complex quantum system by a simpler quantum device. Quantum simulation, thus, is a very powerful tool to study quantum dynamical behaviours in quantum systems which can not or only difficult be studied in the laboratory. In the last few years the field of quantum simulations has been growing very fast, as there exist a lot of useful applications in physics, chemistry and even in biology [17].
In quantum simulation one can distinguish between digital and analog quantum simulation. In digital quantum simulation the wave function is encoded by qubits [125] and universal gates are used to simulate unitary evolutions. In such systems the number of universal gates can be very high to accurately simulate the quantum evolution [17; 126].
In analog quantum simulation a good controllable physical system mimics another complex system. In that case the Hamiltonian of the complex system is directly mapped

on the simulator system [17].
A simulator system has to be highly controllable. Promising candidates for such systems are atoms in optical lattices [127–130], atoms in cavities [131–133], trapped ions [134–137], nuclear spins [138–140], electron spins in semiconductor quantum dots [141], superconducting circuits [142–149] or photons [23; 150–159]. The most advanced platform for analog quantum computing are atoms in optical lattices as it is the only system where more than a few particles can be controlled for quantum simulation, while for digital quantum computing trapped ions are the most promising candidate [17; 160].
Quantum simulation can be used to investigate systems which are experimentally challenging and impossible to simulate classically. Some examples are Hubbard models [127; 132; 133; 161], spin models [149; 160], quantum phase transitions [127], disordered [147] or frustrated systems [119; 152], spin glasses [148], superconductivity [162], metamaterials [163] or topological order [146; 150] in condensed matter physics, problems in high energy physics [164; 165], in cosmology [166–168], in atomic physics [169], in quantum chemistry [151; 170–172], in nuclear physics [17], the investigation of open quantum systems [173; 174], quantum chaos [175; 176] or interferometry [155–157; 159].

Universal gates

In quantum computation quantum states are encoded by qubits. Qubits in contrast to classical bits can not only be in the states 0 or 1, but also in a superposition

$$|\psi\rangle = \alpha|0\rangle + \beta|1\rangle, \tag{11.1}$$

with α and β being complex numbers fulfilling $|\alpha|^2 + |\beta|^2 = 1$.
While in classical computation bits are manipulated by gates, in quantum physics analogous quantum gates can be defined. Such a quantum gate has to be unitary as it has to be invertible to determine the input state. A set of quantum gates is called universal if any unitary operation can be approximated to arbitrary accuracy using only this set of gates. One such universal set of gates consists of CNOT

$$\begin{pmatrix} 1 & 0 & 0 & 0 \\ 0 & 1 & 0 & 0 \\ 0 & 0 & 0 & 1 \\ 0 & 0 & 1 & 0 \end{pmatrix}, \tag{11.2}$$

and single qubit gates. Interestingly any single qubit operation can be approximated by Hadamard

$$\frac{1}{\sqrt{2}}\begin{pmatrix}1 & 1\\ 1 & -1\end{pmatrix}, \tag{11.3}$$

phase

$$\begin{pmatrix}1 & 0\\ 0 & i\end{pmatrix}, \tag{11.4}$$

and $\pi/8$-gates [125]

$$\frac{1}{\sqrt{2}}\begin{pmatrix}1 & 0\\ 0 & e^{i\pi/4}\end{pmatrix}. \tag{11.5}$$

Another example for a universal set of gates is the square root of an i-SWAP gate

$$\hat{U}_{\mathrm{SQiSW}} = \begin{pmatrix}1 & 0 & 0 & 0\\ 0 & \frac{1}{\sqrt{2}} & -\frac{i}{\sqrt{2}} & 0\\ 0 & -\frac{i}{\sqrt{2}} & \frac{1}{\sqrt{2}} & 0\\ 0 & 0 & 0 & 1\end{pmatrix}, \tag{11.6}$$

combined with single qubit gates. A CNOT gate can be implemented by this entangling gate in the following way [177]

$$U_{\mathrm{CNOT}} = R_y(-\pi/2)\otimes\mathbb{I}\cdot R_x(\pi/2)\otimes R_x(-\pi/2)\cdot U_{\mathrm{SQiSW}}\cdot R_x(\pi)\otimes\mathbb{I}\cdot U_{\mathrm{SQiSW}}\cdot R_y(\pi/2)\otimes\mathbb{I}, \tag{11.7}$$

with $\mathbb{I}$ the unity matrix and R_x, R_y, rotations around the x or y-axes.
Note, that although a universal set of gates can be used to implement any unitary operation, most unitary transformations can only be implemented very inefficiently. But according to the Solovay–Kitaev theorem a quantum gate can be approximated to ϵ error very efficiently by a quantum circuit of $O(\log^c(1/\epsilon))$ gates, with c a small constant approximimately equal to 2 [125].

12. Preprint

A versatile quantum simulator for coupled oscillators using a 1D chain of atoms trapped near an optical nanofiber

Daniela Holzmann[1], Matthias Sonnleitner and Helmut Ritsch

The transversely confined propagating light modes of a nano-photonic optical waveguide or nanofiber can mediate effectively infinite-range forces. We show that for a linear chain of particles trapped within the waveguide's evanescent field, transverse illumination with a suitable set of laser frequencies should allow the implementation of a coupled-oscillator quantum simulator with time-dependent and widely controllable all-to-all interactions. At the example of the energy spectrum of oscillators with simulated Coulomb interactions we show that different effective coupling geometries can be emulated with high precision by proper choice of laser illumination conditions. Similarly, basic quantum gates can be selectively implemented between arbitrarily chosen pairs of oscillators in the energy basis as well as in a coherent-state basis. Key properties of the system dynamics and states can be monitored continuously by analysis of the out-coupled fiber fields.

arXiv: 2105.03262

[1]D.H. performed all of the calculations in this publication, while M.S. and H.R. contributed in an advisory role.

12.1. Introduction

Suitably designed laser fields allow one to trap individual quantum particles at well defined locations and cool them to their motional ground state [9; 178]. Already some time ago it has been demonstrated that trapping and cooling is also possible close to optical nano-structures and, in particular, in the vicinity of a tapered optical nanofiber [11; 98; 124]. Once trapped, the atoms interact with the evanescent field of light modes propagating within the fiber [124] exchanging energy and momentum. Thus the light strongly influences the atomic motion in the trap which in turn modifies the light propagation [57; 179–181]. As photons within the fiber propagate over practically infinite distances they collectively couple to all atoms, which induces all-to-all long-range interactions [112]. In this way thousands of atoms can be trapped, which leads to strong collective effects [14].

The individual atom-atom coupling via resonant photon emission by one atom followed by absorption by a second atom is typically rather small [77; 182], but it can already lead to spatial self-ordering of the atoms [183]. The induced force can be significantly increased if the atoms are transversely illuminated far off any internal atomic resonance to induce collective coherent scattering into the fiber [15; 72; 184]. Here the interference between the mode amplitudes created by scattering from different particles leads to gradient or dipole forces, which appear without changing the internal atomic state from spontaneous emission [16]. Properties of these forces can be modified by help of two laser frequencies [80].

The interactions between the particles depend on the properties of the incoming light field. With careful choice of laser frequencies and powers almost arbitrary shapes of interaction forces can be synthesized [185]. In this work we give examples how this property could be used for quantum simulation [17–23; 29; 30] as well as for quantum computation. By designing the incoming light field we show, for example, how the interaction between ions can be simulated, even if they are ordered in 2D or 3D geometries. In contrast to quantum simulation with ions [186; 187] we can even turn off the interactions between arbitrary pairs of particles. In the second part we describe the oscillator states as qubits and use this approach to design quantum gates [25; 26] or produce entangled states [24; 27; 28].

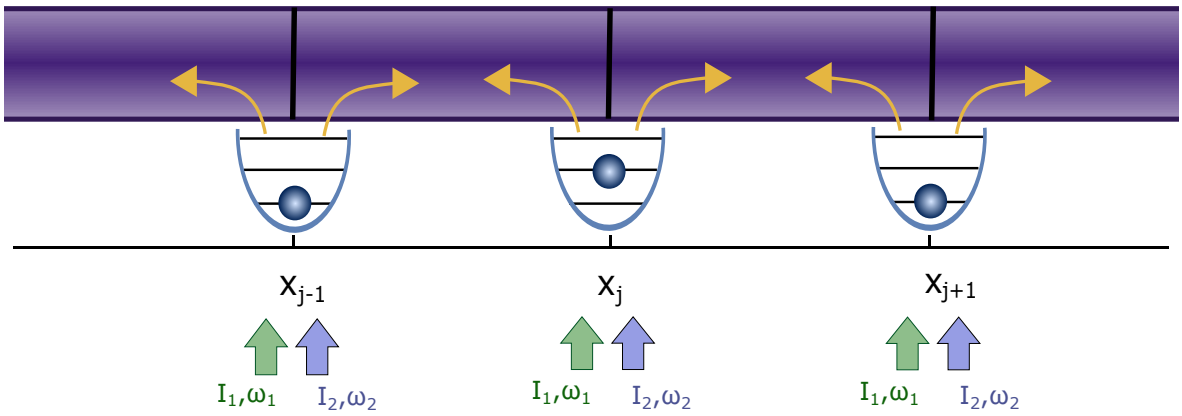

Figure 12.1.: Sketch of our system: N particles are confined in homogeneous traps next to a nanofiber. The particles are illuminated by multi-color transverse pump fields and scatter light into the fiber. Interference of the scattered fields in the fiber leads to effective forces between the particles.

12.2. Materials and Methods

12.2.1. Tailored coupling of the quantized motion of a trapped atom chain

In this work we consider N particles, typically atoms, molecules or nanospheres, harmonically trapped at predefined positions along an optical nanofiber. As depicted in Figure 12.1, these atoms interact with the evanescent field of the propagating nanofiber modes. Additionally, the particles are transversely illuminated by pump fields of tunable frequency. Each particle thus coherently scatters light from the pump fields into the fiber, where it interferes with light scattered by other atoms. The particles thus redistribute the field along the fiber which leads to effective interactions and forces between the particles. The interaction created by each frequency component of the pump light is long-range and depends on the distances between pairs of particles on the wavelength scale. Hence displacing one particle changes the overall fiber field and thus the forces acting on all other particles.

Similar long-range interactions and forces have been discussed already in a pioneering work by Chang et al. in [15]. There the focus was on resonant excitation and radiation pressure induced by internal transitions of an atom coupled to the waveguide. In line with our previous work [185] we will here allow for a very general form of mechanical interaction between the particles which can be achieved via frequency shaping of the

illumination light.
In our model the transverse pump field is a sum of many plane waves with different intensities and frequencies. We assume that the different spectral components are sufficiently distinct such that the interference terms are negligible as the individual components are spatially but not time-coherent and interactions average out in time. The effective pair forces between the particles in such a system can be calculated using a beamsplitter matrix model describing all the scattering processes by the particles [16]. Note that the particles in principle also back-scatter a fraction of the field propagating in the fiber. But since this contribution is typically very small and we assume weak coupling of the particles to the fiber field [15; 185] such that each particle reflects only a tiny fraction of the propagating fiber fields. Hence we neglect back-scattering effects and assume that the force on the particles arises solely due to interference effects of the fields scattered into the fiber from the transverse pump. This assumption generally works well for small particle numbers, but for large system sizes even a small reflection by each particle can lead to significant collective effects [9].
Within this approximation the radiation force F_j on a classical particle at position x_j can be written as a sum of effective two-particle forces $f_{\text{pair}}(x_i, x_j)$ between this particle and all the other particles at positions x_i [185]

$$F_j = \sum_{\substack{i=1 \\ i\neq j}}^{N} f_{\text{pair}}(x_i, x_j) = \sum_{\substack{i=1 \\ i\neq j}}^{N} \sum_k \frac{\sigma_{\text{sc}} I_k \cos\left(k\left(x_j - x_i\right)\right) \operatorname{sign}(x_i - x_j)}{c}, \tag{12.1}$$

with N the number of particles along the fiber, I_k the intensity of the field with frequency $\omega_k = k/c$ and σ_{sc} the scattering cross section between the particles and the beam.
Using this force we define a two-particle potential $u_{\text{pair}}(x_i, x_j)$ such that $f_{\text{pair}}(x_i, x_j) = -\partial_{x_j} u_{\text{pair}}(x_i, x_j)$. For a system of N particles the total potential is thus the sum of all two-particle interactions

$$U_{\text{tot}}(x_1, \ldots, x_N) = \frac{1}{2} \sum_{j=1}^{N} \sum_{\substack{i=1 \\ i\neq j}}^{N} u_{\text{pair}}(x_i, x_j) = \frac{1}{2} \sum_{j=1}^{N} \sum_{\substack{i=1 \\ i\neq j}}^{N} \sum_k \frac{\sigma_{\text{sc}} I_k}{ck} \sin\left(k|x_i - x_j|\right). \tag{12.2}$$

It is clear that any translation of one particle changes the light field along the fiber and thus the optical potential seen by all the other particles. The same result can be obtained following the model of Chang et al. [15] by taking the weak scattering limit

for far-detuned light. Eliminating the internal excited states of the particles then leads to the force given in Equation (12.1).
We studied such a system in a previous work [185] where we assumed classical point particles allowed to move freely along the fiber direction. Here we study locally trapped and very cold particles which requires a quantized description of motional degrees of freedom.
In the present model we thus consider particles trapped in harmonic potentials centered at positions $x_{j,0}$, $j = 1, \ldots, N$, $U_{\mathrm{HO}} = \sum_{i=1}^{N} m\omega_T \Delta_i^2/2$, with m the mass of the particles, ω_T the frequency of the harmonic oscillator traps and $\Delta_i = x_i - x_{i,0}$. We assume that the particles are tightly trapped in transverse direction and linearize the motion along the longitudinal motion of the particles in Equation (12.2) around the center of the harmonic oscillators $x_{i,0}$, $x_i \to x_{i,0} + \Delta_i$, with $k\Delta_i \ll 1$. We thus obtain an effective Hamiltonian

$$\hat{H} = \sum_k \frac{I_k \sigma_{\mathrm{sc}}}{c} \sum_{j=1}^{N} \left(\sum_{i=1}^{j-1} \left(\frac{1}{k} \sin\left(k d_{ij}\right) + \left(\Delta_j - \Delta_i\right) \cos\left(k d_{ij}\right) \right) - \sum_{i=1}^{N} \frac{k \left(\Delta_j - \Delta_i\right)^2}{4} \sin\left(k d_{ij}\right) \right) + \sum_{i=1}^{N} \left(\frac{P_i^2}{2m} + \frac{m\omega_T^2}{2} \Delta_i^2 \right), \quad (12.3)$$

with $d_{ij} = |x_{j,0} - x_{i,0}|$. We quantize the relative motion of the particles with respect to the trap centers by setting

$$\hat{\Delta}_i = \sqrt{\frac{\hbar}{2m\omega_T}} (\hat{a}_i + \hat{a}_i^\dagger) = \delta_0 (\hat{a}_i + \hat{a}_i^\dagger), \quad (12.4a)$$

$$\hat{P}_i = i \sqrt{\frac{\hbar m \omega_T}{2}} (\hat{a}_i^\dagger - \hat{a}_i) = \frac{i\hbar}{2\delta_0} (\hat{a}_i^\dagger - \hat{a}_i), \quad (12.4b)$$

with the oscillator length $\delta_0^2 = \hbar/(2m\omega_T)$.
Ignoring the constant terms in the Hamiltonian we thus obtain

$$\hat{H} = \hat{\tilde{H}}_{\mathrm{osc}} + \hat{H}_{\mathrm{int}} + \hat{H}_{\mathrm{rwa}} \quad (12.5a)$$

$$\hat{\tilde{H}}_{\mathrm{osc}} = \sum_{i=1}^{N} \hbar \left(\omega_T - \sum_{j=1}^{N} \sum_k \Omega_k \sin\left(k d_{ij}\right) \right) \hat{a}_i^\dagger \hat{a}_i = \sum_{i=1}^{N} \hbar \tilde{\omega}_i \hat{a}_i^\dagger \hat{a}_i \quad (12.5b)$$

$$\hat{H}_{\mathrm{int}} = \sum_{j=1}^{N} \sum_{i=1}^{N} \sum_k \hbar \Omega_k \sin\left(k d_{ij}\right) \hat{a}_j^\dagger \hat{a}_i \quad (12.5c)$$

$$\hat{H}_{\mathrm{rwa}} = \hbar \sum_{j=1}^{N} \left(\sum_{i=1}^{j-1} \sum_{k} \epsilon_k \cos\left(k d_{ij}\right) \left(\hat{a}_j + \hat{a}_j^\dagger - \hat{a}_i - \hat{a}_i^\dagger \right) \right.$$
$$\left. - \sum_{i=1}^{N} \sum_{k} \frac{\Omega_k}{2} \sin\left(k d_{ij}\right) \left(\hat{a}_j^2 + \hat{a}_j^{\dagger 2} - \hat{a}_j \hat{a}_i - \hat{a}_j^\dagger \hat{a}_i^\dagger \right) \right), \tag{12.5d}$$

with $\Omega_k := \sigma_{\mathrm{sc}} I_k \delta_0^2 k/(\hbar c)$ and $\epsilon_k := \sigma_{\mathrm{sc}} I_k \delta_0/(\hbar c)$. Here, $\hat{H}_{\mathrm{rwa}}$ generates force terms in the time evolution oscillating at the trapping frequency or higher, which typically cancel out when averaged over one period. Hence we will neglect them later in Section 12.3.2. Effectively they lead to a small displacement of the particles equilibrium and a change of the effective frequency of the oscillators (squeezing). $\hat{H}_{\mathrm{int}}$ describes the interactions between the particles and $\hat{\tilde{H}}_{\mathrm{osc}}$ the harmonic potential with shifted frequency $\tilde{\omega}_i$ due to the interaction of the particles.

12.2.2. Model assumptions and limitations

In our model we assume that the particles are harmonically trapped and we require that the transverse pump fields convey strong enough particle-particle interactions to influence the motion of the trapped particles along the fiber direction. At the same time the fields must be weak enough such that we can neglect saturation effects and eliminate any particle's internal degrees of freedom. In the following we study in some more detail how all these limiting conditions restrict the operating parameters.

The intensity of the light field scattered into the fiber by the particles depends on the incoming photon energy $\hbar\omega$ and flux, the emission rate into the fiber γ_{guid}, the effective mode cross section A of the fiber field and the excited state population ρ_{ee}. We approximate the particles as effective two-level systems and operate at low saturation by choosing large laser detuning $\Delta \gg \Gamma$ from atomic resonance, with Γ the decay rate. In this limit the excited state fraction is $\rho_{ee} \approx I_0/(2I_{\mathrm{sat}}(1 + 4\Delta^2/\Gamma^2)) \ll 1$, with I_0 the intensity of the incoming pump field and I_{sat} the saturation intensity.

The emission rate into the fiber depends on the spatial profile of the fiber field determining the field strength at the atomic position and on the atomic dipole matrix element. A single-mode fiber carries only the fundamental HE_{11} -mode. The explicit expression for the mode profiles are, for example, given in [32]. Here, we assume that the modes and the atomic dipoles are linear polarized perpendicular to the fiber axis. In this case the particles scatter the light symmetrically into the fiber. Using Fermi's

golden rule the emission rate into the fiber can be found with $\gamma_{\text{guid}} \approx 0.13\ \Gamma$, with $\Gamma = |\vec{d}|^2\omega^3/(3\pi\epsilon_0\hbar c^3)$ the free-space emission rate [47]. Usually γ_{guid} for atoms along a nanofiber is between $0.1 - 0.2\ \Gamma$ [47], but can be tuned up to $0.99\ \Gamma$ for quantum dots [50; 51] or superconductory transmon qubits [188]. Recently the coupling efficiency could be improved for atoms, when using a hole-tailored nanofiber and reached $0.6\ \Gamma$ [48]. The intensity scattered into the fiber by the particles can thus be estimated by

$$I_k = \frac{\hbar\omega}{A}\gamma_{\text{guid}}\rho_{\text{ee}} \approx \frac{1}{2}\frac{\hbar\omega}{A}\gamma_{\text{guid}}\frac{I_0/I_{\text{sat}}}{1+4\Delta^2/\Gamma^2}. \tag{12.6}$$

For a nanofiber with radius $r = 200$ nm, the fiber cross section area $A = r^2\pi$, the Cesium D2-line $\omega \approx 2.2 \cdot 10^{15}$ Hz with $\Gamma = 33 \cdot 10^6$ 1/s and the mass of Cesium $m \approx 220 \cdot 10^{-27}$ kg, and a detuning $\Delta = 100\ \Gamma$ we find that the intensity scattered into the fiber is $I_k \approx 6.2 \cdot 10^{-4}\ I_0/I_{\text{sat}}$ W/m^2.
To linearize the interaction potential we require a very deep potential such that the particles are well trapped $k\Delta_i \ll 1$. With $\Delta_i = \delta_0(a_i^\dagger + a_i)$ and $\delta_0 = \sqrt{\hbar/(2m\omega_T)}$, this means

$$k\delta_0 = \frac{\omega}{c}\sqrt{\frac{\hbar}{2m\omega_T}} \ll 1 \tag{12.7}$$

and we find

$$\omega_T \gg \frac{\omega^2}{c^2}\frac{\hbar}{2m}. \tag{12.8}$$

Using the parameters for the Cesium D2-line this implies $\omega_T \gg 10^5$ Hz.
Using these requirements we can compare the trapping potential H_T with the interaction arising from the transverse pump H_{pump}. Starting from the initial potential $\hat{H} = \hat{H}_{\text{pump}} + \hat{H}_T$ without any expansion

$$\hat{H} = \frac{1}{2}\sum_{j=1}^{N}\sum_{l=1}^{N}\frac{\sigma_{\text{sc}}I_k}{ck}\sin(kd_{jl}) + \sum_{j=1}^{N}\hbar\omega_T\hat{a}_j^\dagger\hat{a}_j, \tag{12.9}$$

we find $\hat{H}_{\text{pump}} \propto \sigma_{\text{sc}}I_k/(2kc)$ and $\hat{H}_T \propto \hbar\omega_T$. The scattering cross section can be approximated by the fiber cross section $\sigma_{\text{sc}} \approx A$. Inserting the intensity from Equation (12.6) and the boundary on the trapping frequency from Equation (12.8),

$$\frac{\hbar\omega_T}{\frac{\sigma_{\text{sc}}I_k}{2kc}} \approx \frac{4\omega_T}{\gamma_{\text{guid}}\rho_{\text{ee}}} = \frac{8\omega_T}{\gamma_{\text{guid}}}\frac{1+4\Delta^2/\Gamma^2}{I/I_{\text{sat}}} \gg \frac{8}{\gamma_{\text{guid}}}\left(\frac{\omega}{c}\right)^2\frac{\hbar}{2m}\frac{1+4\Delta^2/\Gamma^2}{I/I_{\text{sat}}}. \tag{12.10}$$

Using again the parameters for Cesium and setting $\rho_{ee} \approx 10^{-2}$ and $\omega_T \approx 10^6 Hz$ we get the condition $\hbar\omega_T / (\sigma_{sc} I_k/(2kc)) \gg 3$.
Assuming tightly trapped particles the interaction strength in the Hamiltonian (12.5a) is thus limited by

$$\Omega_k = \frac{\sigma_{sc} I_k \delta_0^2 \omega}{\hbar c^2} \ll \frac{\gamma_{guid} I/I_{sat}}{2(1+\Delta^2/\Gamma^2)}. \tag{12.11}$$

Using the parameters for Cesium as given above we find $\Omega_k \ll 10^5$ Hz.

12.3. Results

The Hamiltonian in Equation (12.5a) shows that we can design the effective interactions between the particles by choosing the intensities and frequencies of the incoming fields as well as the distances between the trapping positions of the particles. In the following section we show how this can be used to simulate a system where particles interact via some specific physical potential of choice. Here as a generic long range interaction we choose a Coulomb-type $1/r$ potential. In the later Sections 12.3.2 and 12.3.3 we discuss how this approach can be used to design quantum gates or how to entangle the motion of many particles.

12.3.1. Simulating Coulomb interactions between trapped quantum particles

The Hamiltonian in Equation (12.5a) can be used to simulate any symmetric two-body interaction. In the following example we will use the effective atom-atom interaction via the waveguide to mimic the Coulomb interaction between ions.
In principle one could tune the light fields to mimic a full Coulomb potential, but since $1/r$ is difficult to approximate in a Fourier series this would require a very large number of laser fields. However, if we assume that the ions are also harmonically trapped, we only have to tune the atom-light interaction to mimic the Coulomb interaction at the position of the trapped ions.
To simulate the Coulomb (or any other) potential we first linearize it around the trapping positions, quantize the motional degrees of freedom and then compare the terms with the Hamiltonian from Equation (12.5a). Using this concept one can even map higher-dimensional systems of interacting particles to our 1D-system.

Figure 12.2 shows an example, where we simulate the interaction between three ions distributed along a line by a system of particles along a nanofiber. The Coulomb potential V_{coul} of N interacting ions along a line of charge q_i at distances D_{ij} is given by

$$V_{\text{coul}} = \sum_{i=1}^{N} \sum_{j \neq i} \frac{1}{8\pi\epsilon_0} \frac{q_i q_j}{D_{ij}}. \tag{12.12}$$

Linearizing around their trapping position, quantizing the motional degrees of freedom and ignoring the constant terms we find for $q = q_i = q_j$.

$$\hat{H}_{\text{coul}} = \hat{\tilde{H}}_{\text{coul}_{\text{osc}}} + \hat{H}_{\text{coul}_{\text{int}}} + \hat{H}_{\text{coul}_{\text{rwa}}}, \tag{12.13a}$$

$$\hat{\tilde{H}}_{\text{coul}_{\text{osc}}} = \sum_{i=1}^{N} \hbar \left(\omega_T' + \frac{1}{8\pi\epsilon_0\hbar} \sum_{j \neq i} \frac{4q^2\delta_0'^2}{D_{ij}^3} \right) \hat{a}_i^\dagger \hat{a}_i, \tag{12.13b}$$

$$\hat{H}_{\text{coul}_{\text{int}}} = -\frac{1}{8\pi\epsilon_0} \sum_{i=1}^{N} \sum_{j \neq i} \frac{4q^2\delta_0'^2}{D_{ij}^3} \hat{a}_i^\dagger \hat{a}_j, \tag{12.13c}$$

$$\begin{aligned} \hat{H}_{\text{coul}_{\text{rwa}}} = \frac{1}{8\pi\epsilon_0} \sum_{j=1}^{N} \Bigg(& \sum_{i=1}^{j-1} \frac{-2q^2\delta_0'}{D_{ij}^2} \left(\hat{a}_j + \hat{a}_j^\dagger - \hat{a}_i - \hat{a}_i^\dagger \right) \\ & + \sum_{j \neq i} \frac{2\delta_0'^2 q^2}{D_{ij}^3} \left(\hat{a}_j^2 + \hat{a}_j^{\dagger 2} - \hat{a}_j \hat{a}_i - \hat{a}_j^\dagger \hat{a}_i^\dagger \right) \Bigg). \end{aligned} \tag{12.13d}$$

This Hamiltonian from Equation (12.13a) describes tightly trapped ions interacting via a Coulomb potential.

To simulate this system with particles interacting via a waveguide we compare the terms of H_{coul} with the Hamiltonian from Equation (12.5a). We find that the individual terms agree if we choose distances d_{ij}, wavenumbers k and interaction strengths Ω_k such that:

$$\frac{\delta_0'}{4\pi\epsilon_0\hbar\omega_T'} \frac{q^2}{D_{ij}^2} = -\sum_k \frac{\epsilon_k}{\omega_T} \cos(k d_{ij}), \tag{12.14a}$$

$$\frac{\delta_0'^2}{2\pi\epsilon_0\hbar\omega_T'} \frac{q^2}{D_{ij}^3} = -\sum_k \frac{\Omega_k}{\omega_T} \sin(k d_{ij}). \tag{12.14b}$$

Note, that the distances between the particles in our system, d_{ij}, are different from the distances in the simulated Coulomb system, D_{ij}. Also the harmonic trapping frequencies ω_T and ω_T' can be chosen independently.

For given distances d_{ij} and frequencies $k_l = k_0 + l\Delta_k$, Equations (12.14) become a set of linear equations for the interaction strengths $\Omega_l \equiv \Omega_{k_l}$. Choosing $D_{12} = D$ as a reference we define an interaction strength $\widetilde{\Omega}$ such that

$$\frac{q^2\delta_0'^2}{2\pi\epsilon_0\hbar\omega_T'}\frac{1}{D^3} = \frac{\widetilde{\Omega}}{\omega_T}. \tag{12.15}$$

Equations (12.14) then simplify to

$$\begin{aligned}\frac{D^3}{2D_{ij}^2} &= -\delta_0' \sum_l \frac{\epsilon_l}{\widetilde{\Omega}} \cos((k_0 + l\Delta_k)d_{ij}) \\ &= -\frac{\delta_0'}{\delta_0} \sum_l \frac{\Omega_l}{\widetilde{\Omega}(k_0 + l\Delta_k)} \cos((k_0 + l\Delta_k)d_{ij}), \qquad (12.16a)\\ \frac{D^3}{D_{ij}^3} &= -\sum_l \frac{\Omega_l}{\widetilde{\Omega}} \sin((k_0 + l\Delta_k)d_{ij}). \qquad (12.16b)\end{aligned}$$

These equations form a linear system of equations for the interaction strength depending on the intensities of the incoming fields. Consequently, we have two equations for every different distance D_{ij} and thus need the same number of fields. One way to solve this system is to assume that the particles are equally distributed with $d_{i,i+1} = 3\lambda_0/8$ and then choose the frequency spacing Δ_k such that the intensities I_k are positive. Although the fiber system is a 1D-system, one could even map 2D or 3D-systems on it. In this case we have $N \cdot N_D$ oscillators, with N the number of ions and N_D the number of dimensions. And in general this means we also need $N \cdot N_D$ particles in the simulation. Here the first N particles correspond to the interactions between the ions in the first dimension and the second N particles to the interactions in the second dimension and so on.

Figure 12.3 shows three ions arranged in an equilateral triangle. In this case we have $N_D = 2$ dimensions and $N = 3$ ions and thus need six particles along the fiber. The Coulomb potential then is given by

$$V_{\text{coul}} = \sum_{i=1}^{N} \sum_{i \neq j} \frac{1}{8\pi\epsilon_0} \frac{q_i q_j}{\sqrt{D_{ij_x}^2 + D_{ij_y}^2}}, \tag{12.17}$$

with D_{ij_x} and D_{ij_y} the distances between the ions in x and y-direction and $D_{ij}^2 = D_{ij_x}^2 + D_{ij_y}^2$. Here we have to linearize in the x as well as in the y direction. We assume

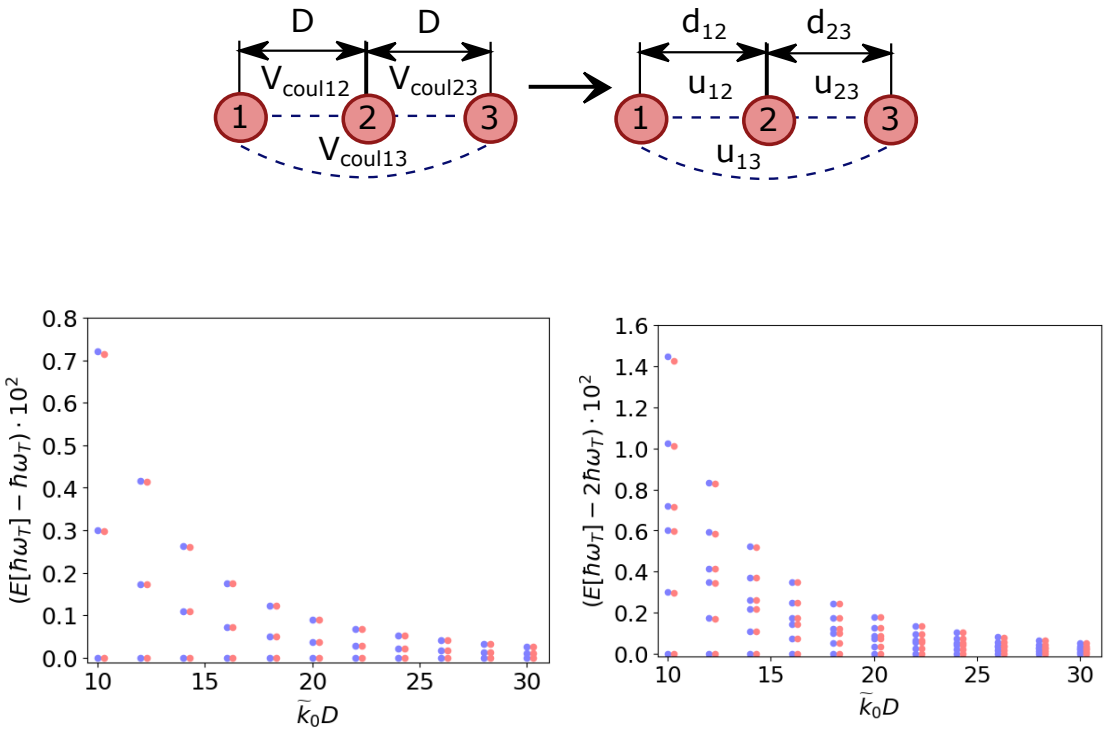

Figure 12.2.: We map three ions along a line, which interact via the Coulomb force separated at a distance D on a system of particles along a nanofiber, with distances d_{12} and d_{23}. This can be done by finding the right distances, frequencies and interactions strengths to solve Equations (12.16). The lower figures show the eigenenergies of these three harmonically trapped ions with Coulomb repulsion (blue) in comparison to particles trapped along the fiber with simulated interaction (red) as function of the distance between the interacting particles. In the simulation the particles are trapped along the fiber at fixed distances $d_{12} = d_{23} = 3/8\ \lambda_0$ and the pump laser parameters are adjusted to mimic Coulomb interaction at arbitrary distances between the ions. We use $\Delta_k = 0.7\ k_0$ and $\Omega_0/\widetilde{\Omega} = 0.34 + 1.07\ \widetilde{k}_0 D$, $\Omega_1/\widetilde{\Omega} = 1.16 + 1.34\ \widetilde{k}_0 D$, $\Omega_2/\widetilde{\Omega} = 1.68 + 1.58\ \widetilde{k}_0 D$, $\Omega_3/\widetilde{\Omega} = 0.74 + 1.4\ \widetilde{k}_0 D$, with $\widetilde{k}_0 = k_0 \delta_0/\delta_0'$. We define $\widetilde{\Omega}/\omega_T$ in a way so that every $\Omega_l/\omega_T < 0.004$ is restricted as required by Equation (12.11). So $\widetilde{\Omega}/\omega_T = \mathrm{Max}(\Omega_l/\widetilde{\Omega})/(0.004\widetilde{k}_0 D)^3$. The figure on the left side shows the energies corresponding to the first oscillator state and the right figure shows the energies corresponding to the second oscillator state.

that the oscillators in x and y directions have the same trapping frequency ω_T'. To reduce the number of equations, we here ignore the fast oscillating terms $\hat{H}_{\mathrm{coul_{rwa}}}$ and find

$$\hat{H}_{\mathrm{coul}} = \hat{\tilde{H}}_{\mathrm{coul_{osc}}} + \hat{H}_{\mathrm{coul_{int}}}, \tag{12.18a}$$

$$\begin{aligned}\hat{\tilde{H}}_{\mathrm{coul_{osc}}} = \sum_{i=1}^{N} \hbar \left(\omega_T' + \frac{1}{8\pi\epsilon_0\hbar}\sum_{j\neq i}\frac{4q^2\delta_0'^2}{D_{ij}^5}\right)\Bigg(\left(D_{ij_x}^2 - \frac{1}{2}D_{ij_y}^2\right)\hat{a}_{i_x}^\dagger\hat{a}_{i_x} \\ + \left(D_{ij_y}^2 - \frac{1}{2}D_{ij_x}^2\right)\hat{a}_{i_y}^\dagger\hat{a}_{i_y}\Bigg),\end{aligned} \tag{12.18b}$$

$$\begin{aligned}\hat{H}_{\mathrm{coul_{int}}} = -\frac{1}{8\pi\epsilon_0}\sum_{i=1}^{N}\sum_{j\neq i}\frac{4q^2\delta_0'^2}{D_{ij}^5}\Bigg(\left(D_{ij_x}^2 - \frac{1}{2}D_{ij_y}^2\right)\hat{a}_{i_x}^\dagger\hat{a}_{j_x} + \left(D_{ij_y}^2 - \frac{1}{2}D_{ij_x}^2\right)\hat{a}_{i_y}^\dagger\hat{a}_{j_y} \\ -\frac{3}{2}D_{ij_x}D_{ij_y}\left(\hat{a}_{i_x}^\dagger\hat{a}_{j_y} + \hat{a}_{i_x}\hat{a}_{j_y}^\dagger - \hat{a}_{i_x}\hat{a}_{i_y}^\dagger - \hat{a}_{i_x}^\dagger\hat{a}_{i_y}\right)\Bigg).\end{aligned} \tag{12.18c}$$

Defining an interaction strength $\widetilde{\Omega}$, $D = D_{12}$ and $k_l = k_0 + l\Delta_k$ as in Equation (12.15) we have to solve the following 15 equations

$$\frac{D^3}{D_{ij}^5}\left(D_{ij_x}^2 - \frac{1}{2}D_{ij_y}^2\right) = -\sum_l \frac{\Omega_l}{\widetilde{\Omega}}\sin((k_0 + l\Delta_k)d_{i_xj_x}), \tag{12.19a}$$

$$\frac{D^3}{D_{ij}^5}\left(D_{ij_y}^2 - \frac{1}{2}D_{ij_x}^2\right) = -\sum_l \frac{\Omega_l}{\widetilde{\Omega}}\sin((k_0 + l\Delta_k)d_{i_yj_y}), \tag{12.19b}$$

$$\frac{3}{2}\frac{D^3}{D_{ij}^5}D_{ij_x}D_{ij_y} = \sum_l \frac{\Omega_l}{\widetilde{\Omega}}\sin((k_0 + l\Delta_k)d_{i_xj_y}), \tag{12.19c}$$

$$\sum_j \frac{3}{2}\frac{D^3}{D_{ij}^5}D_{ij_x}D_{ij_y} = -\sum_l \frac{\Omega_l}{\widetilde{\Omega}}\sin((k_0 + l\Delta_k)d_{i_xi_y}). \tag{12.19d}$$

A special feature of such a mapping is that the interactions between specific pairs of particles can be individually tuned or even turned off as in Figure 12.3 for the particles at the bottom of the triangle. This allows one to implement any graph of interacting particles. Obviously such systems could not be implemented with actual ions. To show the validity of this mapping we calculate the eigenenergies of the waveguide system and compare them with the original Coulomb system (cf. Figure 12.2 for the ions along a line and Figure 12.4 for the ions ordered like a triangle). The energy levels of the oscillators split up due to the interaction between the particles. As long as the tight-binding condition for the ions is met, we find excellent agreement for all three systems. Note

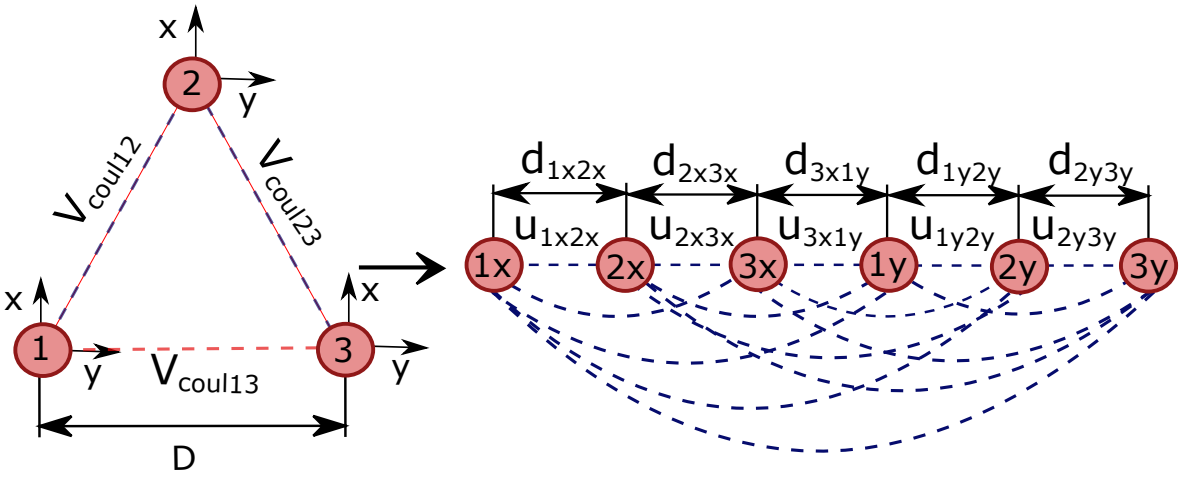

Figure 12.3.: We simulate the Coulomb interaction of three ions arranged in an equilateral triangle by a 1-D particle chain along a nanofiber. The first three particles correspond to the interaction in x-direction, while the next three particles correspond to the interaction in y-direction. In Fig. 12.4 we also show an example where the interaction between the ions number 1 and 3 is turned off.

that the frequencies to solve Equations (12.16) and (12.19) are distributed over a large spectrum between k_0 and 3.8 k_0 and k_0 and 5.3 k_0, respectively. But other methods to solve the equations might avoid this issue.

12.3.2. Bipartite quantum gates between distant particles

In the previous section we showed how changing the distances between the traps or the intensity and frequency of the incoming light fields allows one to tailor the interaction between the particles. Here we demonstrate how this can be used to design quantum gates.

Writing the Hamiltonian from Equation (12.5a) in an interaction picture we find that the terms $\propto \hat{a}_i,\ \hat{a}_i^\dagger$ oscillate with $\tilde{\omega}_i$ and the terms $\propto \hat{a}_i^2,\ \hat{a}_i^{\dagger 2},\ \hat{a}_j\hat{a}_i,\ \hat{a}_j^\dagger\hat{a}_i^\dagger$ oscillate even with $2\tilde{\omega}_i$, while the terms $\propto \hat{a}_j^\dagger\hat{a}_i,\ \hat{a}_j^\dagger\hat{a}_j$ do not oscillate. The rapidly oscillating terms average to zero and thus the Hamiltonian of Equation (12.5a) simplifies to

$$\hat{H}_{int} = \sum_{j=1}^{N}\sum_{i=1}^{N}\sum_{k}\hbar\Omega_k \sin\left(k|x_{j,0} - x_{i,0}|\right) a_j^\dagger a_i = \sum_{i,j=1}^{N}\hbar g_{ij} a_j^\dagger a_i, \tag{12.20}$$

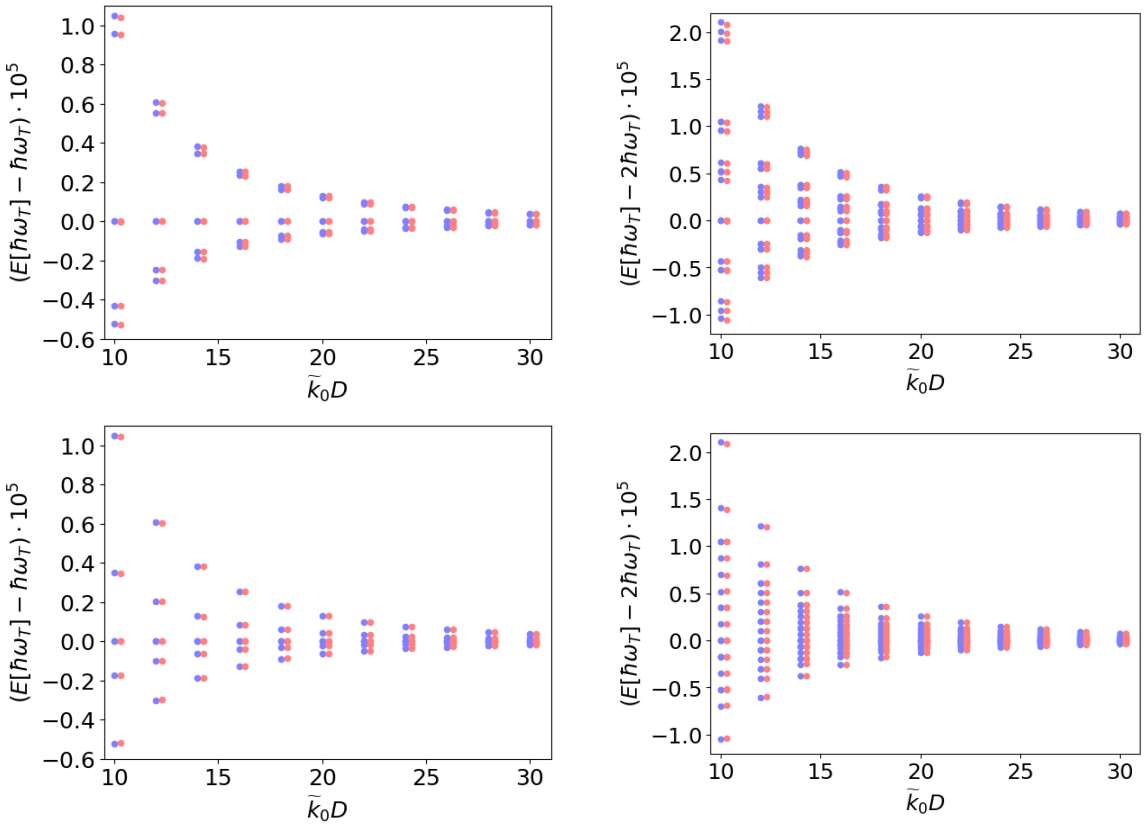

Figure 12.4.: Eigenenergies of three harmonically trapped ions with Coulomb repulsion ordered like a triangle (blue) in comparison to particles trapped along a fiber with light-induced interaction (red) as shown in Figure 12.3 as function of the distance between the interacting ions. This can be done by finding the right distances, frequencies and interactions strengths to solve Equations (12.19). In the simulation the particles are trapped along the fiber at fixed distances $d_{12} = d_{23} = 1/3\ \lambda_0$, $d_{34} = \lambda_0$ and $d_{45} = d_{56} = 1/4\ \lambda_0$ and the pump laser parameters are adjusted to mimic Coulomb interaction at arbitrary distances between the ions with $\Delta_k = 0.33\ k_0$. $\widetilde{k}_0$ and $\widetilde{\Omega}/\omega_T$ are defined as above in Figure 12.2. The figures in the upper row show the eigenenergies when all particles are interacting, while in the lower figures the interaction between ions number 1 and 3 at the bottom of the triangle is suppressed. The figures on the left side show the energies corresponding to the first oscillator state and the right figures show the energies corresponding to the second oscillator state. Data values can be found in the appendix in Table 12.1.

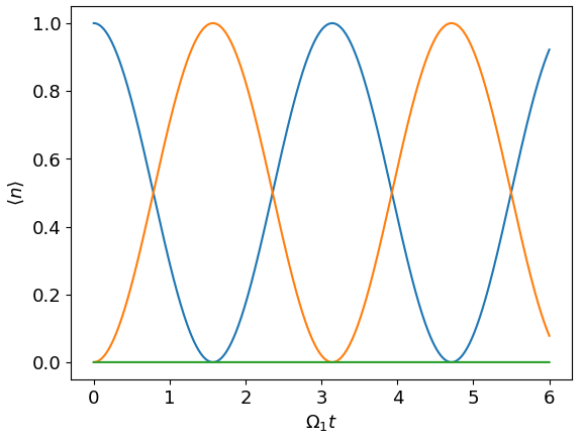

Figure 12.5.: Time evolution of the excited motional state occupation for three coupled particles. The blue line corresponds to the first particle, the orange line to the second particle and the green line to the third particle. We start from a state $|100\rangle$ where only the first particle is excited and set the distances to $d_{12} = 3/4\ \lambda_1$, $d_{23} = 7/8\ \lambda_1$, $k_2 = 4/3k_1$ and $\Omega_2 = 0.82\ \Omega_1$. Choosing these parameters, the interaction between the third and the other two particles can be turned off, while the first two particles still interact with each other.

with $\Omega_k = \sigma_{sc} I_k \delta_0^2/(\hbar k c)$ and $g_{ij} := \sum_k \Omega_k \sin(k d_{ij})$. Now it is obvious that the interaction between any particle pair i and j can be turned off by finding frequencies, positions and intensities such that the coupling g_{ij} vanishes. This is very important for gates as they should only act on special and not on all particles.
Figure 12.5 shows an example for three particles, where only two particles interact. Choosing the distances and frequencies with $k_l = k_0 + l\Delta_k$ with $\Delta_k < k_0$, we have to solve $N(N-1)/2$ equations, with N the number of the particles in the system and, thus, need $N(N-1)/2$ frequencies and intensities. Note, that the distances have to be chosen such that they are different for interacting and non-interacting pairs.

Using the two lowest oscillator states as qubit basis

The simplest way to map the harmonic oscillator to a qubit-system is to consider only the ground $|0\rangle$ and first excited state $|1\rangle$. As the Hamiltonian from Equation (12.20) is $\propto a_j^\dagger a_i$ the resulting dynamics do not leave the subspace of these two states. For the basis ($|0\rangle|0\rangle$, $|0\rangle|1\rangle$, $|1\rangle|0\rangle$ and $|1\rangle|1\rangle$), the states evolve with the time-evolution

operator $\hat{U}(t) = \exp(-i\hat{H}t/\hbar)$,

$$\hat{U}(t) = \begin{pmatrix} 1 & 0 & 0 & 0 \\ 0 & \cos(2gt) & -i\sin(2gt) & 0 \\ 0 & -i\sin(2gt) & \cos(2gt) & 0 \\ 0 & 0 & 0 & 1 \end{pmatrix}, \tag{12.21}$$

which is equivalent to a mapping

$$|0\rangle|0\rangle \to |0\rangle|0\rangle \tag{12.22a}$$
$$|0\rangle|1\rangle \to \cos(2gt)|0\rangle|1\rangle - i\sin(2gt)|1\rangle|0\rangle \tag{12.22b}$$
$$|1\rangle|0\rangle \to -i\sin(2gt)|0\rangle|1\rangle + \cos(2gt)|1\rangle|0\rangle \tag{12.22c}$$
$$|1\rangle|1\rangle \to |1\rangle|1\rangle \tag{12.22d}$$

In this case the states $|0\rangle|0\rangle$ and $|1\rangle|1\rangle$ are not affected by the interaction, but we see oscillations between $|0\rangle|1\rangle$ and $|1\rangle|0\rangle$.
After an interaction time such that $gt = \pi/4 + 2\pi n$, $n \in \mathbb{Z}$, $U(t)$ changes to

$$\hat{U}_{\text{SWAP}} = \begin{pmatrix} 1 & 0 & 0 & 0 \\ 0 & 0 & -i & 0 \\ 0 & -i & 0 & 0 \\ 0 & 0 & 0 & 1 \end{pmatrix}. \tag{12.23}$$

This corresponds to an i-SWAP gate, which swaps the states of the two particles and introduces a phase, if the two particles are in different states.
Similarly the square root of an i-SWAP-gate (SQiSW) can be implemented by choosing $g_{ij}t = \pi/8 + \pi n$, $n \in \mathbb{Z}$. Then $U(t)$ changes to

$$\hat{U}_{\text{SQiSW}} = \begin{pmatrix} 1 & 0 & 0 & 0 \\ 0 & \frac{1}{\sqrt{2}} & -\frac{i}{\sqrt{2}} & 0 \\ 0 & -\frac{i}{\sqrt{2}} & \frac{1}{\sqrt{2}} & 0 \\ 0 & 0 & 0 & 1 \end{pmatrix}. \tag{12.24}$$

$\hat{U}_{\text{SQiSW}}$ is a universal entangling gate and any quantum computation can be implemented using only single qubit rotations and the SQiSW-gate [177]. However note that

single qubit rotations cannot be implemented in the formalism described here as every interaction changes the state of (at least) two particles. One would thus need a separate mechanism to rotate the state of each particle individually.

Coherent states as computational basis

As our individual quantum systems are oscillators we can go beyond the two-state approximations and also use higher excited motional states as computational basis. One particularly useful approach, which has been put forward and intensively studied for photons, is the use of coherent states as qubits. Typically the computational basis is then a pair of coherent states $|-\alpha\rangle,\ |+\alpha\rangle$ [189–192],

$$|\alpha\rangle = \sum_{i=0}^{\infty} e^{-\frac{|\alpha|^2}{2}} \frac{\alpha^i}{\sqrt{i!}} |i\rangle, \tag{12.25}$$

with complex amplitude α. Although the two states are not perfectly orthogonal, the overlap between $|+\alpha\rangle$ and $|-\alpha\rangle$ is negligibly small for sufficiently large $|\alpha|$. For example,

$$|\langle +\alpha|-\alpha\rangle|^2 = e^{-4|\alpha|^2} \approx 0.018, \tag{12.26}$$

for amplitudes as small as $\alpha = 1$. In this basis quantum calculations can be performed relatively loss and fault tolerant [191] and it turns out that all relevant two qubit interactions can be based on the so-called beamsplitter coupling between two sites [192]. The interaction is then simply given by $U(t) = \exp\left(i\theta/2\left(\hat{a}_1^\dagger \hat{a}_2 + \hat{a}_1 \hat{a}_2^\dagger\right)\right)$, with θ the polarization angle between the two interacting beams. It turns out that this is just the dominant term of light scattering interaction (12.20) which can be well controlled in strength, time and space.
The subset of coherent states $\{|\alpha\rangle|\alpha'\rangle\}$, with $|\alpha| = |\alpha'|$ evolves as

$$e^{i\hat{H}_{int}t/\hbar}|\alpha\rangle|\alpha'\rangle = |\alpha\cos(gt) + i\alpha'\sin(gt)\rangle|\alpha'\cos(gt) + i\alpha\sin(gt)\rangle. \tag{12.27}$$

such that

$$|-\alpha\rangle|-\alpha\rangle \to |-e^{igt}\alpha\rangle|-e^{igt}\alpha\rangle \tag{12.28a}$$
$$|-\alpha\rangle|+\alpha\rangle \to |-e^{-igt}\alpha\rangle|e^{-igt}\alpha\rangle \tag{12.28b}$$
$$|+\alpha\rangle|-\alpha\rangle \to |e^{-igt}\alpha\rangle|-e^{-igt}\alpha\rangle \tag{12.28c}$$
$$|+\alpha\rangle|+\alpha\rangle \to |e^{igt}\alpha\rangle|e^{igt}\alpha\rangle \tag{12.28d}$$

A more detailed calculation of this evolution can be found in the Appendix 12.5.2. As discussed in [191], this evolution corresponds to a beamsplitter interaction for photonic states. There it is also discussed that one can use this and a single-qubit rotation to implement a CNOT gate.
In contrast to what we found in Equation (12.22), we here see that the state $|-\alpha\rangle|-\alpha\rangle$ can be flipped to $|+\alpha\rangle|+\alpha\rangle$ and vice versa. Note also that the coherent qubits evolve outside the subspace $\{|+\alpha\rangle, |-\alpha\rangle\}$ for $gt \neq n\pi$.

12.3.3. Entanglement propagation via controlled long-range interaction

The discussion above focused on entangling any two particles in a larger system using quantum gates realized by two-particle-gates. Here we shall briefly investigate how a larger number of particles can be entangled.
If we only have a single pump field of frequency k_0 and put all particles at equal distance $n\pi k_0$, with arbitrary integer n, then no particle will interact with any other particle as $\sin(k_0 d_{ij}) = 0$. If we now displace one particle by $\zeta \neq n\pi k_0$, this particle starts to interact with all other particles, but there are still no direct interactions between the remaining particles.
But as shown in Figure 12.6, this is sufficient to create an effective all-to-all interaction. There we have three particles where the first and the second particle do not interact directly, but both interact with the third particle.
This is demonstrated using the mutual von-Neumann entropy,

$$S_i = -\mathrm{tr}\left(\rho_i \ln \rho_i\right), \tag{12.29}$$

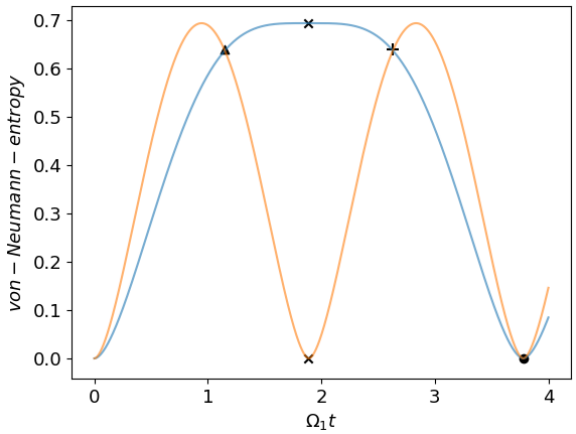

Figure 12.6.: Entanglement buildup for three coupled particles as a function of time with $d_{12} = \lambda_0/2$ and $d_{23} = (1/2 + 0.1)\,\lambda_0$ for the initial state $|001\rangle$. The two curves show the entanglement entropy of the subsystem containing particles 2 and 3 (blue) and the subsystem containing particles 1 and 2 (yellow). So, the blue line describes the entanglement between the subsystem containing particle 1 and the subsystem containing particles 2 and 3, and the yellow line between the subsystem containing particle 3 and the subsystem containing particles 1 and 2. (▲) corresponds to the state $1/\sqrt{3}\,(|001\rangle - i|010\rangle + i|100\rangle)$, (×) to the state $1/\sqrt{2}\,(|01\rangle - |10\rangle)\,|0\rangle$ and (+) to the state $\frac{1}{\sqrt{3}}\,(-|001\rangle + i|010\rangle - i|100\rangle)$ and (•) to the state $-|001\rangle$.

with ρ_i being the reduced density matrix of the subsystem i.
In the left plot of Figure 12.6 we start with a pure state, $|001\rangle$. But after a time such that $\cos\left(2\sqrt{2}\Omega_1 \sin(k\zeta)\, t\right) = 1/\sqrt{3}$, indicated by the triangle, all three particles are entangled. Later, at the time indicated by the (×), particle one and two are maximally entangled with each other, but disentangled from the third particle.

12.3.4. State read out via the outgoing fiber fields

In the previous chapters we discussed how the motional states of the particles can be manipulated, but how would such a manipulation be measured?
The fields leaving the fiber at the left and right edges contain information about the states of the particles in the system and by measuring the outgoing intensities one can determine the states of the particles.
Following the beamsplitter matrix formalism introduced in [16] we find for the amplitudes of the outgoing fields to the left $E_-(x_1)$ and to the right $E_+(x_N)$ of a system with N

particles ,

$$E_-(x_1) = \sum_k \sum_{i=1}^{N} \sqrt{\frac{I_k}{c\epsilon_0}} e^{ik(x_i - x_1)}, \tag{12.30a}$$

$$E_+(x_N) = \sum_k \sum_{i=1}^{N} \sqrt{\frac{I_k}{c\epsilon_0}} e^{ik(x_N - x_i)}. \tag{12.30b}$$

As the particles are well trapped we can linearize these amplitudes as we did for the Hamiltonian and find

$$\begin{aligned}\hat{E}_-(x_1) = \sum_k \sum_{i=1}^{N} \sqrt{\frac{I_k}{c\epsilon_0}} \Big(& e^{ik(x_i - x_1)} + ik\delta_0 e^{ik(x_i - x_1)} \left(\hat{a}_i + \hat{a}_i^\dagger - \hat{a}_1 - \hat{a}_1^\dagger\right) \\ & - \frac{1}{2} k^2 \delta_0^2 e^{ik(x_i - x_1)} \left(\hat{a}_i + \hat{a}_i^\dagger - \hat{a}_1 - \hat{a}_1^\dagger\right)^2 \Big),\end{aligned} \tag{12.31a}$$

$$\begin{aligned}\hat{E}_+(x_N) = \sum_k \sum_{i=1}^{N} \sqrt{\frac{I_k}{c\epsilon_0}} \Big(& e^{ik(x_N - x_i)} + ik\delta_0 e^{ik(x_N - x_i)} \left(\hat{a}_N + \hat{a}_N^\dagger - \hat{a}_i - \hat{a}_i^\dagger\right) \\ & - \frac{1}{2} k^2 \delta_0^2 e^{ik(x_N - x_i)} \left(\hat{a}_N + \hat{a}_N^\dagger - \hat{a}_i - \hat{a}_i^\dagger\right)^2 \Big).\end{aligned} \tag{12.31b}$$

This way we can calculate the expectation vales for amplitudes and intensities for any given particle state.
Figure 12.7 shows an example for the outgoing intensity expectation values for three particles. It confirms that the outgoing intensity depends on the states of the particles. Here, the states $|100\rangle$ and $|011\rangle$ cannot be distinguished in the left outgoing intensity, I_-, but they can be distinguished in I_+.
In Figure 12.8 we plot the outgoing intensity for the initial conditions as above in Figure 12.6. From the outgoing intensity we can learn which particles are entangled and which are not.

12.4. Discussion

Mechanical interactions of particles trapped in the vicinity of an optical nanofiber can be controlled in a versatile form by choosing the properties of incoming transverse pump light. Using spatial and spectral light shaping of the illumination lasers the interactions between the particles can be tailored to simulate a wide class of interaction potentials between the particles.

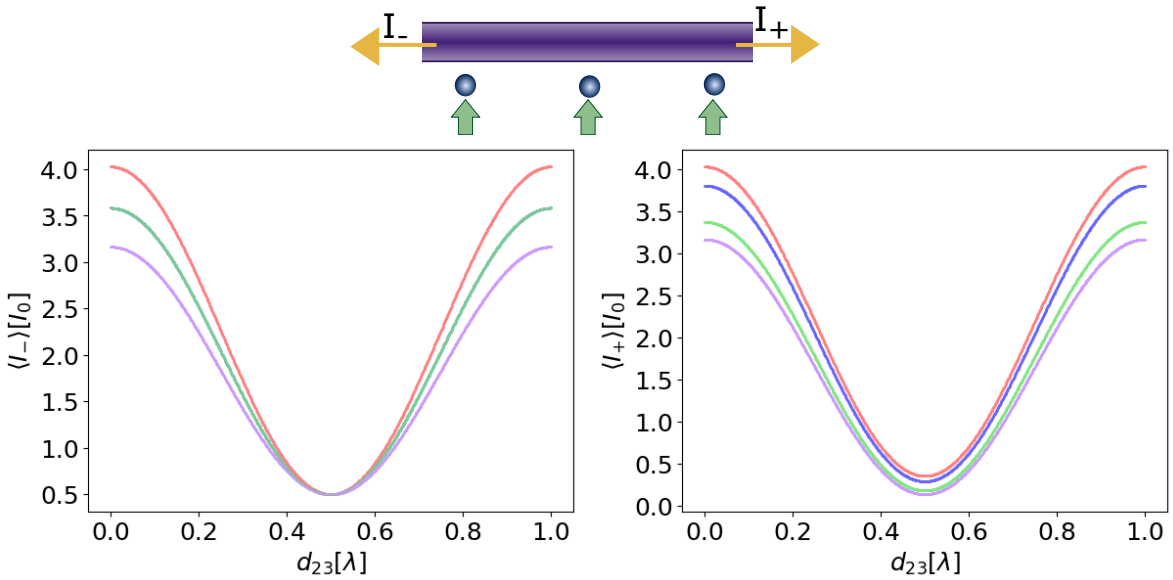

Figure 12.7.: State-dependent light intensities emitted from the fiber to the left I_- and to the right I_+ for a system with three particles. Here the distance between the first two particles stays constant with $d_{12} = \lambda_0$, while we vary the position of the third particle. Red lines correspond to the ground state $|000\rangle$, blue lines to the a single excited state $|100\rangle$, green lines to a doubly excited state $|011\rangle$ and purple lines corresponds to the state $|111\rangle$. Note, that in the left figure the green and blue line overlap.

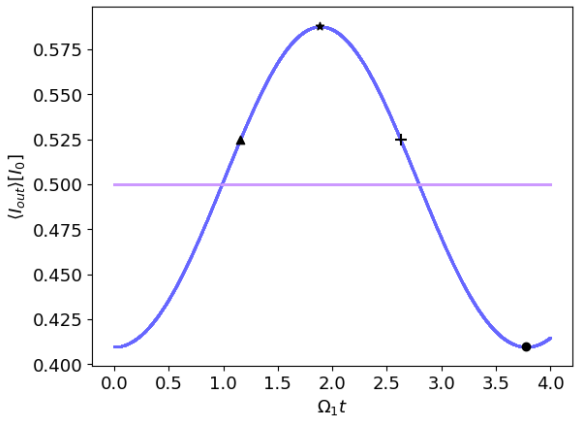

Figure 12.8.: Average output power I_- emitted on the left side of the fiber and I_+ on the right side for a system of two particles as a function of time. The initial condition is the same as in Figure 12.6. We start with the state $|001\rangle$ and the particles are placed at a distance $d_{12} = 1/2\lambda_0$ and $d_{23} = (\frac{1}{2} + 0.1)\lambda_0$. The blue line corresponds to the outgoing intensity to the left side $\langle I_-\rangle$ and the purple line to the (constant) outgoing intensity to right $\langle I_+\rangle$. (▲) corresponds to the state $\frac{1}{\sqrt{3}}(|001\rangle - i|010\rangle + i|100\rangle)$, (⋆) to the state $\frac{1}{\sqrt{2}}(|01\rangle - |10\rangle|\,0\rangle$, (+) to the state $\frac{1}{\sqrt{3}}(-|001\rangle + i|010\rangle - i|100\rangle)$ and (·) to $-|001\rangle$

Here we studied the low temperature limit using a quantum mechanical description of the particle motion along the fiber direction at the trap sites and couple the particles via a nonlocal interaction through collective coherent light scattering into the fiber. We demonstrate that this system can be used to simulate, for example, Coulomb interactions between harmonically trapped particles with high precision. The idea can be extended in a straightforward manner beyond linear equidistant chains to effectively mimic a very general class of geometries including 2D-configurations. Using time dependent laser illumination one can even turn on and off specific interactions between arbitrary particle pairs simultaneously. By monitoring the spectrum and intensity of the light scattered out of the fiber ends ample information on the particle motion can be extracted in a minimally invasive way.

As another natural application the system offers variable possibilities to design two-qubit-gates, using not only oscillator eigenstates but also coherent states as computational basis. The virtually infinite range of the fiber mediated interaction should allow to implement larger systems of many qubits, without the requirement of closely spaced trapping sites allowing independent pairwise addressing control of quantum gates. As generic examples we studied the preparation of multi partite entangled states by placing the particles at specific positions with respect to the illumination lasers. Again, monitoring the outgoing intensity at the fiber ends allows to continuously determine key properties of the collective motional states of the particles with minimal perturbation of the entanglement properties.

Although in our example we used a very simplified model system, it provides strong evidence that fiber coupled atoms could be a powerful, very versatile and scalable tool for quantum simulation as well as quantum computation. Certainly there are technical challenges to be met as e.g. ensuring sufficient radial confinement and cooling. In a more precise model one should also include back scattering inside the fiber and chirality related scattering control [55–57; 193; 194]. This on the one hand could be very challenging to calculate but on the other hand a very promising extension towards even further control possibilities of this system.

12.5. Appendix

12.5.1. Data values for Figure 12.4

Here we list the distances, frequencies and interaction strengths used to create Figure 12.4 for different shapes of interacting ions.

Table 12.1.: Data values for Figure 12.4

	Triangle	**Triangle with suppressed interactions**
$\Omega_0/\widetilde{\Omega}$	251.5	251.4
$\Omega_1/\widetilde{\Omega}$	643	642.6
$\Omega_2/\widetilde{\Omega}$	580.5	580.1
$\Omega_3/\widetilde{\Omega}$	72	72
$\Omega_4/\widetilde{\Omega}$	0	0
$\Omega_5/\widetilde{\Omega}$	666.2	665.8
$\Omega_6/\widetilde{\Omega}$	1149.7	1149.1
$\Omega_7/\widetilde{\Omega}$	754.3	754.3
$\Omega_8/\widetilde{\Omega}$	104.7	104.8
$\Omega_9/\widetilde{\Omega}$	115.5	115.3
$\Omega_{10}/\widetilde{\Omega}$	591.3	590.8
$\Omega_{11}/\widetilde{\Omega}$	724.8	724.5
$\Omega_{12}/\widetilde{\Omega}$	392.4	392.4
$\Omega_{13}/\widetilde{\Omega}$	81.2	81.3

12.5.2. Time evolution of the coherent states

In this section we go into more details on how the time evolution of coherent states $|\alpha\rangle|\alpha'\rangle$

$$\hat{U}(t)|\alpha\rangle|\alpha'\rangle = e^{-igt\left(\hat{a}_1\hat{a}_2^\dagger+\hat{a}_1^\dagger\hat{a}_2\right)}|\alpha\rangle|\alpha'\rangle, \tag{12.32}$$

with $\alpha,\ \alpha'$ taking values of $\pm\alpha$ can be calculated.

Using the definition of a coherent state, the facts that $\hat{U}(t)|00\rangle = |00\rangle$ and that $\hat{U}(t)$ is unitary, we can rewrite this equation

$$\hat{U}(t)|\alpha\rangle|\alpha'\rangle = e^{-\frac{|\alpha|^2+|\alpha'|^2}{2}} \sum_{m,n=0}^{\infty} \frac{\alpha^m\alpha'^n}{\sqrt{m!n!}} \left(\hat{U}(t)\hat{a}_1^\dagger\hat{U}^\dagger(t)\right)^m \left(\hat{U}(t)\hat{a}_2^\dagger\hat{U}^\dagger(t)\right)^n |00\rangle. \tag{12.33}$$

To evaluate $\hat{B}_i(t) := \hat{U}(t)\hat{a}_i^\dagger\hat{U}^\dagger(t)$ we use

$$\frac{d}{dt}\hat{B}_i(t) = ig\hat{U}(t)\left[\hat{a}_1^\dagger\hat{a}_2 + \hat{a}_1\hat{a}_2^\dagger, \hat{a}_i^\dagger\right]\hat{U}^\dagger(t) = ig\hat{A}_j, \tag{12.34}$$

for $j \neq i$. The solution of this system of differential equations is

$$\hat{A}_i = \hat{a}_i^\dagger\cos(gt) + i\hat{a}_j^\dagger\sin(gt). \tag{12.35}$$

This way the sum in Equation (12.33) can be rewritten to

$$\begin{aligned}\sum_{m,n=0}^{\infty}\frac{\alpha^m\alpha'^n}{\sqrt{m!n!}}&\left(\hat{a}_1^\dagger\cos(gt) + i\hat{a}_2^\dagger\sin(gt)\right)^m\left(i\hat{a}_1^\dagger\sin(gt) + \hat{a}_2^\dagger\cos(gt)\right)^n|00\rangle\\ &= e^{\alpha\left(\hat{a}_1^\dagger\cos(gt)+i\hat{a}_2^\dagger\sin(gt)\right)}e^{\alpha'\left(i\hat{a}_1^\dagger\sin(gt)+\hat{a}_2^\dagger\cos(gt)\right)}|00\rangle\\ &= e^{\hat{a}_1^\dagger(\alpha\cos(gt)+i\alpha'\sin(gt))}e^{\hat{a}_2^\dagger(\alpha' i\sin(gt)+\alpha\cos(gt))}|00\rangle\end{aligned} \tag{12.36}$$

As $e^{-\alpha^\star(i\hat{a}\sin(gt)+\hat{a}\cos(gt))}|0\rangle = |0\rangle$ and the displacement operator is defined as $\hat{D}(\alpha) = e^{-|\alpha|^2/2}e^{\alpha\hat{a}^\dagger}e^{-\alpha^\star\hat{a}}$, with $D(\alpha)|0\rangle = |\alpha\rangle$ we find the desired result

$$\begin{aligned}\hat{U}(t)|\alpha\rangle|\alpha'\rangle &= \hat{D}_1\left(\alpha\cos(gt) + i\alpha'\sin(gt)\right)\hat{D}_2\left(\alpha'\cos(gt) + i\alpha\sin(gt)\right)|0\rangle|0\rangle\\ &= |\alpha\cos(gt) + i\alpha'\sin(gt)\rangle|\alpha'\cos(gt) + i\alpha\sin(gt)\rangle.\end{aligned} \tag{12.37}$$

Contributions: Conceptualization, D.H.; methodology, D.H., M.S. and H.R.; formal analysis, D.H.; investigation, D.H.; writing-original draft preparation, D.H. and M.S.; writing-review and editing, D.H., M.S. and H.R.; visualization, D.H.; supervision, M.S. and H.R.; project administration, H.R. All authors have read and agreed to the published version of the manuscript.

Acknowledgements: D.H. was funded by a DOC Fellowship of the Austrian Academy of Sciences ÖAW and H.R. acknowledges support from the FET Network Cryst3 funded by the European Union (EU) via Horizon 2020.

13. Additional calculations

13.1. Approximation of the eigenvalues and eigenvectors using perturbation theory

The transverse pump field only has a tiny effect on the particles in the deep harmonical oscillator trap. So let us treat this effect as a small perturbation. As we exactly know the eigenvalues and eigenvectors of the harmonical oscillators we can use perturbation theory to approach the eigenvalues and eigenvectors of the whole system.

13.1.1. Perturbation on the ground state

The ground state of the harmonic oscillator Hamiltonian

$$H_0 = \sum_i \hbar\omega_T a_i^\dagger a_i, \tag{13.1}$$

is the Fock state $|g^0\rangle = \bigotimes_{i=1}^N |0\rangle$ with eigenvalues $E_n^0 = 0$ [195].
The Hamilton operator describing the perturbation 12.5a is

$$H_1 = \sum_{j=1}^{N} \left(\sum_{i=1}^{j-1} \sum_k \epsilon_k \cos\left(kd_{ij}\right) \left(a_j + a_j^\dagger - a_i - a_i^\dagger\right) \right.$$
$$\left. - \sum_{i=1}^{N} \sum_k \Omega_k \sin\left(kd_{ij}\right) \left(a_j^\dagger a_j - a_j^\dagger a_i + \frac{1}{2}\left(a_j^2 + a_j^{\dagger 2} - a_j a_i - a_j^\dagger a_i^\dagger\right)\right)\right). \tag{13.2}$$

So it follows

$$H = H_0 + \lambda H_1, \tag{13.3a}$$
$$H|n\rangle = E_n|n\rangle, \tag{13.3b}$$

with λ a small real parameter so that $H_0 \ll \lambda H_1$ and eigenstates and eigenvalues of H, $|n\rangle$ and E_n.
For the perturbation in first order of our model we find

$$E_n^1 = \langle g^0|H_1|g^0\rangle = 0, \tag{13.4}$$

$$\begin{aligned}|n^1\rangle &= \sum_{m\neq n} \frac{\langle m^0|H_1|g^0\rangle}{E_n^0 - E_m^0}|m^0\rangle \\ &= -\sum_{j=1}^{N}\sum_{i=1}^{j-1}\sum_k \frac{\epsilon_k}{\omega_T}\cos\left(kd_{ij}\right)\left(\bigotimes_{l=1,l\neq j}^{N}|0\rangle^l|1\rangle^j - \bigotimes_{l=1,l\neq i}^{N}|0\rangle^l|1\rangle^i\right) \\ &+ \sum_{j=1}^{N}\sum_{i=1}^{N}\sum_k \frac{\Omega_k \sin(kd_{ij})}{4\omega_T}\left(\sqrt{2}\bigotimes_{l=1,l\neq j}^{N}|0\rangle^l|2\rangle^j - \bigotimes_{l=1,l\neq i,j}^{N}|0\rangle^l|1\rangle^i|1\rangle^j\right)\end{aligned} \tag{13.5}$$

and for the perturbation in second order

$$\begin{aligned}E_n^2 &= \sum_{m\neq n}\frac{|\langle m^0|H_1|n^0\rangle|^2}{E_n^0 - E_m^0} \\ &= -\frac{\hbar}{\omega_T}\sum_{j=1}^{N}\left(\sum_{i=1}^{j-1}\sum_k \epsilon_k\cos(kd_{ij}) - \sum_{i=j+1}^{N}\sum_k \epsilon_k\cos(kd_{ij})\right)^2 \\ &- \frac{\hbar}{4\omega_T}\sum_{j=1}^{N}\left(\sum_{i=1}^{N}\sum_k \Omega_k\sin(kd_{ij})\right)^2 - \frac{\hbar}{2\omega_T}\sum_{j=1}^{N}\sum_{i=1}^{j-1}\left(\sum_k \Omega_k\sin(kd_{ij})\right)^2.\end{aligned} \tag{13.6}$$

The perturbation in first order leads to new excited states, even to doubly excited states, and the eigenvalues in second order to a small energy shift compared to the oscillator potential.
Let us discuss this perturbation for two particles

$$|n\rangle \approx |00\rangle + \frac{\sum_k \epsilon_k\cos\left(kd\right)}{\omega_T}\left(|10\rangle - |01\rangle\right) + \frac{\sum_k \Omega_k\sin(kd)}{4\omega_T}\left(\sqrt{2}\left(|20\rangle + |02\rangle\right) - 2|11\rangle\right), \tag{13.7}$$

and

$$E_n \approx -\frac{\hbar}{\omega_T}\left(2\left(\sum_k \epsilon_k\cos(kd)\right)^2 + \left(\sum_k \Omega_k\sin(kd)\right)^2\right). \tag{13.8}$$

As the two particle case is the simplest one we can use it to discuss how the transverse pump affects the system. By changing the distance d and using several frequencies we can manipulate the states of the particles. As $\sum_k \epsilon_k \cos(kd)$ is just the cosine-part of a Fourier series we can generate several symmetric functions by using special intensities and frequencies. Then the part $\sum_k \Omega_k \sin(kd)$ is just the derivative of this Fourier series. So these two parts can be tailored by choosing a function which has the needed values at a special position of the function and of its derivative. We can adjust every pairwise interaction by choosing $2\left(\sum_{i=1}^{N-1} i - (N-1)\right)$ frequencies and the distances between the particles.

Part IV.

Forces and self-ordering of nanoparticles moving on multimode optical fibres

14. Introduction

Up to now we have only considered single mode nanofibres. When also allowing higher order modes to propagate along the fibre the coupling between the fibre field and the particles is enhanced and the individual particles can be controlled easier. As a consequence we then also have to consider scattering between different modes. Such scattering processes can be described by a tritter scattering-matrix approach [196]. The scattering between the different fibre modes can even induce a stationary tractor force against the injection direction when directly launching light from one direction into the fibre.

15. Publication

Nonlinear force dependence on optically bound micro-particle arrays in the evanescent fields of fundamental and higher order microfibre modes

Aili Maimaiti, Daniela Holzmann[1], Viet Giang Truong, Helmut Ritsch and Síle Nic Chormaic

Particles trapped in the evanescent field of an ultrathin optical fibre interact over very long distances via multiple scattering of the fibre-guided fields. In ultrathin fibres that support higher order modes, these interactions are stronger and exhibit qualitatively new behaviour due to the coupling of different fibre modes, which have different propagation wave-vectors, by the particles. Here, we study one dimensional longitudinal optical binding interactions of chains of 3 μm polystyrene spheres under the influence of the evanescent fields of a two-mode microfibre. The observation of long-range interactions, self-ordering and speed variation of particle chains reveals strong optical binding effects between the particles that can be modelled well by a tritter scattering-matrix approach. The optical forces, optical binding interactions and the velocity of bounded particle chains are calculated using this method. Results show good agreement with finite element numerical simulations. Experimental data and theoretical analysis show that higher order modes in a microfibre offer a promising method to not only obtain stable, multiple particle trapping or faster particle propulsion speeds, but that they also allow

[1]D.H. and H.R. carried out the theoretical analyses in this publication, A.M. did the experiment, A.M. and V.G.T contributed to the experimental data analyses and the numerical simulations, S.N.C. and H.R. contributed in an advisory role.

for better control over each individual trapped object in particle ensembles near the microfibre surface.

Scientific Reports 6, 30131(2016) doi:10.1038/srep30131

15.1. Introduction

Optical trapping with a tightly focussed laser beam was first reported by Ashkin et al. [3]. Following this early work, optical tweezers have been widely used and further developed to provide stable trapping and manipulation of small objects [197]. Shortly after Ashkin et al.'s pioneering work, the self-ordered distribution of particles in the maxima of an optical lattice formed by the interference of up to five beams was demonstrated by Burns et al. [92]. This multi-particle self-arrangement was attributed to the electromagnetic field redistribution caused by each particle due to the presence of neighbouring particles. The observed effect was termed "optical binding". More than a decade later, the observation of long-range, one dimensional (1D) longitudinally optically bound chains of microparticles in the field of two weakly-focussed counter propagating Gaussian [198] and non-diffracting Bessel beams [199] was reported. In those works, the net scattering force from each beam was cancelled out and the coherently scattered light from each trapped particle interfered to create attractive or repulsive forces between the particles. The balance between these forces of the dispersed particles caused them to re-arrange their positions with preferential interparticle spacings that were roughly equal to several times the particle diameter. Following this, there have been many theoretical and experimental studies explaining this scattered field interaction with regard to dielectric objects [74; 200–204], cells [205] in free space beams [74; 200; 201], as well as in the evanescent fields of prisms [202; 203] and waveguides [204–206].

Unlike a 3D optical binding geometry - where the interaction between the trapped objects rapidly decays with distance - long-range, strong binding interactions can be realised if scattered polarisable particles are spatially confined in a 1D geometry [69]. In certain circumstances it could provide ultrastrong and self-consistent traps for small particles, or even atomic ensembles, if the light fields are optically confined to resonators [70] or waveguides [15; 16]. Along with the use of prisms to generate evanescent fields, optical micro/nanofibres (MNFs) are attractive alternatives [207–209]. The tightly confined optical fields at the waist regions of MNFs make them distinctly valuable for a wide range of applications such as propelling dielectric and biological particles in liquid dispersion [210–212], particle sorting [213] and cold atom characterisation, trapping and detection [34; 214–217].

Recently, Frawley et al. reported on optical binding of silica spheres on the surface of a nanofibre [114]. The discussion focussed on how a fundamental fibre mode (FM) can

interact with surrounding objects, causing mutual interactions between them. There have been several theoretical proposals on using the first group of higher order fibre modes (HOMs) for particle trapping and detection, particularly in relation to cold atoms [218–221]. Here, HOMs imply the coexistence of true TE_{01}, TM_{01} and $HE_{21o,e}$ modes of a fibre, also referred to as the first order linearly polarised (LP_{11}) mode family. Preliminary experimental studies on the interaction of nanofibre HOMs with cold atoms [222] and particle manipulation [223] have been published. These works illustrate the advantages of HOM-supporting MNFs, such as achievable higher field amplitudes, larger field extensions from the fibre surface and a larger fibre taper cut-off diameter compared to that needed for FM propagation. Most importantly, the 3D geometries that can be obtained from the interference of co-propagating HOMs and FMs could facilitate studies in the retrieval and storage of orbital angular momentum of light in atomic ensembles near an MNF surface.

While previously published work has shown that the speed of single particles for HOM compared to FM propagation is increased [223], our recent study on two-particle binding in a HOM [224] field manifested new phenomena - the speed of two coupled particles and their inter-particle distances are clearly different from those of the fundamental mode case.

In this work, we study the dynamics of longitudinal, self-ordered structures of dielectric microparticles under the influence of the FM and HOMs of a 2 μm tapered fibre, both theoretically and experimentally. The first group of HOMs, which corresponds to the LP_{11} mode family, was generated by launching a first-order Laguerre-Gaussian beam (LG_{01}) into a suitable fibre. The LG_{01} beam was formed using a spatial light modulator (SLM). With the assistance of a custom-built optical tweezer it was possible to trap and move a fixed number of particles to the fibre. Particle speeds and inter-particle distances were compared for each chain. Additionally, the experimental data is supported by analytical and numerical analyses based on an intuitive three-mode scattering-matrix model for large particle ensembles on the microfibre surface. The optical binding forces on the particles for the HOMs and the FM are also verified using the full Maxwell stress tensor method.

15.2. Theoretical Analysis

15.2.1. Scattering-matrix approach and forces acting on multi-particle trapping

In order to calculate the optical forces acting on the particles, one first needs to calculate the E-field surrounding them by solving the scattering problem and then use these fields to obtain the forces. For this calculation, we first develop a 2D numerical model based on the finite element method (FEM) to calculate the field distribution and the forces exerted on the particles. This method of numerical analysis is similar to that reported in our previous work [114; 223]. Parameters used in this numerical simulation are: the propagating wavelength, $\lambda = 1064$ nm, the refractive index of the fibre, $n_{\text{fibre}} = 1.456$, of water, $n_{\text{water}} = 1.33$ and of the beads, $n_{\text{bead}} = 1.57$. In order to be consistent with the experimental data, in all simulations the propagating power at the fibre waist was assumed to be 30 mW. Although this FEM model can be used to investigate the interaction of the scattering objects and the guided surface modes very accurately, it requires high performance computing resources even for symmetrical configurations. Therefore, we use this method to calculate the forces only for the case of a single particle and two particles. These numerical results are used to precisely determine the mode propagation loss and mode coupling strengths for the case of several trapped particles on a fibre surface.

To obtain the scattered field solution for more than two particles trapped in the evanescent fields of a microfibre, a tritter scattering-matrix approach is proposed [196]. Since the chosen trapped particles are larger than the excitation wavelength, the forward scattered light from the particles is much stronger than the backward scattering. In this alternative force calculation method, we make the simplifying assumption that the backward scattered light from particles is negligible. The physical model consists of N dielectric particles that are longitudinally bounded along the fibre surface as specified in Fig. 15.1. Figure 15.1 shows an example of how the laser light incident from the left is coupled into the microfibre and represented by the electromagnetic field, E(x), at a chosen wavelength, $\lambda = 1064$nm. Here, the particles act as beam splitters with the input incident beam split into three beams. The sinusoidal orange (A_j) and pink (B_j) arrows represent the total incoming and outgoing light fields, respectively. The white and red arrows indicate the attractive ($\mathbf{F}_{n,j}$) and repulsive ($\mathbf{F}_{b,j}$) optical binding

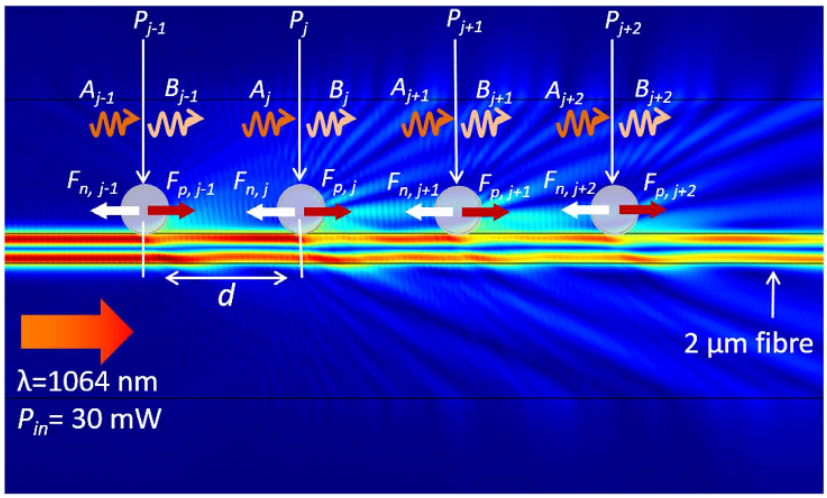

Figure 15.1.: 1D array of N particles scattering light under the influence of the HOM evanescent fields of a 2 μm fibre.
Laser light is coupled into the microfibre from the left at a wavelength of 1064 nm. The power at the waist is $P_{\text{in}} = 30$ mW, $\mathbf{F}_n$ (white arrow) and $\mathbf{F}_p$ (red arrow) indicate the attractive and repulsive binding forces; A_j (orange sinusoidal arrow) and B_j (pink sinusoidal arrow) are the amplitudes of the incoming and outgoing light fields from the particles; d is the relative distance between the particles.

forces, respectively. For a particle at position, x_j, along the fibre axis, the E-field can be written as:

$$E(x) = A_j \exp\left(i \sum_{q=a,b,c} k_q(x - x_j)\right) + B_j \exp\left(-i \sum_{q=a,b,c} k_q(x - x_j)\right), \tag{15.1}$$

for $j = 1$ to N and $k_{tot} = k_a, k_b, k_c$ represents the complex wave-vector of three forward scattered modes propagating both inside and outside the fibre surface. When a fibre mode evanescently interacts with particles, the scattered light can be described by a wave-vector, $k_b = k_a/cos(\alpha_0)$, where k_a is the wave-vector length of the incident field in the medium surrounding the particles and α_0 is the polar angle between the incident and the scattered light. The parameter k_c is the complex wave-vector component attributed to the effective propagation lossy modes which penetrate into the surrounding host. As has been proposed by Schnabel et al. [196], for general three-port beam-splitters, if the phases are chosen such that the scattering-matrix, $\mathbf{M}$, is symmetric, the complex

component, $\mathbf{B}_j = \mathbf{M} \times \mathbf{A}_j$, can be written as

$$\begin{pmatrix} B_{ja} \\ B_{jb} \\ B_{jc} \end{pmatrix} = \begin{pmatrix} \eta_1 e^{i\phi_0} & \eta_4 e^{i\phi_1} & \eta_5 e^{i\phi_3} \\ \eta_4 e^{i\phi_1} & \eta_2 e^{i\phi_0} & \eta_6 e^{i\phi_2} \\ \eta_5 e^{i\phi_3} & \eta_6 e^{i\phi_2} & \eta_3 e^{i\phi_0}, \end{pmatrix} \tag{15.2}$$

where $0 < \eta_i < 1$ describes the amplitude and represents the phase coupling. A_{ja}, A_{jb} and A_{jc} are the incoming field components of the scattered beams on particle j that allow us to identify the complex outgoing fields B_{ja}, B_{jb} and B_{jc}. The outgoing field $B_j = B_{ja}, B_{jb}, B_{jc}$ is then, in turn, used as an input to the neighbouring particle 'beam splitter' via:

$$\begin{pmatrix} A_{ja+1} \\ A_{jb+1} \\ A_{jc+1} \end{pmatrix} = \begin{pmatrix} e^{ik_a(x_{j+1}-x_j)} & 0 & 0 \\ 0 & e^{ik_b(x_{j+1}-x_j)} & 0 \\ 0 & 0 & e^{ik_c(x_{j+1}-x_j)}. \end{pmatrix} \tag{15.3}$$

To simplify our calculation, we set the initial transmitted light phase, ϕ_0, to be zero. In an effective 1D configuration of bounded microparticles on a microfibre surface, the amplitudes η_4, η_5 and η_6 can be assigned to the particles' scattered mode coupling strengths between the fundamental and the higher order, the fundamental and the free-space and the higher order and the free-space modes, respectively. Here we assume that z_l is the effective background scattering that represents the coupling to the lossy modes. For the unitary condition, $\mathbf{M}^{-1}\mathbf{M} = 1$, the transmitted amplitudes can be expressed as:

$$\eta_1^2 = 1 - \eta_4^2 - \eta_5^2 - z_l^2, \tag{15.4a}$$
$$\eta_2^2 = 1 - \eta_4^2 - \eta_6^2 - z_l^2, \tag{15.4b}$$
$$\eta_3^2 = 1 - \eta_5^2 - \eta_6^2 - z_l^2. \tag{15.4c}$$

The phases of the scattering matrix, $\mathbf{M}$, can be written as:

$$\phi_1 = \frac{1}{2} \arccos\left(\frac{\eta_1^2\eta_4^2 + \eta_2^2\eta_4^2 - \eta_5^2\eta_6^2}{2\eta_4^2\eta_1\eta_2} \right) - \frac{\pi}{2}, \tag{15.5a}$$
$$\phi_2 = \frac{1}{2} \arccos\left(\frac{\eta_4^2\eta_6^2 + \eta_1^2\eta_5^2 - \eta_3^2\eta_5^2}{2\eta_5^2\eta_1\eta_3} \right), \tag{15.5b}$$

$$\phi_3 = \frac{1}{2}\arccos\left(\frac{\eta_2^2\eta_6^2 + \eta_3^2\eta_6^2 - \eta_4^2\eta_5^2}{2\eta_6^2\eta_2\eta_3}\right) + \frac{\pi}{2}. \tag{15.5c}$$

The scattering force acting on the particle, P_j, along the fibre axis can finally be calculated from the Maxwell stress tensor and is given by:

$$F_s = \frac{1}{2}\epsilon_0\epsilon_r\left(|A_j|^2 - |B_j|^2\right), \tag{15.6}$$

where ϵ_0 and ϵ_r are the vacuum and the relative surrounding medium permittivity, respectively [74]. In the following section, we investigate the optical binding forces on several particles trapped along the fibre surface. Out of these, the particle-field dynamics, numerous stable configurations of particles and the influence of these effects on speed variations of particle chains are carefully discussed.

15.3. Results

15.3.1. Optical binding forces between trapped particles within a chain

In Fig. 15.2 we present the optical binding forces and their corresponding potentials as a function of the interparticle separation, d, for both the FM and HOM cases. The position of the first particle, P_1, is fixed with respect to the fibre and the scattering forces are calculated while varying the position of the next particles, P_j, along the fibre axis. The longitudinal optical binding forces can be extracted by subtracting the scattering forces on the first particle from those on the next neighbouring particles. The solid and dashed lines in Fig. 15.2(a,d) represent the binding forces which are calculated for a two-particle model based on the FEM and the scattering-matrix methods. These figures show that the optical binding forces modulate around zero as a function of the distance between two particles. Positive and negative values represent repulsive and attractive forces on the trapped particles. A stationary particle order can be achieved if the repulsive and attractive forces vanish. When using the FEM method, there exists a short periodic oscillation in the binding forces, where the peak-to-peak distance is close to $\lambda/2$ on both particles P_1 and P_2. Although this effect is very weak, the phenomenon is more pronounced when the interparticle distance, d, is less than 10 μm. In this case,

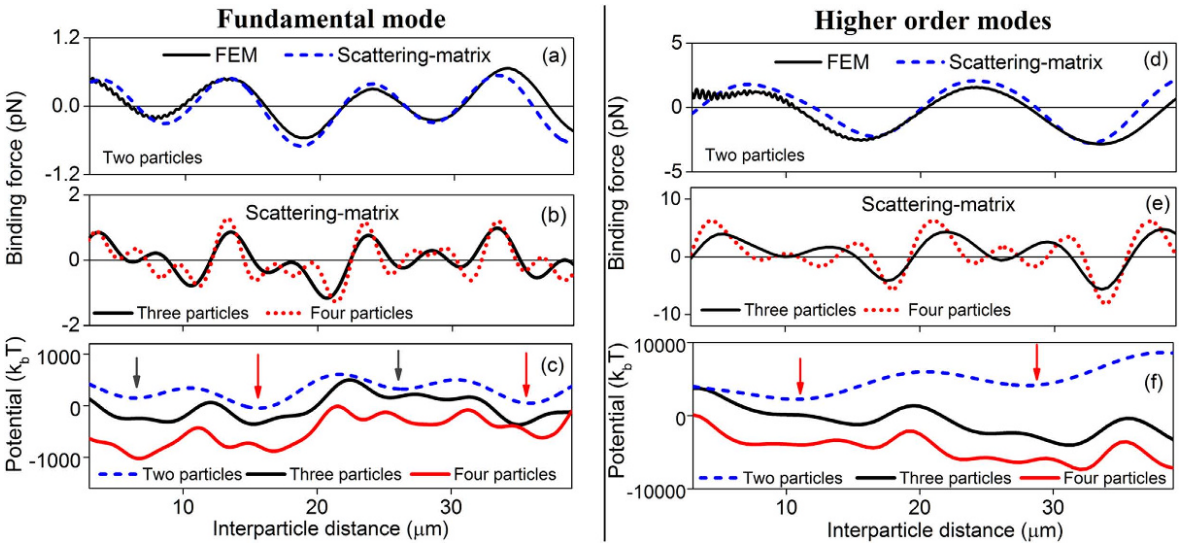

Figure 15.2.: Optical binding forces and their corresponding potentials on two-, three- and four-particle models.
Binding forces of two particles in the evanescent fields of the FM (a) and HOMs (d) calculated from both the FEM and the scattering-matrix methods; (b,e) are the binding forces for three and four particles; (c,f) are the binding potentials of the corresponding binding forces. The potential is in units of k_BT, where k_B is Boltzmann's constant relating the thermal energy to an absolute temperature T around the trapped particles. The fibre diameter is 2 μm.

the backward scattered spherical waves from neighbouring particles propagate in the opposite direction to the incident light and interfere, causing short-period modulations of the optical forces. Since we neglect the backward scattered light when using the scattering-matrix method, the observed results are smooth curves with no short-period modulation of the scattering forces over long interparticle distances.

Table 15.1 shows the parameters used for the scattering-matrix approach which gave us the best fit of the optical forces when compared to the FEM method. It is worth noting that here we assume that microparticles trapped in the evanescent fields of higher order microfibre modes scatter photons from one mode into another. In this case, each coupling coefficient, η_i and the wave-vector component, k_{tot}, introduced in equations (15.2) and (15.3) represent different physical properties. Modifying these parameters will directly affect the fit of the binding forces, in both their shape and magnitude, for a given particle in a bounded particle chain at the fibre waist. We first choose the amplitudes of the incoming fields, A_j, to match the FEM force calculations for a chosen incident power of 30 mW. The wave-vector components, k_b and k_c, are then

	Wave-vector length ratio		**Coupling coefficients η_i**		
	k_b/k_a	k_c/k_a	η_4	η_5	η_6
Fundamental mode (LP_{01})	0.9	0.96	0.13	0.1	0.08
Higher order modes (LP_{11})	0.93	0.86	0.11	0.16	0.09

Table 15.1.: Wave-vector length ratios of the scattered lights, k_b and k_c, to the incident field, k_a ($k_a = 2\pi/\lambda$, where $\lambda = 1064$ nm). The coupling coefficients, η_i, are used in the scattering-matrix approach for both FM and HOM propagation in a 2 μm microfibre.

used to fit the frequency oscillations, the peak positions and the damping parameters of the binding forces ($\mathbf{F}_{n,j}$, $\mathbf{F}_{b,j}$). The coupling coefficients, η_4, η_5 and η_6, of the scattering particles identify the curve shape and slopes of the mean force values and the propagation lossy modes between the trapped particles.

In order to study the binding mechanisms for large particle ensembles on a microfibre surface, the scattering-matrix approach is applied. Here, we use the parameters of Table 15.1 to calculate the binding forces of three- and four-particle chain formations in the evanescent fields of a MNF system. The main assumption in these calculations is that the changes of the mode coupling strengths, η_l and the wave-vector components, k_b and k_c, among the scattering particles and the microfibre light modes are negligible when compared to the two-particle case. This is a reasonable assumption since the transmission loss of the incident beam due to the light scattering from each individual particle is negligible. If we additionally assume that the relative distances, d, between the next neighbouring particles within a chain are equal, we can also investigate the modulations of the binding force on each individual particle over the whole complex, bounded-particle chains using this very simple model. Figure 15.2(b,e) show the variation of the binding forces for the end particle of a chain as a function of interparticle distances; for example, the third particle, P_3 (black curve) and the fourth particle, P_4(red dotted curve), of the three- and four-particle chains. The binding forces on these end particles are greater and the oscillations are more frequent if the chain has more particles in it for both the FM and HOM cases.

Figure 15.2(c,f) show the optical binding potentials calculated from the corresponding binding forces. Several potential well regions are created (indicated by the black and red arrows) where the particles could form multistable configurations due to these binding force modulations for both the FM and HOMs. For the two-particle case (dark blue dashed lines), the periods of the potential depth modulation are 10 μm and

16 μm for the FM and HOM fields, respectively. The larger stable potential distance of the HOMs compared to the FM is due to the longer extension of the HOM's electric field distribution in the surrounding medium. This first generic observation of the potential depths and their behaviours is similar to the previous reports using Bessel beams [199; 201], as well as our earlier work using a nanofibre [114].

It is interesting to note that the FM potential plots for the two-particle case in Fig. 15.2c (dark blue dashed line) exhibit shallower potential minima ($\approx 200\ k_BT$) at the positions of 6 μm and 26 μm (black arrows) when compared to the potential minima ($\approx 600\ k_BT$) at the positions of 16 μm and 37 μm (red arrows). These metastable positions (6 μm, 26 μm) only create long-range local oscillations of the particles before they eventually reach the deeper potential wells at 16 μm and 37 μm. In contrast, Fig. 15.2f (dark blue dashed line) shows that the depths of the HOM's potential wells for two particles appear to be similar to one another, at approximately $2,500\ k_BT$, within the studied range of the interparticle distance. The expected stable interparticle distances for two particles are at 12 μm and 28 μm (red arrows), which are shorter than for the FM case. We can make initial conclusions here that a pair of particles trapped in the HOM evanescent fields in a microfibre system (i) shows shorter stable interparticle distances, (ii) creates deeper potential wells along the fibre waist and hence, theoretically, (iii) exhibits stronger optical binding forces between the particles than compared to the FM propagating fields.

The black and red curves in Fig. 15.2(c,f) show the potential profiles of the bounded three- and four-particle chains. These potential wells exhibit complex patterns with varying potential minima depths over the large interparticle distance range along the fibre waist region for both the FM and HOMs cases. We see that the observed shallower potential wells strongly depend on the particle numbers within the chain and the chosen coupling strength, η_6, which describes the propagation loss outside the fibre. These shallow potential oscillations disappear when η_6 approaches zero.

The shallow potential wells, which cause the particles to oscillate, can be overcome by thermal activation. The particles would then approach the deeper potential regions. The stronger binding force observed due to additional particles would also cause the stable interparticle distances to fall until the new deepest potential well can be created. This results in closer localisations of the particles with slightly non-equilibrium interparticle distances in the chain. To confirm this hypothesis, we consider non-symmetrical conditions where the interparticle distances are not identical. For the three-particle

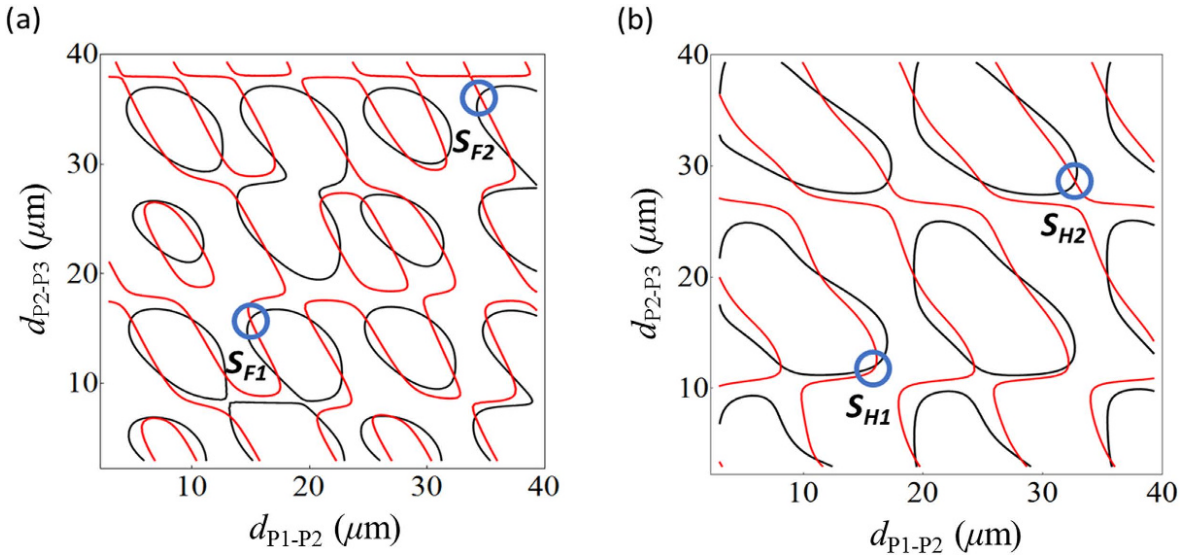

Figure 15.3.: Contour plots for equilibrium positions of particles.
Equivalent force lines for a three-particle chain formation as a function of the two independent interparticle distances in the FM (a) and HOM (b) evanescent fields. Intersections of these equal force contours indicate the equilibrium configurations but only those denoted by the blue circles are under stable conditions.

chain calculations, Fig. 15.3(a,b) show the force lines of the particles, P_2 and P_3, as a function of the two interparticle distances, d_{P1-P2} and d_{P2-P3}, for the case where the forces acting on all three particles are equal. Here, the distances d_{P1-P2} and d_{P2-P3} are assigned to the spacing between the particles, P_1 and P_2 and to the particles, P_2 and P_3, respectively. There are many intersections of these lines where the binding forces on particles vanish and the equilibrium configurations can be observed.

Although many equilibrium possibilities are denoted in Fig. 15.3(a,b), we consider that stable configurations of particles in the chains can only be achieved when they localise at a potential minimum deeper than the particles' thermal energy. In addition, the propelling particles along the fibre surface also increase the particle kinetic motions and hence, would allow them to jump between the nodes before they approach the deeper potential minima. Assessing the results in Fig. 15.2(c,f) alongside Fig. 15.3, we can finally predict that there are two major stable configurations which are considered the most preferable locations for the particles. As shown in Fig. 15.3(a,b), these two stable configurations (circled) correspond to the stable positions, $S_{F1}(d_{P1-P2} = 15\ \mu\text{m}, d_{P2-P3} = 16\ \mu\text{m})$ and $S_{F2}(d_{P1-P2} = 24.5\ \mu\text{m}, d_{P2-P3} = 36\ \mu\text{m})$ for the FM case and the stable positions, $S_{H1}(d_{P1-P2} = 16\ \mu\text{m}, d_{P2-P3} = 12\ \mu\text{m})$ and $S_{H2}(d_{P1-P2} = 29\ \mu\text{m}, d_{P2-P3} = 32.5\ \mu\text{m})$

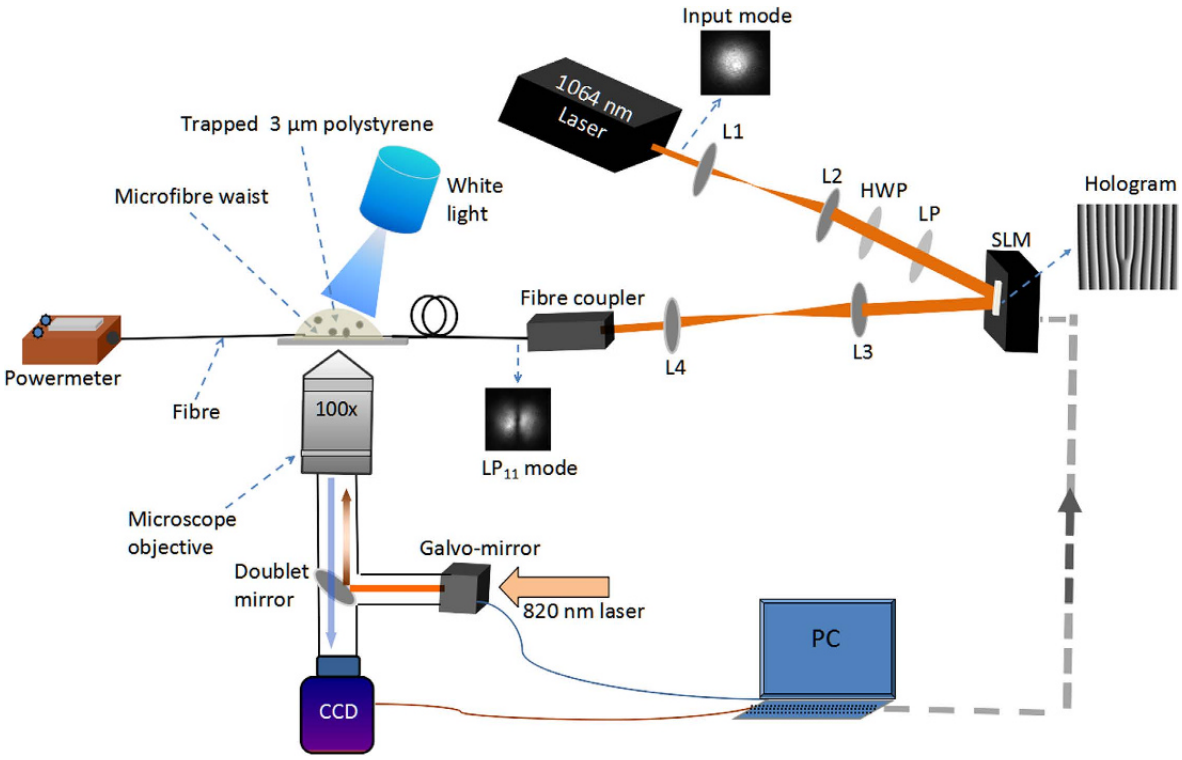

Figure 15.4.: Experimental setup for particle propulsion.
L1, L2, L3, L4: lenses; LP: linear polariser; HWP: half-wave plate; CCD: charge-coupled device camera; computer. Orange lines represent the free beam path.

for the HOMs case. We notice that, although there are slight shifts of the observed d_{P1-P2} compared to the d_{P2-P3} values for the non-symmetrical configurations, they are still very close to the deep potential positions, as shown in Fig. 15.2(c,f) for the FM and HOMs.

15.3.2. Experimental observation

As shown in Fig. 15.4, the experiment consists of three components: (i) LG beam generation and HOM excitation, (ii) tapered fibre fabrication and (iii) the optical tweezers (see Methods). A specific number of particles was trapped using a time-sharing optical tweezer and all were brought close to the tapered fibre simultaneously. As soon as the particles are released from the tweezers trap, the fibre's evanescent field propels them along its axis.

Figure 15.5 is a micrograph of the particle speed under the influence of the propagating

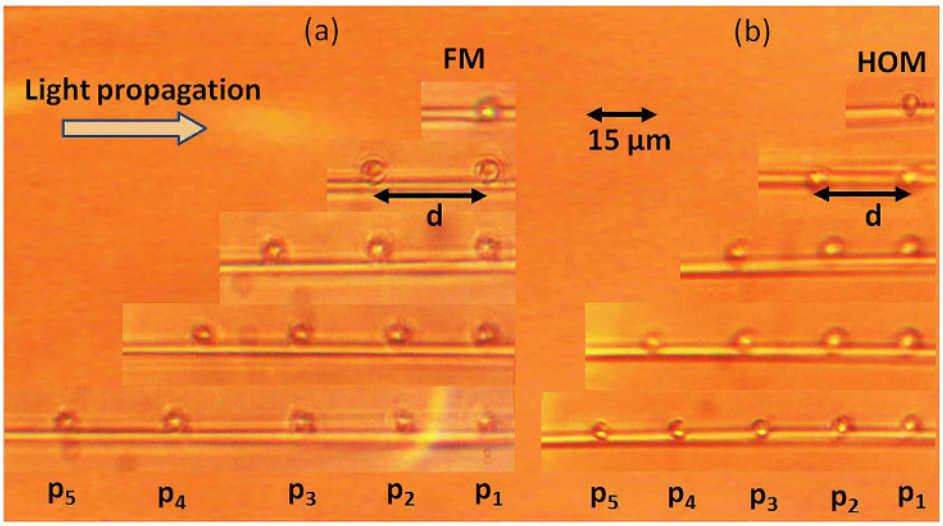

Figure 15.5.: Micrograph of inter-particle distance for particle numbers changing from 1 to 5 in particle chains.
(a) Fundamental mode propagation; (b) Higher order mode propagation. The power at the microfibre waist is $P_{in} = 30$ mW.

FM and HOM fields extracted from videos of particle motion (see Supplementary Movies S1, S2, S3 and S4 as examples). Starting from the first particle, the incident laser beam interacts with all particles, labelled from P_1 to P_5. As is clearly seen in the micrographs, the particles self-arrange along the fibre. The more particles used, the smaller the interparticle distances between P_1, P_2 and P_3. Once the particles settled at their equilibrium positions, the interparticle distances for each particle pair were measured.

Any small imperfection on the fibre surface may cause a local acceleration or deceleration of some particles in the chain. When this acceleration/deceleration breaks the stable interparticle distance, there is always an attractive or a repulsive kick on neighbouring particles to compensate the change in position and to return the system to equilibrium. This self-adjustment of the particle distance was far more obvious for the FM work than for the HOM studies. When we used HOMs, sometimes the particles were not able to re-establish their equidistance; as a result, they behaved as independent particles and left the chain.

As we discussed in the theoretical section, by assuming that the particles localise at the first stable configuration within the chains and using the values derived in Fig. 15.3, d_{P1-P2}, d_{P2-P3}, we plot in Fig. 15.6a the calculated particle speeds (dashed curves) of

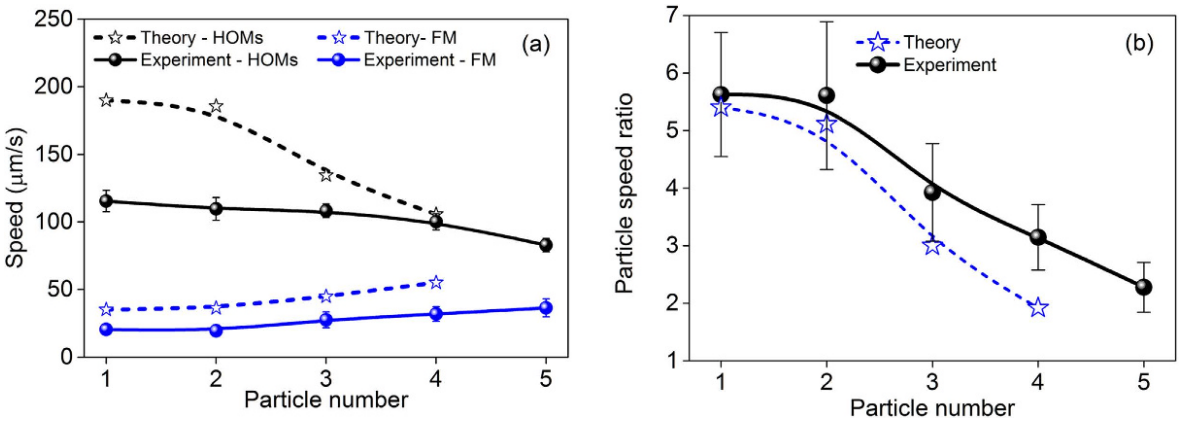

Figure 15.6.: Speed comparison of particles under the FM and HOMs.
(a) Theoretical data (dashed lines) and experimental observation (solid lines) of particle speed change with respect to the number of particles for both HOMs and FM. (b) Theoretical calculation (dashed lines) and experiment (solid lines) of particle speed ratio between the HOM and the FM cases.

up to four bounded particle chains using the standard bulk Stokes' drag coefficient, $F = 6\pi\mu a\nu$, where μ is the viscosity and ν is the particle velocity. The solid curves in Fig. 15.6a show the experimental observation of up to five particle formation chains. We present in Fig. 15.6b the theoretical and experimental data of the ratio between the corresponding speed of particles in the HOMs and FM fields. Taking a closer look at the particle speed ratios, the original speed ratio of 5.5 (experiment) and 5.4 (theory) for a single particle was found to have approximately halved to 3 (experiment) and 2 (theory) for four particles. Even though theory and experiment show some discrepancy, it is clear that they are somewhat in agreement.

In the case of FM propagation, changes to the particle speeds were slow, but the plot shows a clear trend towards higher speeds with increasing particle number. This is consistent with predictions in previous works [114; 204]. However, this increase has a saturation limit and the particle speed tends to be constant after five or six particles. Consequently, the binding between spheres was found to be weaker. Interestingly, in the case of HOM propagation, this speed trend was opposite to that observed for the FM propagation. The more particles present, the slower the observed particle speeds. The particles' kinetic motions sometimes allow them to escape from the stable configuration. The interparticle distances between neighbouring particles in various lengths of particles chain are given in Fig. 15.7 for the FM and HOMs. The experimentally obtained

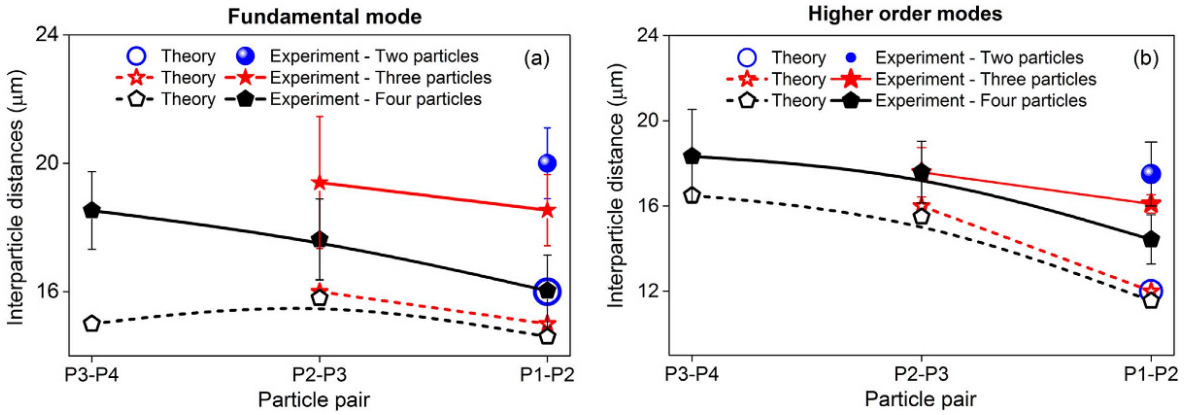

Figure 15.7.: Interparticle distance with respect to the number of particles in a chain (in μm unit).
Theoretical prediction (dashed lines) and experimental observation (solid lines) of interparticle distances between neighbouring particles in various length of particle chains under the FM (a) and HOMs (b) evanescent fields.

interparticle distance (solid curves) appears to be largest when only two particles are present in the chain and it decreases slowly as more particles are added. This self-adjustment of interparticle distance within the chain matches with the trend of the theoretical prediction (dashed curves). The discrepancy between the theoretical prediction and the experimental observation may be due to the fact that we calculate the optical forces on the particles using a 2D configuration for the original FEM method. When there are only two particles, they essentially share the incident beam with little scattering loss and the interparticle spacing can be set accordingly. As the particle number increases, the incident beam is distributed over the particles with certain ratios. The particles closest to the incident light source receive larger portions of the power than distant particles due to scattering losses. The non-uniform distribution of scattered light on the particles requires different interparticle distances in order to maintain the self-arranged chain of particles.

The experimental observation of interparticle distances from Fig. 15.7 confirms our hypothesis that the particles position themselves around the first preferable stable position. An important factor to be gleaned from this result is that, regardless of the particle number, the interparticle distances are always slightly smaller when we use HOMs instead of the FM. This is in good agreement with the theoretical predictions. Smaller particle separations indicate that the stronger evanescent field intensity of the HOMs is not the important factor responsible for ordering the interparticle separation.

Instead, the potential profiles and how the scattered light fields from the particles interfere must play a larger role in determining the interparticle separations.
An important distinction between the binding potentials of the FM and HOM mode cases can be realised from Fig. 15.2. The interparticle stable positions are not only governed by the magnitude of the binding forces, but also the shape of the potential landscape. As shown in Fig. 15.2 for the two-particle case, although the absolute binding potential is deeper under the HOMs when compared with the FM, this potential well is relatively wide, which may be responsible for uncertainties in the particles' positions. Additionally, when the number of particles within the chain increases, the potential landscape transforms to contain multiple potential wells with similar magnitudes rather than a single potential minimum, leading to particles jumping between these potential minima. This may explain why the particles under the HOMs exhibit relatively unstable interparticle separations.
Furthermore, when a dielectric particle is trapped in the evanescent field, the scattering force is responsible for the propulsion of particles along the fibre axis. To better understand how the binding force affects the control of the trapped particles in a chain, we calculate the ratios of the optical binding to the scattering forces. The ratio of the maximum absolute values of the binding force to the scattering force was found to be 0.7 for the FM and 0.5 for the HOMs. This smaller ratio could explain the case in which particles sometimes escape from a stable configuration in the HOM field. This implies that, although a stronger optical binding force is observed for the HOMs, it is still easier to control each individual particle within the particle chain using the scattering force. This is in contrast to the fundamental mode propagation.
In conclusion, we studied the optical binding effect for a number of 3 μm polystyrene particles under the influence of higher order mode propagation in an optical microfibre. By combining the FEM and a simple scattering-matrix approach, we were able to investigate the dynamics and the self-arrangements of particles in both the FM and HOM evanescent fields of MNF systems. In the FM case, the relatively larger interparticle distance and the rigid particle chains hint at a stronger interaction, which in turn, could enhance the speed. For HOM propagation, both theory and experimental results show a smaller interparticle distance and an instability of chains consisting of a large number (five) of particles. Comparing the observed behaviour with that obtained for FM propagation, a reasonable explanation of the particle speed and the interparticle distances can be provided. These interesting physical properties of HOMs offer a better

understanding of the interactions of light with matter. The expected reduced optical interaction of HOMs due to the spin and the orbital angular momentum may make it a better candidate for 3D manipulation of micro and nano-objects. In particular, this study could be very useful for applications such as atom trapping and nanoparticle trapping, etc.

15.4. Methods

15.4.1. Higher order mode generation

To create a beam with a doughnut-shaped intensity cross-section, a linearly polarised 1064 nm Nd^{3+}: YAG laser was launched onto the SLM (SLM-BNS 1064). A computer-generated vortex phase discontinuity combined with a blazed grating was applied to the SLM so that a first order Laguerre-Gaussian (LG_{01}) beam was created in the far field. Two-mode fibre (Thorlabs, SM1250G80) operating at 1064 nm with a cladding diameter of 80 μm was chosen for the experiment. The fibre supports both the fundamental LP_{01} and the LP_{11} family of higher order modes. The LG_{01} beam was coupled into the fibre and a two-lobed pattern corresponding to the LP_{11} mode can be obtained at the fibre output. With the right objective lens, approximately 40 % of the HOM power could be coupled into the fibre and a LabVIEW programme allowed us to easily switch between different orders of LG beams. By switching back to the FM, 70 % of the output power was coupled into the fibre.

15.4.2. Preparation of higher-mode tapered fibre

A brushed hydrogen flame was used to make the tapered fibres, which can be customised to any desired taper shape [208; 225; 226]. A double linear taper with physical taper angles of 0.6 mrad and 1 mrad was predesigned and the fibre was fabricated with this profile. After pulling, $\approx$ 80 % transmission of the HOMs was achieved for a fibre with a 2 μm waist. The same fibre had 95 % transmission for the FM mode. In real applications it is always more reasonable to state the power at the fibre waist. Assuming a symmetrical fibre taper, the power at the waist is estimated to be the square root of the product of the input and output powers [223].

15.4.3. Integrating an optical tapered fibre into the optical tweezer

The prepared fibre was mounted onto a U-shaped metal mount and attached to a 3D translational stage positioned in an optical tweezer. The taper's vertical and horizontal positions were adjusted over the trapping plane of the optical tweezer. The optical tweezer was also equipped with a galvo mirror array, controlled using a MATLAB code to achieve time sharing between the multiple traps. The reason for integrating the fibre into the optical tweezer system was to facilitate trapping of a specific number of particles and to minimise any disturbances due to unwanted particles [223]. A dilute 3 μm polystyrene particle dispersion was dropped onto the microfibre, which was located at the focal plane of the tweezer. First, the optical tweezer was used to trap targeted particles and to move them to the microfibre. Then the tweezer was switched off. The particles are attracted to the fibre by the evanescent field and are propelled along the waist region. By monitoring the particle motion via a camera (Thorlabs 1240), particle speeds and relative particle distances can be extracted. The same waist power (30 mW) was used for both the FM and the HOMs. The experiment was repeated three times for each set of particles in a chain, ranging from one to five. For each sequence, the speed and inter-particle distances of the corresponding particles in each chain were analysed for both the FM and the HOM evanescent fields.

Contributions: S.N.C. proposed and supervised the project; A.M. performed the experiment; H.R. and D.H. carried out the theoretical analyses; A.M. and V.G.T. contributed to the experimental data analyses and the numerical simulations; All authors participated in manuscript writing. All authors reviewed the manuscript.
Acknowledgements: This work was supported in part by the Okinawa Institute of Science and Technology Graduate University. H.R. and D.H. acknowledge the support of the Austrian Science Fund (FWF) through SFB Foqus Project F4013. This article is based upon work from COST Action MP1403 "Nanoscale Quantum Optics", supported by COST (European Cooperation in Science and Technology). The authors wish to thank M. Daly, P.S. Mekhail and S.D. Aird for useful comments about the manuscript.

16. Publication

Generating a stationary infinite range tractor force via a multimode optical fibre

Christiane A. Ebongue, Daniela Holzmann[1], Stefan Ostermann and Helmut Ritsch

Optical fibers confine and guide light almost unattenuated and thus convey light forces to polarizable nano-particles over very long distances. Radiation pressure forces arise from scattering of guided photons into free space while gradient forces are based on coherent scattering between different fiber modes or propagation directions. Interestingly, even scattering between co-propagating modes induces longitudinal forces as the transverse confinement of the light modes creates mode dependent longitudinal wave-vectors and photon momenta. We generalize a proven scattering matrix based approach to calculate single as well as inter-particle forces to include several forward and backward propagating modes. We show that an injection of the higher order mode only in a two mode fiber will induce a stationary tractor force against the injection direction, when the mode coupling to the lower order mode dominates against backscattering and free space losses. Generically this arises for non-absorbing particles at the center of a waveguide. The model also gives improved predictions for inter-particle forces in evanescent nanofiber fields as experimentally observed recently. Surprisingly strong tractor forces can also act on whole optically bound arrays.

Journal of Optics 19 065401(2017) doi:10.1088/2040-8986/aa69f2

[1]D.H., S.O. and H.R. contributed in an intensive advisory role, while all the calculations were done by C.A.E.

16.1. Introduction

In an optical fiber, light is transversely confined and transmitted over very long distances without attenuation. The field can be well decomposed in transverse modes, each of them associated with a specific transverse field pattern and a corresponding longitudinal propagation wave vector. For specially designed fibers as optical nano-fibers or hollow core fibers a significant fraction of the light intensity is propagating in free space outside the actual fiber material and can interact with particles in this region [11; 227].
If one places a nanoscopic particle or even a single atom into the fiber fields, it will significantly perturb the light propagation and redistribute the field among different modes and propagation directions. As the light carries momentum, the corresponding photon redistribution leads to a net optical force [115]. The magnitude and direction of this force strongly depends on the fiber and particle geometry and the properties of the injected field. For several particles coupled to the same fiber, collective scattering enhances these forces and creates strong inter-particle forces depending on their relative distance. This leads to optical binding, selfordering and nonlinear motional dynamics [15; 64; 72].
In some recent work we exhibited that important properties of these forces can be well understood from a generalized beam splitter approach involving only two fiber modes and an additional free space loss mode [115]. Surprisingly this model also allows to identify a parameter regime, where the total force on a particle points against the wave-vector of the impinging light, i.e. we get a tractor beam force [228]. This feature even persists for arrays of several bound particles.
Physically the tractor beam phenomenon is tight to the fact, that scattering from a higher order to a lower order mode requires a momentum contribution from the particle along the field propagation. Thus due to momentum conservation the particle is pushed in the opposite direction. The momentum exchange is, however, smaller than for backscattering a photon into the opposite direction. Hence for a more realistic calculation one needs to include the backscattered fields and absorption as competing processes.
Note that injecting phase coherent superpositions of light simultaneously into two transverse modes can create 3D optical trapping positions along the fiber [45]. Particles in these traps can be moved along the fiber in any direction by moving the traps via a relative phase control of the two modes in time [229]. This is different from our tractor

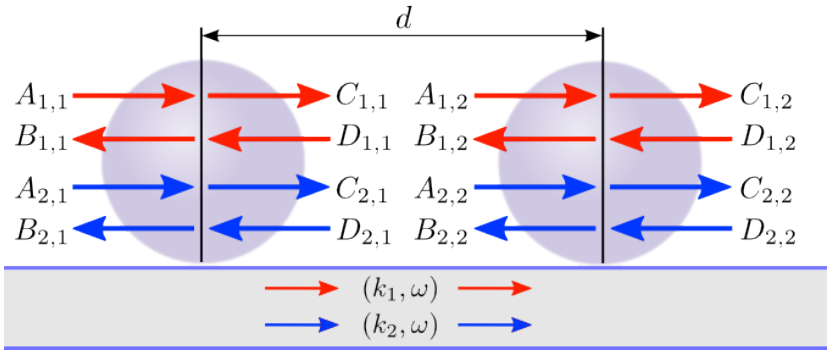

Figure 16.1.: (Colour online) Schematic picture of two micro-spheres trapped close to a optical two mode fiber. In the presented model the spheres are approximated as beam splitters and the fields are determined by the incoming and outgoing amplitudes. The red arrows denote the amplitudes for the first (fundamental) mode and blue arrows characterize the second (higher order) mode. The first index for the amplitudes defines the mode number whereas the second index stands for the particle number. An analogous picture holds for a particle in the field of a hollow waveguide [95; 230].

beam mechanism, which is independent of position along the fiber and does not require external phase control.

Here we will investigate the properties and limitations of implementing such a generic tractor beam mechanism for small beads trapped in an optical two-mode nanofiber. While a full numerical calculation using 3D finite element software is possible [223], it does not allow to scan large parameter and size ranges. Hence it is difficult to get good qualitative understanding and the whole range of possibilities offered by such a system. Hence to better get the central idea, we will first study a rather idealized two mode model including only for forward scattering and some general absorption losses to identify the key parameter region for the appearance of tractor forces. In a second step we will generalize to a more realistic description including the backscattered fields and loss to free space. While it seems difficult to find realistic favorable parameters for tractor forces in multi mode nanofibers, hollow core fibers seem much more promising. Finally we go beyond the case of single particles and study how ordering and optical binding can be combined with tractor forces.

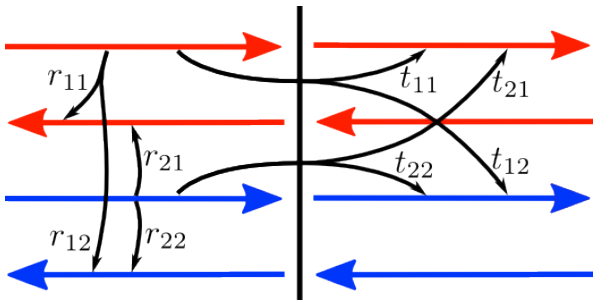

Figure 16.2.: (Colour online) The fundamental processes which are described by the presented model. All reflection processes are shown on the left side of the beam-splitter and all transmission processes are shown towards the right side of the beam-splitter. Of course, all processes are mirror symmetric and can also occur into the opposite direction.

16.2. Model

We consider N polarizable spherical particles within the field of a multimode optical waveguide [95; 230; 231]. Such a geometry can either be realized by placing the particles inside a multi-mode hollow core fiber [232; 233] or trap them close to the surface of a tapered nanofiber with strong evanescent field components [115]. The beads in the field are modeled as effective beam-splitters as shown in fig. 16.1, which couple the local field mode amplitudes left and right of the beam splitter. These mode amplitudes are connected via an effective scattering matrix representing the underlying microscopic scattering processes integrated over the bead volume. As the bead only interacts with a spatial fraction of the mode, this matrix on the one hand includes forward and backward scattering of photons into the same transverse fiber mode as well as on the other hand it allows cross-coupling between the fundamental and the higher order transverse modes. As depicted in 16.2 the amplitudes $0 \leq t_{ij} \leq 1$ describe forward scattering processes (into the same mode for $i = j$ and into any other mode for $i \neq j$) the reflection coefficients $0 \leq r_{ij} \leq 1$ describe reflections into the same mode as well as mode mixing reflections into the other transverse mode (*cf.* 16.2). In principle all these coefficients have to be derived from solving the corresponding Helmholtz equations for any specific implementation and boundary conditions. This has to be done numerically or by fitting experimental results [115]. We will stay with a general approach for the moment and only give some estimates for specific examples in Appendix A. At this point we thus end up with four independent mode amplitudes connected via a four-port beam splitter matrix. The most general matrix, which describes the occurring processes as they are

depicted in 16.2 takes the form

$$\mathbf{M}_{4p} = \begin{pmatrix} t_{11}e^{i\phi_{11}} & t_{21}e^{i\phi_{21}} & r_{11}e^{i\psi_{11}} & r_{21}e^{i\psi_{21}} \\ t_{12}e^{i\phi_{12}} & t_{22}e^{i\phi_{22}} & r_{12}e^{i\psi_{12}} & r_{22}e^{i\psi_{22}} \\ r_{11}e^{i\psi_{11}} & r_{21}e^{i\psi_{21}} & t_{11}e^{i\phi_{11}} & t_{21}e^{i\phi_{21}} \\ r_{12}e^{i\psi_{12}} & r_{22}e^{i\psi_{22}} & t_{12}e^{i\phi_{12}} & t_{22}e^{i\phi_{22}} \end{pmatrix}. \tag{16.1}$$

It connects the four input and output fields of the jth particle via

$$\begin{pmatrix} C_{1,j} \\ C_{2,j} \\ B_{1,j} \\ B_{1,j} \end{pmatrix} = \mathbf{M}_{4p} \begin{pmatrix} A_{1,j} \\ A_{2,j} \\ D_{1,j} \\ D_{2,j} \end{pmatrix}. \tag{16.2}$$

Due to the fact that photon losses are neglected within our treatment the matrix (16.1) has to fulfil the unitary condition $\mathbf{M}_{4p}^{\dagger}\mathbf{M}_{4p} = \mathbb{I}$. This ensures that the number of photons is conserved. A generalization to include some internal loss or scattering to other modes is straightforward and certainly helps to quantitatively model a specific experiment, but will not give qualitatively new insights.

In order to make statements about a tractor beam behavior of the injected light fields, we need to calculate the light induced force onto the particles. This can be done by following proven recipes [64; 115]. We calculate the forces acting on the particle via a Maxwell stress tensor based approach. In the effective 1D geometry of a fiber, it suffices to consider the Minkwoski's photon momenta P inside a medium with refractive index n

$$P = n\hbar k. \tag{16.3}$$

The total momentum of the light propagating in the i-th ($i \in \{1, 2\}$) mode at the left and right side of the j-th bead can be expressed in terms of the propagating photon numbers

$$N_{i,j}^{\mathrm{L}} = \frac{cn\epsilon_0}{2}\left(|A_{i,j}|^2 + |B_{i,j}|^2\right), \tag{16.4}$$

$$N_{i,j}^{\mathrm{R}} = \frac{cn\epsilon_0}{2}\left(|C_{i,j}|^2 + |D_{i,j}|^2\right) \tag{16.5}$$

at each side of the bead. The momentum left and right of the beads then reads

$$P_{tot}^{\mathrm{L}} = N_{1,j}^{\mathrm{L}}\hbar k_1 + N_{2,j}^{L}\hbar k_2, \tag{16.6}$$

$$P_{tot}^{\mathrm{R}} = N_{1,j}^{\mathrm{R}}\hbar k_1 + N_{2,j}^{\mathrm{R}}\hbar k_2. \tag{16.7}$$

The force on the jth bead thus can be simply found from the missing momentum which results in

$$F_j = \hbar k_1(N_{1,j}^{L} - N_{1,j}^{R}) + \hbar k_2(N_{2,j}^{\mathrm{L}} - N_{2,j}^{\mathrm{R}}). \tag{16.8}$$

Hence, the force onto the jth beam-splitter in terms of the amplitudes is given as

$$F_j = \frac{cn\epsilon_0\hbar}{2}(k_1(|A_{1,j}|^2 + |B_{1,j}|^2 - |C_{1,j}|^2) + k_2(|A_{2,j}|^2 + |B_{2,j}|^2 - |C_{2,j}|^2)). \tag{16.9}$$

The presented model allows us to efficiently calculate the force onto N beads for several different parameters. However, a full analytic treatment is rather tedious and we will focus on some special cases of reduced complexity before including all possible processes in the following. A concrete generic example can be found in Appendix A.

16.3. Forces for two forward propagating modes

While for very small point like scatterers there is a symmetry between forward and backward scattered light [64], for larger or thicker objects forward scattering is usually dominant with respect to reflection [106; 115] and the coupling between modes of the same propagation direction dominates (see e.g. Appendix A). Therefore we first consider larger particles of lower contrast and restrict our treatment to two different transverse forward propagating modes and injection from a single side. This already will show the essential physics without requiring a too complex analytic form.

16.3.1. Single particle

To study the fundamental effects of transverse forward mode coupling, we first investigate only a single particle in the fibre field, which will introduce coherent coupling between the two propagating modes. In this special case the nontrivial part of the four port matrix (16.1) reduces to a two port matrix and the amplitudes left and right of the

beam splitter are connected via the following matrix

$$\begin{pmatrix} C_1 \\ C_2 \end{pmatrix} = \mathbf{M}_{2p} \begin{pmatrix} A_1 \\ A_2 \end{pmatrix} = \begin{pmatrix} t_{11}e^{i\phi_{11}} & t_{21}e^{i\phi_{21}} \\ t_{12}e^{i\phi_{12}} & t_{22}e^{i\phi_{22}} \end{pmatrix} \begin{pmatrix} A_1 \\ A_2 \end{pmatrix}, \tag{16.10}$$

where we chose $A_1 \equiv A_{1,1}$, $A_2 \equiv A_{2,1}$, $C_1 \equiv A_{1,1}$ and $C_2 \equiv C_{2,1}$. The scattering process changes the relative mode amplitudes and adds a light phase via $e^{i\phi_{ij}}$. Here we can choose $\phi_{11} = 0$ without any restriction and for a single particle also ϕ_{22} will not change the force expression.
The unitarity condition $\mathbf{M}_{2p}^{\dagger} \cdot \mathbf{M}_{2p} = \mathbb{I}$ then reduces the number of physically relevant parameters to

$$t_{11} = t_{22} = t, \tag{16.11}$$

$$t_{12} = t_{21} = \sqrt{1-t^2}, \tag{16.12}$$

$$\phi_{12} = -\phi_{21} + (2n+1)\pi = \phi,\ n \in \mathbb{N}, \tag{16.13}$$

which finally leads to a much simpler form of the scattering matrix

$$\mathbf{M}'_{2p} = \begin{pmatrix} t & -e^{-i\phi}\sqrt{1-t^2} \\ e^{i\phi}\sqrt{1-t^2} & t \end{pmatrix}. \tag{16.14}$$

As a result the output amplitudes are connected with the input amplitudes via

$$C_1 = tA_1 + e^{i\phi}\sqrt{1-t^2}A_2, \tag{16.15}$$

$$C_2 = -e^{-i\phi}\sqrt{1-t^2}A_1 + tA_2. \tag{16.16}$$

To calculate the force we insert this result into (16.9) which leads to the force onto a single particle in two forward propagating modes

$$F_{\mathrm{SP}}^{2p} = \frac{cn\epsilon_0\hbar}{2}(k_2 - k_1)\left(\left(t^2-1\right)\left(|A_1|^2 - |A_2|^2\right) + t\sqrt{1-t^2}\left(e^{i\phi}A_1^*A_2 + e^{-i\phi}A_1A_2^*\right)\right). \tag{16.17}$$

The two wavenumbers (k_1 for the fundamental and k_2 for the higher order mode) differ in general and fulfil the condition $k_1 > k_2$. Let us now look at the special translation invariant case, where only one of the two modes is pumped and the other mode is only populated by scattered photons. There are two possible cases to consider. On the one

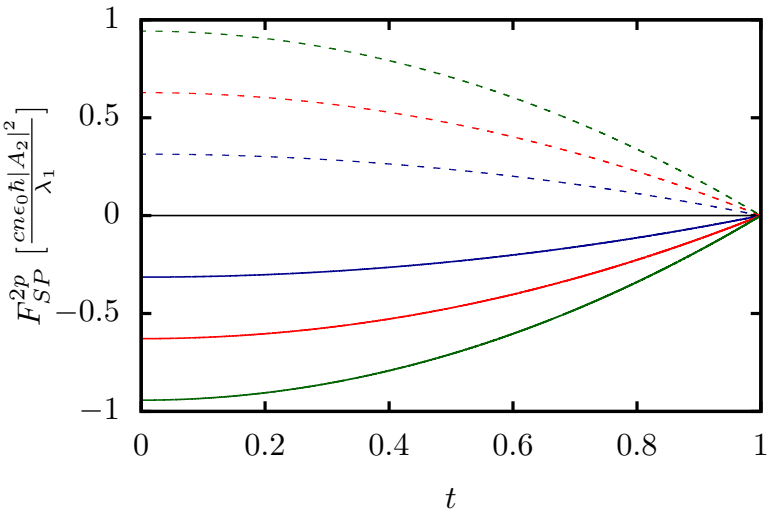

Figure 16.3.: Force on a single particle in only forward propagating modes considering only the fundamental (dashed line) or the higher order mode field (solid line) as input. The blue line corresponds to $k_2 = 0.9\ k_1$, the red line to $k_2 = 0.8\ k_1$ and the green line to $k_2 = 0.7\ k_1$.

hand only the fundamental mode can be pumped ($A_1 \neq 0$, $A_2 = 0$) and on the other hand only the higher order mode can be injected ($A_1 = 0$, $A_2 \neq 0$). The corresponding forces are shown in 16.3. One finds that the force on the particle is always negative, if the higher order mode is chosen as the input field. The negative force implies that for this configuration the particle is pulled in the direction against the incoming beam. It is fundamental to state that due to translation symmetry of the system, this force is the same anywhere along the fibre and the particle will be continuously pulled towards the source over very long distances.
Mathematically this behavior gets obvious, if one looks at the analytic expression for the force (16.18). Assuming only a higher order mode input field ($A_1 = 0$, $A_2 \neq 0$) the force simplifies to

$$F_{\mathrm{SP}}^{2p}|_{A_1=0} = \frac{cn\epsilon_0\hbar}{2}(k_1 - k_2)\left(t^2 - 1\right)|A_2|^2. \tag{16.18}$$

As mentioned above the conditions $0 \leq t \leq 1$ and $k_2 < k_1$ have to hold. Consequently, the force is always negative in this case. Following the same procedure but using the fundamental mode field as the input beam, leads to a positive force as depicted in 16.3 following the conventional expectation.

Lets now discuss the essential physics leading to this somewhat counterintuitive result. Due to the fact that the higher order mode contains a higher amount of transverse momentum and thus less longitudinal momentum than the fundamental mode, the scattering process between those modes (with amplitude t_{12}) is generally suppressed. Only some additional momentum provided by the bead closes this momentum gap and allows for scattering between the two modes. This is quite analogous to the case of Bessel tractor beams [234], but due to the presence of a light confining geometry the range of the effect is infinite in the studied case.

16.3.2. Two particles

As it has been seen and experimentally demonstrated in previous work [115] the two mode forward scattering model also well describes the long range inter-particle forces in this system. In the simplified case with no backscattering, however, the fields and the force on the first particle cannot be affected by a second one downstream the mode. Nevertheless, the field impinging on the second particle is the result of the mode mixing by the first and thus significantly depends on the relative distance allowing for stable configurations. Using the scattering matrix approach the outgoing amplitudes after the second particle can be calculated in the following manner:

$$\begin{pmatrix} C_{1,2} \\ C_{2,2} \end{pmatrix} = \mathbf{M}'_{2p} \cdot \mathbf{P}(d) \cdot \mathbf{M}'_{2p} \begin{pmatrix} A_{1,1} \\ A_{2,1} \end{pmatrix}, \tag{16.19}$$

with $A_{i,j}$ and $C_{i,j}$ being the input and output fields with mode i at the j-th particle. In addition, the free field propagation over a distance d (*i. e.* the propagation face shift) is included via a transfer matrix which connects the amplitudes on the right hand side of the first and the left side of the second beam-splitter

$$\mathbf{P}(d) = \begin{pmatrix} e^{ik_1 d} & 0 \\ 0 & e^{ik_2 d}. \end{pmatrix} \tag{16.20}$$

Here we assume identical particles for simplicity so that the scattering process is the same for both particles. Of course, the presented scheme can be generalized to more particles in a straightforward manner. The force on the j-th particle is then again defined by (16.9). To keep the discussion compact, we will restrict our treatment here

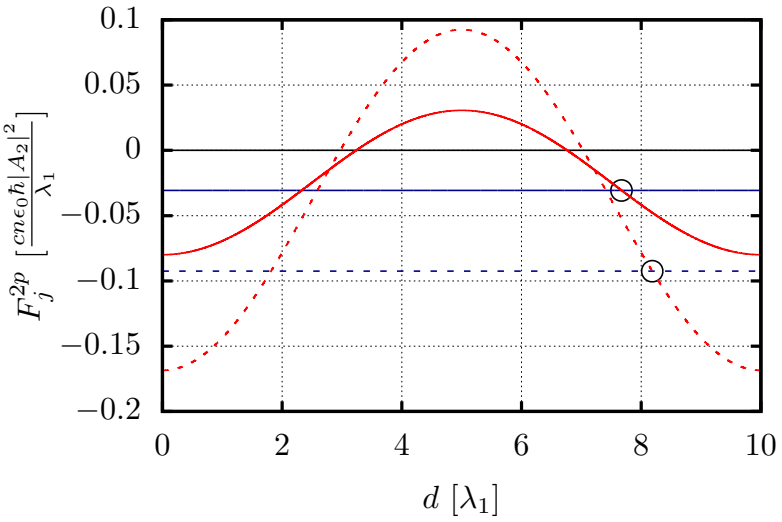

Figure 16.4.: Force on the first (blue) and second particle (red) in only forward propagating modes considering only the higher order mode field as input and choosing $k_2 = 0.9\ k_1$. The solid line corresponds to $t = 0.95$, thus (16.12) implies $t_{12} = 0.31$. The dashed line shows the results for $t = 0.84$ and $t_{12} = 0.54$. The black circles indicate stable distances.

to the two particle case. Due to the fact that the analytical expression of the forces is rather lengthy, it will be omitted here but the spatial dependence of the forces is presented in 16.4. Interestingly, one finds that for certain distances between the two particles, both particles can experience a negative or tractor force. Obviously as a next step one can ask for stable configurations of the two particles, *i. e.* configurations in which the particle's distance d remains constant and locked against small perturbations. This requires both forces to have the same value ($F_1 - F_2 = 0$) and at the same time one needs $\frac{\partial F_1}{\partial d} > 0$ and $\frac{\partial F_2}{\partial d} < 0$, i.e. a restoring force if the particles deviate from this equilibrium equal force position.

As an example we again choose the higher order mode as the input field ($A_1 = 0$, $A_2 \neq 0$). Interestingly, here stable distance configurations with a negative force on both particles can be found for the chosen parameters. Therefore, the particles are commonly attracted towards the beam source while they stay at a constant distance. This corresponds to a stable collective tractor beam configuration for the particles. Another interesting fact, which can be seen in 16.4 is that for certain distances beyond the stable point, the tractor force on the second particle can even be stronger than the one on a single particle. Hence the mode phase lock introduced by the first particle

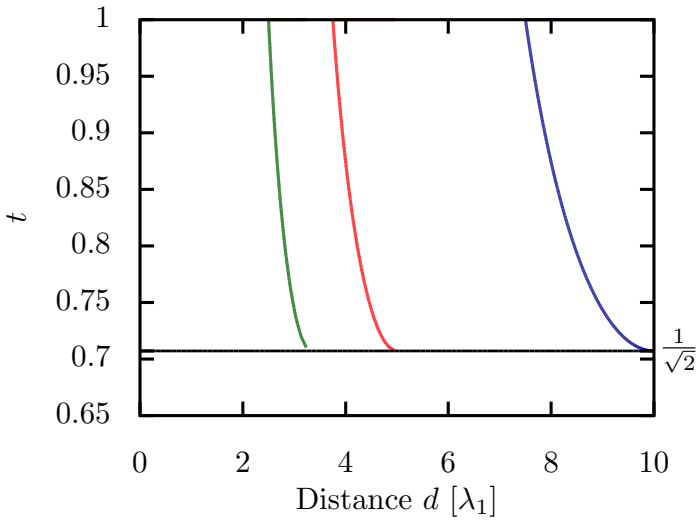

Figure 16.5.: Optical binding distances d as a function of the transmission coefficient t for two particles in forward propagating modes considering only the higher order mode field as input. The blue line corresponds to $k_2 = 0.9\ k_1$, the red line to $k_2 = 0.8\ k_1$ and the green line to $k_2 = 0.7\ k_1$.

creates an even stronger trap than on itself. Note the lower cutoff of the distances in 16.5, which reflects the fact that stable tractor beam configurations cannot be found for values of t below certain values. In particular the transmission t by the first particle has to exceed a certain threshold value in order to find a stationary two particle configuration. This is due to the fact that if too much light is scattered to the fundamental mode by the first particle, the relative mode amplitude ratio in the fiber between the two particles will be rather small and the tractor force on the second particle will always be too small to follow the first one against the beam propagation direction at a constant distance. Note that the particle force can also be seen as the simplest possible form of optical binding as the scattering of the first particle creates a series of dipole traps for the second one.

16.4. Four mode model including backscattering

Lets now turn to a more realistic model. While the relative magnitude of backward versus forward scattering can be small for large particles at low index contrast, it will of course never be exactly zero [115]. As the momentum transfer per photon in reflection is much larger than for forward mode mixing even a small amplitude could induce some

changes. In this section we will thus treat the whole 4-mode model as already described above and investigate, how much even small backscattering at the particles position can induce substantial force contributions. The scattering processes in this case are described by the general 4-port matrix (16.1). Losses to other modes or absorption also can be included by modifying the diagonal of this matrix.
Obviously the set of available parameters is rather large in this case and hardly can be exhaustively treated. Nevertheless, at least in principle for any concrete bead size, position, shape and mode geometry, they could be at least numerically calculated from a generalized Helmholtz equation. Here we will use a different approach and look at physically interesting parameter ranges. Once interesting parameters are found, one could look for geometries, where one could implement such scattering properties. In order to reduce the complexity we will first assume that both modes experience the same forward scattering amplitudes and phase shifts with negligible backscattering into the very same mode. This allows us to concentrate on the effects of mode cross-scattering processes which are at the origin of interesting multi-mode physics. A concrete example is presented in the appendix. Based on the above arguments we first set:

$$t_{11} = t_{22} = t, \tag{16.21}$$

$$r_{11} = r_{22} = 0. \tag{16.22}$$

We again also set the reference phases to zero ($\phi_{11} = \phi_{22} = 0$). The unitary condition for the full coupling matrix then again gives the following set of necessary conditions

$$t_{12} = t_{21}, \tag{16.23}$$

$$r_{12} = r_{21}, \tag{16.24}$$

$$t_{12} = \sqrt{1 - t^2 - r_{12}^2}, \tag{16.25}$$

$$\phi_{21} = -\phi + (2m - 1)\pi, \tag{16.26}$$

$$\psi_{21} = -\phi - (n + 1/2)\pi, \tag{16.27}$$

$$\psi_{12} = \phi + (n - 1/2)\pi, \quad m, n \in \mathbb{N}, \tag{16.28}$$

where we defined $\phi = \phi_{12}$. In this case the scattering matrix simplifies to

$$\mathbf{M}'_{4p} = \begin{pmatrix} t & -e^{-i\phi}t_{12} & 0 & ie^{-i\phi}r_{12} \\ e^{i\phi}t_{12} & t & ie^{i\phi}r_{12} & 0 \\ 0 & ie^{-i\phi}r_{12} & t & -e^{-i\phi}t_{12} \\ ie^{i\phi}r_{12} & 0 & e^{i\phi}t_{12} & t \end{pmatrix}. \tag{16.29}$$

Of course the two-port system as it has been investigated in the previous section can be reproduced by setting $r_{12} = 0$.

16.4.1. Single particle

We again start with investigating the forces acting on a single particle along the fiber. We follow the same procedure as presented above but with more amplitudes coupled by a larger matrix. Using (16.9) in order to calculate the force leads to

$$\begin{aligned} F_{\mathrm{SP}}^{4p} =& \frac{cn\epsilon_0\hbar}{2}\left(|A_1|^2\left(k_1\left(r_{12}^2+t_{12}^2\right)+k_2\left(r_{12}^2-t_{12}^2\right)\right)\right. \\ &+|A_2|^2\left(k_1\left(r_{12}^2-t_{12}^2\right)+k_2\left(r_{12}^2+t_{12}^2\right)\right) \\ &\left.+t_{12}t\left(k_1-k_2\right)\left(A_1A_2^*e^{i\phi}+A_1^*A_2e^{-i\phi}\right)\right). \end{aligned} \tag{16.30}$$

For injection of only a higher order mode field ($A_1 = 0$) this reduces to

$$F_{\mathrm{SP}}^{4p} = \frac{cn\epsilon_0\hbar}{2}\left[t_{12}^2\left(k_2-k_1\right)+r_{12}^2\left(k_1+k_2\right)\right]|A_2|^2, \tag{16.31}$$

which can be negative as long as the parameters fulfil the following condition:

$$\frac{r_{12}^2}{t_{12}^2} \leq \frac{k_1-k_2}{k_1+k_2}. \tag{16.32}$$

Fig. 16.6 shows an example how the backscattering process gives a negative force on the particle as long as r_{12} is not too large. Note that as the two momenta are usually not too different the condition on the smallness of back-reflection can be rather stringent.

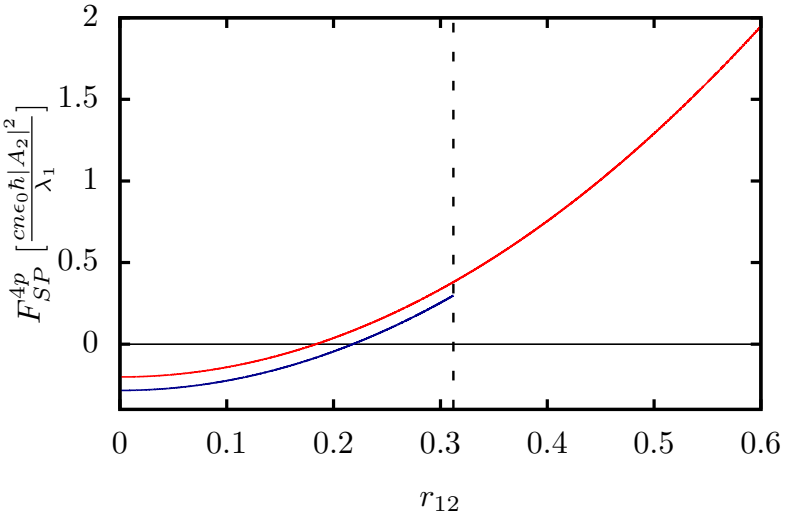

Figure 16.6.: Force on a single particle including back-reflection and considering only the higher order mode field as input field and $k_2 = 0.9\ k_1$. The blue line corresponds to $t_{12} = 0.95$ and the red line to $t_{12} = 0.8$. The dashed line illustrates the threshold on the reflection r_{12} defined by (16.25).

16.4.2. Two particles

As the scattering matrix (16.29) expresses the outgoing fields in terms of the incoming fields the expression for the fields generated by two beads formally looks similar to the case above. However, to find the amplitudes on two beads, the total transfer matrix M_{TM} has to be found in accordance with the prescribed boundary conditions. Here one immediately gets an infinite series of reflections and back reflections. As shown in previous work [80] this can be efficiently calculated by rearranging the terms of the matrix in a form which connects the amplitudes to the left and to the right of a particle in the form

$$\mathbf{M}_{TF} = \begin{pmatrix} \frac{t}{1-r_{12}^2} & \frac{ir_{12}t_{12}}{1-r_{12}^2} & -\frac{t_{12}e^{-i\phi}}{1-r_{12}^2} & -\frac{ir_{12}te^{-i\phi}}{1-r_{12}^2} \\ \frac{ir_{12}t_{12}}{1-r_{12}^2} & \frac{t}{1-r_{12}^2} & \frac{ir_{12}te^{-i\phi}}{1-r_{12}^2} & \frac{t_{12}e^{-i\phi}}{1-r_{12}^2} \\ \frac{t_{12}e^{i\phi}}{1-r_{12}^2} & -\frac{ie^{i\phi}r_{12}t}{1-r_{12}^2} & \frac{t}{1-r_{12}^2} & -\frac{ir_{12}t_{12}}{1-r_{12}^2} \\ \frac{ir_{12}te^{i\phi}}{1-r_{12}^2} & -\frac{t_{12}e^{i\phi}}{1-r_{12}^2} & -\frac{ir_{12}t_{12}}{1-r_{12}^2} & \frac{t}{1-r_{12}^2} \end{pmatrix}, \tag{16.33}$$

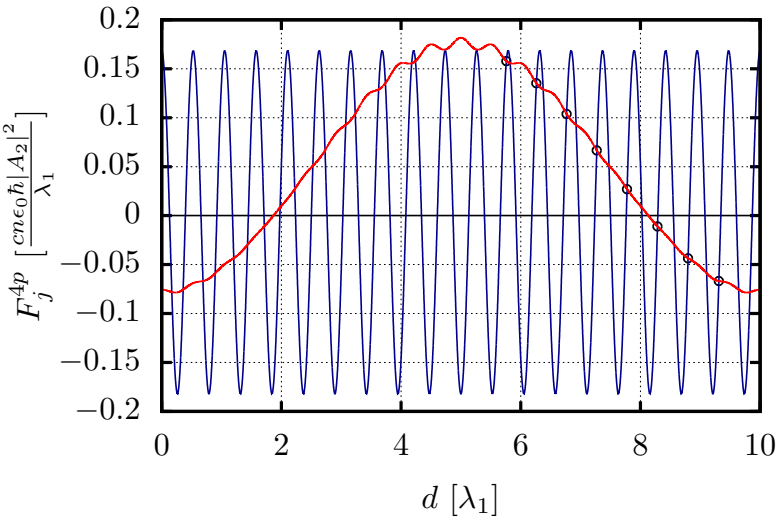

Figure 16.7.: Force on two particles including back-reflection and considering only the higher order mode field as input field and $k_2 = 0.9\ k_1$. The blue line corresponds to the force on the first and the red line to the force on the second particle. Here, we chose $t_{12} = 0.54$ and $r_{12} = 0.12$. Black circles indicate stable points.

so that

$$\begin{pmatrix} C_{1,2} \\ D_{1,2} \\ C_{2,2} \\ D_{2,2} \end{pmatrix} = \mathbf{M}_{TF} \cdot \mathbf{P}_4(d) \cdot \mathbf{M}_{TF} \begin{pmatrix} A_{1,1} \\ B_{1,1} \\ A_{2,1} \\ B_{2,1} \end{pmatrix}, \tag{16.34}$$

where $\mathbf{P}_4(d)$ is the 4 mode generalized propagation matrix for the fields:

$$\mathbf{P}_4(d) = \begin{pmatrix} e^{ik_1 d} & 0 & 0 & 0 \\ 0 & e^{-ik_1 d} & 0 & 0 \\ 0 & 0 & e^{ik_2 d} & 0 \\ 0 & 0 & 0 & e^{-ik_2 d} \end{pmatrix}. \tag{16.35}$$

In this rearranged form, the amplitudes on the particles can be found by solving these four equations for the required input and output fields. As the analytical expression even for the single particle force is rather complex, we will not give it here and simply show some numerical examples. We see that the presence of the second particle changes the interaction between the particles and the fields in a much more complex way as above. Indeed, both particles now are influenced by the presence and position of the

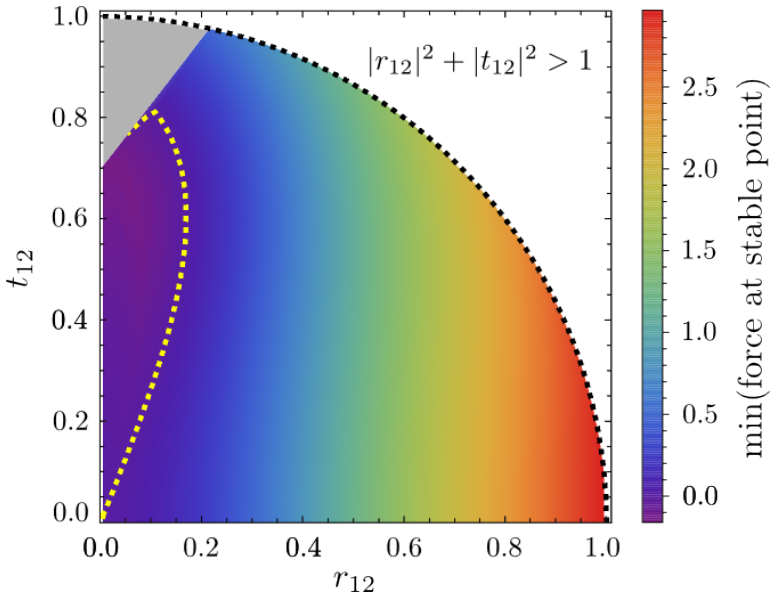

Figure 16.8.: The minimal possible force at a stable point plotted for different values of r_{12} and t_{12}. The yellow dashed line marks the zero line. In the grey region no stable solution exists at all and the black dashed line shows the threshold for reflection and transmission imposed by (16.25).

other one. Indeed, as demonstrated in Fig. 16.7 the force on the second particle now exhibits small but spatially fast fluctuations due to the interference of the reflected fields in addition to the larger oscillations from mode beating. Also the force on the first particle is oscillating now. These oscillations are a consequence of the interference between the incoming and backscattered fields. Here we see that the effective total backscattered field can be less than for a single bead as the field amplitudes from the two particles interfere like in a Fabry-Perot resonator driven with a resonant wavelength. Hence we can find parameter ranges with an even bigger tractor force than for a single particle. This can be enhanced by a collective mode coupling of the two particles. In general the distance of maximal tractor force on the first particle does not correspond to a stable distance, but we find a large number of potentially stable distances. A fair fraction of these correspond to a net negative force on both particles. Hence, we see that also the full model allows for a many particle tractor beam configurations.
If we analyze this fact in more detail, we find that there exists a certain region of parameters in which a stable two particle tractor beam, i.e. a collectively enhanced tractor, can be realized. This region corresponds to the one on the left side of the yellow dashed line in 16.8. Obviously, in order to establish a negative tractor beam force the

reflection as well as the transmission coefficients between the two modes must not exceed a certain critical value. On the one hand if the transmission is above a certain critical value no more stable point (*i. e.* points which fulfil the condition $F_1 - F_2 = 0$) can be found.) On the other hand, if the reflection coefficient exceeds a certain value the force can no longer be negative and the particles will always be pushed in the direction of the incoming laser beam. This effect is related to the result for two particles in forward propagating fields (*cf.* (16.32)). Nevertheless, due to the fact that the back-reflection for extended objects is in general rather small, the necessary parameter regime can be reached in some specific geometries like for example for beads trapped inside a two-mode hollow core fibre (see Appendix A).

16.5. Conclusions and outlook

We demonstrated that optical fibers supporting at least two transverse modes can be the basis of translation invariant tractor beam implementations dragging particles and even pairs of optically bound particles against the injected beam direction without the need of any external control or feedback. The results are easily generalizable to several particles. In practical implementations the remaining backscattering seems to be one of the central obstacles to overcome here. For the implementation, only the higher order mode has to be pumped via the one end of the fibre, where the particles should be transported with hardly any restrictions on the bandwidth or coherence length. Apart from being a neat physical mechanism, the tractor effect could be helpful in setups where one plans to extract particles from a trap source and load them into a dipole trap at the other end of the fiber [235].
In this work we have primarily shown that such tractor beams are theoretically possible and given the necessary boundary conditions on the parameters to be achieved. The main challenge in practice actually is to design the fibre in a way to maximize cross coupling between two modes and minimizing loss to others. In a multi-mode fibre the tractor force will be the bigger the higher the order of the injected mode and the larger the amplitude of the fundamental mode at the particle position. For a hollow core fibre coupling should be good using modes of the same symmetry as the TEM_{00} and TEM_{20} mode with a particle of about wavelength size at its center as shown in the appendix.

Acknowledgements: We thank C. Genes for helpful discussions and acknowledge support by the Austrian Science Fund FWF through projects SFB FoQuS P13 and I1697-N27. We also acknowledge fruitful discussions from S. Nic Chormaic, V. G. Truong and A. Maimaiti from the Okinawa Institute of Science and Technology Japan.

16.6. Appendix

A small particle placed inside the mode field of an optical waveguide or optical fiber will locally perturb the field and change its propagation. If one considers positions significantly left and right of the bead, where near field effects can be neglected, the propagation field can still be expanded in terms of the transverse eigenmodes of the waveguide. For a bead made of linear optical material the corresponding expansion coefficients on both sides are linearly connected by an effective transfer matrix.
The effect of the particle will be phase and amplitude changes of the modes induced by light scattering between various forward and backward propagation modes. In addition, some of the field could be absorbed or, equivalently, scattered to free space modes not guided by the fiber so that the transfer matrix is not necessarily unitary. As the latter effect cannot positively contribute to the tractor effect or inter-particle forces we will neglect it for this calculation of the mode coupling coefficients.
To obtain the coefficients one needs to solve the corresponding Helmholtz equation including proper boundary conditions, which for a detailed modelling requires rather extensive numerical calculations as e.g. presented in [115; 223]. Here we are mainly interested in the basic physics of the tractor force effect, which is contained in the relative magnitude of the effective coupling between different transverse modes. As shown above a strong tractor force requires stronger coupling of a mode to lower order modes than to higher order modes as well as very low reflection. For only two modes the coupling between the modes needs to be stronger than free space losses. In order to keep the complexity low we thus refrain to a paraxial approximation for the propagation of the fields. In this case the field evolution along a non-absorbing bead can be approximated by the effective optical Schrödinger equation, where the bead creates an effective potential for the transverse light field amplitude $\psi(r_\perp)$ propagating

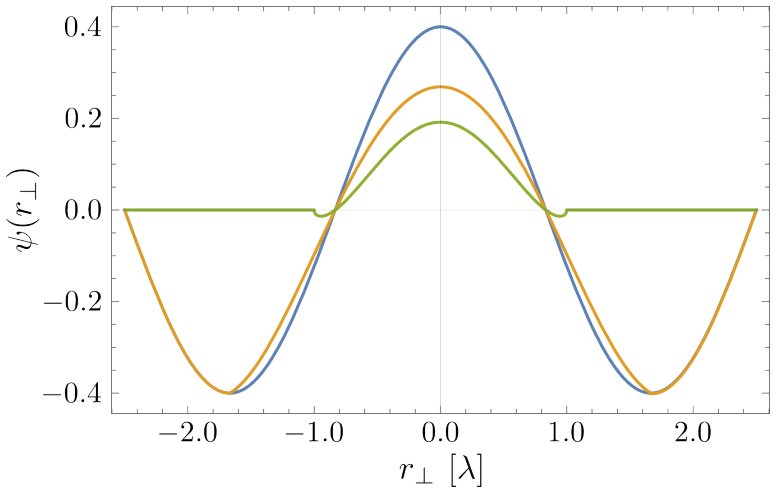

Figure 16.9.: Shape of the original (blue) and distorted mode function (real part orange, imaginary part green) for a spherical bead of refractive index $n = 1.25$ and diameter 2λ in the center of a rectangular waveguide for a waveguide diameter $a = 5\lambda$.

along the fiber direction z [236]:

$$\frac{i}{n_0 k_0}\partial_z \psi(r_\perp) = \left[\frac{-\Delta_\perp}{2n_0 k_0^2} + V_{opt}(r_\perp)\right]\psi(r_\perp). \tag{16.36}$$

In this case the optical potential of the bead

$$V_{opt}(r_\perp) = \frac{n_0^2 - n(r_\perp^2)}{2n_0^2} \tag{16.37}$$

creates an effective local attractive potential which couples the various transverse modes. Here $n(r_\perp)$) is the bead refractive index distribution and n_0 the background refractive index. Below we will try to identify a favorable case for generating a tractor force in a simple configuration. To show the qualitative behaviour we simply assume a perfect square waveguide with a certain diamater a [231] or a hollow guide with sharp (metallic) boundaries [230] where the mode functions are simply given by harmonic functions vanishing at the boundaries.

For a small refractive index of the bead and a not too large size, the effect of a bead of diameter d on the field can then be simply estimated by the spatially accumulated phase shift

$$e^{i\phi(r_\perp)} \approx e^{i\int_0^d V_{opt}(r_\perp)dz} \tag{16.38}$$

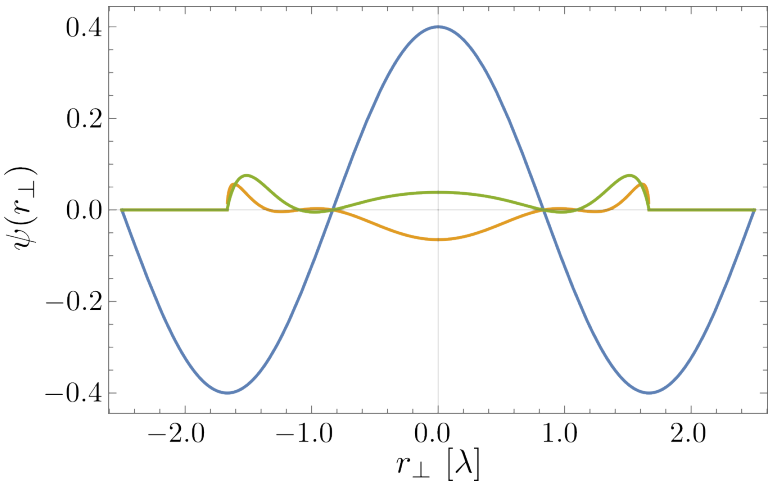

Figure 16.10.: Shape of the original (blue) and the reflected mode function for a spherical bead of refractive index $n = 1.25$ and diameter 2λ in the center of a rectangular waveguide for a waveguide diameter $a = 5\lambda$.

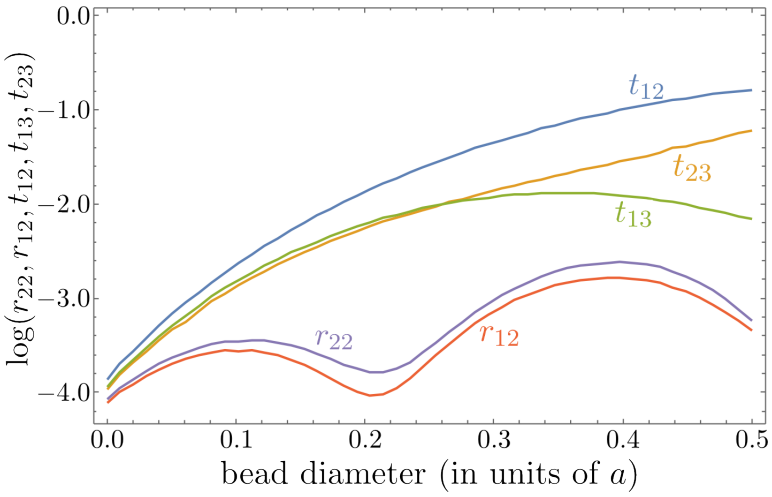

Figure 16.11.: Mode coupling coefficients for the three lowest order symmetric modes for a spherical bead of index $n = 1.5$ in the center of a rectangular waveguide as function of bead diameter in units of the waveguide diameter $a = 9\lambda$.

by field while traversing the bead and a small reflected component [95]. This is shown in the example in 16.9 below, where we plot the original third order mode function and its distorted form (real and imaginary part) after the bead on a cut along the x-axis. Similarly we can estimate the reflected contribution as shown in 16.10.
In this limit the mode coupling coefficients can then be simply obtained by projecting the distorted and reflected fields onto the original modes. This will strongly depend on position, size and refractive index of the bead. If we want strong overlap between a higher order and a lower order mode it is thus favourable to put the bead at a position, where the target mode has a high amplitude but the unwanted modes are low or strongly varying. As an example here in 16.11 we show the case of a bead of varying size exactly at the center of the waveguide where the first and third order mode amplitudes are large, while others are small. We see that indeed the desired coupling between mode one and two is about one order of magnitude bigger than the other couplings and reflections. Hence, this configuration should lead to a sizeable tractor force for a suitable particle size range.

17. Conclusions and outlook

As part of the wider field of quantum optics and AMO physics the present thesis is specially devoted to the theoretical modelling and study of the dynamics of nanoparticles and atoms coupled to the field of optical nanofibres. The publications presented in this thesis investigate various central and intriguing physical phenomena and it is shown that particles trapped along a nanofibre can provide a physical basis for various applications.

As an introductory step we developed a new model, where particles trapped in the evanescent field of a nanofibre are additionally illuminated by a transverse pump field and scatter light from this field into the fibre. Although the model is quite simplified, it still provides a powerful tool to describe the interactions between the particles and the fibre field and to study important physical properties of their collective dynamics.

The first section of the thesis introduces the theoretical background and the model to understand the new physical phenomena in the publications presented subsequently. A scattering matrix approach was developed to describe the interactions between the particles and the fibre field. Based on this the forces acting on the particles were calculated.

Using this approach it could be demonstrated that particles trapped in the evanescent field of a nanofibre and transversely illuminated by a pump field collectively interact with the fibre field and can self-order in stable configurations depending on the coupling strength between the particles and the fibre field. The particles self-order to localize high field intensities between them and thus act like mirrors. When slightly shifting a particle from its stable position it affects all the other particles and collective oscillations of all particles arise.

In a next step the transverse pump field was described by a broadband field, which leads to an exponentially decaying force depending on the bandwidth of the field. The particles are still able to find stable self-ordered configurations. Using several broadband fields with different frequencies and intensities the forces between the particles can be

tailored and even turned off. We developed a quantum model where we used this fact to simulate Coulomb interactions between trapped ions and implemented quantum gates. Such a system is challenging to realize experimentally as the transverse pump field could exert a high radiation pressure on the particles, but recently, Rauschenbeutel and coworkers managed to transversely illuminate particles trapped along a nanofibre [46]. The particles scatter this field and part of this field couples to the guided fibre mode. Some calculations reported in this thesis could reproduce results of Chang et al. [15], where he assumed resonant excitations of the internal states of atoms coupled to a waveguide. When taking the weak scattering limit for far detuned light and eliminating the internal states, the oscillation frequencies from eq. (5.18) and the optical potentials from eq. (12.2) coincide in both works.

In conclusion, the present thesis demonstrates that particles coupled to a nanofibre provide a powerful and versatile tool for many applications. As the particles can be trapped along the fibre and their interactions can be manipulated, more complex systems can be simulated. After further development this model can be used for quantum simulation as well as for quantum computation. When additionally including backscattering effects and chirality related scattering [55–57; 193; 194] the calculations could be very challenging, but also improve the model and provide further control possibilities of this system.

In the present thesis we only considered the motion of the particles along the nanofibre, but in an extended approach one can also develop a 3D system and include transverse motion of the particles. Furthermore, the study of the interactions of multistate atoms with the nanofibre field or investigating cooling effects of the system are also promising research directions. Our scattering model describing the interaction of particles with a nanofibre field can also be adjusted to other systems with particles coupled to guided fields, e.g. particles in a hollow core or photonic crystal fibre.

Bibliography

[1] J. Kepler, "De cometis libelli tres i. astronomicus, theoremata continens de novam... iii. astrologicus, de significationibus cometarum annorum motu cometarum... ii. physicus, continens physiologiam cometarum 1607 et 1618," *De cometis libelli tres I. astronomicus*, 1619.

[2] A. Ashkin, "Acceleration and trapping of particles by radiation pressure," *Phy. Rev. Lett*, vol. 24, no. 4, p. 156, 1970.

[3] A. Ashkin, J. M. Dziedzic, J. E. Bjorkholm, and S. Chu, "Observation of a single-beam gradient force optical trap for dielectric particles," *Opt. Lett.*, vol. 11, no. 5, pp. 288–290, 1986.

[4] P. Horak, G. Hechenblaikner, K. M. Gheri, H. Stecher, and H. Ritsch, "Cavity-induced atom cooling in the strong coupling regime," *Phy. Rev. Lett*, vol. 79, no. 25, p. 4974, 1997.

[5] V. Vuletić and S. Chu, "Laser cooling of atoms, ions, or molecules by coherent scattering," *Phy. Rev. Lett*, vol. 84, no. 17, p. 3787, 2000.

[6] P. Domokos and H. Ritsch, "Collective cooling and self-organization of atoms in a cavity," *Phy. Rev. Lett*, vol. 89, no. 25, p. 253003, 2002.

[7] N. Hodgson and H. Weber, *Optical resonators: fundamentals, advanced concepts, applications*, vol. 108. Springer Science & Business Media, 2005.

[8] F. Mivehvar, F. Piazza, T. Donner, and H. Ritsch, "Cavity qed with quantum gases: New paradigms in many-body physics," *arXiv preprint arXiv:2102.04473*, 2021.

[9] A. S. Sheremet, M. I. Petrov, I. V. Iorsh, A. V. Poshakinskiy, and A. N. Poddubny, "Waveguide quantum electrodynamics: collective radiance and photon-photon correlations," *arXiv preprint arXiv:2103.06824v1*, 2021.

[10] T. A. Birks and Y. W. Li, "The shape of fiber tapers," *J. Light. Technol.*, vol. 10, no. 4, pp. 432–438, 1992.

[11] E. Vetsch, D. Reitz, G. Sagué, R. Schmidt, S. Dawkins, and A. Rauschenbeutel, "Optical interface created by laser-cooled atoms trapped in the evanescent field surrounding an optical nanofiber," *Phy. Rev. Lett*, vol. 104, no. 20, p. 203603, 2010.

[12] D. Kornovan, N. Corzo, J. Laurat, and A. Sheremet, "Extremely subradiant states in a periodic one-dimensional atomic array," *Phys. Rev. A*, vol. 100, no. 6, p. 063832, 2019.

[13] Y. Li and C. Argyropoulos, "Controlling collective spontaneous emission with plasmonic waveguides," *Opt. Express*, vol. 24, no. 23, pp. 26696–26708, 2016.

[14] A. S. Prasad, J. Hinney, S. Mahmoodian, K. Hammerer, S. Rind, P. Schneeweiss, A. S. Sørensen, J. Volz, and A. Rauschenbeutel, "Correlating photons using the collective nonlinear response of atoms weakly coupled to an optical mode," *Nat. Photonics*, vol. 14, no. 12, pp. 719–722, 2020.

[15] D. E. Chang, J. I. Cirac, and H. J. Kimble, "Self-organization of atoms along a nanophotonic waveguide," *Phys. Rev. Lett.*, vol. 110, p. 113606, 2013.

[16] D. Holzmann, M. Sonnleitner, and H. Ritsch, "Self-ordering and collective dynamics of transversely illuminated point-scatterers in a 1d trap," *Eur. Phys. J. D*, vol. 68, no. 11, p. 352, 2014.

[17] I. M. Georgescu, S. Ashhab, and F. Nori, "Quantum simulation," *Rev. Mod. Phys.*, vol. 86, no. 1, p. 153, 2014.

[18] E. Kim, X. Zhang, V. S. Ferreira, J. Banker, J. K. Iverson, A. Sipahigil, M. Bello, A. González-Tudela, M. Mirhosseini, and O. Painter, "Quantum electrodynamics in a topological waveguide," *Phys. Rev. X*, vol. 11, no. 1, p. 011015, 2021.

[19] R. P. Feynman, "Simulating physics with computers," *Int. J. Theor. Phys*, vol. 21, no. 6/7, 1982.

[20] M. J. Hartmann, "Quantum simulation with interacting photons," *J. Opt.*, vol. 18, no. 10, p. 104005, 2016.

[21] C. Noh and D. G. Angelakis, "Quantum simulations and many-body physics with light," *Reports on Progress in Physics*, vol. 80, no. 1, p. 016401, 2016.

[22] T. Tashima, H. Takashima, and S. Takeuchi, "Direct optical excitation of an nv center via a nanofiber bragg-cavity: a theoretical simulation," *Opt. Express*, vol. 27, no. 19, pp. 27009–27016, 2019.

[23] D. G. Angelakis, M.-X. Huo, D. Chang, L. C. Kwek, and V. Korepin, "Mimicking interacting relativistic theories with stationary pulses of light," *Phy. Rev. Lett*, vol. 110, no. 10, p. 100502, 2013.

[24] W. S. Leong, M. Xin, Z. Chen, S. Chai, Y. Wang, and S.-Y. Lan, "Large array of schrödinger cat states facilitated by an optical waveguide," *Nat. Commun.*, vol. 11, no. 1, pp. 1–7, 2020.

[25] G. Kewes, M. Schoengen, O. Neitzke, P. Lombardi, R.-S. Schönfeld, G. Mazzamuto, A. W. Schell, J. Probst, J. Wolters, B. Löchel, *et al.*, "A realistic fabrication and design concept for quantum gates based on single emitters integrated in plasmonic-dielectric waveguide structures," *Sci. Rep.*, vol. 6, no. 1, pp. 1–10, 2016.

[26] V. Paulisch, H. Kimble, and A. González-Tudela, "Universal quantum computation in waveguide qed using decoherence free subspaces," *New J. Phys.*, vol. 18, no. 4, p. 043041, 2016.

[27] Y. Li, L. Aolita, D. E. Chang, and L. C. Kwek, "Robust-fidelity atom-photon entangling gates in the weak-coupling regime," *Phy. Rev. Lett*, vol. 109, no. 16, p. 160504, 2012.

[28] A. Gonzalez-Tudela, D. Martin-Cano, E. Moreno, L. Martin-Moreno, C. Tejedor, and F. J. Garcia-Vidal, "Entanglement of two qubits mediated by one-dimensional plasmonic waveguides," *Phy. Rev. Lett*, vol. 106, no. 2, p. 020501, 2011.

[29] S. Longhi, "Optical realization of the two-site bose–hubbard model in waveguide lattices," *J. Phys. B: Atomic, Molecular and Optical Physics*, vol. 44, no. 5, p. 051001, 2011.

[30] M.-X. Huo, C. Noh, B. Rodríguez-Lara, and D. G. Angelakis, "Quantum simulation of cooper pairing with photons," *Phys. Rev. A*, vol. 86, no. 4, p. 043840, 2012.

[31] J. Hoffman, S. Ravets, J. Grover, P. Solano, P. Kordell, J. Wong-Campos, L. Orozco, and S. Rolston, "Ultrahigh transmission optical nanofibers," *AIP Adv.*, vol. 4, no. 6, p. 067124, 2014.

[32] A. Snyder, "Optical waveguide theory," *Springer US*, 1983.

[33] G. Brambilla, "Optical fibre nanowires and microwires: a review," *J. Opt.*, vol. 12, no. 4, p. 043001, 2010.

[34] T. Nieddu, V. Gokhroo, and S. N. Chormaic, "Optical nanofibres and neutral atoms," *J. Opt.*, vol. 18, no. 5, p. 053001, 2016.

[35] F. Le Kien, J. Liang, K. Hakuta, and V. Balykin, "Field intensity distributions and polarization orientations in a vacuum-clad subwavelength-diameter optical fiber," *Opt. Commun.*, vol. 242, no. 4-6, pp. 445–455, 2004.

[36] Smith, King, and Wilkins, "Optics and photonics," *Wiley*, 2007.

[37] A. Masalov and V. Minogin, "Pumping of higher-order modes of an optical nanofiber by laser excited atoms," *Laser Phys. Lett.*, vol. 10, no. 7, p. 075203, 2013.

[38] R. Kumar, V. Gokhroo, and S. N. Chormaic, "Multi-level cascaded electromagnetically induced transparency in cold atoms using an optical nanofibre interface," *New J. Phys.*, vol. 17, no. 12, p. 123012, 2015.

[39] A. Masalov and V. Minogin, "Spontaneous decay rates of the hyperfine structure atomic states into an optical nanofiber," *J. Exp. Theor. Phys.*, vol. 118, no. 5, pp. 714–722, 2014.

[40] J. Dalibard and C. Cohen-Tannoudji, "Dressed-atom approach to atomic motion in laser light: the dipole force revisited," *J. Opt. Soc. Am.*, vol. 2, no. 11, 1985.

[41] P. Domokos and H. Ritsch, "Mechanical effects of light in optical resonators," *J. Opt. Soc. Am. B*, vol. 20, no. 5, pp. 1098–1130, 2003.

[42] D. A. Steck, "Quantum and atom optics," 2007.

[43] J. Jackson, "Classical electrodynamics," *John Wiley & Sons: New York*, 1998.

[44] Y. B. Ovchinnikov, S. Shul'Ga, and V. Balykin, "An atomic trap based on evanescent light waves," *Journal of Physics B: Atomic, Molecular and Optical Physics*, vol. 24, no. 14, p. 3173, 1991.

[45] F. Le Kien, V. Balykin, and K. Hakuta, "Atom trap and waveguide using a two-color evanescent light field around a subwavelength-diameter optical fiber," *Phys. Rev. A*, vol. 70, no. 6, p. 063403, 2004.

[46] Y. Meng, C. Liedl, S. Pucher, A. Rauschenbeutel, and P. Schneeweiss, "Imaging and localizing individual atoms interfaced with a nanophotonic waveguide," *Phy. Rev. Lett*, vol. 125, no. 5, p. 053603, 2020.

[47] F. Le Kien, S. Dutta Gupta, V. I. Balykin, and K. Hakuta, "Spontaneous emission of a cesium atom near a nanofiber: Efficient coupling of light to guided modes," *Phys. Rev. A*, vol. 72, p. 032509, Sep 2005.

[48] X. Wang, P. Zhang, G. Li, and T. Zhang, "High-efficiency coupling of single quantum emitters into hole-tailored nanofibers," *Opt. Express*, vol. 29, no. 7, pp. 11158–11168, 2021.

[49] T. Lund-Hansen, S. Stobbe, B. Julsgaard, H. Thyrrestrup, T. Sünner, M. Kamp, A. Forchel, and P. Lodahl, "Experimental realization of highly efficient broadband coupling of single quantum dots to a photonic crystal waveguide," *Phy. Rev. Lett*, vol. 101, no. 11, p. 113903, 2008.

[50] L. Scarpelli, B. Lang, F. Masia, D. Beggs, E. Muljarov, A. Young, R. Oulton, M. Kamp, S. Höfling, C. Schneider, *et al.*, "99% beta factor and directional coupling of quantum dots to fast light in photonic crystal waveguides determined by spectral imaging," *Phys. Rev. B*, vol. 100, no. 3, p. 035311, 2019.

[51] F. Liu, A. J. Brash, J. O'Hara, L. M. Martins, C. L. Phillips, R. J. Coles, B. Royall, E. Clarke, C. Bentham, N. Prtljaga, *et al.*, "High purcell factor generation of indistinguishable on-chip single photons," *Nat. Nanotechnol.*, vol. 13, no. 9, pp. 835–840, 2018.

[52] A. Goban, C.-L. Hung, J. Hood, S.-P. Yu, J. Muniz, O. Painter, and H. Kimble, "Superradiance for atoms trapped along a photonic crystal waveguide," *Phy. Rev. Lett*, vol. 115, no. 6, p. 063601, 2015.

[53] J. McGuirk, D. Harber, J. M. Obrecht, and E. A. Cornell, "Alkali-metal adsorbate polarization on conducting and insulating surfaces probed with bose-einstein condensates," *Phys. Rev. A*, vol. 69, no. 6, p. 062905, 2004.

[54] D. Chang, J. Douglas, A. González-Tudela, C.-L. Hung, and H. Kimble, "Colloquium: Quantum matter built from nanoscopic lattices of atoms and photons," *Rev. Mod. Phys.*, vol. 90, no. 3, p. 031002, 2018.

[55] P. Lodahl, S. Mahmoodian, S. Stobbe, A. Rauschenbeutel, P. Schneeweiss, J. Volz, H. Pichler, and P. Zoller, "Chiral quantum optics," *Nature*, vol. 541, no. 7638, pp. 473–480, 2017.

[56] S. Mahmoodian, G. Calajó, D. E. Chang, K. Hammerer, and A. S. Sørensen, "Dynamics of many-body photon bound states in chiral waveguide qed," *Phys. Rev. X*, vol. 10, no. 3, p. 031011, 2020.

[57] R. Jones, G. Buonaiuto, B. Lang, I. Lesanovsky, and B. Olmos, "Collectively enhanced chiral photon emission from an atomic array near a nanofiber," *Phy. Rev. Lett*, vol. 124, no. 9, p. 093601, 2020.

[58] N. V. Corzo, B. Gouraud, A. Chandra, A. Goban, A. S. Sheremet, D. V. Kupriyanov, and J. Laurat, "Large Bragg Reflection from One-Dimensional Chains of Trapped Atoms Near a Nanoscale Waveguide," *ArXiv e-prints*, Apr. 2016.

[59] R. Coles, D. Price, J. Dixon, B. Royall, E. Clarke, P. Kok, M. Skolnick, A. Fox, and M. Makhonin, "Chirality of nanophotonic waveguide with embedded quantum emitter for unidirectional spin transfer," *Nat. Commun.*, vol. 7, no. 1, pp. 1–7, 2016.

[60] M. Scheucher, A. Hilico, E. Will, J. Volz, and A. Rauschenbeutel, "Quantum optical circulator controlled by a single chirally coupled atom," *Science*, vol. 354, no. 6319, pp. 1577–1580, 2016.

[61] A. Javadi, D. Ding, M. H. Appel, S. Mahmoodian, M. C. Löbl, I. Söllner, R. Schott, C. Papon, T. Pregnolato, S. Stobbe, *et al.*, "Spin–photon interface and spin-controlled photon switching in a nanobeam waveguide," *Nat. Nanotechnol.*, vol. 13, no. 5, pp. 398–403, 2018.

[62] A. Xuereb, C. Genes, and A. Dantan, "Collectively enhanced optomechanical coupling in periodic arrays of scatterers," *Phys. Rev.*, vol. A 88, no. 5, p. 053803, 2013.

[63] I. Deutsch, R. Spreeuw, S. Rolston, and W. Phillips, "Photonic band gaps in optical lattices," *Phys. Rev. A*, vol. 52, no. 2, p. 1394, 1995.

[64] J. Asbóth, H. Ritsch, and P. Domokos, "Optomechanical coupling in a one-dimensional optical lattice," *Phys. Rev. A*, vol. 77, no. 6, p. 063424, 2008.

[65] L. Novotny and B. Hecht, "Principles of nano-optics," *Cambridge*, 2006.

[66] G. Birkl, M. Gatzke, I. Deutsch, S. Rolston, and W. Phillips, "Bragg scattering from atoms in optical lattices," *Phy. Rev. Lett*, vol. 75, no. 15, p. 2823, 1995.

[67] A. T. Black, H. W. Chan, and V. Vuletić, "Observation of collective friction forces due to spatial self-organization of atoms: from rayleigh to bragg scattering," *Phy. Rev. Lett*, vol. 91, no. 20, p. 203001, 2003.

[68] N. Piovella, R. Bonifacio, B. McNeil, and G. Robb, "Superradiant light scattering and grating formation in cold atomic vapours," *Opt. Commun.*, vol. 187, no. 1, pp. 165–170, 2001.

[69] V. Demergis and E.-L. Florin, "Ultrastrong optical binding of metallic nanoparticles," *Nano Lett.*, vol. 12, no. 11, pp. 5756–5760, 2012.

[70] H. Ritsch, P. Domokos, F. Brennecke, and T. Esslinger, "Cold atoms in cavity-generated dynamical optical potentials," *Rev. Mod. Phys.*, vol. 85, pp. 553–601, 2013.

[71] G. Labeyrie, E. Tesio, P. M. Gomes, G.-L. Oppo, W. J. Firth, G. R. Robb, A. S. Arnold, R. Kaiser, and T. Ackemann, "Optomechanical self-structuring in a cold atomic gas," *Nat. Photonics*, vol. 8, no. 4, pp. 321–325, 2014.

[72] T. Grießer and H. Ritsch, "Light induced crystallization of cold atoms in a thin 1D optical tube," *arXiv preprint arXiv:1303.7359*, 2013.

[73] E. Shahmoon, I. Mazets, and G. Kurizki, "Giant vacuum forces via transmission lines," *Proc. Natl. Acad. Sci. USA*, vol. 111, no. 29, pp. 10485–10490, 2014.

[74] K. Dholakia and P. Zemánek, "Colloquium: Gripped by light: Optical binding," *Rev. Mod. Phys.*, vol. 82, no. 2, p. 1767, 2010.

[75] W. Singer, M. Frick, S. Bernet, and M. Ritsch-Marte, "Self-organized array of regularly spaced microbeads in a fiber-optical trap," *J. Opt. Soc. Am. B*, vol. 20, pp. 1568–1574, Jul 2003.

[76] J.-M. R. Fournier, G. Boer, G. Delacretaz, P. M. Jacquot, J. Rohner, and R. P. Salathe, "Building optical matter with binding and trapping forces," *Proc. SPIE*, vol. 5514, pp. 309–317, 2004.

[77] D. Chang, L. Jiang, A. Gorshkov, and H. Kimble, "Cavity qed with atomic mirrors," *New J. Phys.*, vol. 14, no. 6, p. 063003, 2012.

[78] J. Asboth and P. Domokos, "Comment on „coupled dynamics of atoms and radiation-pressure-driven interferometers" and „superstrong coupling regime of cavity quantum electrodynamics"," *Phys. Rev. A*, vol. 76, no. 5, p. 057801, 2007.

[79] J. Asbóth, H. Ritsch, and P. Domokos, "Collective excitations and instability of an optical lattice due to unbalanced pumping," *Phys. Rev. Lett.*, vol. 98, no. 20, p. 203008, 2007.

[80] S. Ostermann, M. Sonnleitner, and H. Ritsch, "Scattering approach to two-colour light forces and self-ordering of polarizable particles," *New J. Phys.*, vol. 16, no. 4, p. 043017, 2014.

[81] M. Sonnleitner, M. Ritsch-Marte, and H. Ritsch, "Optomechanical deformation and strain in elastic dielectrics," *New J. Phys.*, vol. 14, no. 10, p. 103011, 2012.

[82] A. Xuereb, P. Domokos, J. Asbóth, P. Horak, and T. Freegarde, "Scattering theory of cooling and heating in optomechanical systems," *Phys. Rev. A*, vol. 79, no. 5, p. 053810, 2009.

[83] M. I. Antonoyiannakis and J. B. Pendry, "Electromagnetic forces in photonic crystals," *Phys. Rev. B*, vol. 60, pp. 2363–2374, Jul 1999.

[84] T. Ramos, H. Pichler, A. J. Daley, and P. Zoller, "Quantum spin dimers from chiral dissipation in cold-atom chains," *Phys. Rev. Lett.*, vol. 113, p. 237203, Dec 2014.

[85] G. Hétet, L. Slodička, M. Hennrich, and R. Blatt, "Single atom as a mirror of an optical cavity," *Phys. Rev. Lett.*, vol. 107, no. 13, p. 133002, 2011.

[86] R. M. Gray, *Toeplitz and circulant matrices: A review.* now publishers inc, 2006.

[87] P. W. Courteille, S. Bux, E. Lucioni, K. Lauber, T. Bienaime, R. Kaiser, and N. Piovella, "Modification of radiation pressure due to cooperative scattering of light," *Eur. Phys. J. D*, vol. 58, no. 1, pp. 69–73, 2010.

[88] S. L. Bromley, B. Zhu, M. Bishof, X. Zhang, T. Bothwell, J. Schachenmayer, T. L. Nicholson, R. Kaiser, S. F. Yelin, M. D. Lukin, *et al.*, "Collective atomic scattering and motional effects in a dense coherent medium," *Nat. Commun.*, vol. 7, 2016.

[89] T. Bienaime, S. Bux, E. Lucioni, P. W. Courteille, N. Piovella, and R. Kaiser, "Observation of a cooperative radiation force in the presence of disorder," *Phy. Rev. Lett*, vol. 104, no. 18, p. 183602, 2010.

[90] H. Bender, C. Stehle, S. Slama, R. Kaiser, N. Piovella, C. Zimmermann, and P. W. Courteille, "Observation of cooperative mie scattering from an ultracold atomic cloud," *Phys. Rev. A*, vol. 82, no. 1, p. 011404, 2010.

[91] K. M. Douglass, S. Sukhov, and A. Dogariu, "Superdiffusion in optically controlled active media," *Nat. Photonics*, vol. 6, pp. 834–837, Dec. 2012.

[92] M. M. Burns, J.-M. Fournier, and J. A. Golovchenko, "Optical binding," *Phy. Rev. Lett*, vol. 63, no. 12, p. 1233, 1989.

[93] E. Tesio, G. Robb, T. Ackemann, W. Firth, and G.-L. Oppo, "Spontaneous optomechanical pattern formation in cold atoms," *Phys. Rev. A*, vol. 86, no. 3, p. 031801, 2012.

[94] H. Zoubi and H. Ritsch, "Hybrid quantum system of a nanofiber mode coupled to two chains of optically trapped atoms," *New J. Phys.*, vol. 12, no. 10, p. 103014, 2010.

[95] P. Domokos, P. Horak, and H. Ritsch, "Quantum description of light-pulse scattering on a single atom in waveguides," *Phys. Rev. A*, vol. 65, no. 3, p. 033832, 2002.

[96] P. Horak, P. Domokos, and H. Ritsch, "Giant light shift of atoms near optical microstructures," *arXiv preprint quant-ph/0108006*, 2001.

[97] J. Lee, D. Park, S. Mittal, M. Dagenais, and S. Rolston, "Integrated optical dipole trap for cold neutral atoms with an optical waveguide coupler," *arXiv preprint arXiv:1303.2922*, 2013.

[98] A. Goban, K. Choi, D. Alton, D. Ding, C. Lacroûte, M. Pototschnig, T. Thiele, N. Stern, and H. Kimble, "Demonstration of a state-insensitive, compensated nanofiber trap," *Phy. Rev. Lett*, vol. 109, no. 3, p. 033603, 2012.

[99] H. Sørensen, J.-B. Béguin, K. Kluge, I. Iakoupov, A. Sørensen, J. Müller, E. Polzik, and J. Appel, "Coherent backscattering of light off one-dimensional atomic strings," *arXiv preprint arXiv:1601.04869*, 2016.

[100] D. Holzmann and H. Ritsch, "Collective scattering and oscillation modes of optically bound point particles trapped in a single mode waveguide field," *Opt. Express*, vol. 23, pp. 31793–31806, Dec 2015.

[101] S. Ostermann, F. Piazza, and H. Ritsch, "Spontaneous crystallization of light and ultracold atoms," *Phys. Rev. X*, vol. 6, p. 021026, May 2016.

[102] H. Pichler, T. Ramos, A. J. Daley, and P. Zoller, "Quantum optics of chiral spin networks," *Phys. Rev. A*, vol. 91, no. 4, p. 042116, 2015.

[103] G. Brügger, L. S. Froufe-Pérez, F. Scheffold, and J. J. Sáenz, "Controlling dispersion forces between small particles with artificially created random light fields," *Nat. Commun.*, vol. 6, 2015.

[104] J. S. Douglas, T. Caneva, and D. E. Chang, "Photon molecules in atomic gases trapped near photonic crystal waveguides," *arXiv preprint arXiv:1511.00816*, 2015.

[105] A. Asenjo-Garcia, J. Hood, D. Chang, and H. Kimble, "Atom-light interactions in quasi-1d nanostructures: a green's function perspective," *arXiv preprint arXiv:1606.04977*, 2016.

[106] M. Sonnleitner, M. Ritsch-Marte, and H. Ritsch, "Optical forces, trapping and strain on extended dielectric objects," *Europhys Lett.*, vol. 94, no. 3, p. 34005, 2011.

[107] M. Sonnleitner, M. Ritsch-Marte, and H. Ritsch, "Attractive optical forces from blackbody radiation," *Phy. Rev. Lett*, vol. 111, no. 2, p. 023601, 2013.

[108] G. K. Brennen, I. H. Deutsch, and P. S. Jessen, "Entangling dipole-dipole interactions for quantum logic with neutral atoms," *Phys. Rev. A*, vol. 61, no. 6, p. 062309, 2000.

[109] H. R. Stuart and D. G. Hall, "Enhanced dipole-dipole interaction between elementary radiators near a surface," *Phy. Rev. Lett*, vol. 80, no. 25, p. 5663, 1998.

[110] T. Fischer, P. Maunz, T. Puppe, P. Pinkse, and G. Rempe, "Collective light forces on atoms in a high-finesse cavity," *New J. Phys.*, vol. 3, no. 1, p. 11, 2001.

[111] C. A. Ebongue, D. Holzmann, S. Ostermann, and H. Ritsch, "Generating a stationary infinite range tractor force via a multimode optical fibre," *J. Opt.*, vol. 19, no. 6, p. 065401, 2017.

[112] D. Holzmann and H. Ritsch, "Tailored long range forces on polarizable particles by collective scattering of broadband radiation," *New J. Phys.*, vol. 18, no. 10, p. 103041, 2016.

[113] J.-B. Béguin, E. Bookjans, S. L. Christensen, H. L. Sørensen, J. Müller, J. Appel, and E. Polzik, "Generation and detection of a sub-poissonian atom number distribution in a one-dimensional optical lattice," *arXiv preprint arXiv:1408.1266*, 2014.

[114] M. C. Frawley, I. Gusachenko, V. G. Truong, M. Sergides, and S. N. Chormaic, "Selective particle trapping and optical binding in the evanescent field of an optical nanofiber," *arXiv preprint arXiv:1403.7599*, 2014.

[115] A. Maimaiti, D. Holzmann, V. G. Truong, H. Ritsch, and S. N. Chormaic, "Nonlinear force dependence on optically bound micro-particle arrays in the evanescent fields of fundamental and higher order microfibre modes," *Sci. Rep.*, vol. 6, no. 30131, 2016.

[116] J. Petersen, J. Volz, and A. Rauschenbeutel, "Chiral nanophotonic waveguide interface based on spin-orbit interaction of light," *Science*, vol. 346, no. 6205, pp. 67–71, 2014.

[117] P. Domokos and H. Ritsch, "Efficient loading and cooling in a dynamic optical evanescent-wave microtrap," *Europhys Lett.*, vol. 54, no. 3, p. 306, 2001.

[118] S. Kirkpatrick, "Frustration and ground-state degeneracy in spin glasses," *Phys. Rev. B*, vol. 16, no. 10, p. 4630, 1977.

[119] K. Kim, M.-S. Chang, S. Korenblit, R. Islam, E. E. Edwards, J. K. Freericks, G.-D. Lin, L.-M. Duan, and C. Monroe, "Quantum simulation of frustrated ising spins with trapped ions," *Nature*, vol. 465, no. 7298, pp. 590–593, 2010.

[120] A. Asenjo-Garcia, M. Moreno-Cardoner, A. Albrecht, H. J. Kimble, and D. E. Chang, "Exponential improvement in photon storage fidelities using subradiance and "selective radiance" in atomic arrays," *Phys. Rev. X*, vol. 7, p. 031024, Aug 2017.

[121] V. Torggler, S. Krämer, and H. Ritsch, "Quantum annealing with ultracold atoms in a multimode optical resonator," *Phys. Rev. A*, vol. 95, no. 3, p. 032310, 2017.

[122] A. B. Finnila, M. Gomez, C. Sebenik, C. Stenson, and J. D. Doll, "Quantum annealing: A new method for minimizing multidimensional functions," *Chem. Phys. Lett.*, vol. 219, no. 5-6, pp. 343–348, 1994.

[123] T. Tiecke, J. D. Thompson, N. P. de Leon, L. Liu, V. Vuletić, and M. D. Lukin, "Nanophotonic quantum phase switch with a single atom," *Nature*, vol. 508, no. 7495, pp. 241–244, 2014.

[124] J.-B. Béguin, J. H. Müller, J. Appel, and E. S. Polzik, "Observation of quantum spin noise in a 1d light-atoms quantum interface," *Phys. Rev. X*, vol. 8, no. 3, p. 031010, 2018.

[125] M. A. Nielsen and I. L. Chuang, *Quantum Computation and Quantum Information*. Cambridge University Press, 2000.

[126] H. F. Trotter, "On the product of semi-groups of operators," *Proc. Am. Math. Soc.*, vol. 10, no. 4, pp. 545–551, 1959.

[127] M. Greiner, O. Mandel, T. Esslinger, T. W. Hänsch, and I. Bloch, "Quantum phase transition from a superfluid to a mott insulator in a gas of ultracold atoms," *Nature*, vol. 415, no. 6867, pp. 39–44, 2002.

[128] M. W. Zwierlein, J. R. Abo-Shaeer, A. Schirotzek, C. H. Schunck, and W. Ketterle, "Vortices and superfluidity in a strongly interacting fermi gas," *Nature*, vol. 435, no. 7045, pp. 1047–1051, 2005.

[129] C. Regal, M. Greiner, and D. S. Jin, "Observation of resonance condensation of fermionic atom pairs," *Phy. Rev. Lett*, vol. 92, no. 4, p. 040403, 2004.

[130] J. Dalibard, F. Gerbier, G. Juzeliūnas, and P. Öhberg, "Colloquium: Artificial gauge potentials for neutral atoms," *Rev. Mod. Phys.*, vol. 83, no. 4, p. 1523, 2011.

[131] A. Kay and D. G. Angelakis, "Reproducing spin lattice models in strongly coupled atom-cavity systems," *Europhys Lett.*, vol. 84, no. 2, p. 20001, 2008.

[132] A. D. Greentree, C. Tahan, J. H. Cole, and L. C. Hollenberg, "Quantum phase transitions of light," *Nat. Phys.*, vol. 2, no. 12, pp. 856–861, 2006.

[133] M. J. Hartmann, F. G. Brandao, and M. B. Plenio, "Strongly interacting polaritons in coupled arrays of cavities," *Nat. Phys.*, vol. 2, no. 12, pp. 849–855, 2006.

[134] T. Schätz, A. Friedenauer, H. Schmitz, L. Petersen, and S. Kahra, "Towards (scalable) quantum simulations in ion traps," *J. Mod. Opt.*, vol. 54, no. 16-17, pp. 2317–2325, 2007.

[135] R. Blatt and D. Wineland, "Entangled states of trapped atomic ions," *Nature*, vol. 453, no. 7198, pp. 1008–1015, 2008.

[136] M. Johanning, A. F. Varón, and C. Wunderlich, "Quantum simulations with cold trapped ions," *J. Phys. B: Atomic, Molecular and Optical Physics*, vol. 42, no. 15, p. 154009, 2009.

[137] T. Schaetz, M. D. Barrett, D. Leibfried, J. Chiaverini, J. Britton, W. M. Itano, J. D. Jost, C. Langer, and D. J. Wineland, "Quantum dense coding with atomic qubits," *Phy. Rev. Lett*, vol. 93, no. 4, p. 040505, 2004.

[138] X.-h. Peng and D. Suter, "Spin qubits for quantum simulations," *Front. Phys. China*, vol. 5, no. 1, pp. 1–25, 2010.

[139] X. Peng, J. Zhang, J. Du, and D. Suter, "Quantum simulation of a system with competing two-and three-body interactions," *Phy. Rev. Lett*, vol. 103, no. 14, p. 140501, 2009.

[140] J. Zhang, M.-H. Yung, R. Laflamme, A. Aspuru-Guzik, and J. Baugh, "Digital quantum simulation of the statistical mechanics of a frustrated magnet," *Nat. Commun.*, vol. 3, no. 1, pp. 1–10, 2012.

[141] R. Hanson and D. D. Awschalom, "Coherent manipulation of single spins in semiconductors," *Nature*, vol. 453, no. 7198, pp. 1043–1049, 2008.

[142] R. Harris, M. W. Johnson, T. Lanting, A. Berkley, J. Johansson, P. Bunyk, E. Tolkacheva, E. Ladizinsky, N. Ladizinsky, T. Oh, *et al.*, "Experimental investigation of an eight-qubit unit cell in a superconducting optimization processor," *Phys. Rev. B*, vol. 82, no. 2, p. 024511, 2010.

[143] A. A. Houck, H. E. Türeci, and J. Koch, "On-chip quantum simulation with superconducting circuits," *Nat. Phys.*, vol. 8, no. 4, pp. 292–299, 2012.

[144] J. Koch, A. A. Houck, K. Le Hur, and S. Girvin, "Time-reversal-symmetry breaking in circuit-qed-based photon lattices," *Phys. Rev. A*, vol. 82, no. 4, p. 043811, 2010.

[145] M. R. Geller, J. M. Martinis, A. T. Sornborger, P. C. Stancil, E. J. Pritchett, H. You, and A. Galiautdinov, "Universal quantum simulation with prethreshold

superconducting qubits: Single-excitation subspace method," *Phys. Rev. A*, vol. 91, no. 6, p. 062309, 2015.

[146] J. You, X.-F. Shi, X. Hu, and F. Nori, "Quantum emulation of a spin system with topologically protected ground states using superconducting quantum circuits," *Phys. Rev. B*, vol. 81, no. 1, p. 014505, 2010.

[147] J. J. García-Ripoll, E. Solano, and M. A. Martin-Delgado, "Quantum simulation of anderson and kondo lattices with superconducting qubits," *Phys. Rev. B*, vol. 77, no. 2, p. 024522, 2008.

[148] D. I. Tsomokos, S. Ashhab, and F. Nori, "Fully connected network of superconducting qubits in a cavity," *New J. Phys.*, vol. 10, no. 11, p. 113020, 2008.

[149] D. I. Tsomokos, S. Ashhab, and F. Nori, "Using superconducting qubit circuits to engineer exotic lattice systems," *Phys. Rev. A*, vol. 82, no. 5, p. 052311, 2010.

[150] C.-Y. Lu, W.-B. Gao, O. Gühne, X.-Q. Zhou, Z.-B. Chen, and J.-W. Pan, "Demonstrating anyonic fractional statistics with a six-qubit quantum simulator," *Phy. Rev. Lett*, vol. 102, no. 3, p. 030502, 2009.

[151] B. P. Lanyon, J. D. Whitfield, G. G. Gillett, M. E. Goggin, M. P. Almeida, I. Kassal, J. D. Biamonte, M. Mohseni, B. J. Powell, M. Barbieri, *et al.*, "Towards quantum chemistry on a quantum computer," *Nat. Chem.*, vol. 2, no. 2, pp. 106–111, 2010.

[152] X.-s. Ma, B. Dakic, W. Naylor, A. Zeilinger, and P. Walther, "Quantum simulation of the wavefunction to probe frustrated heisenberg spin systems," *Nat. Phys.*, vol. 7, no. 5, pp. 399–405, 2011.

[153] D. G. Angelakis, M. Huo, E. Kyoseva, and L. C. Kwek, "Luttinger liquid of photons and spin-charge separation in hollow-core fibers," *Phy. Rev. Lett*, vol. 106, no. 15, p. 153601, 2011.

[154] D. G. Angelakis, P. Das, and C. Noh, "Probing the topological properties of the jackiw-rebbi model with light," *Sci. Rep.*, vol. 4, no. 1, pp. 1–6, 2014.

[155] S. Aaronson and A. Arkhipov, "The computational complexity of linear optics," in *Proceedings of the forty-third annual ACM symposium on Theory of computing*, pp. 333–342, 2011.

[156] M. A. Broome, A. Fedrizzi, S. Rahimi-Keshari, J. Dove, S. Aaronson, T. C. Ralph, and A. G. White, "Photonic boson sampling in a tunable circuit," *Science*, vol. 339, no. 6121, pp. 794–798, 2013.

[157] A. Crespi, R. Osellame, R. Ramponi, D. J. Brod, E. F. Galvao, N. Spagnolo, C. Vitelli, E. Maiorino, P. Mataloni, and F. Sciarrino, "Integrated multimode interferometers with arbitrary designs for photonic boson sampling," *Nat. Photonics*, vol. 7, no. 7, pp. 545–549, 2013.

[158] J. B. Spring, B. J. Metcalf, P. C. Humphreys, W. S. Kolthammer, X.-M. Jin, M. Barbieri, A. Datta, N. Thomas-Peter, N. K. Langford, D. Kundys, *et al.*, "Boson sampling on a photonic chip," *Science*, vol. 339, no. 6121, pp. 798–801, 2013.

[159] M. Tillmann, B. Dakić, R. Heilmann, S. Nolte, A. Szameit, and P. Walther, "Experimental boson sampling," *Nat. Photonics*, vol. 7, no. 7, pp. 540–544, 2013.

[160] B. P. Lanyon, C. Hempel, D. Nigg, M. Müller, R. Gerritsma, F. Zähringer, P. Schindler, J. T. Barreiro, M. Rambach, G. Kirchmair, *et al.*, "Universal digital quantum simulation with trapped ions," *Science*, vol. 334, no. 6052, pp. 57–61, 2011.

[161] D. Jaksch, C. Bruder, J. I. Cirac, C. W. Gardiner, and P. Zoller, "Cold bosonic atoms in optical lattices," *Phys. Rev. Lett.*, vol. 81, pp. 3108–3111, Oct 1998.

[162] F. Yamaguchi and Y. Yamamoto, "Quantum simulation of the t–j model," *Superlattice Microst.*, vol. 32, no. 4-6, pp. 343–345, 2002.

[163] A. L. Rakhmanov, A. M. Zagoskin, S. Savel'ev, and F. Nori, "Quantum metamaterials: Electromagnetic waves in a josephson qubit line," *Phys. Rev. B*, vol. 77, p. 144507, Apr 2008.

[164] T. Byrnes and Y. Yamamoto, "Simulating lattice gauge theories on a quantum computer," *Phys. Rev. A*, vol. 73, p. 022328, Feb 2006.

[165] L. Lamata, J. León, T. Schätz, and E. Solano, "Dirac equation and quantum relativistic effects in a single trapped ion," *Phys. Rev. Lett.*, vol. 98, p. 253005, Jun 2007.

[166] P. M. Alsing, J. P. Dowling, and G. J. Milburn, "Ion trap simulations of quantum fields in an expanding universe," *Phys. Rev. Lett.*, vol. 94, p. 220401, Jun 2005.

[167] S. Giovanazzi, "Hawking radiation in sonic black holes," *Phys. Rev. Lett.*, vol. 94, p. 061302, Feb 2005.

[168] U. R. Fischer and R. Schützhold, "Quantum simulation of cosmic inflation in two-component bose-einstein condensates," *Phys. Rev. A*, vol. 70, p. 063615, Dec 2004.

[169] J. Q. You and F. Nori, "Quantum information processing with superconducting qubits in a microwave field," *Phys. Rev. B*, vol. 68, p. 064509, Aug 2003.

[170] A. Aspuru-Guzik, A. D. Dutoi, P. J. Love, and M. Head-Gordon, "Simulated quantum computation of molecular energies," *Science*, vol. 309, no. 5741, pp. 1704–1707, 2005.

[171] I. Kassal, S. P. Jordan, P. J. Love, M. Mohseni, and A. Aspuru-Guzik, "Polynomial-time quantum algorithm for the simulation of chemical dynamics," *Proc. Natl. Acad. Sci. U. S. A.*, vol. 105, no. 48, pp. 18681–18686, 2008.

[172] D. A. Lidar and H. Wang, "Calculating the thermal rate constant with exponential speedup on a quantum computer," *Phys. Rev. E*, vol. 59, pp. 2429–2438, Feb 1999.

[173] J. Piilo and S. Maniscalco, "Driven harmonic oscillator as a quantum simulator for open systems," *Phys. Rev. A*, vol. 74, p. 032303, Sep 2006.

[174] C. H. Tseng, S. Somaroo, Y. Sharf, E. Knill, R. Laflamme, T. F. Havel, and D. G. Cory, "Quantum simulation with natural decoherence," *Phys. Rev. A*, vol. 62, p. 032309, Aug 2000.

[175] J. C. Howell and J. A. Yeazell, "Linear optics simulations of the quantum baker's map," *Phys. Rev. A*, vol. 61, p. 012304, Dec 1999.

[176] Y. S. Weinstein, S. Lloyd, J. Emerson, and D. G. Cory, "Experimental implementation of the quantum baker's map," *Phys. Rev. Lett.*, vol. 89, p. 157902, Sep 2002.

[177] Y. I. Bogdanov, V. F. Lukichev, A. A. Orlikovsky, and S. A. Nuyanzin, "Quantum noise and the quality control of hardward components of quantum computers based on superconducting phase qubits," *Russ. Microelectron.*, no. 41, p. 325–335, 2012.

[178] A. M. Kaufman, B. J. Lester, and C. A. Regal, "Cooling a single atom in an optical tweezer to its quantum ground state," *Phys. Rev. X*, vol. 2, no. 4, p. 041014, 2012.

[179] S. B. Markussen, J. Appel, C. Østfeldt, J.-B. S. Béguin, E. S. Polzik, and J. H. Müller, "Measurement and simulation of atomic motion in nanoscale optical trapping potentials," *Appl. Phys. B*, vol. 126, no. 4, pp. 1–5, 2020.

[180] I. Shomroni, S. Rosenblum, Y. Lovsky, O. Bechler, G. Guendelman, and B. Dayan, "All-optical routing of single photons by a one-atom switch controlled by a single photon," *Science*, vol. 345, no. 6199, pp. 903–906, 2014.

[181] V. Pivovarov, L. Gerasimov, J. Berroir, T. Ray, J. Laurat, A. Urvoy, and D. Kupriyanov, "Single collective excitation of an atomic array trapped along a waveguide: a study of cooperative emission for different atomic chain configurations," *arXiv preprint arXiv:2101.05398*, 2021.

[182] J. I. Cirac, "Atomic self-organization around tappered nanofibers," in *Laser Science*, pp. LW1J–6, J. Opt. Soc. Am., 2012.

[183] N. K. Metzger, E. M. Wright, W. Sibbett, and K. Dholakia, "Visualization of optical binding of microparticles using a femtosecond fiber optical trap," *Opt. Express*, vol. 14, no. 8, pp. 3677–3687, 2006.

[184] G. Buonaiuto, F. Carollo, B. Olmos, and I. Lesanovsky, "Dynamical phases and quantum correlations in an emitter-waveguide system with feedback," *arXiv preprint arXiv:2102.02719*, 2021.

[185] D. Holzmann, M. Sonnleitner, and H. Ritsch, "Synthesizing variable particle interaction potentials via spectrally shaped spatially coherent illumination," *New J. Phys.*, vol. 20, no. 10, p. 103009, 2018.

[186] Z. Davoudi, M. Hafezi, C. Monroe, G. Pagano, A. Seif, and A. Shaw, "Towards analog quantum simulations of lattice gauge theories with trapped ions," *Phys. Rev. Res.*, vol. 2, no. 2, p. 023015, 2020.

[187] J. I. Cirac and P. Zoller, "Quantum computations with cold trapped ions," *Phy. Rev. Lett*, vol. 74, no. 20, p. 4091, 1995.

[188] M. Mirhosseini, E. Kim, X. Zhang, A. Sipahigil, P. B. Dieterle, A. J. Keller, A. Asenjo-Garcia, D. E. Chang, and O. Painter, "Cavity quantum electrodynamics with atom-like mirrors," *Nature*, vol. 569, no. 7758, pp. 692–697, 2019.

[189] P. Kok, W. J. Munro, K. Nemoto, T. C. Ralph, J. P. Dowling, and G. J. Milburn, "Linear optical quantum computing with photonic qubits," *Rev. Mod. Phys.*, vol. 79, no. 1, p. 135, 2007.

[190] H. Jeong and M. S. Kim, "Efficient quantum computation using coherent states," *Phys. Rev. A*, vol. 65, no. 4, p. 042305, 2002.

[191] T. C. Ralph, A. Gilchrist, G. J. Milburn, W. J. Munro, and S. Glancy, "Quantum computation with optical coherent states," *Phys. Rev. A*, vol. 68, no. 4, p. 042319, 2003.

[192] P. Marek and J. Fiurášek, "Elementary gates for quantum information with superposed coherent states," *Phys. Rev. A*, vol. 82, no. 1, p. 014304, 2010.

[193] O. A. Iversen and T. Pohl, "Strongly correlated states of light and repulsive photons in chiral chains of three-level quantum emitters," *Phy. Rev. Lett.*, vol. 126, no. 8, p. 083605, 2021.

[194] H. Jen, "Bound and subradiant multi-atom excitations in an atomic array with nonreciprocal couplings," *arXiv preprint arXiv:2102.03757*, 2021.

[195] C. Cohen-Tannoudji, B. Diu, and F. Laloe, *Quantum Mechanics, Volume 1: Basic Concepts, Tools, and Applications*. Wiley, 2019.

[196] R. Schnabel, A. Bunkowski, O. Burmeister, and K. Danzmann, "Three-port beam splitters-combiners for interferometer applications," *Opt. Lett.*, vol. 31, no. 5, pp. 658–660, 2006.

[197] R. W. Applegate, J. Squier, T. Vestad, J. Oakey, and D. W. Marr, "Optical trapping, manipulation, and sorting of cells and colloids in microfluidic systems with diode laser bars," *Opt. Express*, vol. 12, no. 19, pp. 4390–4398, 2004.

[198] S. Tatarkova, A. Carruthers, and K. Dholakia, "One-dimensional optically bound arrays of microscopic particles," *Phy. Rev. Lett.*, vol. 89, no. 28, p. 283901, 2002.

[199] V. Karásek, O. Brzobohatỳ, and P. Zemánek, "Longitudinal optical binding of several spherical particles studied by the coupled dipole method," *J. Opt. A: Pure and Applied Optics*, vol. 11, no. 3, p. 034009, 2009.

[200] M. Guillon, "Field enhancement in a chain of optically bound dipoles," *Opt. Express*, vol. 14, no. 7, pp. 3045–3055, 2006.

[201] O. Brzobohatỳ, T. Čižmár, V. Karásek, M. Šiler, K. Dholakia, and P. Zemánek, "Experimental and theoretical determination of optical binding forces," *Opt. Express*, vol. 18, no. 24, pp. 25389–25402, 2010.

[202] V. Garcés-Chávez, K. Dholakia, and G. Spalding, "Extended-area optically induced organization of microparticles on a surface," *Appl. Phys. Lett.*, vol. 86, no. 3, p. 031106, 2005.

[203] M. Šiler, T. Čižmár, M. Šerỳ, and P. Zemánek, "Optical forces generated by evanescent standing waves and their usage for sub-micron particle delivery," *Appl. Phys. B*, vol. 84, no. 1, pp. 157–165, 2006.

[204] K. Grujic and O. G. Hellesø, "Dielectric microsphere manipulation and chain assembly by counter-propagating waves in a channel waveguide," *Opt. Express*, vol. 15, no. 10, pp. 6470–6477, 2007.

[205] H. Xin, R. Xu, and B. Li, "Optical formation and manipulation of particle and cell patterns using a tapered optical fiber," *Laser Photonics Rev.*, vol. 7, no. 5, pp. 801–809, 2013.

[206] S. Skelton, M. Sergides, R. Patel, E. Karczewska, O. Maragó, and P. Jones, "Evanescent wave optical trapping and transport of micro-and nanoparticles on tapered optical fibers," *J. Quant. Spectrosc. Radiat. Transfer*, vol. 113, no. 18, pp. 2512–2520, 2012.

[207] J. M. Ward, D. G. O'Shea, B. J. Shortt, M. J. Morrissey, K. Deasy, and S. G. Nic Chormaic, "Heat-and-pull rig for fiber taper fabrication," *Rev. Sci. Instrum.*, vol. 77, no. 8, p. 083105, 2006.

[208] J. Ward, A. Maimaiti, V. H. Le, and S. N. Chormaic, "Contributed review: Optical micro-and nanofiber pulling rig," *Rev. Sci. Instrum.*, vol. 85, no. 11, p. 111501, 2014.

[209] M. Sumetsky and L. Tong, "Subwavelength and nanometer diameter optical fibers (zhejiang)," 2010.

[210] M. Daly, M. Sergides, and S. Nic Chormaic, "Optical trapping and manipulation of micrometer and submicrometer particles," *Laser Photonics Rev.*, vol. 9, no. 3, pp. 309–329, 2015.

[211] H. Lei, Y. Zhang, X. Li, and B. Li, "Photophoretic assembly and migration of dielectric particles and escherichia coli in liquids using a subwavelength diameter optical fiber," *Lab on a Chip*, vol. 11, no. 13, pp. 2241–2246, 2011.

[212] H. Xin, C. Cheng, and B. Li, "Trapping and delivery of escherichia coli in a microfluidic channel using an optical nanofiber," *Nanoscale*, vol. 5, no. 15, pp. 6720–6724, 2013.

[213] L. Xu, Y. Li, and B. Li, "Size-dependent trapping and delivery of submicro-spheres using a submicrofibre," *New J. Phys.*, vol. 14, no. 3, p. 033020, 2012.

[214] K. Nayak, P. Melentiev, M. Morinaga, F. Le Kien, V. Balykin, and K. Hakuta, "Optical nanofiber as an efficient tool for manipulating and probing atomic fluorescence," *Opt. Express*, vol. 15, no. 9, pp. 5431–5438, 2007.

[215] G. Sagué, E. Vetsch, W. Alt, D. Meschede, and A. Rauschenbeutel, "Cold-atom physics using ultrathin optical fibers: Light-induced dipole forces and surface interactions," *Phy. Rev. Lett*, vol. 99, no. 16, p. 163602, 2007.

[216] M. J. Morrissey, K. Deasy, Y. Wu, S. Chakrabarti, and S. Nic Chormaic, "Tapered optical fibers as tools for probing magneto-optical trap characteristics," *Rev. Sci. Instrum.*, vol. 80, no. 5, p. 053102, 2009.

[217] M. J. Morrissey, K. Deasy, M. Frawley, R. Kumar, E. Prel, L. Russell, V. G. Truong, and S. Nic Chormaic, "Spectroscopy, manipulation and trapping of neutral atoms, molecules, and other particles using optical nanofibers: a review," *Sensors*, vol. 13, no. 8, pp. 10449–10481, 2013.

[218] J. Fu, X. Yin, and L. Tong, "Two-colour atom guide and 1d optical lattice using evanescent fields of high-order transverse modes," *J. Phys. B: Atomic, Molecular and Optical Physics*, vol. 40, no. 21, p. 4195, 2007.

[219] J. Fu, X. Yin, N. Li, and L. Tong, "Atom waveguide and 1d optical lattice using a two-color evanescent light field around an optical micro/nano-fiber," *Chin. Opt. Lett.*, vol. 6, no. 2, pp. 112–115, 2008.

[220] G. Sagué, A. Baade, and A. Rauschenbeutel, "Blue-detuned evanescent field surface traps for neutral atoms based on mode interference in ultrathin optical fibres," *New J. Phys.*, vol. 10, no. 11, p. 113008, 2008.

[221] C. Phelan, T. Hennessy, and T. Busch, "Shaping the evanescent field of optical nanofibers for cold atom trapping," *Opt. Express*, vol. 21, no. 22, pp. 27093–27101, 2013.

[222] R. Kumar, V. Gokhroo, K. Deasy, A. Maimaiti, M. C. Frawley, C. Phelan, and S. N. Chormaic, "Interaction of laser-cooled 87rb atoms with higher order modes of an optical nanofibre," *New J. Phys.*, vol. 17, no. 1, p. 013026, 2015.

[223] A. Maimaiti, V. G. Truong, M. Sergides, I. Gusachenko, and S. N. Chormaic, "Higher order microfibre modes for dielectric particle trapping and propulsion," *Sci. Rep.*, vol. 5, no. 1, pp. 1–8, 2015.

[224] A. Maimaiti, V. G. Truong, and S. N. Chormaic, "Ultrathin optical fibers for particle trapping and manipulation," in *Asia Communications and Photonics Conference*, pp. ATh2B–1, J. Opt. Soc. Am., 2016.

[225] A. Petcu-Colan, M. Frawley, and S. N. Chormaic, "Tapered few-mode fibers: mode evolution during fabrication and adiabaticity," *J. Nonlinear Opt. Phys. Mater.*, vol. 20, no. 03, pp. 293–307, 2011.

[226] M. C. Frawley, A. Petcu-Colan, V. G. Truong, and S. N. Chormaic, "Higher order mode propagation in an optical nanofiber," *Opt. Commun.*, vol. 285, no. 23, pp. 4648–4654, 2012.

[227] S. Marksteiner, C. Savage, P. Zoller, and S. Rolston, "Coherent atomic waveguides from hollow optical fibers: quantized atomic motion," *Phys. Rev. A*, vol. 50, no. 3, p. 2680, 1994.

[228] O. Brzobohatỳ, V. Karásek, M. Šiler, L. Chvátal, T. Čižmár, and P. Zemánek, "Experimental demonstration of optical transport, sorting and self-arrangement using a 'tractor beam'," *Nat. Photonics*, vol. 7, no. 2, pp. 123–127, 2013.

[229] M. Sadgrove, S. Wimberger, and S. N. Chormaic, "Quantum coherent tractor beam effect for atoms trapped near a nanowaveguide," *Sci. Rep.*, vol. 6, no. 1, pp. 1–13, 2016.

[230] R. Gómez-Medina, P. San José, A. García-Martín, M. Lester, M. Nieto-Vesperinas, and J. Sáenz, "Resonant radiation pressure on neutral particles in a waveguide," *Phy. Rev. Lett*, vol. 86, no. 19, p. 4275, 2001.

[231] P. Horak, P. Domokos, and H. Ritsch, "Giant lamb shift of atoms near lossy multimode optical micro-waveguides," *Europhys Lett.*, vol. 61, no. 4, p. 459, 2003.

[232] P. Russell, "Photonic crystal fibers," *Science*, vol. 299, no. 5605, pp. 358–362, 2003.

[233] M. J. Renn, D. Montgomery, O. Vdovin, D. Anderson, C. Wieman, and E. Cornell, "Laser-guided atoms in hollow-core optical fibers," *Phy. Rev. Lett*, vol. 75, no. 18, p. 3253, 1995.

[234] D. B. Ruffner and D. G. Grier, "Optical conveyors: a class of active tractor beams," *Phy. Rev. Lett*, vol. 109, no. 16, p. 163903, 2012.

[235] S. Vorrath, S. Möller, P. Windpassinger, K. Bongs, and K. Sengstock, "Efficient guiding of cold atoms through a photonic band gap fiber," *New J. Phys.*, vol. 12, no. 12, p. 123015, 2010.

[236] C. Lamprecht and M. A. Marte, "Comparing paraxial atom and light optics," *Quantum and Semiclassical Optics: J. Eur. Opt. Soc. Part B*, vol. 10, no. 3, p. 501, 1998.

List of publications

Publications during the PhD

- D. Holzmann; M. Sonnleitner, H. Ritsch. A versatile quantum simulator for coupled oscillators using a 1D chain of atoms trapped near an optical nanofiber. *arXiv preprint arXiv*: 2105.03262 (2021).
- D. Holzmann; M. Sonnleitner, H. Ritsch. Synthesizing variable particle interaction potentials via spectrally shaped spatially coherent illumination. *New J. Phys.* 20, 103009 (2018).
- C. Ebongue, D. Holzmann, S. Ostermann, H. Ritsch. Generating a stationary infinite range tractor force via a multimode optical fibre. *J. Opt.* 19, 065401 (2017).
- D. Holzmann, H. Ritsch. Tailored long range forces on polarizable particles by collective scattering of broadband radiation. *New J. Phys.* 18, 103041 (2016).
- A. Maimaiti, D. Holzmann, V.G. Truong, H. Ritsch, S.N. Chormaic. Nonlinear force dependence on optically bound micro-particle arrays in the evanescent fields of fundamental and higher order microfibre modes. *Sci. Rep.* 6, 30131 (2016).
- D. Holzmann, H. Ritsch. Collective scattering and oscillation modes of optically bound point particles trapped in a single mode waveguide field. *Opt. Express* 23/25, 31793 (2015).

Publications before starting the PhD

- D. Holzmann, M. Sonnleitner, H. Ritsch. Self-ordering and collective dynamics of transversely illuminated point-scatterers in a 1D trap. *Eur. Phys. J. D. Atomic, Molecular, Optical and Plasma Physics* 68, 352 (2014).